On the influence of temperature and humidity on interfaces in carbon fiber reinforced polyamide 6

Zur Erlangung des akademischen Grades eines
DOKTORS DER INGENIEURWISSENSCHAFTEN
(Dr.-Ing.)

von der KIT-Fakultät für Maschinenbau des
Karlsruher Instituts für Technologie (KIT)
angenommene

DISSERTATION

von

Nicolas Christ, M.Sc.
geb. in Worms

Tag der mündlichen Prüfung:	30.04.2026
Hauptreferent:	Prof. Dr. rer. nat. Peter Gumbsch
Korreferenten:	PD Dr.-Ing. habil. Jörg Hohe
	Prof. John Montesano, Ph.D.

Wer das Denken zur Hauptsache macht, der kann es darin zwar weit bringen, aber er hat doch eben den Boden mit dem Wasser vertauscht, und einmal wird er ersaufen.

HERMANN HESSE

Kurzfassung

Das Ziel der vorliegenden Arbeit bestand darin die Charakteristiken von Grenzflächen innerhalb Kohlenstofffaserverstärktem Polyamid 6 experimentell sowie numerisch zu untersuchen. Hierbei wurden variable klimatische Randbedingungen in Form von Temperatur und Feuchtigkeit berücksichtigt. Es wurde zwischen der mikroskopischen Grenzfläche, also der Anbindung von Faser und Polymer, sowie einer makroskopischen Grenzfläche zwischen kontinuierlich (Co) und diskontinuierlich (Dico) verstärkten Materialien innerhalb eines Verbund-Hybriden, dem Co-Dico-Verbund, unterschieden. Die verschiedenen Grenzflächen bedingen die Übertragung von Spannungen zwischen Faser und Matrix bzw. den verschiedenen Schichtungen im hybriden Verbund und sind daher entscheidend für die effektiven mechanischen Eigenschaften und die Belastbarkeit des untersuchten Kompositen. Es ist daher essentiell die Mechanismen entlang der Grenzflächen während Belastung und Überlastung zu verstehen. Durch die hygroskope Eigenschaft des untersuchten Polymers ist es zudem von hoher Relevanz die Einflüsse von klimatischen Randbedingungen auf die mechanischen Eigenschaften dieser Grenzflächen zu untersuchen. Um die klimatischen Einflüsse auf die Grenzflächeneigenschaften besser von den Einflüssen auf das Matrixverhalten zu trennen, wurden zunächst Kriechversuche am reinen Polymer unter vier verschiedenen Temperatur-Feuchtigkeits-Kombinationen durchgeführt, worauf ein nichtlineares visko-elastisches Modell nach Schapery mit guter Übereinstimmung angepasst wurde. Zur Untersuchung der Faser-Matrix-Anbindung wurde der Single Fiber Pull-Out Test verwendet, wobei die experimentelle Methodik um eine Klimatisierung während des Versuchs erweitert wurde. Hierdurch konnte ermöglicht werden, dass die Experimente ebenfalls unter den vier verschiedenen Temperatur-Feuchtigkeits-Kombinationen durchgeführt werden konnten. Die

Eigenschaften der makroskopischen Grenzfläche wurden erstmals mithilfe des Climbing-Drum-Peel Tests untersucht, wobei die Proben unter unterschiedlichen relativen Feuchtigkeiten konditioniert wurden. Die experimentellen Ergebnisse zeigen eine starke, nichtlineare Abhängigkeit von Temperatur und Feuchtigkeit, sowohl des reinen Matrixverhaltens, als auch der beiden Grenzflächen. Die Feuchtigkeitsaufnahme führt zu einer Verschlechterung der vorwiegend mechanischen Faser-Matrix-Anbindung. Die numerischen Untersuchungen anhand des kalibrierten Modells konnten die Mechanismen auf reduzierte Eigenspannungsfelder aufgrund hygroskoper Volumenzunahme zurückführen. Im Falle der Co-Dico-Grenzfläche zeigte sich, dass die Feuchtigkeitsaufnahme aufgrund des plastifizierenden Einflusses von Wasser mit einer verbesserten Risszähigkeit einhergeht, bevor eine zusätzliche Feuchtigkeitsaufnahme und die daraus resultierende hydrolylitische Schädigung der Polymerketten zu einer erneuten Verringerung der Zähigkeit führen. Die Kombination der Ergebnisse beider Grenzflächen zeigte, dass es eine komplexe Wechselwirkung zwischen den Grenzflächen gibt, sodass die Abnahme der Haftung innerhalb der Faser-Matrix-Grenzfläche durchaus zu einer gezielten Verbesserung der mechanischen Eigenschaften innerhalb der Co-Dico-Grenzfläche führen kann. Dies verdeutlicht die Bedeutung einer umfassenden Untersuchung der Eigenschaften von Grenzflächen und ihres Einflusses auf das effektive Verhalten von Verbundwerkstoffen unter verschiedenen klimatischen Randbedingungen. Die Ergebnisse dieser Arbeit tragen zum tieferen Verständnis der Grenzflächenmechaniken auf verschiedenen Skalen innerhalb thermoplastischer Faserverbunde bei. Das Berücksichtigen dieser Erkenntnisse in relevanten Anwendungsfällen, wie dem Leichtbau, trägt zu einer gezielten und anwendungsgerechten Auslegung hochkomplexer Bauteile bei.

Abstract

The goal of this work was to experimentally and numerically investigate the characteristics of interfaces within carbon fiber reinforced polyamide 6. Variable climatic boundary conditions, such as temperature and humidity, were considered in the study. A distinction was made between the microscopic interface, which involves the bonding of fiber and polymer, and a macroscopic interface between continuously (Co) and discontinuously (Dico) reinforced materials within a composite hybrid, i.e., the Co-Dico composite. These interfaces significantly influence stress transfer between the fiber and matrix, as well as among the varying layers in the hybrid composite, making them crucial for the effective mechanical properties and load-bearing capacity of the studied composite. Understanding the mechanisms at the interfaces during loading and overstressing is therefore essential. Due to the hygroscopic nature of the investigated polymer, it is also pertinent to examine the effects of climatic boundary conditions on the mechanical properties of these interfaces. To better isolate climatic influences on interfacial properties from those affecting matrix behavior, creep tests were first conducted on the pure polymer under four different temperature-humidity combinations, followed by fitting a nonlinear viscoelastic Schapery model with good agreement. The single fiber pull-out test was employed to study fiber-matrix bonding, with the experimental methodology enhanced to allow conditioning during the test. This enabled experiments to be conducted under the four distinct temperature-humidity combinations. The macroscopic interface properties were investigated for the first time using the climbing drum peel test, with samples conditioned under varying relative humidities. The experimental results exhibit a strong, nonlinear dependency on temperature and humidity for both the pure matrix behavior

and the two interfaces. Moisture absorption leads to a deterioration of the primarily mechanical fiber-matrix bonding. The numerical investigations based on the calibrated model attributed the mechanisms to reduced residual stress fields due to hygroscopic swelling. For the Co-Dico interface, it was observed that moisture absorption, due to the plasticizing effect of water, correlates with improved fracture toughness, before further moisture uptake and resulting hydrolytic damage to the polymer chains lead to a subsequent reduction in toughness. The combined results from both interfaces demonstrated a complex interaction, such that the decrease in adhesion within the fiber-matrix interface can indeed result in targeted improvements of the mechanical properties within the Co-Dico interface. This emphasizes the importance of a comprehensive examination of interface properties and their influence on the effective behavior of composites under varying climatic conditions. The findings of this work contribute to a deeper understanding of interfacial mechanics at different scales within thermoplastic fiber composites. Considering these insights in relevant applications, such as lightweight construction, aids in the targeted and application specific design of highly complex components.

Danksagung

Zunächst möchte ich meinen akademischen Bezugspersonen danken. Ich danke Peter Gumbsch für die übernahme des Hauptreferates und für die kritischen Diskussionen in der Endphase dieser Arbeit. Jörg Hohe danke ich dafür, dass er sich stets die Zeit für Fragen genommen hat und für den mir gegebenen Freiraum für die Gestaltung dieser Arbeit. John Montesano danke ich für seine kritischen Fragen, die mich immer wieder in die richtige Richtung leiten konnten und für die Möglichkeiten, die er mir als Gastwissenschaftler in Kanada gegeben hat. Thomas Böhlke danke ich für die Koordination des Graduiertenkollegs und für sein Interesse am Gelingen dieser Arbeit. Darüber hinaus danke ich ihm für seine Lehre und Förderung, die überhaupt erst den Grundstein für mein Interesses an Fragestellungen der Mechanik gelegt haben. Kay Weidenmann möchte ich für die regen Diskussionen und Lösungsvorschläge danken, die mir in den vergangenen Jahren immer wieder dabei geholfen haben, meine Forschung vorantreiben zu können. Matti Schneider danke ich für seine für Ingenieure unkonventionelle und erfrischende Sichtweise, für seine Lehrinhalte zum Thema Mikrostrukturerzeugung und für die Durchführung des lehrreichen Seminars in Paris.

Innerhalb meines Arbeitsumfeldes danke ich Benedikt Rohrmüller für die Zeit, die er sich genommen hat, mich in die Thematik und den Umgang mit Prüfmaschinen einzuarbeiten und dafür, dass er sich ein Büro mit mir geteilt hat. Gerhard Stöhr und Michael Deissenbeck danke ich für ihr fachliches Wissen im Umgang mit der Versuchsdurchführung und bei der Unterstützung meine Ideen konstruktiv in die Tat umsetzen zu können. Achim Neubrandt danke ich für seine eleganten Lösungsansätze und sein tiefgreifendes Verständnis chemischer und thermodynamischer Zusammenhänge, durch dessen Hilfe mir so einiges Kopfzerbrechen genommen wurde. Hemanth Nallani danke ich für die vielen Hilfestellungen im

Umgang mit Abaqus und seine Kochkünste. Aus dem Gradiuiertenkolleg danke ich Christoph Schelleis und Louis Schreyer für die gemeinsamen kurzweiligen Unternehmungen. Den anderen Doktoranden am Institut danke ich für die vielen witzigen Stunden beim Mittagessen, die länglichen Kaffeerunden und für die schönsten Radausfahrten in Schwarzwald und Umgebung. Hierzu zählen Max Baur, Tobias König, Matthias Quast, Najoua Bolakhrif und insbesondere Johannes Rosenberger und Jan Radners, die sich gerne weiterhin in meiner Kaffee-Strichliste ungefragt eintragen dürfen. Ich möchte mich auch bei Mohammad Jaleh für sein außerordentliches Interesse und seine kreativen Beiträge innerhalb unserer Zusammenarbeit bedanken.

Mein kategorisch nicht einordbarer Dank gelten Juliane Blarr und Benedikt Scheuring. Juliane danke ich dafür, dass sie mich schon seit vielen Jahren vor der Promotion als sehr geschätzte Freundin durchs Leben begleitet. Von Weissach über Karlsruhe, nach Freiburg und wieder zurück warst du immer eine treue Seele für mich und ich hoffe, dass sich unsere Wege weiterhin rege kreuzen werden. Benedikt danke ich für seine ansteckende Begeisterung, seine tollen Ideen, seine ständige Unterstützung und sein einzigartiges Lachen.

Ein besonderer Dank gilt meinen Freunden von daheim und anderswo. Hierzu gehören Frederik und Tanja Willersinn, bei denen ich mich stets wohl gefühlt habe, ob in Freiburg oder daheim. Besonders denke ich auch an Johannes Weigert, Marko Hecht, Maximilian Gerst, Louis Dietrich, Dominik Kaschek und Manuel Görthofer. Ich danke diesen Freunden für ihre Freundschaft, Zeit und Liebe. Große Dankbarkeit verspüre ich besonders für Xiru Wang für die Unterstützung und Liebe in den letzten Jahren.

Mit ganzem Herzen danke ich meinen Eltern Elke Kertels und Hermann Christ und meinem Bruder Maximilian Christ. Ohne eure Unterstützung, euren Rückhalt und eure Liebe hätte aus mir nie nur irgendetwas werden können.

Freiburg, Februar 2026 *Nicolas Christ*

Publications and presentations

Publications

1. N. Christ, J. Montesano, and J. Hohe. Experimental investigation of carbon long fiber reinforced polyamide 6 exposed to environmental conditions. *PAMM*, 22(1), 2023. ISSN 1617-7061. doi: 10.1002/pamm.202200166

2. N. Christ, B. M. Scheuring, J. Montesano, and J. Hohe. A Python package for homogenization procedures in fiber reinforced polymers. *Journal of Open Source Software*, 8(87):5295, 2023. doi: 10.21105/joss.05295

3. N. Christ, B. M. Scheuring, C. Schelleis, W. V. Liebig, J. Montesano, K. A. Weidenmann, and J. Hohe. Characterization and simulation of the interface between a continuous and discontinuous carbon fiber reinforced thermoplastic by using the climbing drum peel test considering humidity. *Polymers*, 16(7), 2024. doi: 10.3390/polym16070976

4. L. Schreyer, B. M. Scheuring, N. Christ, J. Blarr, C. Krauß, W. V. Liebig, K. A. Weidenmann, T. Böhlke, A. Hrymak, and L. Kärger. Continuous simulation of a continuous-discontinuous fiber reinforced thermoplastic (CoDiCoFRTP) compression molding process. In Queen's University Belfast, University Road, Belfast, Northern Ireland, BT7 1NN, editor, *Proceedings of the 2023 International Conference on Composite Materials*. Queen's University Belfast, 2023. doi: 10.5445/IR/1000163456

5. B. M. Scheuring, N. Christ, J. Blarr, W. V. Liebig, J. Hohe, J. Montesano, and K. A. Weidenmann. Experimental and homogenized orientation-dependent

properties of hybrid long fiber-reinforced thermoplastics. *International Journal of Mechanical Sciences*, page 109470, 2024. ISSN 00207403. doi: 10.1016/j.ijmecsci.2024.109470

6. N. Christ, P. Gumbsch, and J. Hohe. Single fiber pull-out investigation at different temperature and humidity conditions: Experimental characterization of the fiber-matrix interface in carbon fiber reinforced polyamide 6. *Journal of Thermoplastic Composite Materials*, 2025. ISSN 0892-7057. doi: 10.1177/08927057251314436

Presentations

1. N. Christ, J. Montesano and J. Hohe. Experimental investigation and modelling of the quasi-static micro-mechanical behavior in carbon long fiber reinforced polyamide 6 exposed to various environmental conditions. *92nd GAMM Annual Meeting*, International Association of Applied Mathematics and Mechanics, Aachen, Germany, 2022.

2. N. Christ, B. M. Scheuring, J. Montesano and J. Hohe. Characterization and simulation of the interface between continuously and discontinuously fiber reinforced thermoplastics. *23rd International Conference on Composite Materials*, International Committee on Composite Materials (ICCM), Belfast, United Kingdom.

3. L. Schreyer, B. M. Scheuring, N. Christ, J. Blarr, C. Krauß, W. V. Liebig, K. A. Weidenmann, T. Böhlke, A. Hrymak and L. Kärger. Continuous simulation of a continuous-discontinuous fiber-reinforced thermoplastic (CoDiCoFRTP) compression molding process. *23rd International Conference on Composite Materials*, International Committee on Composite Materials (ICCM), Belfast, United Kingdom.

4. N. Christ, J. Montesano and J. Hohe. Effects of temperature and humidity on the interfacial shear strength of carbon fiber reinforced polyamide 6: Insights from Single Fiber Pull-Out Tests and Finite Element Analysis. *94th GAMM Annual Meeting*, International Association of Applied Mathematics and Mechanics, Magdeburg, Germany, 2024.

5. N. Christ, J. Blarr and B. M. Scheuring. GRK2078 - Overview research area characterization. *28th National SAMPE Symposium*, SAMPE Deutschland e.V., Karlsruhe, Germany, 2024.

6. N. Christ, B. M. Scheuring, J. Montesano and J. Hohe. Charakterisierung und Simulation der Grenzfläche zwischen kontinuierlich und diskontinuierlich faserverstärkten Thermoplasten. *24. Symposium Verbundwerkstoffe*

und Werkstoffverbunde, Deutsche Gesellschaft für Materialkunde e.V., Freiburg, Germany, 2024.

7. B. M. Scheuring, J. Blarr, N. Christ, J. Hohe, W. V. Liebig, J. Montesano and K. A. Weidenmann. Experimentelle Untersuchung und Homogenisierung der richtungsabhängigen Zugeigenschaften von mono und mischfaser verstärktem LFT. *24. Symposium Verbundwerkstoffe und Werkstoffverbunde*, Deutsche Gesellschaft für Materialkunde e.V., Freiburg, Germany, 2024.

8. N. Christ, B. Rohrmüller, J. Hohe and C. Beckmann. Modeling and mechanical characterization of the uncertainty of injection molded short fiber reinforced polymers. *6th International Conference on Uncertainty Quantification in Computational Science and Engineering*, Europen Community on Computational Methods in Applied Sciences, Rhodes Island, Greece, 2025.

Contents

Acronyms and symbols

Acronyms

1D	One-dimensional
3D	Three-dimensional
ASTM	American Society for Testing and Materials
CDP	Climbing drum peel
CF	Carbon fiber
CF-PA(6)	Carbon fiber reinforced polyamide (6)
CME	Coefficient of moisture expansion
Co	Continuous (fiber reinforced polymer)
Co-Dico	Continuous-discontinuous (fiber reinforced polymer)
CSB	Cracked sandwich beam
CTE	Coefficient of thermal expansion
CZM	Cohesive zone model
DCB	Double cantilever beam
Dico	Discontinuous (fiber reinforced polymer)
DIN EN	German Institute for Standardization European Norm

DMA	Dynamic mechanical analysis
DSC	Differential scanning calorimetry
DSLR	Digital single-lens reflex (camera)
ENF	End notch flexure
Exp.	Experiment
FEA	Finite element analysis
FEM	Finite element method
FIBRE	Faserinstitut Bremen e.V.
FOD	Fiber orientation distribution
FRP	Fiber reinforced polymer
GAB	Guggenheim-Anderson-de-Boer
GPa	Gigapascal
HT	Halpin-Tsai
IFSS	Interfacial shear strength
IRTG	International research training group
LAA	Laminate analogy approach
LFT	Long fiber reinforced thermoplastic
LFT-D	Long fiber reinforced thermoplastic direct process
lin.	Linear
MAF	Mobile amorphous phase fraction
MOSFET	Metal-oxide-semiconductor field-effect transistor
MPa	Megapascal

MT	Mori-Tanaka
MTPB	Modified three-point bending
PA(6)	Polyamide (6)
PAN	Polyacrylonitrile
PID	Proportional-integral-derivative (controller)
PTFE	Polytetrafluoroethylene
PWM	Pulse-width modulation
RAF	Rigid amorphous phase fraction
RC	Room climate
r.H.	Relative humidity
SAM	Sequential addition and migration
SCB	Single cantilever beam
SEM	Scanning electron microscope
SFPO	Single-fiber pull-out
SFT	Short fiber reinforced thermoplastic
Sim.	Simulation
SIP	Single inclusion problem
TMDSC	Temperature modulated differential scanning calorimetry
TSD	Tilted sandwich debond
TSL	Traction separation law
UD	Uni-directional

Latin symbols and variables

a	Water activity, or aspect ratio
A	Area
$\mathbb{A}$	Strain localization tensor, $\mathbb{A} \in \mathbb{R}^{3\times3\times3\times3}$
C	Stiffness value
$\mathbb{C}$	Stiffness tensor, $\mathbb{C} \in \mathbb{R}^{3\times3\times3\times3}$
E	Young's modulus
E'	Storage modulus
E''	Loss modulus
$E^\star$	Complex modulus
F	Force
F_ψ	Cumulative distribution function of FOD
G	Shear modulus
$\mathcal{G}_c$	Critical energy release rate, or cohesive/separation energy
$\mathcal{G}_\mathrm{d}$	Surface specific debonding energy
$\mathcal{G}_\mathrm{f}$	Surface specific frictional energy
H	Heaviside step function
$\mathcal{H}$	Relative humidity
$\mathbb{I}$	Identity tensor, $\mathbb{I} \in \mathbb{R}^{3\times3\times3\times3}$
J	Creep compliance
J_0	Initial creep compliance

ΔJ	Transient creep compliance
K	Bulk modulus
K_0	Cohesive stiffness
$\underline{\underline{K}}$	Cohesive stiffness matrix, $\underline{\underline{K}} \in \mathbb{R}^{3\times3}$
l	Length
$\underline{\underline{M}}$	Matrix mapping operator, $\underline{\underline{K}} \in \mathbb{R}^{6\times6}$
n	Shear-lag parameter
$\boldsymbol{N}$	Fiber orientation tensor of second order
$\mathbb{N}$	Fiber orientation tensor of fourth order
$\mathbb{P}_1$	Spherical projector, i.e., $\mathbb{P}_1 : \boldsymbol{\varepsilon} = \boldsymbol{\varepsilon}^{\circ}$, $\mathbb{P}_1 \in \mathbb{R}^{3\times3\times3\times3}$
$\mathbb{P}_2$	Deviatoric projector, i.e., $\mathbb{P}_2 : \boldsymbol{\varepsilon} = \boldsymbol{\varepsilon}'$, $\mathbb{P}_2 \in \mathbb{R}^{3\times3\times3\times3}$
$\mathcal{P}$	Probability
$\boldsymbol{p}$	Fiber orientation vector
r	Radius
t	Time or scalar traction
$\underline{t}$	Traction vector, $\underline{t} \in \mathbb{R}^{3\times1}$
T_{c}	Crystallization temperature
T_{g}	Glass Transition temperature
T_{m}	Melting temperature
T_{σ}	Stress-free temperature
u	Displacement
V	Volume

v	Volume fraction
W	Mass or work
w	Mass fraction
$\mathcal{W}_{\mathrm{H_2O}}$	Moisture uptake fraction
X_{c}	Crystallinity fraction
X_{MAF}	MAF fraction
X_{RAF}	RAF fraction

Greek symbols and variables

δ	Dirac delta function or separation
$\underline{\delta}$	Cohesive separation vector, $\underline{\delta} \in \mathbb{R}^{3\times 1}$
δ_{ij}	Kronecker delta
ε	Strain
ε_{e}	Elastic strain
$\varepsilon_{\mathrm{ve}}$	Viscoelastic strain
$\varepsilon_{\mathrm{ve}}^{\mathrm{i}}$	Instantaneous viscoelastic strain
$\varepsilon_{\mathrm{ve}}^{\mathrm{inh}}$	Inherited viscoelastic strain
η	Viscosity
μ	Friction coefficient
ν	Poisson's ratio
ρ	Density
σ	(Normal) stress

τ	Shear stress or relaxation time
τ_{IFSS}	Interfacial shear strength
ξ	Normalized interface coordinate
ψ	Fiber orientation distribution function or reduced time

Operators and math symbols

$(\cdot)_{\mathrm{f}}$	Fiber quantity
$(\cdot)_{\mathrm{m}}$	Matrix quantity
$(\cdot)_{\mathrm{L}}$	Longitudinal quantity
$(\cdot)_{\mathrm{T}}$	Transverse quantity
$(\cdot)_{\mathrm{LT}}$	Longitudinal-transverse quantity
$(\cdot)_{\mathrm{TL}}$	Transverse-longitudinal quantity
$(\cdot)_{mn}$	m-n-th tensor/matrix component
$\bar{(\cdot)}$	Average quantity
$\langle\cdot\rangle$	Volume average
$\otimes$	Dyadic product, i.e., $\boldsymbol{p}\otimes\boldsymbol{p}\hat{=}p_ip_j$
$(\cdot)'$	Deviatoric part
$(\cdot)^{\circ}$	Spherical part
$(\cdot)^{-1}$	Inverse
$\dot{(\cdot)}$	Material time derivative
$\langle\cdot\rangle$	Macaulay bracket
:	Double tensor contraction, i.e., $\mathbb{P}:\boldsymbol{\varepsilon}\hat{=}P_{ijkl}\varepsilon_{kl}$

Δ	Increment
d	Total differential
∂	Partial differential
a	Scalar
$\boldsymbol{a}$	Tensor of first order
$\boldsymbol{A}$	Tensor of second order
$\mathbb{A}$	Tensor of fourth order
$\underline{a}$	Vector
$\underline{\underline{A}}$	Matrix
arcosh	Inverse hyperbolic cosine
cos	Cosine
cosh	Hyperbolic cosine
ln	Natural logarithm
sin	Sine
tanh	Hyperbolic tangent

1 Introduction

1.1 Motivation

The following dissertation was written as part of the International Research Training Group (IRTG) GRK 2078 *Integrated engineering of continuous-discontinuous long fiber reinforced polymer structures (Co-Dico FRP)*. The aim of the IRTG was to characterize the behavior of fiber reinforced polymers in the form of hybrid materials, i.e., the combination of continuous and discontinuous composites, from various perspectives. The present work was carried out in the position *C1: Mechanics of interfaces*. The publications produced in the context of the IRTG helped to inspire the author in the following analysis. These include Fliegener [1], Schober [2] and Rohrmüller [3].

Climate change is one of the key challenges of the 21st century and mitigating its effects is of paramount importance. With around 28 % of the European Union's total greenhouse gas emissions in 2023, the transportation sector was the largest single contributor [4]. Within this transportation sector, including automobiles, trains, and aviation, passenger cars accounted for more than half of that figure [5]. In response to this urgent issue, various regulations have been implemented to reduce CO2 emissions, creating a pressing need for innovative lightweight materials, particularly in the automotive industry.

One of the most promising solutions lies in the use of fiber reinforced polymers (FRPs), which offer an exceptional balance of strength and weight. By integrating strong reinforcing fibers within a lightweight polymer matrix, FRPs significantly contribute to mass reduction, thereby decreasing fuel consumption and emissions [6]. The reduced mass results in decreased inertia and operational loads, enabling

further reductions in the structural requirements of vehicles. As material design evolves, continuous (Co) and discontinuous (Dico) fiber reinforced composites are gaining prominence. Continuous fiber reinforced components exhibit higher stiffness and strength due to their increased fiber aspect ratio and alignment, while discontinuous fibers offer enhanced manufacturability and design flexibility [7]. By combining both types of reinforcement in a Co-Dico hybrid the IRTG 2078 seeks to exploit the advantages of both material classes, paving the way for new applications in lightweight design [8]. With the advent of the EU's circular economy action plan [9], one of the main building blocks of the European Green Deal [10], which emphasizes recycling and resource conservation, the shift towards thermoplastic matrix composites is particularly crucial, given their potential for reprocessing and waste reduction.

Thermoplastics are advantageous due to their ease of handling and low production costs, allowing for the creation of efficient and sustainable products. In comparison to thermosetting polymers, thermoplastics provide enhanced properties in regards to recyclability, increased impact resistance and high degree of automation [11]. Although thermoplastic composites are currently dominated by glass fiber reinforcements, recent years have seen increased interest in carbon fibers (CF) due to their superior mechanical properties [12, p. 20]. Moreover, combining injection and compression molding processes with structural inserts of pre-impregnated continuous fibers leads to the creation of mentioned hybrid composites known as continuous-discontinuous fiber reinforced polymers (Co-Dico FRPs), which hold great promise for applications requiring exceptional strength and stiffness [8]. Besides the material properties of its constituents, i.e., the fiber and the matrix material, the Co-Dico FRP consists of two different types of interfaces, as illustrated in Fig. 1.1. These include the microscopic fiber-matrix interface and the macroscopic interface between the Co and Dico reinforcements. Understanding the interfacial mechanics of these composites is vital, as environmental factors such as temperature and moisture can dramatically influence their mechanical behavior. In particular, thermoplastic polymers may experience significant changes in performance due to their viscoelastic properties relative to the glass transition temperature [13]. Therefore, this work aims to investigate

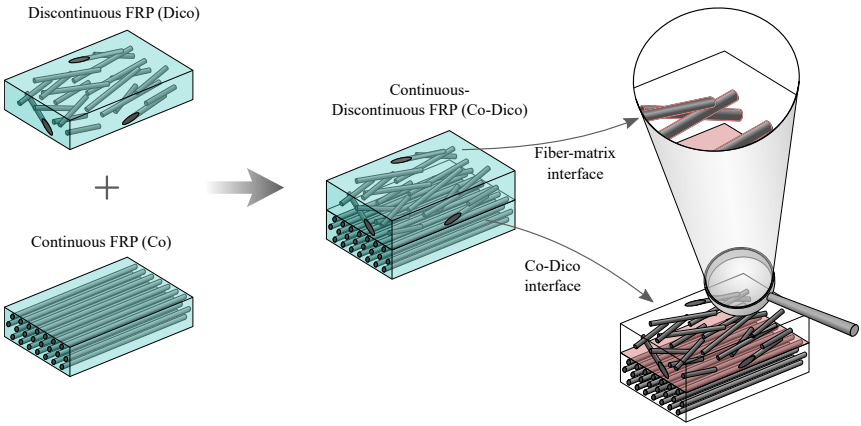

Figure 1.1: Interfaces within a Co-Dico FRP: the (microscopic) fiber-matrix interface and the (macroscopic) interface between Co and Dico.

the interface mechanics in carbon fiber reinforced polyamide 6 (PA6), both on the micro- and macro-mechanical scale, analyzing how various environmental conditions impact material performance.

In summary, this research contributes to the understanding and development of Co-Dico FRPs, facilitating their application in industries striving for efficiency and sustainability. It endeavors to yield insights that can drive the next generation of lightweight materials, ultimately aiding in the reduction of greenhouse gas emissions across the transportation sector.

1.2 Scientific questions

In addition to the two preceding works by Schober [2] and Rohrmüller [3], this dissertation aims to address questions that are useful for characterizing and interpreting interfacial properties within fiber reinforced plastics. In contrast to these works, the focus has shifted from thermosetting to thermoplastic matrix materials. The higher complexity associated with describing the nonlinear, environmentally influenced polymer behavior is, therefore, an essential component of this work.

In addition to characterizing the micro-mechanical interface, i.e., the fiber-matrix interface, the macro-mechanical interface concerning the bonding between the continuous and discontinuous FRPs within Co-Dico will also be characterized under environmental influences. Since these are not standardized methodologies, they need to be appropriately expanded. To numerically validate the experimental investigations, it is crucial to create corresponding models that can help isolate the different influencing factors more effectively. The resulting questions can be summarized as follows:

1. How can the nonlinearly viscoelastic, environmental dependent material behavior of PA6 be modeled?
2. How can the common methodology to assess interfacial properties, both on the micro- and macro-mechanical scale, be extended to account for environmental boundary conditions?
3. What are the characteristics and mechanisms for driving the degradation of the interface throughout the scales and how do temperature and humidity affect those mechanisms?
4. How are the micro- and macro-mechanical interfaces related?

1.3 Thesis outline

The structure of the present work is roughly outlined as follows:

Chapter 2 addresses the current state of the literature. It discusses the influences of temperature and humidity on the investigated polymer, i.e., PA6, and explains the known mechanisms. Fundamental statistical descriptors within fiber reinforced plastics are introduced. Subsequently, analytical models for describing the stress distribution along the fiber-matrix interface are introduced. Furthermore, potential damage mechanisms at the fiber-matrix interface are highlighted, and

experimental methods for characterizing interfaces at both micro and macro levels are presented. A selection of previous approaches to modeling the matrix, interface, and composite is discussed.

Chapter 3 describes the material under investigation. The various constituents are listed, and known parameters are provided according to the available data sheets. Additionally, the manufacturing process under consideration is detailed.

Chapter 4 focuses on the experimental and numerical characterization of PA6. The experimental procedure is described, and the results are evaluated. A numerical approach for describing the matrix behavior is developed, and its implementation is explained in detail. The numerical model is adjusted to fit the experimental data, and the results are presented. A discussion of both experimental and numerical investigations follows.

Chapter 5 examines the characterization of the micro-mechanical interface: the fiber-matrix interface. The methodology employed, the single fiber pull-out test, is described. This method required an extension of the experimental setup to account for climatic boundary conditions, which is explained in detail. Following the presentation of the experimental results, a numerical approach is introduced, and its results for reproducing the measured data are presented, leading to a discussion of both result domains.

Chapter 6 deals with the characterization of the macro-mechanical interface: the Co-Dico interface. As in the previous chapter, the experimental methodology is first explained, and the results are presented. A numerical description approach is then outlined, and again, the results are compared to the experimental findings. Both sets of results are discussed.

Chapter 7 brings together the individual discussions from the preceding chapters for a summarizing discussion.

Chapter 8 concludes the present work with a summary and recommendations for future research.

2 State of the art

2.1 Environmental effects on polymers

In general, the thermo-mechanical properties of all materials show at least some degree of temperature dependence. In most polymers, especially in thermoplastic materials, this dependency is significant. A change in temperature causes a variation in the elastic and viscous properties of a polymer, which are often expressed through the complex modulus $E^\star$, which is defined as the sum of the elastic or storage modulus E' and the viscous or loss modulus E''

$$E^\star = E' + E'' \tag{2.1}$$

[14, p. 88 ff.]. During characterization, e.g., in a dynamic mechanical analysis (DMA), the elastic and viscous response show a temperature dependent phase lag, expressed through the phase angle δ. A basic viscoelastic property of a material is the tangent of the phase angle, which is also the ratio of the loss to the storage modulus and is also called loss factor

$$\tan\delta = \frac{E''}{E'}. \tag{2.2}$$

A central property of thermoplastic polymers is the glass transition temperature or T_g. At temperatures lower than the glass transition, the polymer is in a glassy or energy-elastic state [13]. Above the glass transition temperature, the polymer behaves rubbery or entropy-elastically. During the glass transition, both the loss modulus and the loss factor reach their maximum values, which is often used as its definition, but alternative definitions exist [15, p. 280 ff.].

The variation in thermo-mechanical properties as a function of temperature can be explained by the free volume theory. Free volume is a semi-quantitative concept which describes the empty space between polymer chains, which allows the individual polymer chain to change its configuration. Thereby, it is closely related to diffusion, viscoelastic properties, and other characteristics of the polymer. An increase in temperature is accompanied by an increase in free volume, which consequently leads to a reduction in stiffness and an increase in viscous properties. In general, the temperature dependence of the constitutive relation within FRPs is limited to matrix and interface properties. Technical fibers, especially the investigated carbon fiber, are usually not dependent on environmental factors.

2.1.1 Temperature effects in PA6

Unlike metallic structures, polymers reveal a high temperature dependence of their mechanical properties even at low temperatures, which is especially pronounced for thermoplastic polymers. In the case of PA6, this can be seen in the development of the storage modulus E' and loss modulus E'' over temperature, which is illustrated in Fig. 2.1. In contrast to some other thermoplastic polymers, PA6

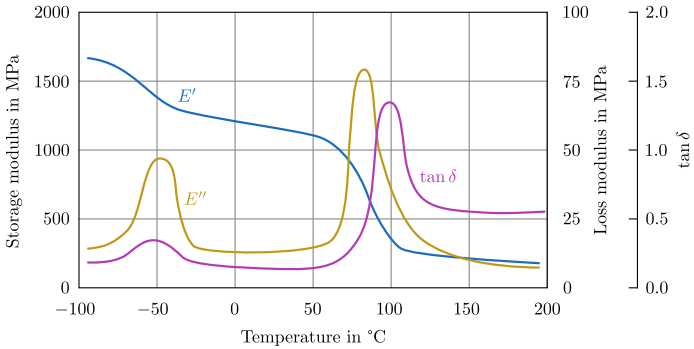

Figure 2.1: Storage modulus E', loss modulus E'' and their ratio $\tan\delta$ over temperature for PA6. Graphic redrawn from Ehrenstein [13, p. 163].

has a relatively high glass transition temperature of over 60 °C in its dry state.

Reasons for this are the strong hydrogen bonds between the polymer chains, which restrict inter-chain mobility [16]. This leads to the mentioned relatively high glass transition and melting temperature [17, p. 339], which is above 200 °C.

PA6 is a semicrystalline thermoplastic polymer, which means that the polymer chains are partly ordered, with an increased local density, and partly amorphous without order [13, p. 15]. The crystalline phase makes it usable above T_g, since the enhanced viscous mechanisms above T_g are mostly located in the amorphous regions and the crystalline phases prevent the storage modulus E' from dropping too severely [13, p. 145]. Since the macromolecule of PA6 is not symmetrical, as can be seen in the chemical structure in Fig. 2.2, alternating counter-running

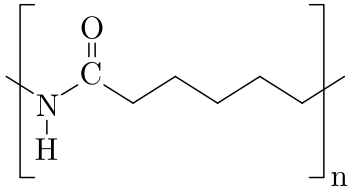

Figure 2.2: Chemical structure of polyamide 6.

molecular chains are required to form crystalline regions, which means that PA6 has a lower degree of crystallization X_c than other semicrystalline thermoplastics [18, p. 49 f.].

Temperature and its rate, i.e., the cooling rate, influence the crystallinity of PA6 [7, p. 87], which raises the question to what extent crystallinity influences the value of T_g. Khanna et al. [19] investigated the effects of the crystallinity on T_g in dried PA6 samples and saw a slight increase of T_g for an increase of crystallinity in the lower crystallinity ratios, which stabilized for crystallinity contents above 5 %. A following study by Parodi et al. [20] also investigated the effects of the crystallinity fraction on T_g in dry PA6 and found no direct correlation. Instead, a dependence on the amorphous structure within PA6 was found, more specifically on the fraction of mobile (MAF) and rigid amorphous phases (RAF) within the specimens. The RAF is considered a nanophase between crystalline structures and MAF, which has a reduced mobility due to covalent interactions

with the immobile crystalline phase. The proportions of MAF and RAF can be derived from differential scanning calorimetry (DSC) and temperature modulated differential scanning calorimetry (TMDSC) measurements [21]. In the mentioned study, it was not the fraction of crystallinity that was decisive for the value of T_g, but rather the thermal history (isothermal or continuous cooling) of the sample and the associated structural development of the amorphous intermediate regions. Both, a low applied cooling rate or a low isothermal temperature of crystallization lead to a higher content of the rigid amorphous phase and a consequent higher glass transition temperature. Based on the assumption of a linear transition between the glass transition temperature for pure RAF, i.e., $T_{\mathrm{g,RAF}}$, and pure MAF, i.e., $T_{\mathrm{g,MAF}}$, they estimated the development of the effective T_g to follow

$$T_\mathrm{g}(X_\mathrm{MAF}/X_\mathrm{RAF}) = T_{\mathrm{g,MAF}} + \frac{1}{1 + X_\mathrm{MAF}/X_\mathrm{RAF}}(T_{\mathrm{g,RAF}} - T_{\mathrm{g,MAF}}), \quad (2.3)$$

where X_MAF and X_RAF are the mass fractions of the respective phase. Since the crystallinity fraction X_c and that of both amorphous constituents need to sum up to one, the following identity is given

$$X_\mathrm{c} + X_\mathrm{RAF} + X_\mathrm{MAF} = 1. \quad (2.4)$$

Based on the model in Eq. 2.3 and the relationship in Eq. 2.4, it becomes clear that for each $X_\mathrm{c} \in [0, 1]$, the $X_\mathrm{MAF}/X_\mathrm{RAF}$ ratio can be a value between zero and infinity. Therefore, the resulting T_g can take on all values between $T_{\mathrm{g,MAF}}$ and $T_{\mathrm{g,RAF}}$ for any X_c and is therefore completely independent of the crystallinity fraction. What is not recognized in the model is that the occurrence of RAF as an intermediate phase between crystalline and fully mobile amorphous regions is possibly not independent of the degree of crystallinity. This is supported through the results by Kolesov and Androsch [22], who investigated the polymer structure after cold ordering of previously quenched PA6 samples. Their findings are that RAF increases with increasing crystallinity fractions up to 20 %, followed by a regressive decrease. Simultaneously, the $X_\mathrm{MAF}/X_\mathrm{RAF}$ ratio decreases from 20 % crystallinity onwards, suggesting an increased decoupling of the crystalline and

amorphous phase for higher crystallinity. This observation calls into question the independence of the glass transition temperature from the degree of crystallinity.

Not only does the degree of crystallinity affect T_{g}, it also affects the thermal shrinkage/expansion behavior following a change in temperature and consequently the residual stresses within the polymer. In amorphous thermoplastics, residual stresses caused by thermal shrinkage can be annealed above their glass transition temperature due to the increased chain mobility [23, 24]. The temperature below which residual stresses start to persist is referred to as stress-free temperature T_{σ}, which, as stated above, coincides with the glass transition temperature for amorphous plastics, i.e., $T_{\sigma} \approx T_{\mathrm{g}}$. The stress-free temperature differs for semicrystalline thermoplastics and is in general above T_{g}. The reason for this is that between T_{g} and the melting temperature T_{m} is the crystallization temperature T_{c}, at which crystallization begins. Below T_{c}, load-bearing crystalline phases are present which limit the annealing of residual stresses [25] and in fact contribute to the formation of residual stresses due to different volumetric expansion ratios between amorphous and crystalline phases and potential reinforcing structures. Experimental evidence for different semicrystalline polymers indicates that the stress-free temperature is their crystallization temperature, i.e., $T_{\sigma} \approx T_{\mathrm{c}}$ [26, 27]. Detassis et al. [28] investigated the formation of residual stresses for carbon fiber reinforced PA6 utilizing the fiber fragmentation test. Their results suggest that the stress-free temperature T_{σ} for semicrystalline polymers is as high as the melting temperature, i.e., $T_{\sigma} \approx T_{\mathrm{m}}$.

In summary, it can be seen that the viscoelastic properties of PA6 are not only temperature-dependent, but also process-dependent due to the degree of crystallization. Even T_{g} does not correspond to an independent material parameter, but varies depending on the present polymer chain configuration.

2.1.2 Humidity effects in PA6

The name giving amide groups within PA6 are responsible for the material being hygroscopic, i.e., a material that absorbs water. The chemical structure of PA6,

$[–NH–(CH_2)_5–CO–]_n$, as was illustrated in Fig. 2.2, enables the molecule chains to form hydrogen bonds with other molecules.

One of the earliest works on the absorption of water in polyamides is given by Puffr and Šebenda [29], who give an explanatory model on the sorption process within PA6. With surrounding moisture, the polar nature of the water molecule draws it towards the similarly polar carbonamide groups present within the molecular chains of PA6 [30]. This results in the formation of hydrogen bonds between the chains, thereby impacting intermolecular interactions. In general, the absorbed water is categorized into tightly and weakly bound water [31]. Due to the higher density in functional groups capable of building hydrogen bonds, the maximum water uptake of PA6 is greater than that of other industrially used polyamides, with a maximum water uptake of over 9 % of its dry mass [17, 32], as is quantitatively illustrated in Fig. 2.3.

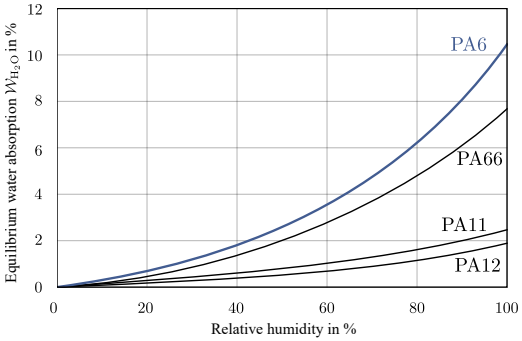

Figure 2.3: Maximum water uptake for different polyamides over relative humidity. Graphic redrawn from Toray Industries, Inc. [33].

In general, the maximum water uptake is related to the relative humidity $\mathcal{H}$ to which the polymer is exposed. Analytical models to express the moisture uptake in the form of the mass fraction $\mathcal{W}_{H_2O} = \Delta m/m_0$, i.e., the mass of absorbed water per mass of dry polymer, as a function of the equilibrium relative humidity are summarized by Launay et al. [34]. According to Broudin et al. [35, p. 16], who compare multiple models to describe the moisture sorption within PA66, the

most widely used model in literature is the Guggenheim-Anderson-de-Boer model or GAB model, respectively. It was shown that the GAB model is equivalent to the Hailwood and Horrobin equation introduced in Hailwood and Horrobin [36], which is widely used to describe the moisture sorption of wood [37]. The model is defined by

$$\mathcal{W}_{\mathrm{H_2O}} = \frac{wCKa}{(1-Ka)(1+Ka(C-1))}, \tag{2.5}$$

where $\mathcal{W}_{\mathrm{H_2O}}$ is called relative mass ratio and $a = \mathcal{H}/100$ is the water activity. C, K and w are sorption parameters whose physical interpretation are explained in detail in Quirijns et al. [38]. In general, the parameters can be modeled as functions of the surrounding temperature, but Suherman et al. [39] found a low influence of temperature on these parameters for PA6. Sabard et al. [40] fitted the general GAB model to sorption measurements of PA6 of different degrees of crystallinity and found a good agreement using the parameters given in Tab. 2.1, while the dependence on the degree of crystallinity was found to be minor. It

Table 2.1: Calibrated parameters for the GAB model for PA6 with a crystallinity of $X_{\mathrm{c}} = 35\,\%$ published in Sabard et al. [40].

w	C	K
0.043	3.735	0.788

needs to be stressed that these parameters are only valid for the amorphous phase, indicated by $\mathcal{W}^{\mathrm{a}}_{\mathrm{H_2O}}$. The motivation to express the GAB model only for the amorphous phase within semicrystalline polymers is that water absorption of the crystalline phase is very limited and often neglected all together [41]. In reference to Broudin et al. [35, p. 12], the relation between the relative mass ratio of the whole polymer $\mathcal{W}_{\mathrm{H_2O}}$ and the relative mass ratio of only the amorphous phase $\mathcal{W}^{\mathrm{a}}_{\mathrm{H_2O}}$ is connected by the degree of crystallinity X_{c}

$$\mathcal{W}_{\mathrm{H_2O}} = \frac{\mathcal{W}^{\mathrm{a}}_{\mathrm{H_2O}}}{1-\mathcal{W}^{\mathrm{a}}_{\mathrm{H_2O}}}(1-X_{\mathrm{c}}). \tag{2.6}$$

It is well known in the literature that an increase in the moisture concentration within PA6 is always accompanied by a reduction in the glass transition temperature [20, 30, 41]. There are various explanatory models, e.g., in Murthy [42], but the debates about the exact mechanism are still ongoing. Water absorption in PA6 predominantly takes place in the amorphous regions. The volume available for diffusion is thereby influenced by the degree of crystallinity and its orientation. A higher crystallinity correlates with lower water absorption. When water is absorbed, it substitutes the interchain hydrogen bonds in the PA6, leading to enhanced mobility of the polymer chains in the amorphous regions. This increased chain mobility is a result of water reducing the spatial restrictions that limit the specific alignment of the polymer chains, consequently leading to a decrease in the glass transition temperature T_g. In essence, water functions as a plasticizer, increasing the flexibility of PA6 by promoting greater chain mobility and thereby lowering the T_g.

The variation of the onset glass transition temperature T_g with a change in relative humidity for PA6 was empirically modeled by Khanna et al. [19] with the following equation

$$T_\mathrm{g}/°\mathrm{C}(\mathcal{H}) = a + b\mathcal{H} + c\sqrt{\mathcal{H}}, \tag{2.7}$$

for which they determined the coefficients based on experimental data to be $a = 53.67$, $b = -0.168$ and $c = -6.208$. According to the model and the set of parameters, the onset of the glass transition temperature monotonically decreases from 53.67 °C to -25.21 °C. Other models relate the glass transition temperature with the relative moisture uptake $\mathcal{W}_{\mathrm{H_2O}}$. Arhant et al. [43] resorted to the Simha-Boyer equation

$$T_\mathrm{g}(\mathcal{W}_{\mathrm{H_2O}}) = \left(\frac{1}{T_{\mathrm{g,dry}}} + \left(\frac{1}{T_{\mathrm{g,H_2O}}} - \frac{1}{T_{\mathrm{g,dry}}}\right)\frac{\rho_{\mathrm{PA6}}}{\rho_{\mathrm{H_2O}}}\mathcal{W}_{\mathrm{H_2O}}\right)^{-1}, \tag{2.8}$$

which is based on free volume theory and for which they found good agreement with experimental data. It also allows for including the degree of crystallinity through Eq. 2.6. Here, $T_{\mathrm{g,dry}}$ is the glass transition temperature of dry PA6, $T_{\mathrm{g,H_2O}}$ is the glass transition temperature of water and ρ_{PA6} and $\rho_{\mathrm{H_2O}}$ are the

densities of PA6 and water, respectively. The combination of Eq. 2.5, Eq. 2.6 and Eq. 2.8 allow to express the glass transition temperature directly as a function of relative humidity $\mathcal{H}$, which is illustrated in Fig. 2.4. The figure illustrates how

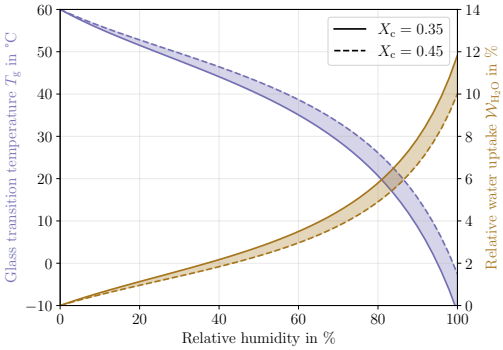

Figure 2.4: Glass transition temperature of PA6 and relative water uptake over relative humidity predicted by Eq. 2.5, Eq. 2.6 and Eq. 2.8 for $X_c = 0.35$ and $X_c = 0.45$. The following parameter were used: $T_{g,dry} = 60\,°C$, $T_{g,H_2O} = -163\,°C$ [43], $\rho_{PA6} = 1.14\,g/cm^3$ [13, p. 67] and $\rho_{H_2O} = 1.00\,g/cm^3$. The sorption was modeled with the parameters in Tab. 2.1.

the relative humidity and crystallinity influence the glass transition temperature and the maximum water uptake for crystallinities of $35\,\%$ and $45\,\%$, which are considered the bounding values of the typical crystallinity range within PA6 [13, p. 67]. Despite T_g being dependent on crystallinity in general, Khanna et al. [19] found no difference for the dry material above a crystallinity of $10\,\%$, which was assumed here. According to the model, higher crystallinity ratios reduce the depression of the glass transition temperature, albeit slightly. For both degrees of crystallinity, the drop in T_g over the entire relative humidity range is more than $60\,°C$, with T_g falling to values below $0\,°C$ in both cases. This highlights that room temperature ($\sim 23\,°C$), which is a commonly used test temperature, can be well below but also well above T_g.

Along with the plasticizing effect of water, influences on the mechanical properties of PA6 can be observed. One of the early studies on this can be found in

Boukal [44], in which it was found that the absorption of water reversibly reduces the effective stiffness of PA6, whereby the stiffness of the crystalline regions was unaffected. Consequently, the effects are located in the amorphous phase. This softening effect was confirmed in other studies [45, 46, 32], although it must be differentiated that a stiffening effect can also be measured below the freezing point of water [13, p. 148]. Water induced effects on the mechanical properties also apply for reinforced PA6, as was demonstrated by Mohammadkhani et al. [47], who report a significant decrease in elastic and strength properties and an increase in failure elongation and toughness. The mechanisms behind the softening/hardening are based on a variation in chain mobility due to the absorption of water.

Numerical investigations on the diffusion process of water into PA6 and its effect on the stiffness were made by Sharma et al. [48], who concluded that the relaxation times decreased with increasing water content based on DMA experiments. They could not determine whether diffused moisture increased or decreased stiffness, but rather saw a dependence on the moisture distribution within the sample. Due to the space occupied by diffused water molecules, the distance between the intermolecular chains in the material is increased, which is illustrated in Fig. 2.5 and is termed hygroscpoic swelling [30].

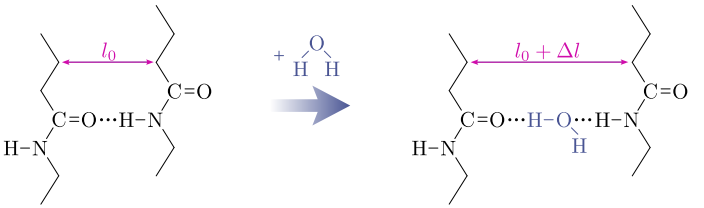

Figure 2.5: Water absorption in polyamide 6 with resulting increased chain distance. Figure redrawn from Shinzawa and Mizukado [49].

Obeid et al. [50] investigated the coefficient of moisture expansion (CME) of neat PA6 samples. They used a multiphysics approach that takes into account the dependence of the Young's modulus and the CME on the moisture content to

model the volume change for the given geometry under moisture-induced ageing. In their investigations, a constant CME proved to be insufficient, so that a nonlinear approach with a sigmoidal shape was chosen. Obeid et al. report a maximum CME for high water contents of 0.3. Combined with a maximum water uptake of roughly 10 %, a volumetric swelling strain of about 3 % is possible, which may cause a significant contribution on the eigenstress field in a given geometry.

Another well known effect caused by water absorption within polyamides is hydrolysis, which describes the breakdown of molecules and a consequent reduction in molecular weight over time during moisture induced aging [51]. One effect is that the resulting shorter molecular chains have an increased chain mobility, which consequently leads to an accelerated reorganization of the amorphous phase into crystalline phases, called chemi-crystallization [52]. As a consequence, the chain scission during hydrolysis degrades the mechanical properties of polyamides and its composites. Arhant et al. [53] report a reduction of the fracture toughness in carbon fiber reinforced PA6 (CF-PA6) to 30 % of its reference value after hydrolytic aging. Furthermore, accelerated fatigue [54] and reduced strength properties [55], as well as a reduction in strain at failure with a simultaneous enhanced embrittlement [56] are reported.

In summary, the absorption of water in PA6 leads to plasticization with a reduced glass transition temperature, which results in reduced stiffness and increased viscous effects. On the other hand, irreversible degradation occurs through hydrolysis, which generally reduces the mechanical properties and can even increase brittle fracture behavior.

2.2 Microstructural descriptors within FRPs

Being a heterogeneous, two-phase composite material consisting of a fibrous and a polymeric phase, it is often necessary to find statistical quantities to describe the effective distribution of the underlying microstructure of an FRP. While the polymer usually exhibits a direction-independent mechanical behavior, i.e., the

polymer is isotropic, the elongated geometry of the fibers leads to an effective anisotropy within the composite, even when the fiber material itself is isotropic. The three major quantities of interest to describe the microstructure of a FRP are the fiber volume content, the fiber length distribution and the fiber orientation distribution.

2.2.1 Fiber volume content

As a composite material, i.e., a composition of different constituents, it is obvious that the mechanical properties of an FRP depend on the ratio of fiber content to matrix content. This idea can be further extended by distinguishing between different groups of fibers, such as longer and shorter fibers, or possibly other undesirable components, such as voids. In the following this concept will be reduced to the ratio of fiber to matrix and all equations are based on Gibson [57, p. 95 ff.].

In general, the fiber content is either expressed as a weight percentage or a volume percentage and expresses the quantity of weight or volume of the fiber material per composite and consequently is dimensionless. The weight fraction of constituent i, which in this case is either fiber, i.e., $i = \mathrm{f}$, or polymeric matrix, i.e., $i = \mathrm{m}$, is given with

$$w_i = \frac{W_i}{W_\mathrm{c}}, \tag{2.9}$$

where W_c is the total weight of the composite and W_i is the weight of the specific constituent. Similarly, the volume fraction is

$$v_i = \frac{V_i}{V_\mathrm{c}}, \tag{2.10}$$

where V_c and V_i are the volumes of the composite and the constituent. A requirement on both the weight and volume fraction is that they must sum up to one,

because the total quantity is equal the sum of all constituents. When voids are neglected, this is

$$\sum_i w_i = \frac{W_\mathrm{f}}{W_\mathrm{c}} + \frac{W_\mathrm{m}}{W_\mathrm{c}} \stackrel{!}{=} 1, \tag{2.11a}$$

$$\sum_i v_i = \frac{V_\mathrm{f}}{V_\mathrm{c}} + \frac{V_\mathrm{m}}{V_\mathrm{c}} \stackrel{!}{=} 1. \tag{2.11b}$$

Combining both expressions with the information that weight and volume are connected through the density, i.e., $W_i = \rho_i V_i$, the density of the composite can be calculated through

$$\begin{aligned} \rho_\mathrm{c} &= \frac{V_\mathrm{f}}{V_\mathrm{c}}\rho_\mathrm{f} + \frac{V_\mathrm{m}}{V_\mathrm{c}}\rho_\mathrm{m}, \\ &= \sum_i v_i \rho_i. \end{aligned} \tag{2.12}$$

That a property of the composite is equal the sum of the properties of its constituents weighted by their volume fraction is generally termed *rule of mixtures*. In the case of the density, the *rule of mixtures* is exact [57, p. 97].

From a manufacturing perspective, it is easier to evaluate the weight percentage, because processes in the industrial scale usually operate with keeping track of the fiber mass flow into the polymeric matrix material. Additionally, measuring weight instead of volume is an easier, quicker and cheaper operation.
From a mechanical perspective, it is usually more desirable to have information on the fiber volume content, because the mechanical properties vary as a function of the spatial occupation of each constituent. Hence, it is useful to have a relation between volume and weight fraction, which based on the relations above simply is

$$w_i = \frac{W_i}{W_\mathrm{c}} = \frac{\rho_i V_i}{\rho_\mathrm{c} V_\mathrm{c}} = \frac{\rho_i}{\rho_\mathrm{c}} v_i. \tag{2.13}$$

Vice versa, it is

$$v_i = \frac{\rho_\mathrm{c}}{\rho_i} w_i, \tag{2.14}$$

which consequently can be used in numerical estimations for effective mechanical properties or detailed simulations.

The effect on how the volume fraction effects the mechanical properties of a composite can be demonstrated by using the *rule of mixtures* on elastic constants. For a unidirectional FRP, in simplified estimates it is often assumed that the *rule of mixtures* is directly applicable to the longitudinal elastic modulus E_{L}, while the same only applies to the reciprocal of the transverse modulus E_{T} [57, p. 104 ff.]. This is equivalent to

$$E_{\mathrm{c,L}} = E_{\mathrm{f,L}} v_{\mathrm{f}} + E_{\mathrm{m,L}} v_{\mathrm{m}}, \tag{2.15a}$$

$$\frac{1}{E_{\mathrm{c,T}}} = \frac{1}{E_{\mathrm{f,T}}} v_{\mathrm{f}} + \frac{1}{E_{\mathrm{m,T}}} v_{\mathrm{m}}. \tag{2.15b}$$

This is demonstrated in Fig. 2.6 for literature data on carbon fiber reinforced PA6, for which the carbon fiber is assumed to be transversely isotropic, i.e., $E_{\mathrm{f,L}} \neq E_{\mathrm{f,T}}$. In this figure and the chosen material combination, it is evident that

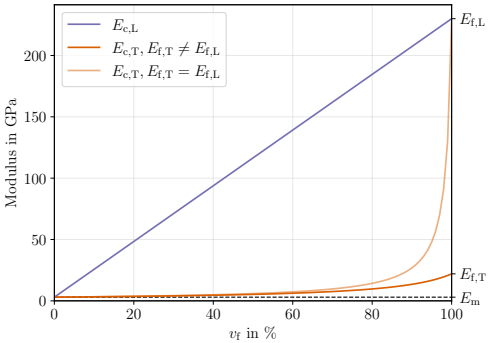

Figure 2.6: Stiffness estimates according to the *rule of mixtures*. The material properties for the fiber were taken from Boming et al. [58] to be $E_{\mathrm{f,L}} = 230\,\mathrm{GPa}$ and $E_{\mathrm{f,T}} = 22\,\mathrm{GPa}$. The modulus of the polymer was assumed to be isotropic to be $E_{\mathrm{m}} = 3\,\mathrm{GPa}$, which is a result of earlier research on the investigated PA6 [59, p. 167]. The washed-out curve for the transverse modulus is based on the assumption that $E_{\mathrm{f,T}} = E_{\mathrm{f,L}} = 230\,\mathrm{GPa}$.

the *rule of mixtures* is insensitive for the transverse modulus of the fiber material for predicting the transverse modulus of the composite up to a fiber volume content of about 70 %, which is close to the technically feasible maximum fiber content. However, it must be emphasized that the *rule of mixtures* generally underestimates the transverse modulus when compared to experimental results [57, p. 111].

In summary, the fiber volume fraction determines how much of the fiber properties are transferred to the effective composite material. This usually means that a higher fiber volume fraction will result in higher stiffness, especially in the fiber direction, since the fiber is usually stiffer than the polymer. On the other hand, a higher fiber volume fraction can also lead to undesirable brittleness or a reduction in fracture toughness, so the optimum fiber volume fraction depends very much on the specific application of the composite.

2.2.2 Fiber length distribution

Just as the effective properties of a composite material are influenced by the respective fiber volume or mass fraction, the length of the fibers is also decisive in this aspect. As was mentioned in the introduction, FRPs may be classified into continuously and discontinuously reinforcements, whereby the discontinuous class can be further split into short and long fiber reinforcements. In the case of thermoplastic FRPs, these are also called short fiber reinforced thermoplastic (SFT) and long fiber reinforced thermoplastic (LFT). While there is no clear definition of when a composite becomes an LFT rather than an SFT as fiber length increases, it can be agreed that the difference lies in the fact that SFT composites are made of fibers that are short enough not to exhibit curvature and therefore have less potential to interact with each other [12, p. 11]. With LFT materials, the curvature along the fibers can be very pronounced depending on the manufacturing process.

An increase in fiber length shows a monotonic effect on the mechanical properties from SFT to LFT to continuous reinforcements. This is illustrated in Fig. 2.7. For the case of the elastic modulus, this can also be demonstrated with reference

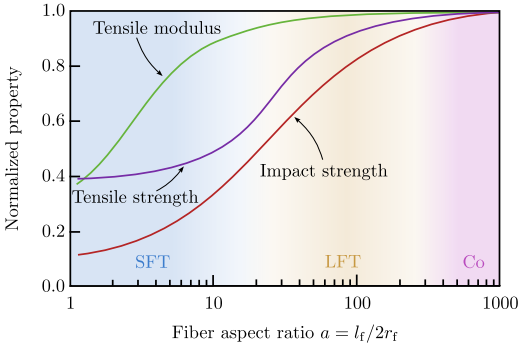

Figure 2.7: Normalized properties over aspect ratio of thermoplastic FRPs with typical aspect ratios of SFT, LFT and continuous FRP (Co). Graphic redrawn from Gandhi et al. [12, p. 114].

to the shear-lag theory introduced later in Sec. 2.3.1. Without going into detail, averaging the stress distribution over the fiber length allows to derive the elastic modulus in longitudinal direction

$$E_\mathrm{L} = v_\mathrm{f} E_\mathrm{f} \left(1 - \frac{\tanh(na)}{na}\right) + (1 - v_\mathrm{f}) E_\mathrm{m}, \tag{2.16}$$

where $a = l_\mathrm{f}/2r_\mathrm{f}$ is the fiber aspect ratio, which relates the fiber length l_f to its radius r_f, and n is called shear-lag parameter. The derivation of this equation will be given in Sec. 2.5.3. The model is illustrated in Fig. 2.8 for three different volume fractions. For the given material, a carbon fiber reinforced PA6, it is evident that the stiffer fiber leads to a stiffer composite as the aspect ratio and fiber volume content increase.

2.2.3 Fiber orientation distribution

Fiber reinforced polymers may consist of fibers all aligned along a single axis, which is generally only the case for unidirectional continuous reinforcements, they may have multiple discrete alignment angles in the case of stacked laminae, i.e., a laminate, or the fibers may be continuously distributed to varying degrees across the unit sphere. As a result, the fiber properties may only have an effect

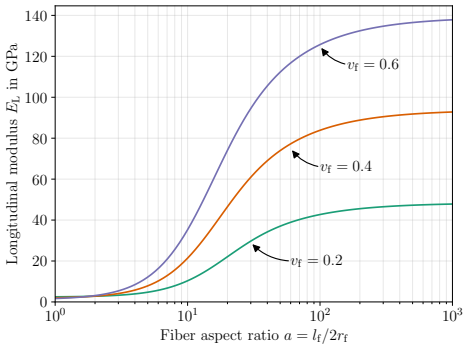

Figure 2.8: Longitudinal modulus of FRP after Eq. 2.16. For the modeling it was assumed that $E_\mathrm{f} = 230\,\mathrm{GPa}$ and that the matrix is isotropic with $E_\mathrm{m} = 3\,\mathrm{GPa}$ and $\nu_\mathrm{m} = 0.38$. The fiber interaction factor was approximated through $\ln(R/r_\mathrm{f}) = 1/2\ln(2\pi/\sqrt{3}v_\mathrm{f})$.

in certain directions, while the remaining directions show a matrix-dominant behavior, resulting in strongly direction-dependent mechanical properties of the composite. However, it is also possible that the directional dependence is averaged to a quasi-isotropic behavior, which is the case when the reinforcing fibers are more evenly distributed over the unit sphere.

As an example, a single ply of a unidirectionally reinforced polymer has strongly aligned fibers in a single direction. In general, this leads to a strong reinforcing effect in the fiber direction of the ply, while other directions are reinforced to a lesser extent. This is most evident in the direction perpendicular to the fiber orientation, which is barely reinforced and thus retains the stiffness properties just above the polymer stiffness in this direction. A laminate consists of several differently orientated, stacked plies. Consequently, a reinforcement effect is created in multiple directions, which can be maximized to a quasi-isotropic behavior [60, p. 206 f.]. This is illustrated in Fig. 2.9. It is clearly visible that the laminate given in Fig. 2.9a has a slightly stronger reinforcing effect in the 0° and 90° direction, whereas it shows less than half the reinforcement effect in the 45° direction compared with the planar isotropic laminates in Fig. 2.9b and Fig. 2.9c. This also

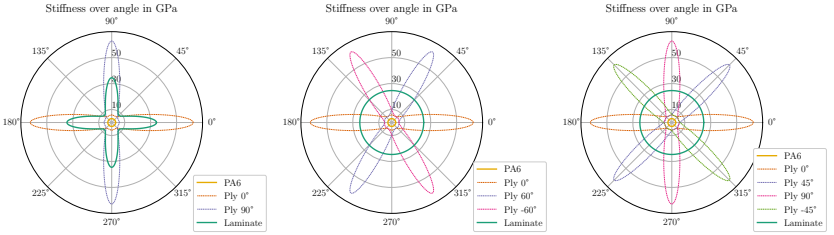

(a) **(b)** **(c)**

Figure 2.9: Example for different laminate stackings: (**a**) shows a [0, 90] stacking, (**b**) a [0, 60, -60] stacking, and (**c**) a [0, 45, -45, 90] stacking. The latter two result in quasi-isotropic laminates. The data was generated using the shear-lag informed Halpin-Tsai homogenization and laminate theory with the following constituent properties: $E_\mathrm{f} = 242\,\mathrm{GPa}$, $G_\mathrm{f} = 105\,\mathrm{GPa}$, $\nu_\mathrm{f} = 0.1$ for the fiber and $E_\mathrm{m} = 3\,\mathrm{GPa}$, $\nu_\mathrm{m} = 0.35$ for the isotropic matrix. The fiber volume content is $v_\mathrm{f} = 0.25$.

demonstrates that a quasi-isotropic behavior does not necessarily require that the fibers need to be distributed equally over all angles.

Instead of keeping track of the orientation of each fiber, which would potentially lead to tracking millions of fibers, the fiber orientation is mathematically described by a continuous distribution function, i.e., the orientation distribution function $\psi(\theta, \phi)$ [61, p. 14]. Here, $\theta \in [0, \pi]$ and $\phi \in [0, 2\pi]$ are the spherical coordinate angles. Choosing an angle representation is evident, since the spherical angles fully describe the orientation of a fiber, which can be equally expressed with the orientation vector

$$\boldsymbol{p}(\theta, \phi) = \begin{pmatrix} \sin\theta\cos\phi \\ \sin\theta\sin\phi \\ \cos\theta \end{pmatrix}, \tag{2.17}$$

which is a unit vector and is illustrated in Fig. 2.10.

The orientation distribution function $\psi(\theta = \theta^*, \phi = \phi^*)$ returns the relative likelihood that a fiber lies in the direction of $\boldsymbol{p}(\theta = \theta^*, \phi = \phi^*)$. This may also be discretized by evaluating the probability of fibers being present in a range of

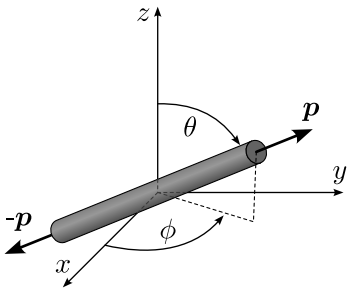

Figure 2.10: Fiber orientation vector in angle representation. Graphic redrawn from Tucker [61, p. 12].

angles, i.e., $\theta \in [\theta^*, \theta^* + \mathrm{d}\theta]$ and $\phi \in [\phi^*, \phi^* + \mathrm{d}\phi]$, which requires to introduce the cumulative distribution function

$$\begin{aligned} F_\psi(\theta, \phi) &= \int_0^\theta \int_0^\phi \psi(\theta, \phi) \sin\theta \, \mathrm{d}\theta \, \mathrm{d}\phi, \\ &= \oint \psi(\boldsymbol{p}) \, \mathrm{d}\boldsymbol{p}, \end{aligned} \tag{2.18}$$

where $\mathrm{d}\boldsymbol{p} = \sin\theta \, \mathrm{d}\theta \, \mathrm{d}\phi$. Hence, the probability $\mathcal{P}$ of a fiber lying within a range of angles is

$$\mathcal{P}(\theta^* \leq \theta < \theta^* + \mathrm{d}\theta, \phi^* \leq \phi < \phi^* + \mathrm{d}\phi) = F_\psi(\theta^* + \mathrm{d}\theta, \phi^* + \mathrm{d}\phi) - F_\psi(\theta^*, \phi^*), \tag{2.19}$$

which for example can be used to build a discrete histogram for a known fiber distribution function. Being a distribution function and given the fact that the same fiber can be described with two orientation vectors, i.e., $\boldsymbol{p}$ and $-\boldsymbol{p}$, $\psi(\boldsymbol{p})$ must fulfill the normalization condition

$$F_\psi(\theta = \pi, \phi = 2\pi) = \int_0^\pi \int_0^{2\pi} \psi(\theta, \phi) \sin\theta \, \mathrm{d}\theta \, \mathrm{d}\phi \stackrel{!}{=} 1, \tag{2.20}$$

and the periodicity condition

$$\psi(\boldsymbol{p}) = \psi(-\boldsymbol{p}). \tag{2.21}$$

While the orientation distribution function contains all orientation information, its interpretation is difficult [61, p. 16]. Therefore, it is often more practical to resort to average measures of the orientation in case of mechanical analysis. This average is expressed in the form of orientation tensors, which are the weighted integral of the orientation distribution function $\psi(\boldsymbol{p})$ by the dyadic product of orientation vectors, i.e., $\boldsymbol{p} \otimes \boldsymbol{p} \otimes \cdots \otimes \boldsymbol{p}$, over all possible orientations

$$\mathbb{N}_{\langle k \rangle} = \oint \psi(\boldsymbol{p}) \boldsymbol{p}^{\otimes k} \, \mathrm{d}\boldsymbol{p}, \tag{2.22}$$

with $\boldsymbol{p}^{\otimes k}$ being the k-th moment of $\boldsymbol{p}$ [62, p. 50]. Due to the symmetry of $\psi(\boldsymbol{p})$, odd orientation tensors, i.e., $k \in \{1, 3, 5, ...\}$, vanish. In the field of continuum mechanics, the most important orientation tensors are the orientation tensors of second and forth order, i.e., $k = 2$ and $k = 4$, which are

$$\mathbb{N}_{\langle 2 \rangle} = \boldsymbol{N} = \oint \psi(\boldsymbol{p}) \boldsymbol{p} \otimes \boldsymbol{p} \, \mathrm{d}\boldsymbol{p}, \tag{2.23a}$$

$$\mathbb{N}_{\langle 4 \rangle} = \mathbb{N} = \oint \psi(\boldsymbol{p}) \boldsymbol{p} \otimes \boldsymbol{p} \otimes \boldsymbol{p} \otimes \boldsymbol{p} \, \mathrm{d}\boldsymbol{p}. \tag{2.23b}$$

The fiber orientation tensor of forth order will be an important measure in the later introduced homogenization methods. The properties of the orientation tensors are well described in Tucker [61] and Bauer [62].

Unfortunately, the exact orientation distribution function is generally not known, so that orientation tensors cannot be computed relying on this information. Instead, based on microstructural information such as CT scans, the average sum of the dyadic product of individual fibers may be computed as a discrete formulation of the orientation tensors

$$\boldsymbol{N} = \frac{1}{n} \sum_{i=1}^{n} (\boldsymbol{p} \otimes \boldsymbol{p})_i, \tag{2.24a}$$

$$\mathbb{N} = \frac{1}{n} \sum_{i=1}^{n} (\boldsymbol{p} \otimes \boldsymbol{p} \otimes \boldsymbol{p} \otimes \boldsymbol{p})_i, \tag{2.24b}$$

where n is the number of fibers in a given volume. Examples for a selection of geometric fiber configurations and their respective orientation tensor of second order are given in Fig. 2.11.

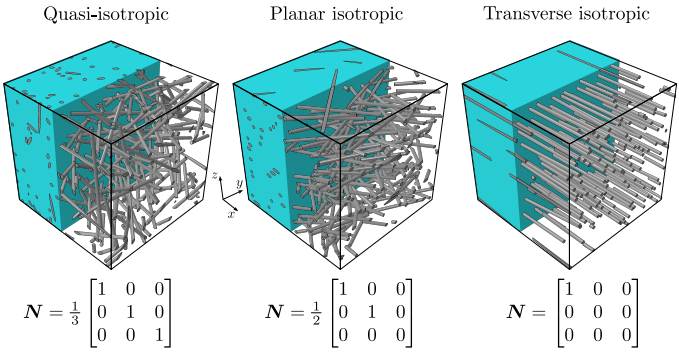

Figure 2.11: Examples for different fiber orientation tensors with their respective (periodic) microstructure and symmetry group. The microstructure was generated by using a sequential addition and migration (SAM) algorithm after Mehta and Schneider [63].

2.3 Fiber-matrix interface characterization

The importance of the fiber-matrix interface must not be underestimated, since as a bond between the two constituents it is responsible for transferring loads in the form of stresses and strains from the matrix to the fiber and from the fiber back to the matrix. Without this interface, the transfer of external loads to the load-bearing fibers would be impossible. The mechanical properties of the composite can only be optimally utilized if the interface is intact and understood.
The following section covers the general load transferring mechanics and failure mechanisms within fiber reinforced thermoplastics, with an enhanced emphasis on the role of the fiber-matrix interface for the given context. After introducing the stress-transfer mechanisms by means of established analytical models, general failure mechanisms in FRPs are presented. The section is concluded with several

common test procedures to quantitatively and qualitatively assess the properties of the fiber-matrix interface.

2.3.1 General load transfer mechanics in FRPs

The general analytical model to describe the stress distributions of a single fiber of length l_f embedded into a matrix cylinder is called shear-lag theory. Pioneering efforts in this field were made in the work of Cox [64], which is illustrated in Fig. 2.12. Similar theories have since been published by Rosen et al. [65, p. 53 ff.], who assumed the fiber-matrix composite cylinder to be encapsulated in an effective medium and Amirbayat and Hearle [66], who investigated the role of the Poisson's ratio of fiber and matrix and the coefficient of friction on the stress transfer, including the case of an imperfect bond.

Generally, the assumption is made that the fiber and matrix behave elastically and are perfectly bonded, i.e., the bonding is coherent and both the displacement jump and traction jump are zero across the interface, respectively. Another assumption is made that at the fiber ends at $x = \pm l_\mathrm{f}/2$ the axial stress transfer vanishes, i.e. $\sigma_\mathrm{f}(\pm l_\mathrm{f}/2) = 0$. The main finding is a general relation between the normal stress within the fiber σ_f and the shear stress along the outer fiber surface τ, from now on called interfacial shear stress. According to Beaumont et al. [67, p. 8], the normal stress must follow the equation

$$\sigma_\mathrm{f} = E_\mathrm{f}\varepsilon_\mathrm{m}\left(1 - \frac{\cosh(na\frac{2x}{l_\mathrm{f}})}{\cosh(na)}\right), \tag{2.25}$$

where E_f and ε_m are the Young's modulus of the fiber and the matrix strain, respectively, and $a = l_\mathrm{f}/2r_\mathrm{f}$ is the aspect ratio. n is called shear-lag parameter following

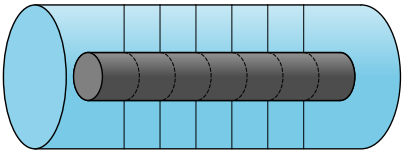

(a) Schematic fiber in matrix cylinder without load.

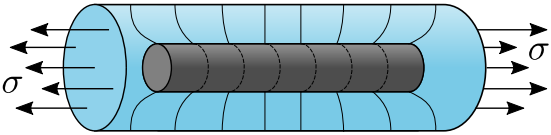

(b) Schematic fiber in matrix cylinder with applied load and indicated strain lines.

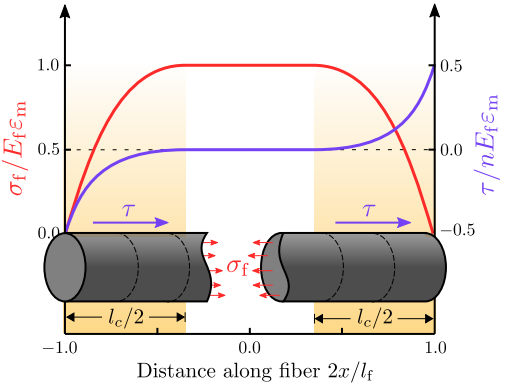

(c) Schematic normal stress σ_f and shear stress τ distributions over fiber length with indicated critical fiber length l_c. E_f and ε_m are the fiber's Young's modulus and the matrix strain, respectively, while n is the shear-lag parameter given in Beaumont et al. [67, p 7].

Figure 2.12: Schematic shear-lag theory after Cox [64], in reference to Gandhi et al. [12, p. 192] and Beaumont et al. [67, p. 9].

$$n = \sqrt{\frac{2G_m}{E_f \ln(R/r_f)}}, \tag{2.26}$$

where G_m is the shear modulus of the matrix and $R > r_f$ is a reference point in the matrix. R is often identified as an interaction parameter describing the radial distance between fibers, as is the case in Cox [64, p. 77] and Fu and Lauke

[68, p. 393], but Goh et al. [69, p. 188] state that this violates the axisymmetry condition in the shear-lag model after Nairn [70] and consequently should be treated as the far field in which the fiber influence on the matrix is negligible.

The main assumption in shear-lag theories is that the resulting force from the interfacial shear stress τ is balanced by the force due to the variation of the axial stress [67, p. 5], hence

$$\frac{\mathrm{d}\sigma_\mathrm{f}}{\mathrm{d}x} = -\frac{2\tau}{r_\mathrm{f}}, \tag{2.27}$$

and consequently an expression for the interfacial shear stress is given by combining Eq. 2.25 and Eq. 2.27

$$\tau = \frac{n}{2} E_\mathrm{f} \varepsilon_\mathrm{m} \frac{\sinh(na\frac{2x}{l_\mathrm{f}})}{\cosh(na)}. \tag{2.28}$$

From Eq. 2.28, it can be derived that the interfacial shear stress reaches its maximum at the fiber ends and its minimum in the center of the fiber, which can be qualitatively seen in Fig. 2.12c. According to this theory, for the given shear stress transfer rate, short fibers with an aspect ratio below a certain threshold do not provide the surface area necessary to build up enough tensile stress within the fiber to cause fiber failure. The critical fiber length l_c is the minimum fiber length required to transfer sufficient interfacial shear stress to induce a normal stress equal the ultimate tensile strength of the fiber $\sigma_{u,\mathrm{f}}$ and consequently break it. This requires the failure strain of the matrix to exceed that of the fiber and occurs when $E_\mathrm{f}\varepsilon_\mathrm{m} > \sigma_{u,\mathrm{f}}$. To the author's knowledge the term critical fiber length was first introduced in the investigation of metallic fiber reinforcements by Kelly and Tyson [71, p. 340]. According to Lacroix et al. [72, p. 383], for the given shear-lag model after Cox, the critical aspect ratio $a_c = l_c/2r_\mathrm{f}$ can be calculated with

$$a_c = \frac{1}{n} \operatorname{arcosh}\left(\frac{E_\mathrm{f}\varepsilon_\mathrm{m}}{E_\mathrm{f}\varepsilon_\mathrm{m} - \sigma_{u,\mathrm{f}}}\right), \quad E_\mathrm{f}\varepsilon_\mathrm{m} > \sigma_{u,\mathrm{f}}, \tag{2.29}$$

which is based on the assumption that the tensile strength of the fiber is independent of the fiber length. The maximum possible stiffness in an FRP is reached only when the aspect ratio of the reinforcing fiber is greater than a_c.

Exceeding the prior theory is the case where debonding of the fiber from the matrix occurs before the fiber begins to fail, which requires to account for an imperfect interface. A simple approach to analyze the stress transfer with a debonded interface is the assumption after Kelly [73], who assumed a constant frictional shear stress τ_f after debonding. The model is described in Piggott [74, p. 280 ff.] and in Lacroix et al. [72]. Incorporating the relation in Eq. 2.27 and the assumption of zero axial stress transfer at the fiber ends, the axial fiber stress will rise linearly from both ends of the fibers. It is assumed that the interface will debond once the shear stress reaches a critical value, which is called interfacial shear strength τ_{IFSS} or IFSS, respectively, and that no matrix damage occurs. The debonding ratio m describes the ratio of unbonded to bonded fiber length and the debonding will occur on both fiber ends symmetrically. The fiber section with intact interface is assumed to behave according to Cox' shear-lag theory. A schematic of this model is illustrated in Fig. 2.13, for which the exact stress formulations are given in Appendix A.

A more elaborated theory about the linear-elastic stress transfer including matrix cracks and fiber fracture is given in McCartney [75], which is based on the results in Steif [76], who investigated the effects of broken fibers on the longitudinal stiffness.

Alternatives to the classical shear-lag models are provided from variational approaches based on the principal of minimum complementary energy, such as given in Nairn [70]. Instead of the assumptions made for the shear-lag theory, this variational model only requires to assume that the axial stresses relies solely on the axial coordinate. A qualitative stress distribution is given in Fig. 2.14, where the curves for the Cox model are indicated in dashed lines for comparison.

Major differences between the two model approaches are obvious. While the interfacial shear stress in the shear-lag model reaches its maximum at the fiber ends, Nairn [70] claims this to be a violation to the boundary conditions, which is

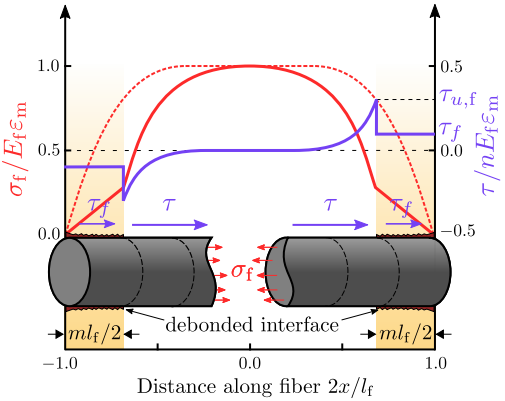

Figure 2.13: Schematic shear-lag theory after Cox [64] with debonded fiber ends after Piggott [74, p. 280 ff.]. The dashed, red curve is the Cox shear-lag result for the same material parameters without debonding ends.

reflected in the variational model where the shear stress becomes zero at the fiber ends and reaches its peak close to it. Moreover, the rates of which the stresses decay vary from model to model. An advantage of the variational approach is that it is also capable of modeling the radial and hoop stresses. Another variational approach is found in the work of Wu et al. [77], which has the advantage of considering the radial variation of axial stresses within the matrix material. Both research groups extended their variational models for imperfect interfaces in Nairn and Liu [78] and Wu [79], respectively.

Linear elastic matrix behavior, which is one of the assumptions in all previously introduced models, is mostly applicable to the stress transfer in fiber reinforced thermosetting polymers. Dealing with thermoplastic systems, the mechanical response of the matrix follows a rate dependency, which raises questions in the applicability of linear elastic models. Since the major load carrying component in FRPs is the fiber, which generally does indeed behave linearly elastic, it seems natural to neglect the viscous nature of the matrix. Hence the literature on analytical expressions for the stress transfer mechanisms in viscoelastic matrix systems is sparse. Thuruthimattam et al. [80] assumed a linear viscoelastic matrix behavior based on a single relaxation time and derived an analytical expression for

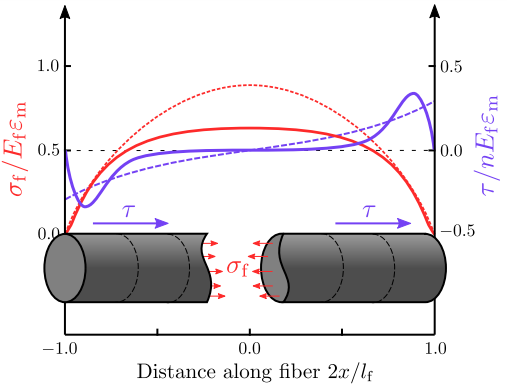

Figure 2.14: Schematic variational model after Nairn [70, p. 145]. The dashed curves are the Cox shear-lag results for the same material parameters for $a < a_c$.

the stress transfer in analogy to the Cox shear-lag model, with the assumption of a constant Poisson's ratio. They investigated the equilibrium time of the system and followed that it is much larger than the relaxation time of the matrix, concluding that a deduction on the overall composite behavior based on the viscoelastic matrix properties is problematic. Also, the shape of the stress curve changes over time significantly. Consequently, the critical aspect ratio is not constant over time, which should be considered when studying interface damage. Da Zhu and Gu [81] derived a model for the fiber pull-out test with a viscoelastic matrix material and a finite interface thickness. They concluded that increasing the embedded length increases the axial stress in the fiber and reduces the shear stress in the interface. An increase of the interface thickness also increased the axial stress, but had mixed results on the interfacial shear stress. Obaid et al. [82] extended the classic shear-lag model after Cox for linear viscoelastic effects of the matrix and studied the model for a short fiber reinforced composite. Their results include that an increase in the fiber volume content leads to an increased relaxation time, indication that the presence of fibers slows the rate of stress relaxation. Their results must be taken with caution though, as it was assumed that the pull-out test takes place rapidly, which is usually not the case in an experimental setup. More recent developments were made in the field of bio-mechanics in the works of Wu

et al. [83] and Wu et al. [84], who investigate the influences of overlapping fiber lengths and loading rates in a viscoelastic matrix on the composite stiffness for different transient models.

Possibly the first to investigate the elastic stress transfer by utilizing the Finite Element Analysis (FEA) were Carrara and Mcgarry [85], who concluded significant alterations of the interfacial shear stress near the fiber ends in comparison to the shear-lag model after Cox and studied the effects of fiber end geometry on the stress curves. An analytical model based on the shear-lag model investigating the fiber end geometry was developed in Topçu et al. [86]. It was stated in Nairn [87, p. 188] that FEA results do not agree well with the model after Cox and that the predictions of the shear-lag theory are at their most accurate when the fiber is much stiffer than the matrix material. One major concern in shear-lag theories is that the shear stress near the fiber end is underpredicted [66, p. 124]. Contrary, Goh et al. [69, p. 188] state that the form of σ_{f} predicted by the shear-lag models after Cox and Nairn is consistent with predictions made in FE-analysis, making it a plausible description of the stress transfer from matrix to fiber. Another early FEA study including the mechanics of debonding fibers was made in Owen and Lyness [88], who concluded that a greater stiffness ratio $E_{\mathrm{f}}/E_{\mathrm{m}}$ requires less matrix strain for the debonding to initiate. A general review study on FEA studies concerning the elastic stress transfer was made in Goh et al. [89].

Concluding, simple shear-lag models meet their limitations when interactions with other fibers or inclusions have to be taken into account, when the fiber volume content is high and when interfacial damage is to be investigated. Nevertheless, they provide a good first idea on the mechanics in FRPs.

2.3.2 Failure mechanisms in FRPs

To begin with, almost every failure mechanism within FRPs is accompanied by the evolution and/or propagation of a single or multiple cracks, which can either happen through the fiber, within the matrix or along the interface. To discuss this further, a general distinction is made between different *Modes*, which describe

different crack propagation and load geometries. Within the framework of linear fracture mechanics, the separation of an interface or the formation of a crack front is categorized into three different groups, depending on the direction in which the interface is loaded or separated, respectively. The three different modes are given in Fig. 2.15. In the coordinate system in the given figure, *Mode I* describes

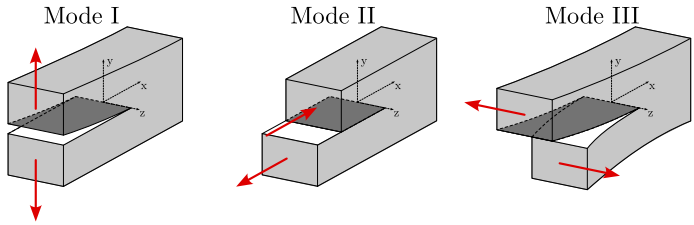

Figure 2.15: Different crack opening modes. Graphic redrawn from Gross and Seelig [90, p. 67].

the normal opening in which the crack faces are pulled away from one another in y-direction [90, p. 67]. *Mode II* and *Mode III* both describe shear separations, whereby the former describes a relative crack displacement normal to the crack front in x-direction, and the latter describes a relative crack displacement tangential to the crack front in z-direction. In most real life applications, the propagation of a crack front is a mixture of the three different modes.

Some failure mechanisms within FRPs occur without the participation of interface mechanics, although the interface plays an important role in the vast majority of cases. Even when the crack does not propagate along the fiber-matrix interface directly, it often follows a path near the interface in the typically softer phase, i.e., the matrix. The typical damage mechanisms in FRPs include fiber breakage, fiber pull-out, fiber bridging, fiber-matrix debonding and cracking of the matrix, which are schematically illustrated in Fig. 2.16. In the preceding work of Fliegener [1, p. 143ff.], it was shown that the assumption of a perfect interface between matrix and fiber leads to a vast overestimation within numerical simulations. To achieve a more realistic prediction of the composite behavior, an imperfect interface must be assumed and a proper model needs to be calibrated on experimental data.

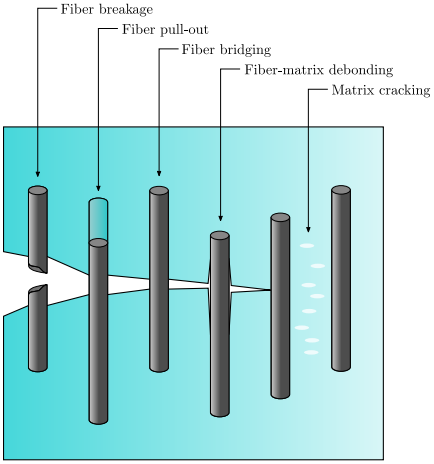

Figure 2.16: Typical damage mechanisms within FRPs. Graphic redrawn from Zollo [91, p. 115].

This allows to capture the effects of actual damage mechanisms on the effective mechanical characteristics of the composite.

Beaumont et al. [67, p. 116] describe that after an initial crack opening in the matrix material, the crack usually develops along the shortest path between and along the fiber-matrix interfaces. Numerical investigations in Sun et al. [92] confirm that the crack propagation takes place between fibers and along the interface, unless the fiber-matrix bonding or IFSS exceeds a critical value at which debonding is prevented and the crack transverses through the matrix only with accompanied fiber fracture [93]. This is one of the reasons for a possible decrease in fracture toughness in a composite material when the IFSS is increased, as the average pull-out length decreases accordingly, which was demonstrated in Harris et al. [94]. The weaker interface leads to an early debonding without fiber breakage and thereby increases the work of friction during pull out and consequently the fracture toughness. In terms of the overall mechanical properties of a composite, it is therefore not easy to say that a higher IFSS is always desirable. Both energetic and strength properties must be investigated to be able to assess the quality of the fiber matrix interface and its effect on the mechanical properties.

2.3.3 Test methods to assess fiber-matrix interface properties

Several properties of the fiber-matrix interface are of interest to industry and researchers in order to gain a better understanding of the overall composite material, which ultimately leads to further improvement in the development of new material systems. Qualitatively, this includes the propagation and location of cracks that occur along and near the interface and between fibers. Quantitatively, this includes energy and strength properties of the interface, which are required as input parameters for FEA simulations or to validate the corresponding results. Several test methods have been developed to characterize the fiber-matrix interface, of which the four most commonly used methods in the literature are shown schematically in Fig. 2.17.

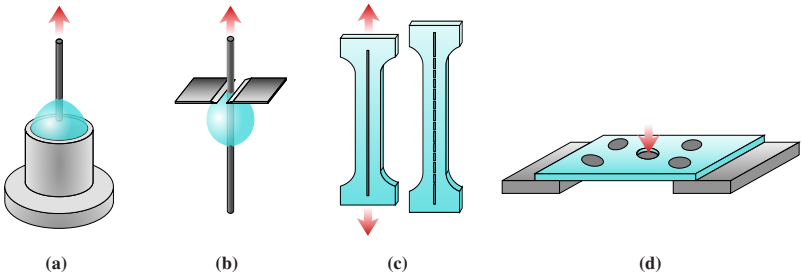

Figure 2.17: Schematic of the four most common single fiber interface characterization methods, which include (**a**) the single fiber pull-out test, (**b**) the microbond test, (**c**) the fiber fragmentation test and (**d**) the single fiber push-out test. Graphic inspired by [95].

It is possible to assign each test to a systematic group of tests, which may be defined differently depending on the point of view. Here, the tests are grouped into single fiber and multi-fiber experiments. Classical single fiber characterization tests include the single fiber pull-out test, the microbond test, the fiber fragmentation test and the single fiber Broutman test [96]. Multi-fiber tests are given with the single fiber push-out test and the multi-fiber pull out test, due to the presence of neighboring fibers [97]. In general, mutli-fiber tests have the advantage of investigating the effects of a fiber volume content and thereby fiber interaction,

which can not be reproduced by specifically designed single fiber lab specimens [98]. Moreover, in the case of the single fiber push-out test, the experiment is performed on the actual composite, which has gone through the industrial processing procedure. This allows to study the influence of production parameters, e.g. temperature and pressure, on the interfacial properties. On the other hand, the presence of other fibers in the vicinity of the tested fiber can lead to complex interaction effects, which makes it hard to conclude on the interfacial properties alone. In addition, the exact geometric configuration of a multi-fiber specimen can only be examined once, which makes the reproducibility of the tests more difficult. This justifies the investigation using single-fiber samples.

Another possible grouping of the tests is realized by differentiating the direction in which the interface is tested in. In general, this includes the shearing in fiber direction and the opening normal to the fiber orientation. While literature on shear failure is abundant, since it includes all above mentioned tests with the exception of the Broutman test, research on the characterization of the normal separation of matrix and fiber is limited [99]. Examples for the investigation of the normal debonding behavior can be found in Tandon et al. [100] and Rohrmüller [3, p. 103 ff.], in which non-standardized experiments are utilized.

The most common single fiber tests are presented below, along with their characteristics, both advantageous and disadvantageous. For all of these tests, there is an abundance of literature for the general case. However, specific literature on the application of the individual tests in combination with varying climatic boundary conditions is scarce, so a possible research question is the applicability and interpretation of the application of these tests at different humidity and temperature levels.

Fiber fragmentation test

The origin of the fiber fragmentation test can be traced back to Kelly and Tyson [71]. It consists of a single fiber completely embedded into a dogbone shaped matrix specimen. A requirement for the test is that the matrix failure strain must

be at least three times larger than the failure strain of the fiber, which leads to repeated fiber breakage each time the failure strain is reached along the embedded fiber under tensile load [101]. Once all fiber segments are shorter or just as long as the critical fiber length l_c, which is the length over which enough shear stress can be transferred for the fiber to break, the measured critcal fiber length is used to calculate the IFSS based on a simple analytical model. The process is illustrated in Fig. 2.17c. Comprehensive literature on the stress concentration along the interface during the fiber fragmentation test is given in Piggott [74, p. 227 ff.].

The fiber fragmentation test has been used to address the effects of environmental conditions on the fiber-matrix interface, i.e., by Schutte et al. [102], who investigated hydrothermal treatment and Ramirez and Carlsson [103], who characterized the IFSS under sea water conditions. Both concluded that the respective conditioned specimens showed a decrease in IFSS. Despite its ease of specimen preparation and test procedure, the test has numerous shortcomings, since it relies on measuring multiple fiber segments with varying lengths shorter than l_c and the test setup is prone for penny-shaped cracks at the fiber-matrix interface, leading to error-prone assessments of the IFSS [104]. Further, the analytical study by Piggott [105] suggests another limitation of the test: it primarily provides frictional data. This conclusion suggests that other testing methods may be more suitable for investigating the fiber-matrix interface characteristics.

Microbond test

The microbond test was developed in the mid-1980s, when a method was sought to alleviate the difficulty of embedding individual fibers in pull-out samples with an embedding length smaller than the critical fiber length l_c, which is necessary to prevent premature fiber rupture [106]. For the microbond test, a single or multiple droplets of a thermosetting resin or a thermoplastic matrix material are applied to a single fiber. After solidification, these droplets are sheared off from the fiber. Advantages of this method include low cost manufacturing of the specimens and the possibility to perform multiple tests on a single fiber, while the downsides are

large scattering in the results and the dependence of the mechanical properties on the droplet size [101].

Research using the microbond test considering environmental effects includes Biro et al. [107], who studied the effects of hygrothermal aging on a carbon-epoxy combination and observed a significant reduction of the IFSS after conditioning, which they attributed to plasticization effects in the matrix and a reduction of radial pressure due to thermal expansion, and Straub et al. [108], who investigated the effects of elevated temperature and pull-out rates on an aramid-epoxy system and concluded that an increase in temperature leads to a decrease in pull-out force. More recent research was conducted by Downes and Thomason [109], who investigated moisture effects on steel fibers inserted in PA6 and concluded that water has a diminishing effect on the IFSS, without further investigating the underlying mechanics, and by Bedi et al. [110], who utilized the microbond test to investigate the dependence of the IFSS and the fracture toughness on the pull-out rate in carbon fiber reinforced epoxy composites, with and without the addition of nanotubes. They concluded that both the IFSS and the fracture toughness show a monotonic nonlinear increase with increasing pull-out rate for the composite without nanotubes.

Single fiber push-out test

The single fiber push-out test resembles the only micro-mechanical in-situ test introduced within this study, which can be applied on the material of interest without the need to fall back on model specimens containing a single fiber [101]. Thereby, important history variables such as the pressure and temperature during manufacturing affect the test results directly. The test requires to cut and polish thin slices from the composite material, followed by pushing down on fibers which are perpendicular to the polished surface using a nano-indenter. A major advantage of the push-out test is that the effects of adjacent fibers, i.e., the fiber volume fraction, are taken into account directly in the experiment, which on the other hand makes it more difficult to isolate the fiber-matrix interaction. A major disadvantage is that the cutting and polishing process usually requires the use of coolant (in the

form of added water) and polishing agent in the form of a diamond suspension. This means that possible damaging influences of water on the interface properties can no longer be separated from the subsequent conditioning and the cutting and polishing procedure may itself induce degradation of the specimen. While nano-indenters with incorporated capabilities to regulate the climate during testing exist, extending a setup which lacks these capabilities is not easily realized, due to the enclosed testing device. This is another draw back when environmental effects need to be considered.

Interfacial properties under hydrothermal aging conditions were assessed using the single fiber push-out test by Bouillaguet et al. [111], who investigated two different glass fiber reinforced resins. They report a reduction of the IFSS of 15 to 20 % after hydrothermal aging, which they contribute to an overall degrading of the constituents. Finding further literature on the single fiber push-out test to investigate environmental effects deemed to be difficult, which may be explained by the difficulty of providing a corresponding climate during testing.

Single fiber pull-out test

The single fiber pull-out (SFPO) test is a direct testing method that offers a straightforward interpretation of the fiber-matrix interface properties under the influence of various climatic conditions. Its key advantage lies in the possibility to directly calculate the IFSS, a critical determinant of load transfer efficiency in composite materials. However, one limitation is that it demands meticulous sample preparation and precise control of experimental parameters to achieve accurate results, which is an attribute shared among micro-mechanical testing methods in general. For the pull-out test, first a single fiber is embedded in the corresponding matrix material. After solidification, the fiber is being pulled out, during which the force and displacement are recorded, from which the interfacial characteristics are calculated from. A theoretical model on the stress distribution along the interface during the SFPO test is given in Piggott [74, p. 221 ff.] and in Marotzke [112]. A detailed methodology will be given in Chapter 5.

Considering environmental effects, Doshi et al. [113] used the single fiber pull-out test to focus on the uncoupled influence of temperature and humidity on the IFSS in glass fiber reinforced epoxy. In their study they saw an increase/decrease of the IFSS when the temperature was decreases/increased. The IFSS also dropped by $25\,\%$ for specimens that were immersed in water. They explained the observed effects by matrix expansion mechanisms due to an alteration of temperature and by a plasticizing effect of moisture on the polymer. Multiple studies on the effects of temperature and humidity on PA based FRPs utilizing the fiber pull-out test were made by the group around researchers K. Tanaka et al. [114, 115, 116]. Conditioning was realized by submersing the specimens directly into distilled water, which is a rather aggressive conditioning method due to the direct water contact. Thereby, different aspects of the contribution of humidity effects may not be captured, because potential hydrolysis effects are emphasized through the diffusion of large amounts of water into the polymer. Their main results are that water absorption not only leads to a softening of the matrix behavior, but also directly decreases the IFSS by diffusing water.
Comparing the mentioned studies, different fracture patterns are described for different conditioning states. While it is mentioned in Tanaka et al. [114] that dried specimens resulted in blank fibers and wet specimens showed an early failure in the matrix which resulted in matrix residue remaining on the pulled out fiber, a later study from the same group in states the opposite for multi-fiber tensile tests [115], leaving room for further investigations. They observed varying effects of water absorption between PA6, PA66 and PA12 based specimens and concluded that the transcrystallinity in the vicinity of the fiber-matrix interface in CF-PA6 and CF-PA12 specimens decreased the water absorption and subsequently saw a lower reduction in the IFSS. In this study the weakening effect of water on the IFSS was found to be reversible, which was demonstrated in re-dried specimens. This is in direct contradiction with the findings in Chen and Piggott [117], who found a reduction of the debonding force of up to $33\,\%$ and the post debonding friction force of up to $50\,\%$, which did not fully restore after drying the specimens again. The explanation for a decreasing IFSS for increased humidity or temperature levels, respectively, as given in Tanaka et al. [116], is strongly based on a comparable expansion mechanism due to both environmental factors and a

consequent decrease in radial pressure within the fiber-matrix interface. This was backed up in a linear-elastic thermal finite element analysis (FEA) in an earlier study [118]. Open questions, which have not been addressed in the mentioned studies are how the simultaneous combination of temperature and humidity within a stable climate affect the IFSS, which remains an unexplored field of research.

2.4 Co-Dico interface characterization

There are several tests available to study different opening modes for the interlaminar separation within fiber reinforced polymers. According to Weidmann et al. [119], the most commonly used test methods are:

- *Mode I*:
  - Double cantilever beam (DCB),
  - Single cantilever beam (SCB),
  - Climbing drum peel (CDP).
- *Mode II*:
  - Tilted sandwich debond (TSD),
  - Modified three-point bending (MTPB),
  - Cracked sandwich beam (CSB),
  - End notch flexure (ENF).

In the following, the focus will be limited to the investigation of the opening direction in *Mode I*, because the tests methods are often easier to evaluate. Furthermore, the critical energy release rate in *Mode I* is generally lower than for the shear loading modes, which is principally attributed to cusp formation in polymer rich regions during *Mode II* testing [120]. Hence, the results from *Mode I* testing may be interpreted as a conservative lower bound for the interface quality. Thereby, environmental effects on the interface can be qualitatively compared by resorting to measurement results from *Mode I* testing.

The DCB test might be the most commonly used test to investigate the *Mode I* characteristics of composite materials [121, p. 174]. It consists of a relatively flat specimen which contains a symmetrizing pre-crack starting at one end of the specimen. During the test, the crack faces are continuously further separated, so that the crack propagates towards the other end of the specimen. The DCB test is standardized in the American Society for Testing and Materials (ASTM) D5528 [122] for unidirectional FRPs. Even though the DCB test has been used successfully to investigate environmental effects in FRPs, e.g., by Uematsu et al. [123] for elevated temperatures and Williams et al. [124] for combined hydro-thermal effects, who saw a general increase in fracture toughness with increased temperature/humidity, the test is not usable for the material system under investigation.

For the investigated material system, it is not possible to induce a pre-crack between the continuous and discontinuous structure which would result in a symmetric specimen, preventing a simple assessment of the interface quality through the DCB experiment. Thus, a method is required that does not depend on a symmetrizing pre-crack. A method that fulfills this requirement can be found with the climbing drum peel (CDP) test.
The climbing drum peel test is used to evaluate the adhesive bond between two materials. The method is standardized according to the German Institute for Standardization European Norm (DIN EN) 2243-3 [125] and ASTM D1781 [126]. This test is typically performed on a flexible structure adhering to a rigid structure. During the test, the flexible structure is continually wrapped around the upwards climbing drum, loading the interface in normal direction. Once the load exceeds a critical value, the interface separates in the normal direction, making the CDP experiment a *Mode I* test. The CDP test rig for testing the interface for Co-Dico FRP can be seen in Fig. 2.18.

Compared to conventional techniques like the DCB test, the CDP method offers several advantages. For instance, due to the inherent kinematics, the crack position can be directly correlated with the current drum position, eliminating the need for separate crack detection. The CDP test can also be used on asymmetric structures without causing the crack to deviate from the intended fracture plane, as was highlighted in Michel et al. [127]. This is a crucial advantage for the

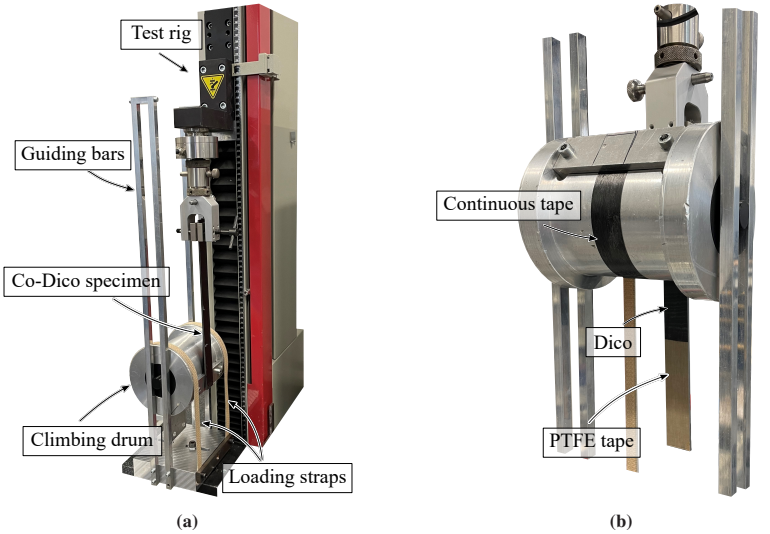

Figure 2.18: (**a**) Test apparatus for the CDP experiment before test and (**b**) detailed view during test from the other side.

scenario of investigating highly asymmetric structures in the given Co-Dico hybrid. Another advantage, as shown through X-ray investigations in Daghia and Cluzel [128], is that an issue with the DCB test is that the crack front may be curved due to anticlastic curvature, while this should not occur in the CDP test, where the crack propagation is essentially imposed by the presence of the drum. Furthermore, the results by Michel et al. [127] reveal that the variability observed in the CDP test data is significantly less than the variability observed in the *Mode I* fracture toughness within DCB specimens. In its common form, the experiment is evaluated to extract the average peel torque. Daghia and Cluzel [128] expanded the evaluation to further extract information about the critical strain energy release rate. For this, the authors state three requirements for the experimental setup:

- the radius of the drum needs to be large enough,
- the peel arm needs to be flexible,
- the winding forces need to be large,

without further specifying numeric values. The necessity for these prerequisites stems from the fact that a structure that lacks coherent wrapping around the drum, such as a structure with a diminished flexural modulus, violates the energy assumptions posited in the analysis, thereby preventing the evaluation of material parameters. A comprehensive explanation regarding this topic is provided in the appendix in Daghia and Cluzel [128].

In the experiment, the top section of a specially prepared sample is affixed to the testing apparatus. The sample's lower portion contains a pre-crack (further details on sample preparation can be found in Section 6.2.2), which results in the detachment of the Co layer's free end from the Dico material. This flexible, detached end of the Co layer is then connected to the drum at the smaller radius, denoted as r_1. Two loading straps, wrapped around the drum's second radius r_2, are grounded to exert the requisite torque on the drum, facilitating the interface's delamination and the crack's propagation. The torque initiation coincides with the start of the test when a steady displacement rate is applied to the upper clamping. The exact kinematics and evaluation methodology are described later in Sec. 6.1.1.

The limitations of the CDP test include the complex loading conditions due to the arrangement of the test apparatus. If the flexural modulus is too high and the material is also brittle, the peeled material may break if the radius of the drum is too small. For the same reason, the test is not applicable if the peeled material is too thick, e.g., in the case of thick laminates.

2.5 Numerical modeling

On the one hand, numerical models are used to investigate experimental phenomena that are not easy to follow during the experiment due to visual obstructions or difficulties in evaluating a single property. On the other hand, validated models can be used to predict unknown scenarios involving, for example, more complicated boundary conditions or the transfer of measured effects on the single fiber

to multi-fiber samples or compounds. An incomplete list of literature is given below.

2.5.1 Matrix model

A multitude of material models exist in the literature to capture the time, temperature and humidity dependent polymer behavior. These models can either be linear or nonlinear in stress/strain. Generally, these models are either applicable to temperatures below or above T_{g}, with only a few models bridging the transition as well [34]. Some models to calculate the humidity dependent T_{g} were introduced in Sec. 2.1.2 in this chapter.

Sharma et al. [48] developed a model to capture the diffusion of water and simulate its effect on the stiffness properties in PA6. For the water diffusion they resort to Fick's diffusion law, as was already done in other studies [129, 130]. They coupled the water concentration and the mechanical response by assuming the material parameters of a linear viscoelastic model to be dependent on the water concentration and by considering moisture induced swelling. Thereby, the model is essentially nonlinear in the moisture content, but still linear in stress and strain. Other models approaching the sorption and swelling behavior are found in the works of Sambale et al. [30, 131] and Wetzel et al. [132]. Potential based models with varying/constant material parameters with varying moisture content are given in Sharma and Diebels [133] and Dyck et al. [134].

Many models have in common that they are based on a configuration of idealized springs and dampers, e.g., in the generalized Maxwell or Kelvin-Voigt model. In general, these models are linear in stress/strain, which means that the creep compliance or relaxation modulus are not dependent on the loading condition. Illustrated in Fig. 2.19 is the reconstructed creep compliance for Ultramid® B3K at different temperatures under different loads. It is clearly evident that the creep compliance is not only temperature dependent, but also varies for different stress levels. Hence, it is necessary to capture this nonlinearity to adequately model the stress distribution within polyamides. An extension to the linear framework

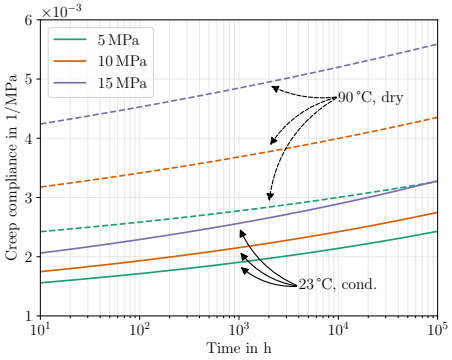

Figure 2.19: Creep compliance for the another type of PA6, i.e., Ultramid® B3K, at different load levels and climates. Data recovered from manufacturer's data sheet by fitting a quartic polynomial to the creep modulus data in log-lin space and inverting to derive the creep compliance [135].

of these models can be found in the theory of Schapery [136]. The theory was successfully applied to modeling DMA experiments of PA6 in Zink et al. [137], albeit limited to one dimension (1D) and without considering environmental effects.

2.5.2 Interface model

Besides continuum damage models, for which a selection can be found in Camacho and Ortiz [138], which approach the propagation of failure within a material and a consequent crack propagation through a degrading elastic stiffness, the model of choice for the propagation of interface failure is the cohesive zone approach or cohesive zone model (CZM), respectively. The CZM is a theoretical framework used to describe the initiation and propagation of cracks in materials. It focuses on the behavior of materials at a crack tip, where the material undergoes damage and separation. In CZM, the interface ahead of a crack is modeled as a cohesive zone characterized by a cohesive law that defines the relationship between separation and traction. While it is common practice to predefine a single possible crack

path, the cohesive zone approach is not limited in this regard and is capable to capture crack nucleation and pervasive cracking [139].

Cohesive zone approaches go as far back as to the work in Prandtl [140] and later to Dugdale [141] and Barenblatt [142], who were looking for a practical solution to avoid infinite stress values at the crack tip, as predicted by classical fracture theories [143]. While Dugdale [141] resorted to constant stresses in front of the crack tip caused by plastic deformation along a thin strip, Barenblatt [142] investigated purely elastic behavior in brittle fracture. Hillerborg et al. [144] proposed a numerical method in which the crack propagates as soon as the stress at the crack tip reaches the material tensile strength. They furthermore proposed that the stress does not fall to zero at once, but rather decreases with increasing crack opening, which can be regarded the first use case of a cohesive zone model in combination with FE calculations. Their approach maps the sharp crack front to a microcrazed zone, i.e., the cohesive zone as shown in Fig. 2.20, which is particularly representative of the crack propagation in polymeric materials.

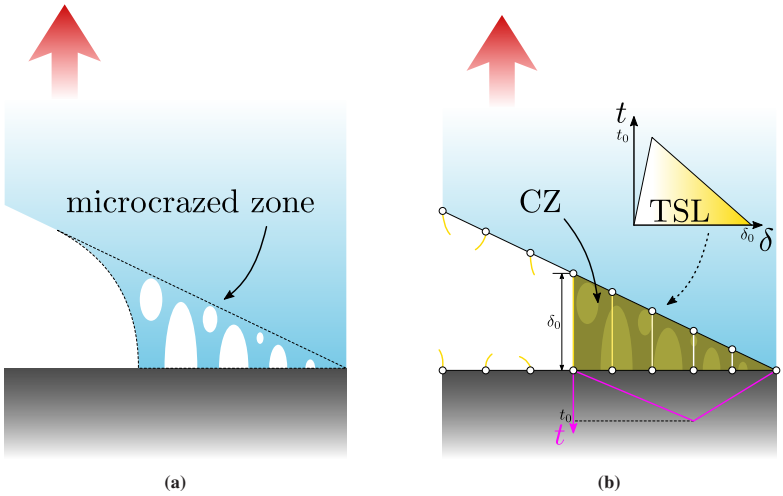

Figure 2.20: Cohesive zone approach, with (**a**) visualizing the simplified physical crack with microcrazing and (**b**) demonstrating the numerical cohesive zone approach including a simplified FE mesh (including elements with zero stiffness) and a bi-linear traction separation law.

Central to all cohesive zone formulations is a cohesive or traction-separation law (TSL), which relates the crack opening, displacement jump or simply separation δ to a stress vector or traction t acting on the crack surfaces [145]. According to Paulino and Zhang [146], CZMs can be categorized into intrinsic and extrinsic CZMs.

In intrinsic formulations, the traction initially increases with an increasing separation, reaches a maximum traction t_0, and then falls to zero at the maximum crack separation δ_0, after which the cohesive element is assumed to be fully damaged and does not carry any load, i.e., the crack is fully open. A typical TSL for an intrinsic CZM is the bilinear TSL as given in Fig. 2.21. The physical interpretation

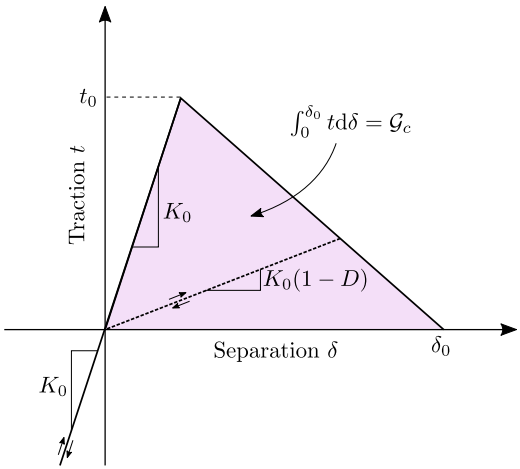

Figure 2.21: Bilinear traction-separation law in reference to Salve and Jalwadi [147], where K_0 is the intial stiffness, D is the damage variable, t_0 is the damage initiation traction, δ_0 is the maximum separation and $\mathcal{G}_c$ is the critical energy release rate. Graphic reused from the author's publication in Christ et al. [148].

in the bilinear TSL is that for small separations the material exhibits linear elastic behavior. Beyond a critical separation, the material transitions into a softening behavior with a linear decrease in traction as separation increases until failure. Besides the bilinear TSL, other TSL exist, such as the exponential TSL, the cubic polynomial TSL and more, which are usually devided into potential based and

non-potential based [139]. For the intrinsic formulation, all cohesive surfaces must be defined in the initial mesh, so that all possible crack propagation paths need to be known beforehand [146]. If the cohesive surfaces are selected in such a way that the crack can propagate in many different directions, this can lead to a high degree of artificial compliance. The advantage of the intrinsic formulation is obviously an easy implementation and avoidance of complicated remeshing during the simulation. An early contribution concerning the use of a bilinear TSL in the intrinsic formulation on composite materials is given in Geubelle and Baylor [149], who investigated the delamination process between epoxy composites plies and found a good agreement with experiments, including crack initiation and propagation between adjacent plies.
In contrast, extrinsic formulations do not contain an initial incline in traction, but assume that the separation between elements remains zero until a critical traction is reached and then the traction follows a monotonous decline instead [146]. The advantages are that cohesive elements are added adaptively and the crack path does not need to be known prior. Hence, the artificial compliance from the intrinsic formulation for complex possible crack paths is avoided. A major disadvantage for the extrinsic formulation lies in the complicated updating scheme of the mesh. Pioneering work in extrinsic CZM can be found in Camacho and Ortiz [138], who demonstrated the capabilites of the model to be used for crack propagation along arbitrary paths.

In the following interface studies, the crack propagation path is known and follows a straight line in general. This occurs either along the fiber-matrix interface or along the Co-Dico interface. Hence, it is feasible to resort to the intrinsic formulation of the CZM, utilizing the bilinear TSL. As mentioned above, cohesive surfaces relate the crack opening separation vector $\underline{\delta}$ at a given location, i.e., the displacement jump of adjacent continuum or shell elements, to the traction vector $\underline{t}$ on this surface in the form of a TSL, which in the case of a linear formulation takes the following form

$$\underline{t} = \underline{\underline{K}}\,\underline{\delta}, \tag{2.30}$$

where $\underline{\underline{K}}$ is the stiffness matrix representing the resistance against a change in separation [150]. The stiffness should not be confused with a material stiffness, but

should be treated as a non-physical parameter [151]. It is also sometimes referred to as penalty stiffness [152]. In its limit, the numerical stiffness should take an infinite value, which is numerically problematic, so it is modeled using a large enough value instead. Incorporating the assumption of an identical stiffness in the normal and both shear directions and no shear coupling, the traction separation law simplifies to

$$\underline{t} = K\underline{\delta}, \tag{2.31}$$

with a single scalar stiffness K. To incorporate the effects of a mechanically degrading interface, a damage model must be assumed. Different damage models exist, which usually are built upon a stress-based or energy-based damage initiation criterion, respectively. Here, the investigations will be limited to a stress-based criterion. The quadratic nominal stress damage initiation criterion is defined as

$$\left(\frac{\langle t_\mathrm{n}\rangle}{t_{n,0}}\right)^2 + \left(\frac{t_\mathrm{s}}{t_{s,0}}\right)^2 + \left(\frac{t_\mathrm{t}}{t_{t,0}}\right)^2 = 1, \quad \text{where } \langle\,\cdot\,\rangle = \max(0,\,\cdot\,), \tag{2.32}$$

where t_n, t_s and t_t are the normal and both shear tractions, respectively, while $t_{\mathrm{n},0}$, $t_{\mathrm{s},0}$ and $t_{\mathrm{t},0}$ are the damage initiation tractions in the corresponding directions. It is often the case that only a single direction has non-vanishing traction components, e.g., the shear direction acting parallel to the fiber alignment during a single fiber pull-out experiment or the normal direction during a double cantilever beam experiment. In these isolated load cases, it is often fair to resort to a single damage initiation traction, i.e., $t_{\mathrm{n},0} = t_{\mathrm{s},0} = t_{\mathrm{t},0} = t_0$, because the contribution of the other two traction components is negligible.

Once the damage initiation criterion in Eq. 2.32 is fulfilled, damage initiates and a model for the evolution of the damage variable is necessary. For the bilinear TSL, the damage variable $D \in [0, 1]$ evolves so that the traction follows a bilinear path. Hence, the stiffness relating traction and separation degrades to $K = K_0(1-D)$ from an initial stiffness K_0. The rate at which D increases for an increasing separation δ depends on the material parameter $\mathcal{G}_c$, which is the critical energy release rate and which is exactly the area enclosed by the TSL, as seen in

Fig. 2.21. When the work per cohesive surface area is equal $\mathcal{G}_c$, it must be that $D = 1$, indicating full separation. Further details on the mechanics of cohesive surfaces are given in Ingo Scheider [150] and Cornec et al. [153]. Since K_0 is essentially a numerical value, as stated above, two parameters, i.e., the damage initiation traction t_0 and critical energy release rate $\mathcal{G}_c$ are free to be chosen to capture interface effects on the effective response within a simulation.

2.5.3 Homogenization methods

Despite massive improvements in computational resources over the last decades, enabling the calculation of more detailed and complex models, it is often still necessary to reduce the level of complexity of material models. When macroscopic structures need to be analyzed numerically, where the smallest relevant element of the microstructure is orders of magnitude smaller than the component itself, averaging methods must be used to avoid the creation of time- and memory-intensive microstructures and the associated computational time. This is achieved by converting the complex microstructure into a homogeneous, but not necessarily isotropic structure by statistical averaging, which is termed *homogenization*.

The primary incentives for utilizing homogenization techniques include the simplification of complex or time-consuming material property expressions in composite materials and the reduction of both experimental and computational costs [154]. These methods are deployed to derive analytical formulas, numerical outcomes, or theoretical limits for effective material properties when the microstructure is multi-phase and/or non-uniform. Introductory resources for general composites are available in Christensen [155] and Aboudi et al. [156], while more specific information on fiber reinforced composites can be found in Chawla [7, p. 341ff.], with a succinct summary provided in Yu [157].

Regarding stiffness properties, in 1889 and 1929 first useful bounds for mechanical parameters were developed in Voigt [158] and Reuss [159], respectively [160, p. 296]. These bounds are easy to implement and provide an initial approximation for effective properties. However, the bounding approach has limitations: the

effective properties envelope is broad if one phase exceeds a dilute inclusion, and there is a common misunderstanding that the Voigt bound for material properties like Young's modulus and Poisson's ratio in isotropic materials follows a simple rule of mixture [161, p. 2198], while this rule only applies to shear and bulk modulus [157, p. 12]. Higher order and more precise bounding techniques are available in the Hashin-Shtrikman variational scheme [162, 163], but the calculation nonlinearly depends on a user-chosen reference material [164, p. 3785 ff.].

In addition to bounding methods, mean-field approximations, based on Eshelby's solution [165], provide analytical expressions to determine effective properties. These methods should fall within variational bounds to be physically meaningful. Prominent among these are the dilute distribution, the Mori-Tanaka [166], and the self-consistent scheme [167, 168], with the Mori-Tanaka and self-consistent scheme being the most favored [154]. However, this work does not evaluate the simple self-consistent scheme due to a lack of motivation for embedding an inclusion into the effective medium [169]. Similarly, the generalized version, which analyzes a three-phase body of inclusion, matrix, and effective material, was not considered due to the dependence of effective properties on the initial stiffness for the iterative process. Moreover, while the self-consistent method adequately predicts the behavior of polycrystals, it is less precise for two-phase composites, as demonstrated by Pierard et al. [170]. Recent studies applying a multi-inclusion self-consistent homogenization to porous polycrystals are provided in Fritsch et al. [171] and Morin et al. [172].

In the case of the present work, the scale of specific investigated specimens require that individual fibers can no longer be resolved in the model and instead the microstructure must be represented statistically, i.e., homogenization methods must be utilized. To find representative homogeneous stiffness tensors for the given case, which effectively behave like the volume averaged inhomogeneously distributed stiffnesses within the microstructure, the frequently used homogenization methods after Mori and Tanaka are used for continuum elements, while shell elements will be homogenized using a shear-lag informed Halpin-Tsai approach.

Mori-Tanaka homogenization

The mean-field homogenization methods are based on the average stress/strain theorem [173, p. 208ff.], which results in a formulation for the effective stiffness within a homogenized material bases on its local microstructure

$$\begin{aligned}\bar{\mathbb{C}} &= \frac{1}{V}\int_V \mathbb{C} : \mathbb{A}\,\mathrm{d}V = \sum_{i=1}^{n} v_i \frac{1}{V_i}\int_{V_i} \mathbb{C} : \mathbb{A}\,\mathrm{d}V \\ &= \langle \mathbb{C} : \mathbb{A} \rangle = \sum_{i=1}^{n} v_i \langle \mathbb{C} : \mathbb{A} \rangle_i . \end{aligned} \tag{2.33}$$

Here, $\bar{\mathbb{C}}$ and $\mathbb{C}$ are called the effective stiffness and local stiffness tensor, respectively, n is the number of individual constituents and the relative volume fraction of a domain of constant phase is given with v_i. The operators $\langle\cdot\rangle$ and $\langle\cdot\rangle_i$ indicate the volume averages of the total volume and the volume of phase i, respectively. $\mathbb{A}$ is the linear mapping of the effective strain $\bar{\boldsymbol{\varepsilon}}$ to the local strain $\boldsymbol{\varepsilon}$ and is called concentration or localization tensor

$$\boldsymbol{\varepsilon} = \mathbb{A} : \bar{\boldsymbol{\varepsilon}}. \tag{2.34}$$

For the given context of fiber reinforced polymers, Eq. 2.33 is further specified for a fibrous phase (subscript f) and a matrix phase (subscript m), resulting in

$$\bar{\mathbb{C}} = v_\mathrm{m} \langle \mathbb{C} : \mathbb{A} \rangle_\mathrm{m} + v_\mathrm{f} \langle \mathbb{C} : \mathbb{A} \rangle_\mathrm{f}. \tag{2.35}$$

The volume average of the concentration tensor $\langle \mathbb{A} \rangle$ must be equal to the identity tensor of fourth order, which allows to express the volume average of the concentration tensor in one phase as a function of the other

$$v_\mathrm{m} \langle \mathbb{A} \rangle_\mathrm{m} = \mathbb{I} - v_\mathrm{f} \langle \mathbb{A} \rangle_\mathrm{f}. \tag{2.36}$$

Together, Eqs. 2.35 and 2.36, give the general homogenization equation for a material consisting of a matrix and fibrous phase

$$\bar{\mathbb{C}} = \mathbb{C}_\mathrm{m} + v_\mathrm{f}\langle(\mathbb{C}_\mathrm{f} - \mathbb{C}_\mathrm{m}) : \mathbb{A}\rangle_\mathrm{f}, \tag{2.37}$$

where $\mathbb{C}_\mathrm{m}$ and $\mathbb{C}_\mathrm{f}$ are the fourth order stiffness tensors of matrix and fiber, respectively. Since the localization tensor $\mathbb{A}$ is not known analytically in general, the challenge for each mean-field homogenization scheme is to approximate this localization tensor based on individual assumptions.

The assumption within the Mori-Tanaka (MT) scheme [166] is based around the single inclusion problem (SIP) after Eshelby [165], who derived an analytical expression for the strain localization for a single linear-elastic inclusion. In reference to Gross and Seelig [90], the SIP for a spheroid inclusion results in the following relation between the local strain within an α-type inclusion $\varepsilon_{\mathrm{f},\alpha}$ and the effective strain $\bar{\varepsilon}$

$$\boldsymbol{\varepsilon}_{\mathrm{f},\alpha} = \underbrace{\left(\mathbb{I} + \mathbb{S}_\alpha : \mathbb{C}_\mathrm{m}^{-1} : (\mathbb{C}_{\mathrm{f},\alpha} - \mathbb{C}_\mathrm{m})\right)^{-1}}_{:=\mathbb{A}_{\mathrm{f},\alpha}^{\infty}} : \bar{\boldsymbol{\varepsilon}}. \tag{2.38}$$

Here, $\mathbb{I}$ and $\mathbb{S}_\alpha$ are the identity tensor and the spheroid Eshelby tensor of fourth order, respectively, and $\mathbb{C}_{\mathrm{f},\alpha}$ is the stiffness tensors of the inclusion of type α. The assumption in the MT approach states that the Eshelby solution in Eq. 2.38 can be used to approximate the mapping from the local matrix strain $\boldsymbol{\varepsilon}_\mathrm{m}$ to the local fiber strain $\boldsymbol{\varepsilon}_{\mathrm{f},\alpha}$ of fiber type α

$$\boldsymbol{\varepsilon}_{\mathrm{f},\alpha} = \mathbb{A}_{\mathrm{f},\alpha}^{\infty} : \boldsymbol{\varepsilon}_\mathrm{m}. \tag{2.39}$$

As before in Eq. 2.34, it is postulated that there exists another concentration tensor, hereinafter referred to as $\mathbb{A}_\mathrm{m}^\mathrm{MT}$, which maps the effective strain on the matrix strain

$$\boldsymbol{\varepsilon}_\mathrm{m} = \mathbb{A}_\mathrm{m}^\mathrm{MT} : \bar{\boldsymbol{\varepsilon}}, \tag{2.40}$$

so that combined Eq. 2.39 becomes

$$\boldsymbol{\varepsilon}_{\mathrm{f},\alpha} = \underbrace{\mathbb{A}^{\infty}_{\mathrm{f},\alpha} : \mathbb{A}^{\mathrm{MT}}_{\mathrm{m}}}_{:=\mathbb{A}^{\mathrm{MT}}_{\mathrm{f},\alpha}} : \bar{\boldsymbol{\varepsilon}}. \tag{2.41}$$

In the same way as in Eq. 2.36, the volume average of the concentration tensors must correspond to the identity, so that

$$\begin{aligned} \langle \mathbb{A}^{\mathrm{MT}} \rangle &= v_{\mathrm{m}} \langle \mathbb{A}^{\mathrm{MT}} \rangle_{\mathrm{m}} + v_{\mathrm{f}} \langle \mathbb{A}^{\mathrm{MT}} \rangle_{\mathrm{f}}, \\ &= v_{\mathrm{m}} \mathbb{A}^{\mathrm{MT}}_{\mathrm{m}} + v_{\mathrm{f}} \sum_{\alpha} c_{\alpha} \mathbb{A}^{\mathrm{MT}}_{\mathrm{f},\alpha} \overset{!}{=} \mathbb{I}, \end{aligned} \tag{2.42}$$

where c_{α} is the volume fraction of the fibers of type α in relation to the total fiber volume, which requires that $\sum_{\alpha} c_{\alpha} = 1$. Again it is assumed that the properties are phase-wise constant. Using the definition of $\mathbb{A}^{\mathrm{MT}}_{\mathrm{f},\alpha}$ from Eq. 2.41 and rearranging results in

$$\mathbb{A}^{\mathrm{MT}}_{\mathrm{m}} = \left(v_{\mathrm{f}} \langle \mathbb{A}^{\infty}_{\mathrm{f},\alpha} \rangle_{\mathrm{f}} + v_{\mathrm{m}} \mathbb{I} \right)^{-1}, \tag{2.43}$$

so that an analytical expression for $\mathbb{A}^{\mathrm{MT}}_{\mathrm{f},\alpha}$ is found. Combined with the general homogenization equation in Eq. 2.37, a general expression for an arbitrary amount of fiber types (e.g. glass and carbon fibers) is derived with

$$\begin{aligned} \bar{\mathbb{C}}^{\mathrm{MT}} &= \mathbb{C}_{\mathrm{m}} + v_{\mathrm{f}} \langle (\mathbb{C}_{\mathrm{f},\alpha} - \mathbb{C}_{\mathrm{m}}) : \mathbb{A}^{\mathrm{MT}}_{\mathrm{f},\alpha} \rangle_{\mathrm{f}}, \\ &= \mathbb{C}_{\mathrm{m}} + v_{\mathrm{f}} \langle (\mathbb{C}_{\mathrm{f},\alpha} - \mathbb{C}_{\mathrm{m}}) : \mathbb{A}^{\infty}_{\mathrm{f},\alpha} \rangle_{\mathrm{f}} : \left(v_{\mathrm{f}} \langle \mathbb{A}^{\infty}_{\mathrm{f},\alpha} \rangle_{\mathrm{f}} + v_{\mathrm{m}} \mathbb{I} \right)^{-1}. \end{aligned} \tag{2.44}$$

The expression in question requires careful handling, as it has been demonstrated in Qiu and Weng [174] and Weng [175] that multi-inclusion materials may not exhibit a symmetric effective stiffness due to variations in the shape and stiffness properties of the different types of inclusions, which would violate the thermodynamic principal following the potential relation of the stress tensor. Additionally, Qiu and Weng [174] demonstrated that for hybrid materials with inclusions that differ in shape and orientation, the MT approach yields an effective stiffness that may fall outside the Hashin-Shtrikman-Walpole bounds.

An equivalent formulation to Lee [176] is found by rearranging Eq. 2.44 to give

$$\bar{\mathbb{C}}^{\mathrm{MT}} = \left(v_{\mathrm{m}}\mathbb{C}_{\mathrm{m}} + v_{\mathrm{f}}\langle\mathbb{C}_{\mathrm{f},\alpha} : \mathbb{A}_{\mathrm{f},\alpha}^{\infty}\rangle_{\mathrm{f}}\right) : \mathbb{A}_{\mathrm{m}}^{\mathrm{MT}}. \tag{2.45}$$

This formulation assumes that all inclusions are unidirectionally aligned. If all fiber types can be described by a single fiber orientation distribution, i.e., all types of fibers are indistinguishably distributed, it is suitable to calculate an average effective stiffness by weighting the effective stiffness in Eq. 2.45 by the fiber orientation tensors of second and fourth order, as it was shown in Brylka [177, p. 40 ff.]. When the types of fibers are individually distributed, the orientation averaging must be included in the expression itself, so that Eq. 2.45 needs to be reformulated to

$$\bar{\mathbb{C}}^{\mathrm{MT}} = \left(v_{\mathrm{m}}\mathbb{C}_{\mathrm{m}} + v_{\mathrm{f}}\langle\{\mathbb{C}_{\mathrm{f},\alpha} : \mathbb{A}_{\mathrm{f},\alpha}^{\infty}\}\rangle_{\mathrm{f}}\right) : \left(v_{\mathrm{m}}\mathbb{I} + v_{\mathrm{f}}\langle\{\mathbb{A}_{\mathrm{f},\alpha}^{\infty}\}\rangle_{\mathrm{f}}\right), \tag{2.46}$$

where $\{\cdot\}$ indicates the orientation average. The calculation of this orientation average is explained in Bauer and Böhlke [178] following Eq. 58, which is in alignment with Advani and Tucker [179]. When only a single type of inclusion is treated, as is the case in the present research work, $\mathbb{A}_{\mathrm{f},\alpha}^{\infty}$ and $\mathbb{C}_{\mathrm{f},\alpha}$ reduce to $\mathbb{A}_{\mathrm{f}}^{\infty}$ and $\mathbb{C}_{\mathrm{f}}$, respectively, and Eq. 2.44 simplifies to

$$\bar{\mathbb{C}}^{\mathrm{MT}} = \mathbb{C}_{\mathrm{m}} + v_{\mathrm{f}}\left(\mathbb{C}_{\mathrm{f}} - \mathbb{C}_{\mathrm{m}}\right) : \left(v_{\mathrm{f}}\mathbb{I} + v_{\mathrm{m}}\mathbb{A}_{\mathrm{f}}^{\infty\,-1}\right)^{-1}. \tag{2.47}$$

Shear-lag informed Halpin-Tsai homogenization

A purely scalar, empirically derived homogenization method for fiber reinforced composites is found in the Halpin-Tsai (HT) scheme [180, 181, 182]. The HT scheme is capable of predicting the in-plane elastic properties of a unidirectional

short fiber composite, such as effective longitudinal and transversal stiffness constants and the Poisson's ratio. According to Fu et al. [183, p. 144], these material parameters are given with

$$E_{\mathrm{L}} = \frac{1 + 2(l/d)\eta_{\mathrm{L}} v_{\mathrm{f}}}{1 - \eta_{\mathrm{L}} v_{\mathrm{f}}} E_{\mathrm{m}}, \tag{2.48a}$$

$$E_{\mathrm{T}} = \frac{1 + 2\eta_{\mathrm{T}} v_{\mathrm{f}}}{1 - \eta_{\mathrm{T}} v_{\mathrm{f}}} E_{\mathrm{m}}, \tag{2.48b}$$

$$\nu_{\mathrm{LT}} = \nu_{\mathrm{f}} v_{\mathrm{f}} + \nu_{\mathrm{m}} v_{\mathrm{m}}, \tag{2.48c}$$

$$\nu_{\mathrm{TL}} = \frac{E_{\mathrm{T}}}{E_{\mathrm{L}}} \nu_{\mathrm{LT}}, \tag{2.48d}$$

$$G_{\mathrm{LT}} = \frac{1 + \eta_{\mathrm{G}} v_{\mathrm{f}}}{1 - \eta_{\mathrm{G}} v_{\mathrm{f}}} G_{\mathrm{m}}, \tag{2.48e}$$

where

$$\eta_{\mathrm{L}} = \frac{E_{\mathrm{f}}/E_{\mathrm{m}} - 1}{E_{\mathrm{f}}/E_{\mathrm{m}} + 2(l/d)}, \tag{2.49a}$$

$$\eta_{\mathrm{T}} = \frac{E_{\mathrm{f}}/E_{\mathrm{m}} - 1}{E_{\mathrm{f}}/E_{\mathrm{m}} + 2}, \tag{2.49b}$$

$$\eta_{\mathrm{G}} = \frac{G_{\mathrm{f}}/G_{\mathrm{m}} - 1}{G_{\mathrm{f}}/G_{\mathrm{m}} + 1}. \tag{2.49c}$$

For a given orientation in which the principal stress directions are in alignment with the principal fiber orientation, the planar stress-strain relation for a transversely isotropic laminate, as is the case for a uni-directional (UD) composite, is given with

$$\begin{bmatrix} \sigma_1 \\ \sigma_2 \\ \tau_{12} \end{bmatrix} = \underbrace{\begin{pmatrix} C_{11} & C_{12} & C_{16} \\ C_{12} & C_{22} & C_{26} \\ C_{16} & C_{26} & C_{66} \end{pmatrix}}_{=C_{ij}} \begin{bmatrix} \varepsilon_1 \\ \varepsilon_2 \\ \gamma_{12} \end{bmatrix} \tag{2.50}$$

[184]. The components of the stiffness matrix above are then given with

$$C_{11} = \frac{E_{\mathrm{L}}}{1 - \nu_{\mathrm{LT}}\nu_{\mathrm{TL}}}, \tag{2.51a}$$

$$C_{12} = \nu_{\mathrm{TL}} C_{11}, \tag{2.51b}$$

$$C_{16} = 0, \tag{2.51c}$$

$$C_{22} = \frac{E_{\mathrm{T}}}{1 - \nu_{\mathrm{LT}}\nu_{\mathrm{TL}}}, \tag{2.51d}$$

$$C_{26} = 0, \tag{2.51e}$$

$$C_{66} = G_{\mathrm{LT}}, \tag{2.51f}$$

since there is no shear-coupling for the principal system. The transformation of the principal stress-strain relation to an in-plane rotated stress-strain relation, i.e.,

$$\begin{bmatrix} \sigma'_1 \\ \sigma'_2 \\ \tau'_{12} \end{bmatrix} = \underbrace{\begin{pmatrix} C'_{11} & C'_{12} & C'_{16} \\ C'_{12} & C'_{22} & C'_{26} \\ C'_{16} & C'_{26} & C'_{66} \end{pmatrix}}_{=C'_{ij}} \begin{bmatrix} \varepsilon'_1 \\ \varepsilon'_2 \\ \gamma'_{12} \end{bmatrix}, \tag{2.52}$$

is given with the linear mapping

$$\begin{bmatrix} C'_{11} \\ C'_{22} \\ C'_{12} \\ C'_{66} \\ C'_{16} \\ C'_{26} \end{bmatrix} = \begin{pmatrix} c^4 & s^4 & 2c^2s^2 & 4c^2s^2 \\ s^4 & c^4 & 2c^2s^2 & 4c^2s^2 \\ c^2s^2 & c^2s^2 & c^4 + s^4 & -4c^2s^2 \\ c^2s^2 & c^2s^2 & -2c^2s^2 & (c^2 - s^2)^2 \\ c^3s & -cs^3 & cs^3 - c^3s & 2(cs^3 - c^3s) \\ cs^3 & -c^3s & c^3s - cs^3 & 2(c^3s - cs^3) \end{pmatrix} \begin{bmatrix} C_{11} \\ C_{22} \\ C_{12} \\ C_{66} \end{bmatrix}, \tag{2.53}$$

where $c = \cos\theta$ and $s = \sin\theta$ and where θ is the rotation angle. It needs to be mentioned that this transformation is only valid for when the non-normalized Voigt notation is used.

Shear-lag extension

The motivation to combine the HT scheme with the results of the shear-lag model after Cox [64], which was introduced in Sec. 2.3.1, is to improve the predictive capability of the solely empirical HT scheme by incorporating analytically derived results for the longitudinal stiffness within a UD composite. To the author's knowledge, this was first introduced in Fu et al. [184].

Based on the derivation in Fu et al. [183, p. 143], the results for the longitudinal fiber stress from Eq. 2.25 are averaged over the fiber length to derive a mean fiber stress, which states

$$\sigma_{\mathrm{f}} = E_{\mathrm{f}}\varepsilon\left(1 - \frac{\tanh(na)}{na}\right), \tag{2.54}$$

for which it was assumed that the matrix strain ε_{m} equals the far field strain ε at $r = R$ and the shear-lag parameter n was defined in Eq. 2.26. The equilibrium of forces at $r = R$ can then be expressed by using the modified *rule of mixtures*, which is given with

$$\begin{aligned} E_{\mathrm{L}}\varepsilon &= v_{\mathrm{f}}\sigma_{\mathrm{f}} + (1 - v_{\mathrm{f}})\sigma_{\mathrm{m}} \\ &= v_{\mathrm{f}}E_{\mathrm{f}}\varepsilon\left(1 - \frac{\tanh(na)}{na}\right) + (1 - v_{\mathrm{f}})E_{\mathrm{m}}\varepsilon, \end{aligned} \tag{2.55}$$

so that the overall longitudinal composite stiffness E_{L} follows with

$$E_{\mathrm{L}} = v_{\mathrm{f}}E_{\mathrm{f}}\left(1 - \frac{\tanh(na)}{na}\right) + (1 - v_{\mathrm{f}})E_{\mathrm{m}}. \tag{2.56}$$

The far field dimension R follows the relation

$$\ln\left(\frac{R}{r_{\mathrm{f}}}\right) = \frac{1}{2}\ln\left(\frac{2\pi}{\sqrt{3}v_{\mathrm{f}}}\right), \tag{2.57}$$

for when a hexagonal fiber packing is assumed, or

$$\ln\left(\frac{R}{r_{\mathrm{f}}}\right) = \frac{1}{2}\ln\left(\frac{\pi}{v_{\mathrm{f}}}\right), \tag{2.58}$$

for when a the underlying micro-structure represents a square fiber packing. Lastly, for the shear-lag informed Halpin-Tsai model, the longitudinal stiffness in Eq. 2.48a is replaced with the results from Cox' shear-lag model in Eq. 2.56. A comparative illustration for the difference of both models for different aspect ratios a in the case of unidirectional reinforcements is given in Fig. 2.22. In general,

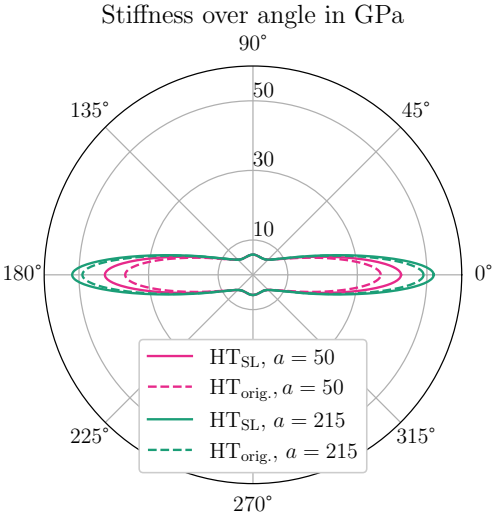

Figure 2.22: Comparison between predicted stiffness over angle for the original Halpin Tsai formulation and the shear-lag informed Halpin Tsai formulation for two different aspect rations. Graphic was first published in Scheuring et al. [185].

the shear-lag informed formulation predicts a higher stiffness in the longitudinal direction, while the transversal direction is unaffected. For higher aspect ratios, the difference between both models decreases.

3 Materials

The material of interest is a continuously-discontinuously (Co-Dico) carbon fiber reinforced polyamide 6. In general, Co-Dico FRPs can be produced using different production methods, e.g., injection or compression molding (cf. Böhlke et al. [186, p. 5f.]). In the present thesis, the material of interest is produced in the long fiber thermoplastic direct (LFT-D) process.

3.1 Neat PA6

The investigated matrix material is a DOMO TECHNYL® STAR PA6 without coloring, which is advertised as a high flow and high strength polyamide. The material was provided by DOMO Chemicals GmbH, Leuna, Germany. Since the material from the TECHNYL® STAR line is usually distributed with reinforcing elements, such as glass or carbon fibers, limited data on the neat PA6 is publicly available. A public data sheet for a potentially different PA6 from DOMO Chemicals GmbH gives a tensile modulus of 3200 MPa for the dry and 1000 MPa for the room climate conditioned material [187]. The melting temperature is given with 221 °C and the density is 1.14 g/cm^3.

3.2 Carbon fibers

The used carbon fibers for the discontinuously reinforced LFT are ZOLTEK™ PX35 continuous high strength carbon fiber tow with a specific sizing for PA6,

manufactured from polyacrylonitrile (PAN) precurso provided by ZOLTEK Corporation, Bridgeton, MO, USA. According to the manufacturer's data sheet, the tensile modulus and strength are given with 242 GPa and 4137 MPa, respectively [188]. The strain to failure is listed as 1.7 %. The nominal fiber diameter is $7.2\,\mu$m, the density is 1.81 g/cm^3 and the carbon content is listed as $95\,\%$. The exact composition of the sizing remains a trade secret and is unknown.

3.3 Continuous tape material and processing

The used tape material is a TECHNYL® Lite C130 C60, also provided by DOMO Chemicals GmbH, Leuna, Germany. This is a unidirectional carbon fiber reinforced PA6 tape with a fiber mass (volume) content of $w_\mathrm{f} = 60\,\%$ ($v_\mathrm{f} = 48\,\%$), which comes in a tape thickness of 0.13 mm. According to the technical data sheet from the manufacturer, the tensile modulus in the $0\,°$-direction is listed as 100 GPa and the strength is given with 1500 MPa. The strain to failure in this direction is $1.6\,\%$. Once again, the melting temperature is $221\,°$C. The areal weight is given with 190 g/m^2, which translates to a density of 1.46 g/cm^3, considering the nominal tape thickness.

As the individual tape is only 100 mm wide, a larger tape layup was produced from individual tapes, which was to be used later in the LFT-D process. To do this, eight tapes with a length of 700 mm were placed next to each other and a further seven tapes were stacked side by side above the first layer with an offset of half a tape width to the side, i.e., 50 mm. This bridges the gaps between the adjacent tapes. To fix the tapes in position, they were locally welded for easier handling. To finally consolidate the laminas of the layup, the layers were pressed together at $80\,°$C and 20 bar between parallel metal plates in a Dieffenbacher DYL 630 t hydraulic press after being heated to $280\,°$C in a contact oven from WICKERT Maschinenbau GmbH, Landau in der Pfalz, Germany. The large plate of $800 \times 700 \times 0.26$ mm^3 was then divided into four equal plates of $350 \times 350 \times 0.26$ mm^3, whereby the outer edge, which consisted of an overlapping single layer, was cut off.

3.4 LFT-D process

The material under investigation is manufactured using the LFT-D process at the Fraunhofer ICT facilities in Pfinztal, Germany, for which the process is shown in Fig. 3.1. The advantage of the LFT-D process in comparison with other methods used for long fiber reinforced thermoplastics is that it avoids the production of semi-finished products, thereby reducing production time and centralizing the production line in a single plant [189].

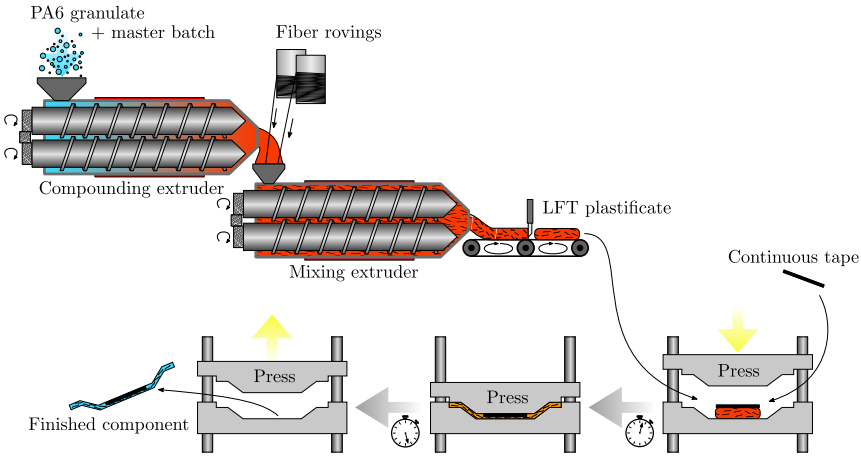

Figure 3.1: Schematic of LFT-D process with continuous inlay to produce continuous-discontinuously (Co-Dico) reinforced PA6 in reference to Scheuring et al. [185].

The production line for the investigated material consists of two co-rotating twin screw extruders. The first extruder, i.e., the compounding extruder, is filled with PA6 granulate and additives from the master batch, which are then melted at 260 °C by external heating elements and homogenized through the moving screws. The liquid polymer then flows into a second extruder, i.e., the mixing extruder, while continuous fiber strands are fed into the system simultaneously. The rotation and small gap size between the two screws exerts large enough shear stresses on the fibers to break them apart irregularly into smaller segments,

producing the discontinuously reinforced LFT plastificate. Process parameters such as rotation speed determine the length distribution of the reinforcing fibers, which was investigated on the given production line for reinforced polycarbonate in Schelleis et al. [190]. At the end of the mixing extruder the plastificate is extracted through a nozzle and cut into smaller pieces of predefined length.

The plastificate is then transferred to a press either manually or supported by handling robots. At this point, continuous tapes may be added as local reinforcement elements, as illustrated in the diagram, but the process also works without further reinforcements. The press is constantly being cooled to a target temperature of $80\,°C$. When the press is closed, the discontinuous plastificate is molded into its desired shape and the continuous tape is consolidated to the discontinuous bulk material, creating a Co-Dico hybrid component. It needs to be highlighted that the compression molding process and the thereby affected micro-structure (e.g. fiber orientation and consolidation quality) is sensitive to the initial position of the plastificate, which was studied in detail in Schelleis et al. [191], but which is not part of the investigation within the present work. Once the component has cooled down enough for the thermoplastic material to solidify, the press is opened and the component can be extracted.

In the case of the present study, the shape of the component is a $400 \times 400 \times 3\,\text{mm}^3$ cubical from which the individual specimens are cut. The matrix specimens are produced without local continuous reinforcements. For the investigation of the consolidation quality within the Co-Dico specimens, local reinforcements in the form of unidirectional tapes are consolidated on both sides of the bulk material, which will be explained in detail in Sec. 6.2.1, which was published before in Christ et al. [148].

4 Matrix

The main focus of the present work is on the characterization of the microscopic and macroscopic interface within carbon long fiber reinforced PA6. In order to understand the mechanisms of the interface, the behavior of the constituents must first be investigated. In contrast to the fiber material, which can be assumed to be linearly elastic with a good approximation and corresponding material parameters can be taken from the literature, the rate- and environment-dependent behavior of the polymer is more complex.

4.1 Experimental investigation

To investigate the presumably nonlinearly viscoelastic response of the matrix material for different environmental conditions, creep tests need to be performed. To guarantee a stable climate during the time consuming tests, the creep tests are performed within a VCV^3 7060-5 climate chamber from Vötsch Industrietechnik GmbH, Balingen, Germany, on an in-house developed creep test rig. The test rig is shown in Fig. 4.1.

4.1.1 Specimen preparation and conditioning

Due to the low viscosity that would occur for unreinforced PA6 within the heated upstream extruders in the LFT-D process, it is impossible to place the ejected material in the press and produce neat PA6 plates in the compression molding process. Instead, neat PA6 plates were produced in an injection molding process

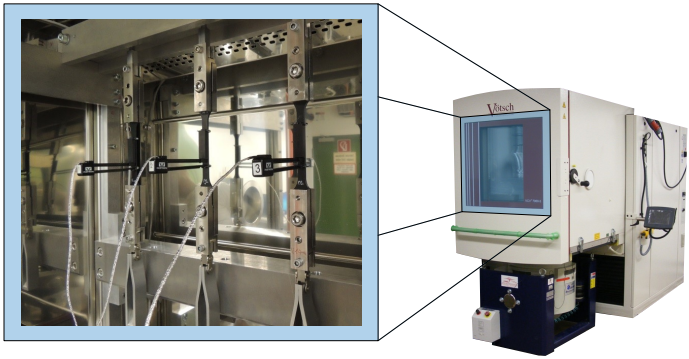

Figure 4.1: Test rig for climatized creep tests with specimen configuration and extensometers to measure the creep displacement. The material displayed is not related to the here investigated material.

using a Engel DUO CombiM 700 from ENGEL AUSTRIA GmbH, Schwertberg, Austria, at the Fraunhofer ICT in Pfinztal, Germany, with final dimensions of $180 \times 180 \times 3\,\mathrm{mm}^3$. Creep specimens were then cut from the neat PA6 plates in dog-bone shape, with the exact dimensions given in Fig. 4.2. Holes with a

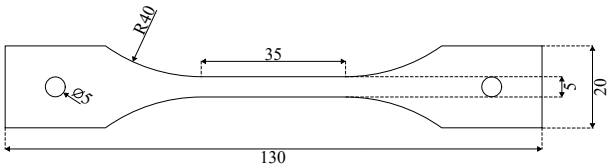

Figure 4.2: Technical drawing of the dog-bone specimen for neat PA6 creep experiments. All measurements are in millimeter and the thickness of the specimen equals the plate thickness of 3 mm.

diameter of 5 mm were drilled in both clamping areas, into which fixing pins were inserted for the test in order to center the specimen within the clamp. To cut the specimens from the plate, an iCUTwater SMART from imes-icore GmbH, Eiterfeld, Germany, was used with a water pressure of 1500 bar, a cutting speed of 300 mm/min and a flow rate of 250 g/min of cutting sand ClassicCut 120 from GMA Garnet (Europe) GmbH, Hamburg, Germany.

For the conditioning, four different climates were chosen to investigate the effects of temperature, humidity and their possible coupling on the viscoelastic properties. The reference state is a dried state at room temperature, i.e., 23 °C and around 10 % relative humidity (r.H.). Individual effects of temperature or humidity are realized by increasing the temperature to 45 °C or the relative humidity to 75 % r.H. To investigate coupled effects, both environmental metrics are increased to have a climate at 45 °C and 75 % r.H.

Although the exact degree of crystallization of the material is not known, previous research on the exact same material measured crystallinities between 27 % and 33 % [192] and the glass transition temperature of dry PA6 to be $T_\mathrm{g} = 64\,°\mathrm{C}$ [59, p. 167]. As the plates were not exposed to undercooling during the injection molding process, it is fair to assume a crystallinity of $X_\mathrm{c} = 30 \pm 3\,\%$. For the modeling parameters introduced in the state of the art (cf. Tab. 2.1), the glass transition temperature develops according to Eq. 2.8, as was shown in Fig. 2.4. Plotting the four different conditioning states and updating the reference crystallinity and glass transition temperature as stated above gives an impression on their position in relation to T_g, as seen in Fig. 4.3. It can be seen that the dry

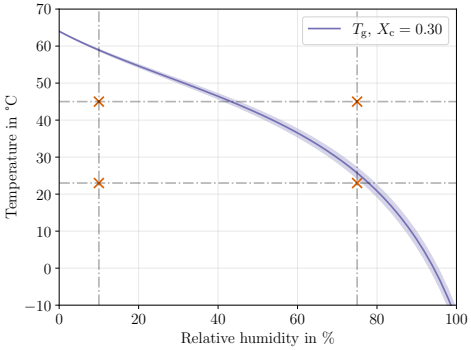

Figure 4.3: Glass transition temperature of PA6 over relative humidity predicted by Eq. 2.5, Eq. 2.6 and Eq. 2.8 for $X_\mathrm{c} = 30 \pm 3\,\%$. The following parameter were used: $T_\mathrm{g,dry} = 64\,°\mathrm{C}$ [59, p. 167], $T_{\mathrm{g,H_2O}} = -163\,°\mathrm{C}$ [43], $\rho_\mathrm{PA6} = 1.14\,\mathrm{g/cm^3}$ [13, p. 67] and $\rho_{\mathrm{H_2O}} = 1.00\,\mathrm{g/cm^3}$. The sorption was modeled with the parameters in Tab. 2.1. The red markers (crosses) indicate the position of the four different conditioning states.

conditioning states at $\mathcal{H} = 10\,\%$ are well below the glass transition temperature and can can therefore be assumed to be in a glassy state. The conditioning at $T = 23\,°\text{C}$ and $\mathcal{H} = 75\,\%$ is positioned right below the glass transition temperature, probably in the early transition state. Only the extreme condition at $T = 45\,°\text{C}$ and $\mathcal{H} = 75\,\%$ is well above the glass transition temperature, so that a drastically more compliant behavior is expected.

Conditioning of the specimens took place pre-testing at the individual mentioned climates within the climate chamber, in which the experiments were also performed. First, the specimens were dried for a duration of 14 days at $50\,°\text{C}$ to remove any moisture absorbed during the cutting process. Following, the desired climate was established in the climate chamber and the specimens were conditioned for another 7 days, after which a stable equilibrium was assumed.

4.1.2 Test procedure

For the testing, four specimens were mounted to the test-rig within the climate chamber at once per climate. An extensiometer was fixed on each specimen, which is used to measure the displacement $u(t)$ during testing. Each leg of an extensiometer was positioned to be equidistant to the center of the specimen. The leg distance, i.e., clip gauge distance $u(t = 0) = u_0$, is not consistent throughout the different test runs. The conditioning of $23\,°\text{C}$, $10\,\%$ r.H. was set to a clip gauge distance of $20\,\text{mm}$, while all other experiments were set to $10\,\text{mm}$. The reason for this is that the climate chamber was used in between for other studies, which required a shorter clip gauge distance, which was then also incorporated for our investigation. As a consequence, the strain calculation requires an adjustment of the reference length and the vibration of the climate chamber compressor will lead to more visible oscillations of the displacement recordings, which was regarded acceptable.

The idea behind choosing appropriate load levels, i.e., the applied weight, was to investigate a maximum large range from linearly viscous effects at low stress levels up to pronounced nonlinearly viscous effects shortly before failure. Thereby, a

wide range of strain rates and nonlinearities can be investigated. Since the test-rig allows to test four specimens simultaneously, the in-between load levels were chosen to be equidistant to the minimum and maximum weight level.
All cases use a weight corresponding to 10 MPa for the lowest tested stress level, which is assumed to be in the linear range for all environments. The maximum stress for the cold and dry climate was set to 40 MPa, which gives in-between loads of 20 MPa and 30 MPa. Since it was expected that the elevated climate conditions will lead to a more compliant behavior which reduces the load the material can endure over a longer time range, a lower maximum weight was selected at 30 MPa, giving 16.6 MPa and 23.3 MPa as in-between loads. The maximum load of 30 MPa deemed to lead to a premature failure for the extreme conditioning of 45 °C, 75 % r.H., which required the experiments to be repeated with an added load level of 20 MPa. This was necessary to have enough data for numerical fitting. Each stress level per climate was tested with only a single sample. Although repeating the test with several samples would provide better information about mean values and statistical distributions, this would also require an enormous amount of time, which is not justified in view of the focus of this work on interfacial behavior.

For the testing, the specimens were mounted in the climate chamber in the test-rig. The test-rig uses levers to effectively multiply the applied weight by a factor of 10. Otherwise, the applied loads would exceed the maximum allowed load of the test-rig. The levers are lockable, so that the appropriate weight can be applied to the lever, without loading the specimen. After preparing all the weights and setting up the extensiometer, the climate chamber was closed again for the climate to stabilize before testing. The displacement recording was started with an initial measuring frequency of 1 Hz for the first hour, followed by 0.02 Hz for the remaining test period. Directly after initializing the measurement readings, the locking of the levers was removed and the weights were lowered together manually in a smooth motion over 5 s to reduce inertia effects. The duration of the each test run was set to 240 h, during which the climate and each extensiometer displacement $u(t)$ was continuously recorded.

Once the tests were finished, the creep strain was processed based on the displacement data. Therefore, the small-strain theory was assumed which gives a creep strain of

$$\begin{aligned}\varepsilon(t) &= \frac{l - l_0}{l_0}, \\ &= \frac{u(t) - u_0}{u_0}.\end{aligned} \tag{4.1}$$

Consequently, the creep compliance can then be calculated with

$$J(t) = \frac{\varepsilon(t)}{\sigma_0}. \tag{4.2}$$

The Norton-Bailey law is introduced in order to quantitatively compare the non-linear stress dependence of the creep compliance between the different conditioning states,

$$\varepsilon(t) = A\sigma^n t^m, \tag{4.3}$$

which goes back to Norton [193] and Bailey [194]. The parameter A scales the strain linearly, while the exponent m indicates a non-linearity in time, if $m \neq 1$. When $0 < m < 1$, the behavior is sometimes described as *time hardening*, as the strain rate decreases with an increase in time. The parameter n describes a non-linearity in stress, if $n \neq 1$. Once all creep tests are completed, the parameter set for each conditioning state is determined by performing a least-squares procedure in the strain residual using `SciPy`.

4.1.3 Results

The experimental results of the creep strain for different climatic conditions are shown in Fig. 4.4. It is evident that there is a climate-dependent material behavior. The only load tested for all conditioning states is $10\,\mathrm{MPa}$. While the total strain after $160\,\mathrm{h}$ for this creep stress is $0.78\,\%$ for the cold/dry conditioning, it increases to $1.40\,\%$ and $0.93\,\%$ for the cold/wet and warm/dry conditioning, respectively.

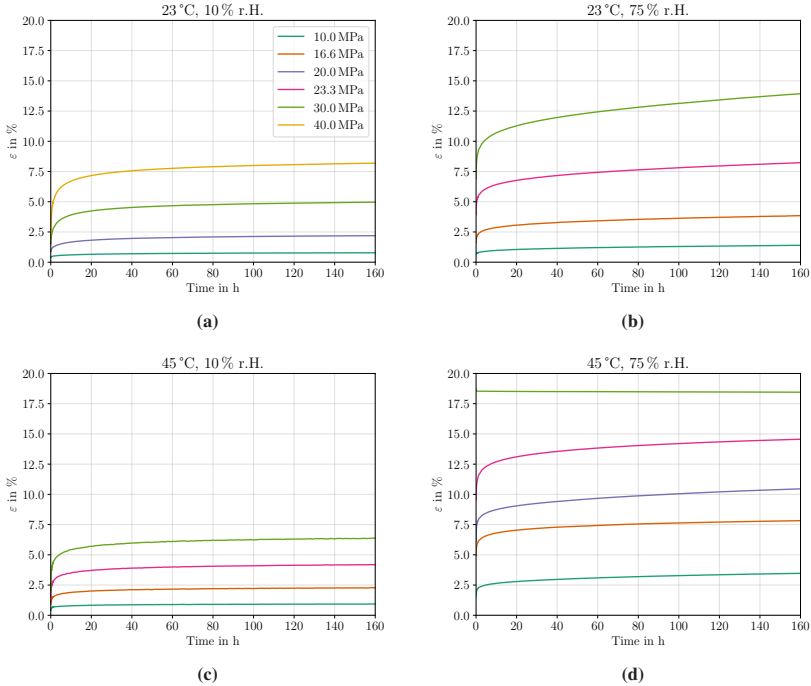

Figure 4.4: Resulting creep strain over time for various conditioning states and constant loads: (**a**) 23 °C and 10 % r.H. with 10.0 MPa, 20.0 MPa, 30.0 MPa and 40.0 MPa, (**b**) 23 °C and 75 % r.H. with 10.0 MPa, 16.6 MPa, 23.3 MPa and 30.0 MPa, (**c**) 45 °C and 10 % r.H. with 10.0 MPa, 16.6 MPa, 23.3 MPa and 30.0 MPa, and (**d**) 45 °C and 75 % r.H. with 10.0 MPa, 16.6 MPa, 20.0 MPa, 23.3 MPa and 30.0 MPa (which is invalid due to the weight touching the ground following excessive deformation).

For the combination of increased moisture and temperature, a strain of $3.50\,\%$ is observed.

A nonlinearity in the viscoelastic material behavior is observable for all conditioning states. For the cold/dry conditioning, a maximum applied stress of 40 MPa results in a strain of $8.19\,\%$ after 160 h. This corresponds to a multiplicative factor of 10.50 for the strain response for an increase in stress by a factor of 4, from 10 MPa to 40 MPa. Similarly, the strain for the cold/wet and warm/dry conditioning increases to $13.93\,\%$ and $6.83\,\%$, respectively, for an increase in stress from

10 MPa to 30 MPa. This corresponds to an increase in creep strain by factors of 9.95 and 7.34, respectively, for the tripled creep stress. For the warm/wet conditioning, a creep load of 30 MPa led to excessive creep deformation, causing the sample to contact the chamber floor and rendering this test invalid. The valid maximum load of 23.33 MPa, which corresponds to a factor of 2.33 compared to 10 MPa, results in an increase in creep strain by a factor of 4.16 to 14.56 % after 160 h.

In general, it is evident that no saturation of creep strain occurs within the investigated period of 160 h, neither above nor below T_g. An exception is observed for the creep strain at the lowest load of 10 MPa for the first three conditioning states. At the higher loads, a non-zero steady-state creep rate is justifiable for the dry conditionings. Especially for the wet conditioning conditions, the creep rate does not reach a constant value even towards the end of the test period.

To quantitatively compare the degree of non-linearity in time and stress between the different conditioning states, the parameters A, m and n of the fitted Norton-Bailey law are listed in Tab. 4.1. A visualization of the fit is given in Appendix B.

Table 4.1: Parameters of the Norton-Bailey law for different conditioning states.

Conditioning		Norton-Bailey law parameters		
Temp.	rel. Hum.	A	m	n
(°C)	(%)		(-)	
23	10	$5.33 \cdot 10^{-5}$	0.119	1.838
23	75	$5.96 \cdot 10^{-5}$	0.080	2.155
45	10	$11.16 \cdot 10^{-5}$	0.089	1.743
45	75	$33.43 \cdot 10^{-5}$	0.053	1.839

While the linear scaling parameter A barely increases for an increase in humidity

alone in the cold climate, it significantly increases for increased temperature. When both temperature and humidity are increased, the fitted A is roughly 6 times as large as for the reference climate. Generally, the fitted exponent parameters m and n take on different values from 1, indicating a non-linear behavior in time and stress for each conditioning case. The parameter for the non-linearity in stress, i.e., m, is rather similar at $m \approx 1.8$ for all conditioning states with the exception of the cold and wet conditioning state, for which m takes on a larger value. The non-linearity parameter in time reduces from the cold and dry reference state at $m \approx 1.2$ to similar values of $m = 0.080$ and $m = 0.089$ for the cold/wet and warm/dry environment. When both environmental factors are elevated simultaneously, the parameter reduces further to $t = 0.053$.

4.2 Numerical modeling

4.2.1 Nonlinear viscoelastic matrix model after Schapery

The preceding chapter showed that the viscous behavior of PA6 is non-linear in stress. To model the nonlinear viscoelastic material behavior of PA6 at different environmental boundary conditions, a generalized Kelvin-Voigt (KV) model consisting of 3 KV-elements and a spring in series is used, which is extended for load induced nonlinearities in accordance to the theory in Schapery [136]. The model is illustrated in Fig. 4.5. A similar, simplified approach has successfully

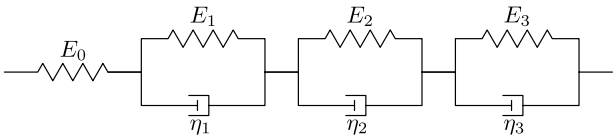

Figure 4.5: Schematic of an elastic spring with three Kelvin-Voigt elements in series.

been used in Fliegener [1] with a different rheological model to describe the nonlinear viscoelastic behavior of another semicrystalline thermoplastic material.

The present work differs fundamentally from the work in Fliegener, since the regular theory according to Schapery is applied here instead of using variable rheological parameters. Furthermore, a numerical implementation is developed which is better suited to describe dynamic loads as they occur when creep loads are applied.

The preliminary theory on linear viscoelastic modeling is derived using the Kelvin-Voigt material in Appendix C, for which the main results are summarized below. The governing equation in incremental form for the one-dimensional (1D) case is

$$\Delta\sigma(t) = \tilde{E}(t)\left(\Delta\varepsilon(t) - \sum_{i=1}^{3}\varepsilon_{\mathrm{ve},i}^{\mathrm{inh}}(t-\Delta t)\left(1-e^{-\frac{\Delta t}{\tau_i}}\right)\right), \tag{4.4}$$

where the contribution of each spring and damper is reflected within the effective stiffness

$$\tilde{E}(t) = \left(\frac{1}{E_0} + \sum_{i=1}^{3}\frac{1}{E_i}\left(1-\frac{\tau_i}{\Delta t}\left(1-e^{-\frac{\Delta t}{\tau_i}}\right)\right)\right)^{-1}. \tag{4.5}$$

The loading history is captured using history variables, which need to be updated after each simulation increment according to

$$\Delta\varepsilon_{\mathrm{ve},i}^{\mathrm{inh}}(t) = \varepsilon_{\mathrm{ve},i}^{\mathrm{inh}}(t-\Delta t)\left(e^{-\frac{\Delta t}{\tau_i}}-1\right) + \frac{1}{E_i}\frac{\Delta\sigma(t)}{\Delta t}\tau_i\left(1-e^{-\frac{\Delta t}{\tau_i}}\right). \tag{4.6}$$

The three-dimensional (3D) generalization in `Abaqus` notation resulted in

$$\begin{aligned}\underline{\Delta\sigma} = &\left(2\tilde{G}(t)\underline{\underline{M'}}_{\varepsilon} + 3\tilde{K}(t)\underline{\underline{M^{\circ}}}\right)\\ &\cdot\left(\underline{\Delta\varepsilon} - \sum_{i=1}^{3}\underline{\boldsymbol{\varepsilon}}_{\mathrm{ve},i}^{\mathrm{inh}}(t-\Delta t)\left(1-e^{-\frac{\Delta t}{\tau_i}}\right)\right),\end{aligned} \tag{4.7}$$

which again requires to update the history variables following

$$\begin{aligned}\underline{\Delta\varepsilon}^{\mathrm{inh}}_{\mathrm{ve},i}(t) = \underline{\varepsilon}^{\mathrm{inh}}_{\mathrm{ve},i}(t-\Delta t)\left(e^{-\frac{\Delta t}{\tau_i}}-1\right) \\ + \frac{\tau_i}{\Delta t}\left(1-e^{-\frac{\Delta t}{\tau_i}}\right)\left(\frac{1}{2G_i}\underline{\underline{M}}'_{\sigma} + \frac{1}{3K_i}\underline{\underline{M}}^{\circ}\right)\underline{\Delta\sigma}.\end{aligned} \tag{4.8}$$

The definitions for the individual components of the equations above are given in the according section within Appendix C.

The equations above are only valid for a linear material. That is a material whose response is both superposable, meaning that the strain output for a varying stress input is equal to the sum of all individual responses [195, p. 202], and also proportional, meaning that double the stress input results in double the strain output [195, p. 208]. Since many polymers do not follow this behavior, but instead show a nonlinear response as a function of stress, the linear theory needs to be extended. The following theory is based on the principals of irreversible thermodynamics mentioned in Schapery [136] and Schapery [196] and it was thoroughly introduced in Schapery [197]. A comprehensive summary on the topic is given in Brinson and Brinson [195, p. 338 ff.].

The starting point for the nonlinear theory is an alternative formulation of Eq. C.20, which is

$$\varepsilon(t) = J_0\sigma(t) + \int_0^t \Delta J(t-\tau)\dot{\sigma}(\tau)\,\mathrm{d}\tau, \tag{4.9}$$

in which the creep compliance $J(t)$ was separated into an initial value J_0 and transient component $\Delta J(t)$, so that

$$J(t) = J_0 + \Delta J(t) \tag{4.10}$$

[197, p. 296 f.]. The linear from in Eq. 4.9 is then extended, such that

$$\varepsilon(t) = g_0 J_0\sigma(t) + g_1\int_0^t \Delta J(\psi-\psi')\frac{\mathrm{d}g_2\sigma(\tau)}{\mathrm{d}\tau}\,\mathrm{d}\tau, \tag{4.11}$$

where g_0, g_1 and g_2 are stress dependent material parameters and ψ and ψ' are reduced times

$$\psi(t,\sigma) = \int_0^t \frac{1}{a_\sigma}\,\mathrm{d}t', \tag{4.12a}$$

$$\psi'(\tau,\sigma) = \int_0^\tau \frac{1}{a_\sigma}\,\mathrm{d}t', \tag{4.12b}$$

where a_σ is another stress dependent material parameter with $a_\sigma > 0$. For when all parameters $g_0 = g_1 = g_2 = a_\sigma = 1$, the Boltzman superposition integral in Eq. 4.9 for linear viscoelasticity is recovered [195, p. 341]. The physical origin and interpretation of all nonlinearizing parameter functions are given in Hiel et al. [198, p. 37 ff.], who also mention restrictions on their functional properties. In general, g_0 and g_2 may increase and decrease with stress, while g_1 should strictly increase. Since in the following the product $g_1 g_2$ is treated as a single parameter, a restriction on a possible monotonicity cannot be made. Also, no general restriction on a_σ is possible.

The Schapery equation for a single step stress input

In theory, in most creep tests a single load σ_0 is applied at $t = 0$ and the resulting strain $\varepsilon(t)$ is measured over time until the experiment is stopped. Hence, the stress as a function of time can be formulated as

$$\sigma(t) = \sigma_0 H(t), \tag{4.13}$$

with the Heaviside step function introduced earlier. Inserting Eq. 4.13 into Eq. 4.11 gives

$$\varepsilon(t) = g_0(\sigma_0) J_0 \sigma_0 H(t) + g_1(\sigma_0) \int_0^t \Delta J(\psi - \psi') \frac{\mathrm{d}\overbrace{g_2(\sigma_0)\sigma_0}^{=\text{const.}} H(\tau)}{\mathrm{d}\tau}\,\mathrm{d}\tau, \tag{4.14}$$

where all nonlinearizing parameters are evaluated at $\sigma = \sigma_0$ and thus become constant. As a result the derivative in the integral is easily evaluated and the expression becomes

$$\varepsilon(t) = g_0(\sigma_0)J_0\sigma_0 H(t) + g_1(\sigma_0)g_2(\sigma_0)\sigma_0 \int_0^t \Delta J(\psi - \psi')\delta(\tau)\,\mathrm{d}\tau, \quad (4.15)$$

where $\delta(t)$ is the derivative of the Heaviside step function or Dirac Delta function, respectively. The Dirac Delta function $\delta(t)$ has the following properties

$$\delta(t) = \begin{cases} +\infty, & \text{if } t = 0, \\ 0, & \text{if } t \neq 0, \end{cases} \quad (4.16a)$$

$$\int_{-\infty}^{\infty} \delta(t)\,\mathrm{d}t = 1. \quad (4.16b)$$

With the given properties, it becomes clear that the integral in Eq. 4.15 must be evaluated at $\tau = 0$ for the integrand to not be zero. Subsequently, with $a_\sigma(\sigma_0) = \text{const.}$, Eqs. 4.12 become

$$\psi(t, \sigma) = \frac{1}{a_\sigma(\sigma_0)} \int_0^t \mathrm{d}t' = \frac{t}{a_\sigma(\sigma_0)}, \quad (4.17a)$$

$$\psi'(\tau = 0, \sigma) = \frac{1}{a_\sigma(\sigma_0)} \int_0^{\tau=0} \mathrm{d}t = 0, \quad (4.17b)$$

so that the transient compliance $\Delta J(\psi - \psi')$ within the integral in Eq. 4.15 becomes $\Delta J(t/a_\sigma(\sigma_0))$, which is independent of the variable of integration τ, i.e., it can be treated as a constant in the integral. As a result, the formulation of the Schapery equation for a single stress input is given with

$$\varepsilon(t) = \left[g_0(\sigma_0)J_0 + g_1(\sigma_0)g_2(\sigma_0)\Delta J\left(\frac{t}{a_\sigma(\sigma_0)}\right)\right]\sigma_0 H(t). \quad (4.18)$$

Since the expression is only evaluated at $t \geq 0$, the nonlinear compliance $\tilde{J}(t) = (\varepsilon(t)/\sigma(t))$ can be expressed without the Heaviside step function as

$$\tilde{J}(t) = \underbrace{g_0(\sigma_0)J_0}_{=\tilde{J}_0(\sigma_0)} + \underbrace{g_1(\sigma_0)g_2(\sigma_0)\Delta J\left(\frac{t}{a_\sigma(\sigma_0)}\right)}_{=\Delta\tilde{J}(t,\sigma_0)}, \tag{4.19}$$

where the nonlinear compliance $\tilde{J}$ was additively separated into an instant part $\tilde{J}_0(\sigma_0)$ and a transient part $\Delta\tilde{J}(t,\sigma_0)$ in analogy to Eq. 4.10. The nonlinearizing material parameters g_0, a_σ and the product $g_1 g_2$ for a given stress σ_0 can be determined by fitting the previous equation to experimental creep data or by evaluating

$$g_0(\sigma_0) = \frac{\tilde{J}_0(\sigma_0)}{J_0}, \tag{4.20a}$$

$$g_1(\sigma_0)g_2(\sigma_0) = \frac{\Delta\tilde{J}(t,\sigma_0)}{\Delta J\left(\frac{t}{a_\sigma(\sigma_0)}\right)}, \tag{4.20b}$$

where the expressions for J_0 and $\Delta J(t)$ are known from fitting the model to a stress input σ_0 in the linear range, i.e., when $g_0 = g_1 = g_2 = a_\sigma = 1$. It has to be noted that a separation of g_1 and g_2 is not possible from Eqs. 4.20. To separate all nonlinearizing parameters, a two step stress input or creep recovery test needs to be performed and evaluated. The necessary equations for this are discussed in Schapery [197, p. 301ff.].

4.2.2 Numerical implementation of the Schapery model

The following section deals with the numerical implementation of the nonlinear Schapery model. The starting point is the derivation of a numerical expression for the 1D case in analogy to the previous section of the linear case and in reference to Woldekidan [199, p. 190 ff.], followed by the derivation of the 3D case. The formulation in Woldekidan is then extended to allow for larger stress and time

increments, both in a single and multiple dimensions. To avoid cumbersome dependencies in the notation, the dependence on time and stress are not explicitly noted here, unless it seems appropriate to stress the dependence. Lastly, the implementation in `Abaqus` is formulated and the iterative scheme within a UMAT is derived.

Eq. 4.11 is rewritten with reduced dependencies

$$\varepsilon(t) = g_0 J_0 \sigma + g_1 \int_0^t \Delta J(\psi - \psi') \frac{\mathrm{d} g_2 \sigma}{\mathrm{d}\tau} \, \mathrm{d}\tau, \tag{4.21}$$

and the components of the compliance for the extended KV model are recalled

$$J_0 = \frac{1}{E_0}, \tag{4.22a}$$

$$\Delta J(\psi) = \sum_{i=1}^{3} \frac{1}{E_i} \left(1 - e^{-\frac{\psi}{\tau_i}}\right). \tag{4.22b}$$

It is important to note that τ_i describe material parameters, while τ is the integration variable and a measure of time. Inserting the previous expressions into Eq. 4.21 gives

$$\varepsilon(t) = g_0 \frac{1}{E_0} \sigma + g_1 \sum_{i=1}^{3} \int_0^t \frac{1}{E_i} \left(1 - e^{-\frac{\psi - \psi'}{\tau_i}}\right) \frac{\mathrm{d} g_2 \sigma}{\mathrm{d}\tau} \, \mathrm{d}\tau, \tag{4.23}$$

which is further split into an instantaneous or elastic part ε_e and an inherited transient or viscoelastic part $\varepsilon_\mathrm{ve}^\mathrm{inh}$

$$\varepsilon(t) = \underbrace{\left(g_0 \frac{1}{E_0} + g_1 g_2 \sum_{i=1}^{3} \frac{1}{E_i}\right) \sigma}_{=\varepsilon_\mathrm{e}} - \sum_{i=1}^{3} \underbrace{g_1 \int_0^t \frac{1}{E_i} e^{-\frac{\psi - \psi'}{\tau_i}} \frac{\mathrm{d} g_2 \sigma}{\mathrm{d}\tau} \, \mathrm{d}\tau}_{=\varepsilon_{\mathrm{ve},i}^\mathrm{inh}}. \tag{4.24}$$

In analogy to the linear section, the integral for $\varepsilon_{\mathrm{ve},i}^{\mathrm{inh}}$ is split into two parts

$$\begin{aligned}\varepsilon_{\mathrm{ve},i}^{\mathrm{inh}}(t) = \overbrace{g_1 \int_0^{t-\Delta t} \frac{1}{E_i} e^{-\frac{\psi-\psi'}{\tau_i}} \frac{\mathrm{d}g_2\sigma}{\mathrm{d}\tau}\,\mathrm{d}\tau}^{=e^{-\frac{\psi(t)-\psi(t-\Delta t)}{\tau_i}}\varepsilon_{\mathrm{ve},i}^{\mathrm{inh}}(t-\Delta t)} \\ + g_1 \int_{t-\Delta t}^{t} \frac{1}{E_i} e^{-\frac{\psi-\psi'}{\tau_i}} \frac{\mathrm{d}g_2\sigma}{\mathrm{d}\tau}\,\mathrm{d}\tau,\end{aligned} \tag{4.25}$$

where it becomes imminent that the first summand can be expressed in a recursive manner. Again, the assumption is made that when the time step Δt is sufficiently small, it can be assumed for the second integral in Eq. 4.25 that the nonlinearizing parameters g_1, g_2 and a_σ are constant and that the stress σ varies linearly over that time increment, so that

$$\varepsilon_{\mathrm{ve},i}^{\mathrm{inh}}(t) = e^{-\frac{\Delta\psi}{\tau_i}} \varepsilon_{\mathrm{ve},i}^{\mathrm{inh}}(t-\Delta t) + g_1 g_2 \frac{1}{E_i} \frac{\Delta\sigma}{\Delta\psi} \tau_i \left(1 - e^{-\frac{\Delta\psi}{\tau_i}}\right), \tag{4.26}$$

where

$$\Delta\psi = \psi(t) - \psi(t-\Delta t). \tag{4.27}$$

Thus, the strain increments are

$$\Delta\varepsilon_{\mathrm{e}} = \left(g_0 \frac{1}{E_0} + g_1 g_2 \sum_{i=1}^{3} \frac{1}{E_i}\right) \Delta\sigma, \tag{4.28a}$$

$$\begin{aligned}\Delta\varepsilon_{\mathrm{ve},i}^{\mathrm{inh}}(t) = \varepsilon_{\mathrm{ve},i}^{\mathrm{inh}}(t-\Delta t) \left(e^{-\frac{\Delta\psi}{\tau_i}} - 1\right) \\ + g_1 g_2 \frac{1}{E_i} \frac{\Delta\sigma}{\Delta\psi} \tau_i \left(1 - e^{-\frac{\Delta\psi}{\tau_i}}\right).\end{aligned} \tag{4.28b}$$

Combined, the full strain increment is

$$\begin{aligned}\Delta\varepsilon(t) =& \Delta\varepsilon_{\mathrm{e}} - \sum_{i=1}^{3} \Delta\varepsilon_{\mathrm{ve},i}^{\mathrm{inh}}(t), \\ =& \left(g_0 \frac{1}{E_0} + g_1 g_2 \sum_{i=1}^{3} \frac{1}{E_i} \left(1 + \frac{\tau_i}{\Delta\psi} \left(e^{-\frac{\Delta\psi}{\tau_i}} - 1 \right) \right) \right) \Delta\sigma \\ &+ \sum_{i=1}^{3} \varepsilon_{\mathrm{ve},i}^{\mathrm{inh}}(t - \Delta t) \left(1 - e^{-\frac{\Delta\psi}{\tau_i}} \right). \end{aligned} \tag{4.29}$$

For the commercial FE program `Abaqus`, which provides a strain increment $\Delta\varepsilon$ and expects a computed stress increment $\Delta\sigma$ from the UMAT, the expression in Eq. 4.29 needs to be inverted to

$$\Delta\sigma(t) = \tilde{E}(t) \left(\Delta\varepsilon(t) - \sum_{i=1}^{3} \varepsilon_{\mathrm{ve},i}^{\mathrm{inh}}(t - \Delta t) \left(1 - e^{-\frac{\Delta\psi}{\tau_i}} \right) \right), \tag{4.30}$$

where

$$\tilde{E}(t) = \left(g_0 \frac{1}{E_0} + g_1 g_2 \sum_{i=1}^{3} \frac{1}{E_i} \left(1 + \frac{\tau_i}{\Delta\psi} \left(e^{-\frac{\Delta\psi}{\tau_i}} - 1 \right) \right) \right)^{-1}. \tag{4.31}$$

3D formulation

In analogy to the derivation of the 3D formulation in the linear case, the derivation of the nonlinear case is done accordingly. From Eq. C.36 it is recalled that Hooke's law can be additively split into a deviatoric and volumetric part

$$\begin{aligned}\Delta\sigma_{ij}(t) &= 2G\Delta\varepsilon'_{ij}(t) + 3K\Delta\varepsilon^{\circ}_{ij}(t), \\ &= (3K\mathbb{P}_1 + 2G\mathbb{P}_2) : \Delta\boldsymbol{\varepsilon}(t). \end{aligned} \tag{4.32}$$

It is further assumed that for the nonlinear viscoelastic formulation in Eq. 4.30, the volumetric and deviatoric parts are likewise separable

$$\begin{aligned}\Delta\sigma_{mn}(t) = 2\tilde{G}(t)\left(\Delta\varepsilon'_{mn}(t) - \sum_{i=1}^{3} {\varepsilon^{\mathrm{inh}}_{\mathrm{ve},i}}'_{mn}(t-\Delta t)\left(1-e^{-\frac{\Delta\psi}{\tau_i}}\right)\right) \\ + 3\tilde{K}(t)\left(\Delta\varepsilon^{\circ}_{mn}(t) - \sum_{i=1}^{3} {\varepsilon^{\mathrm{inh}}_{\mathrm{ve},i}}^{\circ}{}_{mn}(t-\Delta t)\left(1-e^{-\frac{\Delta\psi}{\tau_i}}\right)\right),\end{aligned} \tag{4.33}$$

which is identical to the expression for the linear case in Eq. C.44, with the exception that the exponential decay takes into account the difference in reduced time $\Delta\psi$ instead of real time Δt. Once again, it needs to be highlighted that another way of modeling viscoelasticity is to concentrate the time dependent deformation on the deviatoric deformation only, which is then assumed to be incompressible. This is common practice for materials like bitumunous mastic [1, p. 44] and experimental evidence for a combined viscous effect on bulk and shear modulus is given in [200]. For semicrystalline polymers, as is the case in PA6, viscoelasticity is commonly assumed to affect both the bulk and shear moduli, with the Poisson ratio being constant over time. This approach is also followed here.

The difference of Eq. 4.33 to the linear case becomes obvious in the formulations for $\tilde{G}(t)$ and $\tilde{K}(t)$, respectively, which are

$$\tilde{G}(t) = \left(g_0\frac{1}{G_0} + g_1g_2\sum_{i=1}^{3}\frac{1}{G_i}\left(1+\frac{\tau_i}{\Delta\psi}\left(e^{-\frac{\Delta\psi}{\tau_i}}-1\right)\right)\right)^{-1}, \tag{4.34a}$$

$$\tilde{K}(t) = \left(g_0\frac{1}{K_0} + g_1g_2\sum_{i=1}^{3}\frac{1}{K_i}\left(1+\frac{\tau_i}{\Delta\psi}\left(e^{-\frac{\Delta\psi}{\tau_i}}-1\right)\right)\right)^{-1}, \tag{4.34b}$$

in accordance to Eq. 4.31. With $\tilde{G}(t)$ and $\tilde{K}(t)$ being functions of the nonlinearizing material parameters and thereby being a function of an indicator stress $\bar{\sigma}$, which depends on the current stress increment $\Delta\sigma_{mn}(t)$ and which is yet to be defined, it becomes clear that the nonlinear expression in Eq. 4.33 is an implicit

equation in $\Delta\sigma_{mn}(t)$. To solve the equation for a given strain increment $\Delta\varepsilon_{mn}(t)$, a Newton-Raphson method is used to find a suitable stress increment $\Delta\sigma_{mn}(t)$.

The history variables are updated accordingly to the previous section with

$$\begin{aligned}
\Delta\varepsilon^{\mathrm{inh}\,\prime}_{\mathrm{ve},i\,mn}(t) =& \varepsilon^{\mathrm{inh}\,\prime}_{\mathrm{ve},i\,mn}(t-\Delta t)\left(e^{-\frac{\Delta\psi}{\tau_i}}-1\right) \\
&+ g_1 g_2 \frac{1}{2G_i}\frac{\Delta\sigma'_{mn}(t)}{\Delta\psi}\tau_i\left(1-e^{-\frac{\Delta\psi}{\tau_i}}\right), \\
\Delta\varepsilon^{\mathrm{inh}\,\circ}_{\mathrm{ve},i\,mn}(t) =& \varepsilon^{\mathrm{inh}\,\circ}_{\mathrm{ve},i\,mn}(t-\Delta t)\left(e^{-\frac{\Delta\psi}{\tau_i}}-1\right) \\
&+ g_1 g_2 \frac{1}{3K_i}\frac{\Delta\sigma^{\circ}_{mn}(t)}{\Delta\psi}\tau_i\left(1-e^{-\frac{\Delta\psi}{\tau_i}}\right),
\end{aligned} \tag{4.35}$$

where again the real time increment is replaced with the reduced time increment (cf. Eq. 4.28).

To find the tangential stiffness for the nonlinear formulation, Eq. 4.33 is reformulated with the defintions of the projectors

$$\Delta\boldsymbol{\sigma}(t) = \left(3\tilde{K}(t)\mathbb{P}_1 + 2\tilde{G}(t)\mathbb{P}_2\right) : \left(\Delta\boldsymbol{\varepsilon}(t) - \sum_{i=1}^{3}\boldsymbol{\varepsilon}^{\mathrm{inh}}_{\mathrm{ve},i}(t-\Delta t)\left(1-e^{-\frac{\Delta\psi}{\tau_i}}\right)\right), \tag{4.36}$$

so that again

$$\mathbb{K}(t) = \frac{\partial\Delta\boldsymbol{\sigma}(t)}{\partial\Delta\boldsymbol{\varepsilon}(t)} \approx 3\tilde{K}(t)\mathbb{P}_1 + 2\tilde{G}(t)\mathbb{P}_2. \tag{4.37}$$

Extension for rapidly changing stresses over the time increment

Eq. 4.29 for the 1D and the consecutive derivations for the 3D case are based on the assumption that the stress changes linearly over the time increment and that the nonlinearizing parameter functions g_0, $g_1 g_2$ and a_σ are constant over the time increment. This assumption is violated if the stress increment becomes large, which is the case in a single-step creep experiment, or if in general the nonlinearizing parameter functions vary considerably with slightly varying stresses.

This motivates the extension of Eq. 4.29 to account for changing parameter functions over the time increment. The starting point is Eq. 4.25, for which it is now assumed that not only the stress changes linearly over the time increment with the nonlinearizing parameter functions staying constant, but rather the product of $g_2\sigma$ changes linearly over the time increment and no further restriction on g_0, g_1 and a_σ. This changes the expression for the inherited strains to

$$\begin{aligned}\varepsilon_{\mathrm{ve},i}^{\mathrm{inh}}(t) = & e^{-\frac{\Delta\psi}{\tau_i}} {\varepsilon_{\mathrm{ve},i}^{\mathrm{inh}}}^{t-\Delta t} + \left(g_1 g_2 \sigma(t) - g_1 {g_2}^{t-\Delta t} {\sigma}^{t-\Delta t}\right) \\ & \cdot \frac{1}{E_i} \frac{\tau_i}{\Delta\psi} \left(1 - e^{-\frac{\Delta\psi}{\tau_i}}\right),\end{aligned} \tag{4.38}$$

which is equivalent to the formulations found in [201] and [202]. To avoid cumbersome notation, some of the time dependencies are not explicitly stated. A superscript, e.g., $g_1 g_2^{t-\Delta t}$ or $\sigma^{t-\Delta t}$, indicates that the quantity takes on the value from the recent time step. Again, the product of g_1 and g_2 is evaluated as a single function. From Eq. 4.38 it becomes obvious, that the strain increment is no longer a separable function in the stress increment, so that a total strain formulation is preferred over an incremental formulation. Hence, the current strain is

$$\varepsilon(t) = \left(g_0 \frac{1}{E_0} + g_1 g_2 \sum_{i=1}^{3} \frac{1}{E_i}\right) \sigma(t) - \sum_{i=1}^{3} \varepsilon_{\mathrm{ve},i}^{\mathrm{inh}}(t), \tag{4.39}$$

with the extended definition of $\varepsilon_{\mathrm{ve},i}^{\mathrm{inh}}(t)$ in Eq. 4.38, which is separable in the current stress to yield

$$\begin{aligned}\varepsilon(t) = & \left(g_0 \frac{1}{E_0} + g_1 g_2 \sum_{i=1}^{3} \frac{1}{E_i} \left(1 - \frac{\tau_i}{\Delta\psi} \left(1 - e^{-\frac{\Delta\psi}{\tau_i}}\right)\right)\right) \sigma(t) \\ & - \sum_{i=1}^{3} \left(e^{-\frac{\Delta\psi}{\tau_i}} {\varepsilon_{\mathrm{ve},i}^{\mathrm{inh}}}^{t-\Delta t} - g_1 {g_2}^{t-\Delta t} {\sigma}^{t-\Delta t} \frac{1}{E_i} \frac{\tau_i}{\Delta\psi} \left(1 - e^{-\frac{\Delta\psi}{\tau_i}}\right)\right).\end{aligned} \tag{4.40}$$

Inversely, the total stress at the current time is given with

$$\sigma(t) = \tilde{E}(t)\left(\varepsilon(t) + \sum_{i=1}^{3}\left(e^{-\frac{\Delta\psi}{\tau_i}}\varepsilon_{\mathrm{ve},i}^{\mathrm{inh}\,t-\Delta t} - g_1 g_2{}^{t-\Delta t}\sigma^{t-\Delta t}\frac{1}{E_i}\frac{\tau_i}{\Delta\psi}\left(1-e^{-\frac{\Delta\psi}{\tau_i}}\right)\right)\right), \tag{4.41}$$

with the effective Young's modulus given with

$$\tilde{E}(t) = \left(g_0\frac{1}{E_0} + g_1 g_2\sum_{i=1}^{3}\frac{1}{E_i}\left(1-\frac{\tau_i}{\Delta\psi}\left(1-e^{-\frac{\Delta\psi}{\tau_i}}\right)\right)\right)^{-1}, \tag{4.42}$$

which is equivalent to the previous section.

Extended 3D formulation

The following derivation is analog to the previous derivation of the 3D formulation, so that the individual steps do not need to be repeated. In the extended formulation, the total stress is given with

$$\begin{aligned}\boldsymbol{\sigma}(t) = \left(3\tilde{K}(t)\mathbb{P}_1 + 2\tilde{G}(t)\mathbb{P}_2\right) : \left(\boldsymbol{\varepsilon}(t) + \sum_{i=1}^{3} e^{-\frac{\Delta\psi}{\tau_i}}\boldsymbol{\varepsilon}_{\mathrm{ve},i}^{\mathrm{inh}\,t-\Delta t}\right)\\ - \left(3\tilde{K}(t)D^{\circ}(t)\mathbb{P}_1 + 2\tilde{G}(t)D'(t)\mathbb{P}_2\right) : \boldsymbol{\sigma}^{t-\Delta t},\end{aligned} \tag{4.43}$$

where $\tilde{K}(t)$ and $\tilde{G}(t)$ are unaltered from the previous section and in analogy to Eq. 4.42 to be

$$\begin{aligned}\tilde{G}(t) &= \left(g_0\frac{1}{G_0} + g_1 g_2\sum_{i=1}^{3}\frac{1}{G_i}\left(1+\frac{\tau_i}{\Delta\psi}\left(e^{-\frac{\Delta\psi}{\tau_i}}-1\right)\right)\right)^{-1},\\ \tilde{K}(t) &= \left(g_0\frac{1}{K_0} + g_1 g_2\sum_{i=1}^{3}\frac{1}{K_i}\left(1+\frac{\tau_i}{\Delta\psi}\left(e^{-\frac{\Delta\psi}{\tau_i}}-1\right)\right)\right)^{-1}.\end{aligned} \tag{4.44}$$

The new factors $D^{\circ}(t)$ and $D'(t)$ are given with

$$\begin{aligned} D^{\circ}(t) =& \frac{g_1 {g_2}^{t-\Delta t}}{\Delta\psi} \sum_{i=1}^{3} \frac{\tau_i}{3K_i} \left(1 - e^{-\frac{\Delta\psi}{\tau_i}}\right), \\ D'(t) =& \frac{g_1 {g_2}^{t-\Delta t}}{\Delta\psi} \sum_{i=1}^{3} \frac{\tau_i}{2G_i} \left(1 - e^{-\frac{\Delta\psi}{\tau_i}}\right). \end{aligned} \tag{4.45}$$

Consequently, the tangential stiffness remains unaltered. Eq. 4.43 can then be inverted to give the total strain

$$\begin{aligned} \boldsymbol{\varepsilon}(t) = & \left(\frac{1}{3\tilde{K}(t)}\mathbb{P}_1 + \frac{1}{2\tilde{G}(t)}\mathbb{P}_2\right) : \boldsymbol{\sigma}(t) + \left(D^{\circ}(t)\mathbb{P}_1 + D'(t)\mathbb{P}_2\right) : {\boldsymbol{\sigma}}^{t-\Delta t} \\ & - \sum_{i=1}^{3} e^{-\frac{\Delta\psi}{\tau_i}} {\boldsymbol{\varepsilon}_{\mathrm{ve},i}^{\mathrm{inh}}}^{t-\Delta t}, \end{aligned} \tag{4.46}$$

which is necessary for the iterative procedure to find the correct stress.

Finally, the new inherited strains are given with

$$\begin{aligned} \boldsymbol{\varepsilon}_{\mathrm{ve},i}^{\mathrm{inh}}(t) = & e^{-\frac{\Delta\psi}{\tau_i}} {\boldsymbol{\varepsilon}_{\mathrm{ve},i}^{\mathrm{inh}}}^{t-\Delta t} + \left(\frac{1}{3K_i}\mathbb{P}_1 + \frac{1}{2G_i}\mathbb{P}_2\right) \\ & : \left(g_1 g_2 \boldsymbol{\sigma}(t) - g_1 {g_2}^{t-\Delta t} {\boldsymbol{\sigma}}^{t-\Delta t}\right) \frac{\tau_i}{\Delta\psi} \left(1 - e^{-\frac{\Delta\psi}{\tau_i}}\right). \end{aligned} \tag{4.47}$$

4.2.3 Implementation in `Abaqus`

Since `Abaqus` stores stress and strain quantities in the non-normalized Voigt notation, the tensor expressions above need to be reformulated into a suitable matrix representation. First, the total stress from Eq. 4.43 is transferred to give

$$\begin{aligned} \underline{\sigma}(t) = & \left(3\tilde{K}(t)\underline{\underline{M}}^{\circ} + 2\tilde{G}(t)\underline{\underline{M}}'_{\varepsilon}\right) \left(\underline{\varepsilon}(t) + \sum_{i=1}^{3} e^{-\frac{\Delta\psi}{\tau_i}} {\underline{\varepsilon}_{\mathrm{ve},i}^{\mathrm{inh}}}^{t-\Delta t}\right) \\ & - \left(3\tilde{K}(t)D^{\circ}(t)\underline{\underline{M}}^{\circ} + 2\tilde{G}(t)D'(t)\underline{\underline{M}}'\right) {\underline{\sigma}}^{t-\Delta t}, \end{aligned} \tag{4.48}$$

for which the definitions of the matrix representations of the projector tensors are given in the appendix. It is again pointed out that $\underline{\underline{M}}^{\circ}$ is the matrix representation of the spherical projector, for which there is no distinction between covariant and contravariant bases, since the spherical projector operates only on the main diagonal of a tensor, which is represented equivalently in both bases. However, a distinction must be made for the deviatoric projector. In general, a distinction must be made between three different matrix representations. $\underline{\underline{M}}'_{\varepsilon}$ projects the deviatoric part of a tensor from the contravariant base into the covariant base. This is necessary in order to calculate from a given strain matrix into a desired stress matrix. Conversely, $\underline{\underline{M}}'_{\sigma}$ projects the deviatoric part of a tensor from the covariant base into the contravariant base in order to calculate from a given stress matrix into a desired strain matrix. $\underline{\underline{M}}'$ without index projects the deviatoric part without a change of basis, i.e., from covariant to covariant and from contravariant to contravariant, respectively.

Since Eq. 4.48 is an implicit equation in stress, due to $\tilde{K}(t)$ and $\tilde{G}(t)$ being implicit functions of stress themselves, the strain residual needs to be minimized to find the correctly updated stress $\underline{\sigma}$. Therefore, Eq. 4.46 is reformulated in matrix notation

$$\underline{\varepsilon}(t) = \left(\frac{1}{3\tilde{K}(t)}\underline{\underline{M}}^{\circ} + \frac{1}{2\tilde{G}(t)}\underline{\underline{M}}'_{\sigma}\right)\underline{\sigma}(t) + \left(D^{\circ}(t)\underline{\underline{M}}^{\circ} + D'(t)\underline{\underline{M}}'_{\sigma}\right)\underline{\sigma}^{t-\Delta t} - \sum_{i=1}^{3} e^{-\frac{\Delta\psi}{\tau_i}}\,\underline{\varepsilon}_{\mathrm{ve},i}^{\mathrm{inh}\;t-\Delta t}. \tag{4.49}$$

Once a suitable stress increment is found, the history variables are updated with

$$\underline{\varepsilon}_{\mathrm{ve},i}^{\mathrm{inh}}(t) = e^{-\frac{\Delta\psi}{\tau_i}}\,\underline{\varepsilon}_{\mathrm{ve},i}^{\mathrm{inh}\;t-\Delta t} + \left(\frac{1}{3K_i}\underline{\underline{M}}^{\circ} + \frac{1}{2G_i}\underline{\underline{M}}'_{\sigma}\right) \cdot \left(g_1 g_2\underline{\sigma}(t) - g_1 g_2{}^{t-\Delta t}\underline{\sigma}^{t-\Delta t}\right)\frac{\tau_i}{\Delta\psi}\left(1 - e^{-\frac{\Delta\psi}{\tau_i}}\right). \tag{4.50}$$

Indicator stress: Since the nonlinearizing parameters g_0, g_1g_2, a_σ are functions of a scalar stress measure, the current stress state, which is represented as a 6×1

vector in Abaqus, needs to be reduced to a scalar. For this purpose the von Mises stress $\bar{\sigma}$ is most commonly used which is often found in elasto-plastic material models as a yield criterion with the properties of having a convex yield surface and which is suitable for ductile materials. In Abaqus notation it is defined as

$$\bar{\sigma}(\underline{\sigma}) = \sqrt{\sigma_1^2 + \sigma_2^2 + \sigma_3^2 - \sigma_1\sigma_2 - \sigma_1\sigma_3 - \sigma_2\sigma_3 + 3\,(\sigma_4^2 + \sigma_5^2 + \sigma_6^2)}. \quad (4.51)$$

This indicator stress is used to evaluate the nonlinearizing parameter functions for a given stress state.

Iterative procedure

The UMAT in Abaqus expects a strain increment as input $\underline{\Delta\varepsilon}$ and returns the updated stress $\underline{\sigma}$ as output. Since the updated stress in Eq. 4.48 cannot be solved directly because it is an implicit formulation, it must be solved iteratively.

The starting point for the iterative procedure is that all nonlinearizing parameters g_0, g_1g_2, a_σ are evaluated at the indicator stress at the previous time step $\bar{\sigma}(\underline{\sigma}(t - \Delta t))$. This is again indicated by ${g_0}^{t-\Delta t}$, ${g_1g_2}^{t-\Delta t}$ and ${a_\sigma}^{t-\Delta t}$. With the given set of parameters and the new strain increment for the current step $\underline{\Delta\varepsilon}(t)$ provided by Abaqus, a new total strain $\underline{\varepsilon}$ is calculated and a trial stress state is evaluated using Eq. 4.48

$$\underline{\sigma}^{\mathrm{trial}} = f_\sigma \left({g_0}^{t-\Delta t}, {g_1g_2}^{t-\Delta t}, {a_\sigma}^{t-\Delta t}, \Delta t, \underline{\varepsilon}(t), {\underline{\varepsilon}_{\mathrm{ve},i}^{\mathrm{inh}}}^{t-\Delta t} \right). \quad (4.52)$$

The trial stress $\underline{\sigma}^{\mathrm{trial}}$ is subsequently used to update the nonlinearizing material parameters to g_0, g_1g_2, a_σ using the updated indicator stress. Then a trial strain increment is recalculated using Eq. 4.49

$$\underline{\Delta\varepsilon}^{\mathrm{trial}} = f_\varepsilon \left(g_0, g_1g_2, a_\sigma, \Delta t, \underline{\sigma}^{\mathrm{trial}}, {\underline{\varepsilon}_{\mathrm{ve},i}^{\mathrm{inh}}}^{t-\Delta t} \right) - \underline{\varepsilon}^{t-\Delta t}. \quad (4.53)$$

With the given strain increment from Abaqus $\underline{\Delta\varepsilon}(t)$ and the calculated trial strain increment $\underline{\Delta\varepsilon}^{\mathrm{trial}}$, a residual vector is formulated in matrix notation

$$\underline{R}(\underline{\sigma}^{\mathrm{trial}}) = \underline{\Delta\varepsilon}^{\mathrm{trial}} - \underline{\Delta\varepsilon}(t), \tag{4.54}$$

which needs to be minimized using the Newton-Raphson method. For this, the residual vector $\underline{R}$ is linearized around a given stress input $\underline{\sigma}$ in accordance to the Taylor series

$$\underline{R}(\underline{\sigma} + \underline{\Delta\sigma}) = \underline{R}(\underline{\sigma}) + \underline{\underline{J}}(\underline{\sigma})\underline{\Delta\sigma}, \tag{4.55}$$

where terms of higher order are neglected. $\underline{\underline{J}}$ is called the Jacobian, which is the matrix representing the first order derivatives in respect to all components of the stress vector

$$\underline{\underline{J}}(\underline{\sigma}) = \left.\frac{\partial \underline{R}}{\partial \underline{\sigma}}\right|_{\underline{\sigma}}. \tag{4.56}$$

The formulations above are then used to iteratively find the roots of Eq. 4.55 with an updated stress vector for each iteration

$$\underline{R}(\underline{\sigma} + \underline{\Delta\sigma}) \stackrel{!}{=} \underline{0}. \tag{4.57}$$

The k^{th} iteration is given with

$$\underline{R}({}^{k}\underline{\sigma}^{\mathrm{trial}}) + \underline{\underline{J}}({}^{k}\underline{\sigma}^{\mathrm{trial}})\,{}^{k}\underline{\Delta\sigma}^{\mathrm{trial}} = \underline{0} \tag{4.58}$$

which can be solved for the stress increment ${}^{k}\underline{\Delta\sigma}^{\mathrm{trial}}$

$${}^{k}\underline{\Delta\sigma}^{\mathrm{trial}} = -\underline{\underline{J}}({}^{k}\underline{\sigma}^{\mathrm{trial}})^{-1}\,\underline{R}({}^{k}\underline{\sigma}^{\mathrm{trial}}), \tag{4.59}$$

and the next stress increment for iteration $k+1$ is given with

$${}^{k+1}\underline{\sigma}^{\mathrm{trial}} = {}^{k}\underline{\sigma}^{\mathrm{trial}} + {}^{k}\underline{\Delta\sigma}^{\mathrm{trial}}. \tag{4.60}$$

Eqs. 4.58 to 4.60 are iteratively repeated until the relative residual is close to zero

$$\frac{\|\underline{R}(^{k+1}\underline{\sigma})\|}{\|\underline{\Delta\varepsilon}(t)\|} < \epsilon \approx 0, \tag{4.61}$$

or until the iteration variable reaches a termination criterion. A flow chart of the implemented UMAT is given below in Fig. 4.6 and the full code is given in Appendix E.

4.2.4 Verification of UMAT

Since the commercial FEA software `Abaqus` does not provide a material model to describe a nonlinear viscoelastic material relationship, a direct verification of the implementation of the UMAT is not possible. However, since the nonlinear theory derived above is an extension of the linear viscoelastic theory and `Abaqus` provides a linear viscoelastic model, it is possible to verify the implementation for the linear realm.

The implementation of a viscoelastic response in `Abaqus` is based on the generalized Maxwell model, which is closely related to the generalized Kelvin-Voigt model that was used in the UMAT. The generalized Maxwell model is shown in Fig. 4.7. While the individual elements, i.e., a spring and a dashpot in series for the Maxwell model and a spring and dashpot in parallel for the Kelvin-Voigt element, respectively, are not equivalent, their generalized versions are equivalent and therefore the parameters for each model can be transferred into the other model representation [203]. Nevertheless, this is only easily accessible up to the second order, i.e., $n = 2$, due to higher order polynomials in the denominator within the Laplace domain. Consequently, the verification will take place for $n = 2$ to avoid having to resort to numerical algorithms to find the corresponding set of parameters for the generalized Maxwell model for a chosen set of parameters for the generalized Kelvin-Voigt model. Since the UMAT is implemented for $n = 3$, the last element will be inactivated, which is realized by a large value for E_3 and/or a large value for η_3, respectively. This implies that the deformation of

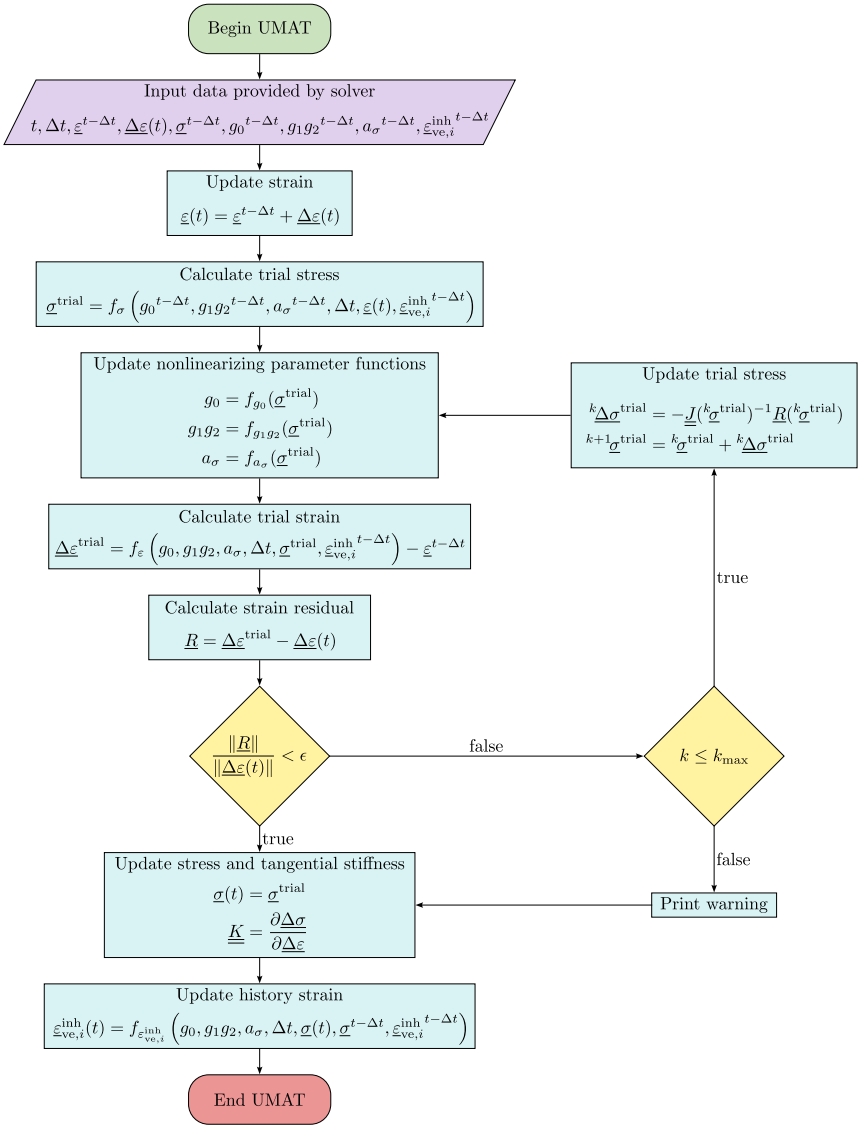

Figure 4.6: Flowchart of UMAT implemented in `Abaqus`.

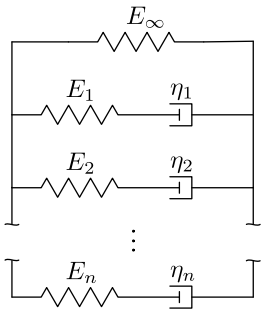

Figure 4.7: Generalized Maxwell model as it is used in viscoelastic modeling in `Abaqus`.

the third element is prohibited. Additionally, to stay within the linear viscoelastic realm, the nonlinearizing parameter functions are locked at a value of one, i.e., $g_0 = g_1 g_2 = a_\sigma = 1$.

Without further derivation, which is given to a great extend in Flügge [204, p. 6 ff.], the response of the Maxwell model is usually expressed with the relaxation modulus $Y(t)$, which relates the the stress response over time for a given strain input. This is given with

$$\sigma(t) = \underbrace{\left(E_\infty + \sum_{i=1}^{2} E_i e^{-\frac{t}{\tau_i}} \right)}_{=Y(t)} \varepsilon_0, \tag{4.62}$$

where once more $\tau_i = \eta_i / E_i$. The initial elastic response at $t = 0$ is indicated as

$$\begin{aligned} E_0 &= Y(t=0), \\ &= E_\infty + \sum_{i=1}^{2} E_i = E_\infty + E_1 + E_2, \end{aligned} \tag{4.63}$$

so that

$$Y(t) = E_0 - \sum_{i=1}^{2} E_i \left(1 - e^{-\frac{t}{\tau_i}} \right). \tag{4.64}$$

In general, this is referred to as *Prony series*. In Abaqus, the *Prony series* is expressed dimensionless by dividing Eq. 4.64 by the initial elastic response E_0 to result in

$$\frac{Y(t)}{E_0} = 1 - \sum_{i=1}^{2} \frac{E_i}{E_0} \left(1 - e^{-\frac{t}{\tau_i}}\right). \tag{4.65}$$

To express the viscoelastic response in 3D, the isotropic elastic relations

$$\begin{aligned} G_i &= \frac{E_i}{2(1+\nu)}, \\ K_i &= \frac{E_i}{3(1-2\nu)}, \end{aligned} \tag{4.66}$$

are applied, which is identical to the assumptions made for the nonlinear model above (cf. Appendix C). Consequently, the dimensionless shear and bulk moduli for each element of the *Prony series* are

$$\begin{aligned} \bar{g}_i^{\mathrm{P}} &= \frac{G_i}{G_0} = \frac{E_i}{E_0}, \\ \bar{k}_i^{\mathrm{P}} &= \frac{K_i}{K_0} = \frac{E_i}{E_0}, \end{aligned} \tag{4.67}$$

whereby the notation of the Abaqus manual was adopted [205]. Since no distinction between the volumetric and deviatoric model parameters are made here, the dimensionless shear and bulk moduli are equal, i.e., $\bar{g}_i^{\mathrm{P}} = \bar{k}_i^{\mathrm{P}}$. In addition to the relaxation times τ_i and the initial elastic response E_0, $\bar{g}_i^{\mathrm{P}}$ and $\bar{k}_i^{\mathrm{P}}$ are the model parameters for the user to control the viscoelastic behavior within Abaqus.

To verify the implementations of the UMAT, a longitudinal and shear deformation are compared for a single element cube with the viscoelastic implementation in Abaqus. For this, arbitrary model parameters are chosen for the Kelvin-Voigt model, i.e., $E_0 = 1000\,\mathrm{MPa}$, $E_1 = 500\,\mathrm{MPa}$, $E_2 = 200\,\mathrm{MPa}$, $\tau_1 = 10\,\mathrm{s}$ and $\tau_2 = 50\,\mathrm{s}$. To determine the corresponding model parameters for the Maxwell model, the formulas in Serra-Aguila et al. [203] were used, which can also be found in Appendix D. The resulting model parameter, which ought to give the same viscoelastic response are listed in Tab. 4.2.

Table 4.2: Equivalent parameter sets between the Kelvin-Voigt and Maxwell model. The latter is used in `Abaqus`, where the spring constants E_i are expressed as the dimensionless shear and bulk moduli $\bar{g}_i^{\mathrm{P}}$ and $\bar{k}_i^{\mathrm{P}}$ in accordance to Eq. 4.67.

Kelvin-Voigt (UMAT)					Maxwell (`Abaqus`)				
E_0	E_1	E_2	τ_1	τ_2	E_0	E_1	E_2	τ_1	τ_2
(MPa)			(s)		(MPa)			(s)	
1000.0	500.0	200.0	10.0	50.0	1000.0	90.76	784.24	23.6	2.65

The investigated load scenarios are illustrated in Fig. 4.8. The geometry is a single

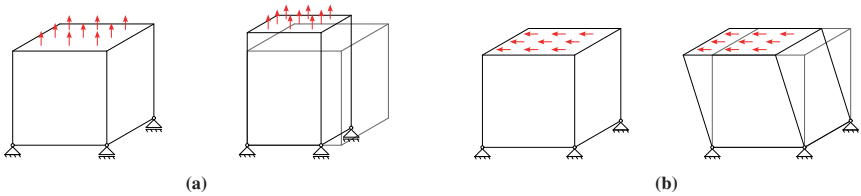

Figure 4.8: Load scenarios to verify UMAT implementation against the linear viscoelastic model in `Abaqus`.

element unit cube with a side length of 1 mm. For the tensile load, the bottom is only fully constrained on a single node, while the others are free to displace within the plane. For the shear loading, all bottom nodes are constrained and the top nodes are constrained to only move in the direction of load. Both simulations contain four steps. In the first step a pressure/traction load of 5 MPa is applied instantaneously followed by a 100 s creep period. In the second step, the load is increased to 10 MPa with another 100 s creep period. In the third step, the load is decreased to 2.5 MPa, followed by 100 s creep. In the last step, the creep load is removed, but a sudden displacement jump is applied instead and held for 100 s to investigate the relaxation behavior. For the tensile scenario, the displacement jump is 5 % of the cube side length in the previous load direction and for the shear scenario it is 10 %.

4.2.5 Results

Verification of UMAT

The results of the UMAT implementation in comparison to the linear viscoelastic implementation in `Abaqus` are visualized in Fig. 4.9. The left figure shows the

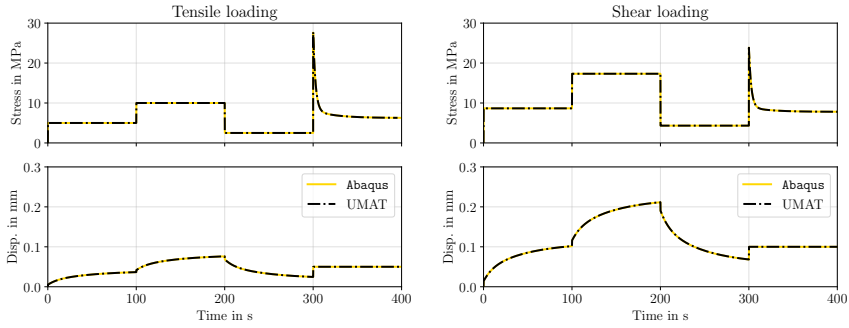

Figure 4.9: Verification results of the UMAT implementation compared to the linear Maxwell model natively implemented in `Abaqus`.

tensile results; the right figure shows the shear results. The upper row shows the applied or reaction stress, while the lower row shows the reaction or applied displacement in load direction. Shown are the results of one of the nodes on the top, for which the selection is arbitrary, as the results are identical for all nodes within a load scenario. It is clearly visible that for both load scenarios, stresses and displacements are perfectly in agreement between the `Abaqus` implementation and the linear UMAT.

Modeling of experimental results

The numerical fit of the full compliance, i.e., the static and time dependent part of the creep compliance, to the experimental curves are given in Fig. 4.10. The

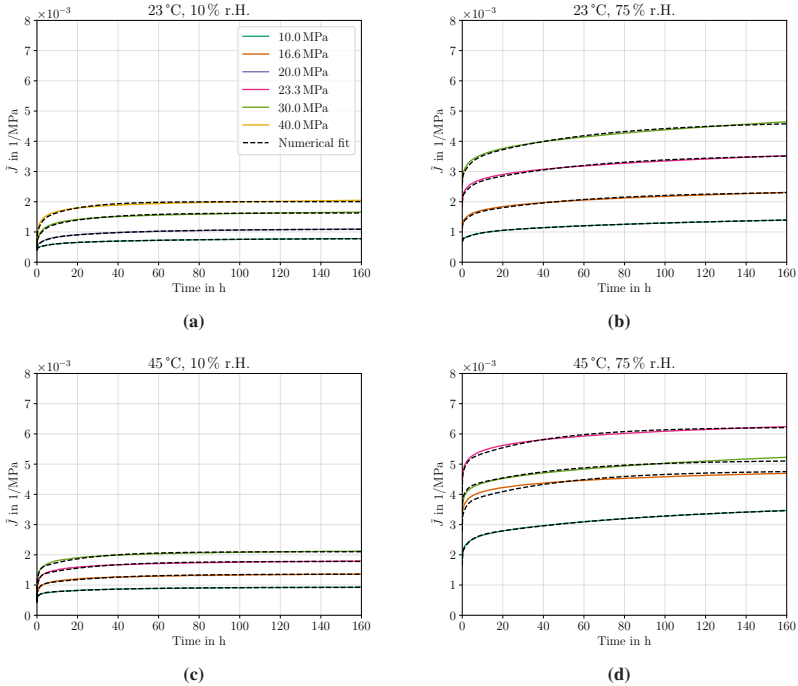

Figure 4.10: Numerical fit of the full creep compliance over time for various conditioning states and constant loads: (**a**) 23 °C and 10 % r.H. with 10.0 MPa, 20.0 MPa, 30.0 MPa and 40.0 MPa, (**b**) 23 °C and 75 % r.H. with 10.0 MPa, 16.6 MPa, 23.3 MPa and 30.0 MPa, (**c**) 45 °C and 10 % r.H. with 10.0 MPa, 16.6 MPa, 23.3 MPa and 30.0 MPa, and (**d**) 45 °C and 75 % r.H. with 10.0 MPa, 16.6 MPa, 20.0 MPa and 23.3 MPa. For each conditioning state, the lowest stress of 10 MPa was assumed to behave linearly.

numerical model is capable of fitting the experimental data well, in general. A near perfect fit is achieved for all but the warm and wet conditioning, where experimental and numerical curves align without deviation. Small deviations are visible for the higher stresses in the extreme case for 45 °C and 75 % r.H., especially for a creep stress of 16.6 MPa. Multiple regions of deviation are visible here. The initial incline is underpredicted and the numerical curve overshoots the experimental data after 60 h.

The model parameter for each conditioning state are given in Tab. 4.3. Most

Table 4.3: Kelvin-Voigt model parameters for different conditioning states. Each parameter was rounded to the next integer.

Conditioning		Kelvin-Voigt model parameters						
Temp.	rel. Hum.	E_0	E_1	E_2	E_3	τ_1	τ_2	τ_3
(°C)	(%)	(MPa)				(s)		
23	10	2600	11676	7509	5434	932	21258	201109
23	75	1538	8783	4493	1810	947	26965	434516
45	10	2441	5897	6290	5337	326	4998	128417
45	75	612	2105	2058	937	633	14291	345828

of the Kelvin-Voigt model parameters are in a comparable range of magnitude for the different conditioning states. The initial spring constant E_0 is in the magnitude of $1 \cdot 10^3$ MPa, ranging from 612 MPa to 2600 MPa. The viscoelastic spring constants E_1 and E_2 show a slightly increased range of magnitude within $1 \cdot 10^3$ and lower $1 \cdot 10^4$ MPa, with exact numbers ranging between 2105 MPa and 11676 MPa for E_1, and 2058 MPa and 7509 MPa for E_2. The range for the E_3 values is again slightly lower with values ranging from 937 MPa and 5434 MPa. In general, the cold/dry conditioning has the highest values for all E_i, followed by hot/dry and then cold/wet. The warm/wet conditioning has the lowest stiffness values. An exception is given for E_1, where the stiffness parameter for cold/wet is higher than for hot/dry.

The relaxation times are found to be in a more narrow range of magnitude. The first relaxation time τ_1 is in the range of $1 \cdot 10^2$ s to $1 \cdot 10^3$ s, ranging from 326 s to 947 s. The second relaxation time τ_2 is within the range of $1 \cdot 10^3$ and $1 \cdot 10^5$ s, with exact values ranging from 4998 to 26965 s. τ_3 lies within the range of $1 \cdot 10^5$ and $1 \cdot 10^6$ s, with the lowest value being 128417 s and the highest being 434516 s. Generally, the shortest relaxation times are always given for the warm/dry conditioning and the longest are given for the cold/wet case.

The fitted nonlinearizing parameters for the individual stress levels are given in Tab. 4.4. Visually, this is also shown in Fig. 4.11. The scaling parameter for the

Table 4.4: Nonlinear parameter for the Kelvin-Voigt model after Schapery for different conditioning states.

Cond.	23 °C 10 % r.H.				23 °C 75 % r.H.				45 °C 10 % r.H.				45 °C 75 % r.H.			
σ (MPa)	10.0	20.0	30.0	40.0	10.0	16.6	23.3	30.0	10.0	16.6	23.3	30.0	10.0	16.6	20.0	23.3
$g_0(\sigma)$	1.00	1.07	1.22	1.62	1.00	1.72	3.01	3.93	1.00	1.04	1.28	1.43	1.00	1.70	2.10	2.50
$g_1 g_2(\sigma)$	1.00	1.69	2.87	3.43	1.00	1.38	1.83	2.38	1.00	1.80	2.44	2.94	1.00	0.99	0.84	1.05
$a_\sigma(\sigma)$	1.00	0.72	0.44	0.32	1.00	0.49	0.51	0.50	1.00	0.90	0.79	0.66	1.00	0.50	0.50	0.42

transient creep compliance, i.e., $g_1 g_2$, is found to monotonically increase with an increasing creep stress for all conditioning states but the warm/wet conditioning, which is a direct consequence of the increasing experimental transient creep compliances for increasing load levels. The static scaling parameter g_0 shows a monotonic increase with stress for all conditioning states, and the time shift parameter a_σ shows a monotonic decrease with a small interruption for the cold/wet conditioning.

The fitted parameter functions for the different conditioning states are given in the following and are plotted in Fig. 4.11, along with the calculated values optimally fitting the experimental data given in Tab. 4.4. With the exception of $g_1 g_2$ for the warm/wet conditioning, all parameter have a near monotonic curve, which was fitted with a symmetric sigmoidal function

$$f(\sigma_\mathrm{v}) = d + \frac{a-d}{1+\left(\frac{\sigma_\mathrm{v}}{c}\right)^b}, \tag{4.68}$$

with a, b, c and d being the fitting parameters. The advantage of this parametric function is that it is smooth and does not grow rapidly outside the fitted region, which helps with numerical stability. In order to be able to estimate how the fitted

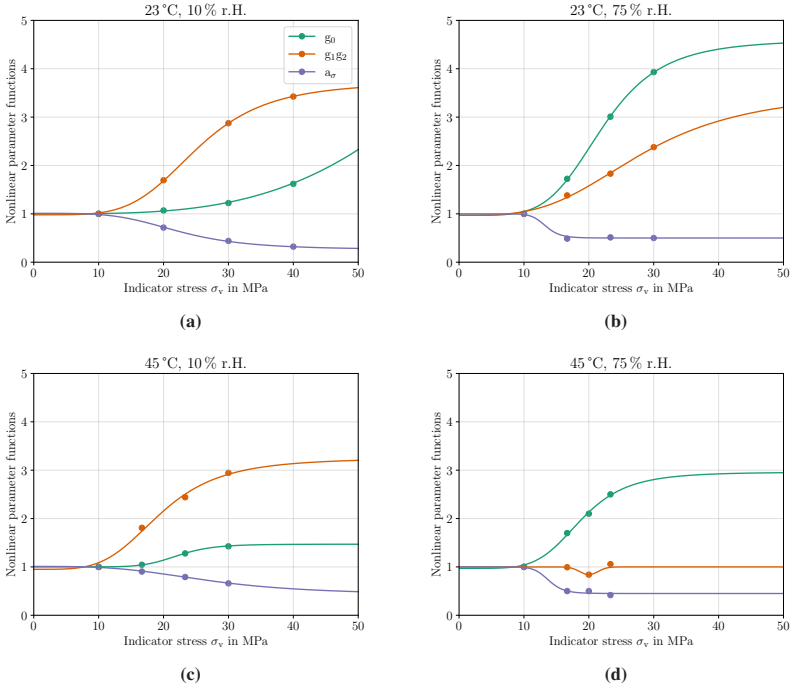

Figure 4.11: Numerical fit of the nonlinearizing parameter functions g_0, $g_1 g_2$ and a_σ: (**a**) 23 °C and 10 % r.H. with 10.0 MPa, 20.0 MPa, 30.0 MPa and 40.0 MPa, (**b**) 23 °C and 75 % r.H. with 10.0 MPa, 16.6 MPa, 23.3 MPa and 30.0 MPa, (**c**) 45 °C and 10 % r.H. with 10.0 MPa, 16.6 MPa, 23.3 MPa and 30.0 MPa, and (**d**) 45 °C and 75 % r.H. with 10.0 MPa, 16.6 MPa, 20.0 MPa and 23.3 MPa. The assumption for linearity below 10 MPa implies a value of one.

functions behave for extrapolated stresses beyond the experimental range, a plot range up to 50 MPa was selected.

For the cold/dry conditioning, the functions were found to be

$$g_0^{23\,^\circ\mathrm{C},\,10\,\%\,\mathrm{r.H.}}(\sigma) = 19.57 + \frac{1. - 19.57}{1 + (\frac{\sigma}{104.23})^{3.49}}, \tag{4.69a}$$

$$g_1 g_2{}^{23\,^\circ\mathrm{C},\,10\,\%\,\mathrm{r.H.}}(\sigma) = 3.72 + \frac{0.98 - 3.72}{1 + (\frac{\sigma}{25.19})^{4.61}}, \tag{4.69b}$$

$$a_\sigma{}^{23\,^\circ\mathrm{C},\,10\,\%\,\mathrm{r.H.}}(\sigma) = 0.26 + \frac{1.01 - 0.26}{1 + (\frac{\sigma}{22.42})^{4.22}}. \tag{4.69c}$$

Their coefficients of determination, or R^2 values, for the optimal calculated parameters in Tab. 4.4 at 10, 20, 30, and 40 MPa are given with 0.998, 1.000 and 1.000, indicating good fits.
The parameter functions for the cold/wet conditioning are given with

$$g_0^{23\,^\circ\mathrm{C},\,75\,\%\,\mathrm{r.H.}}(\sigma) = 4.6 + \frac{0.97 - 4.6}{(1 + (\frac{\sigma}{22.11})^{4.84})}, \tag{4.70a}$$

$$g_1 g_2{}^{23\,^\circ\mathrm{C},\,75\,\%\,\mathrm{r.H.}}(\sigma) = 3.54 + \frac{0.97 - 3.54}{(1 + (\frac{\sigma}{28.41})^{3.34})}, \tag{4.70b}$$

$$a_\sigma{}^{23\,^\circ\mathrm{C},\,75\,\%\,\mathrm{r.H.}}(\sigma) = 0.5 + \frac{1 - 0.5}{(1 + (\frac{\sigma}{13.33})^{12})}, \tag{4.70c}$$

Their R^2 values for the optimal parameters in Tab. 4.4 at 10, 16.6, 23.3, and 30 MPa are given with 1.000, 0.996 and 0.987, again indicating good fits.
The parameter functions for the warm/dry conditioning are given with

$$g_0^{45\,^\circ\mathrm{C},\,10\,\%\,\mathrm{r.H.}}(\sigma) = 1.47 + \frac{1 - 1.47}{(1 + (\frac{\sigma}{22.20})^{8.22})}, \tag{4.71a}$$

$$g_1 g_2{}^{45\,^\circ\mathrm{C},\,10\,\%\,\mathrm{r.H.}}(\sigma) = 3.25 + \frac{0.95 - 3.25}{(1 + (\frac{\sigma}{19.52})^{4.12})}, \tag{4.71b}$$

$$a_\sigma{}^{45\,^\circ\mathrm{C},\,10\,\%\,\mathrm{r.H.}}(\sigma) = 0.42 + \frac{1.01 - 0.42}{(1 + (\frac{\sigma}{27.11})^{3.35})}, \tag{4.71c}$$

Their R^2 values for the optimal parameters in Tab. 4.4 at 10, 16.6, 23.3, and 30 MPa are given with 0.999, 0.992 and 0.997, again indicating good fits.
Lastly, the parameter functions for the warm/wet conditioning are given with

$$g_0^{45\,^\circ\text{C},\,75\,\%\,\text{r.H.}}(\sigma) = 2.96 + \frac{0.97 - 2.96}{(1 + (\frac{\sigma}{18.75})^{5.27})}, \tag{4.72a}$$

$$g_1 g_2{}^{45\,^\circ\text{C},\,75\,\%\,\text{r.H.}}(\sigma) = 1 - 0.16 \cdot \exp\left(-\frac{(\sigma - 20)^2}{2 \cdot 1.4^2}\right), \tag{4.72b}$$

$$a_\sigma{}^{45\,^\circ\text{C},\,75\,\%\,\text{r.H.}}(\sigma) = 0.45 + \frac{1 - 0.45}{(1 + (\frac{\sigma}{13.8})^{11.9})}, \tag{4.72c}$$

Their R^2 values for the optimal parameters in Tab. 4.4 at 10, 16.6, 20, and 23.3 MPa are given with 0.997, 0.828 and 0.985, indicating good fits for g_0 and a_σ, while the fit for $g_1 g_2$ is not exact.

The combined numerical fits of the experimental strain data using the calibrated UMAT with Kelvin-Voigt parameters and the nonlinearizing parameter functions evaluated at the respective stress values (in contrast to using the optimally calculated parameters) are given in Fig. 4.12. With the exception of the most extreme conditioning state of 45 °C and 75 % r.H., the experimental data is captured with excellent agreement. The agreement of the numerical data to the experimental data for the critical conditioning state mentioned above is still very good for the lower stress level of 10 MPa. Above that, the initial creep strain is underpredicted, while still approaching the measured creep strain in a later stage for 16.6 MPa and 20 MPa. For the extreme loading of 23.3 MPa, the creep strain is continuously underpredicted of up to 3 %.

4.3 Discussion

In the present chapter, the hygrothermal material behavior of PA6 was characterized based on creep tests under various climatic conditions. Four different climate states were selected, of which at least the warm/humid condition is above the glass

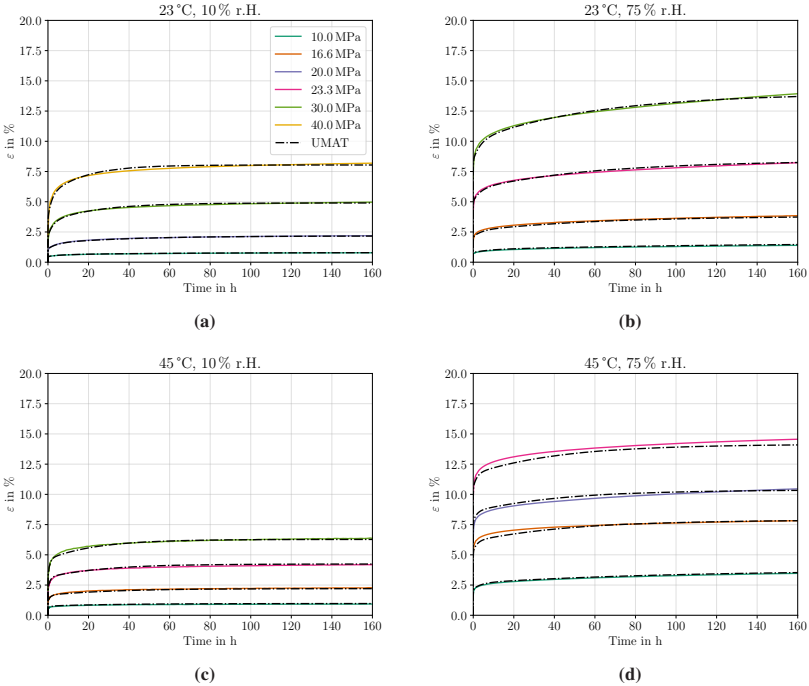

Figure 4.12: Simulation of the total strain with calibrated UMAT over time for various conditioning states and constant loads using the fitted nonlinearizing parameter functions instead of the exactly calculated nonlinearizing parameter values: (**a**) 23 °C and 10 % r.H. with 10.0 MPa, 20.0 MPa, 30.0 MPa and 40.0 MPa, (**b**) 23 °C and 75 % r.H. with 10.0 MPa, 16.6 MPa, 23.3 MPa and 30.0 MPa, (**c**) 45 °C and 10 % r.H. with 10.0 MPa, 16.6 MPa, 23.3 MPa and 30.0 MPa, and (**d**) 45 °C and 75 % r.H. with 10.0 MPa, 16.6 MPa, 20.0 MPa and 23.3 MPa. For each conditioning state, the lowest stress of 10 MPa was assumed to behave linearly.

transition temperature of PA6, while both dry states are below T_g. The warm/dry condition lies within the glass transition range.

Based on the experimental creep data, it was determined that there is both a hygrothermal material dependence and a nonlinear viscoelastic behavior present. While increasing the ambient temperature in the dry state, i.e., below T_g, led to a moderate increase in creep compliance, the qualitative progression of strain over

time remained unchanged. In contrast, a qualitative change in material response due to a humid environment is clearly evident. In the humid state, particularly under high loads, stable creep rates are not achieved, resulting in a noticeable increase in strain even after $160\,\mathrm{h}$. This also applied to the wet/cold conditioning case, confirming that the polymer had crossed into the rubbery state. Consequently, the creep curves indicate whether the polymer is above or below T_g. Whether the higher creep rates are solely due to the exceeding of the glass transition temperature caused by the plasticizing effect of water absorption or whether this change would also occur at moderate humidity below the glass transition temperature cannot be definitively determined from the evaluated climatic ranges. However, it is reasonable to assume that the physical explanation lies in the fact that the moisture in PA6 leads to plasticization with increased chain mobility, which effectively lowers the glass transition temperature and facilitates the relative sliding of molecular chains in the amorphous regions. This is effectively observed in the increased creep compliance and increased creep rates at the end of the testing period for higher loads for the wet conditioning states. This condition not only leads to a changed material response but also reduces the load-bearing capacity of the material in a humid state. It was observed that in a cold/dry climate, a load of $40\,\mathrm{MPa}$ did not lead to failure in the form of an unstable increase in creep rate over the tested period. In contrast, a load of $30\,\mathrm{MPa}$ in the warm/humid condition resulted in immediate creep failure.

To numerically represent the nonlinear viscoelastic material behavior measured in the experiment, the nonlinear extension of the hereditary integral according to Schapery was introduced and translated into an incremental form for suddenly applied loads, as is the case with creep loading. This model is based on the nonlinear material functions g_0, $g_1 g_2$ and a_σ. These nonlinear material parameter functions allow for the modeling of stress-dependent material behavior. The parameter functions are to be interpreted in the following way: g_0 scales the elastic material response, where values greater than 1 indicate increased compliance, while values less than 1 indicate increased elastic stiffness. Similarly, $g_1 g_2$ scales the time-dependent material response, with an identical interpretation. The function a_σ is a scaling parameter for time. A value less than 1 represents an accelerated

creep or relaxation mechanism. Since `Abaqus` only includes an implementation of a linear viscoelastic material, the proposed Schapery model had to be implemented as a UMAT. Being an extension of the linear model, the linear case can be modeled as a special case. The verification of the linear model against the model implemented in `Abaqus` showed perfect agreement, allowing for the conclusion that the implementation is valid.

The Kelvin-Voigt parameters for the spring constants and viscosities were determined through error minimization between numerical results and experiments using an optimizer in `SciPy`, assuming that a stress of $10\,\mathrm{MPa}$ or less causes a linear viscoelastic behavior. The calculated material parameters are within physically reasonable limits. This means that the stiffness parameters (spring constants) are of a similar order of magnitude to the elastic stiffness of the base material according to its data sheet. Furthermore, the calculated relaxation times adequately cover the investigated time period. If some of the stiffness parameters or relaxation times were significantly larger, it would suggest that the chosen number of Kelvin-Voigt elements, $n = 3$, possesses too many degrees of freedom. A very large stiffness or relaxation time would effectively deactivate one of the Kelvin-Voigt elements. This would be the case if fewer than $n = 3$ elements were sufficient to reproduce the experimental behavior. Based on this reasoning and the excellent representation of the creep behavior at $10\,\mathrm{MPa}$, it can be assumed that $n = 3$ elements, and consequently 7 parameters, provide a good starting point for the modeling. Nevertheless, it must be acknowledged that the calculated parameters are not unique, and a different pairing of material parameters could result in effectively similar material behavior.

Based on the viscoelastic material parameters, the nonlinear parameter functions g_0, $g_1 g_2$ and a_σ were calculated using the same error minimization method to replicate the nonlinear behavior of the creep compliance. Generally, the monotonic nature of the calculated parameter functions is notable. g_0 increases monotonically with applied stress, resulting in an increased elastic compliance of the material for higher stress levels. The rate at which g_0 increases is higher under moist conditioning states. This can be interpreted to mean that, for the chosen conditioning conditions, an increase in humidity exerts a stronger nonlinear effect

compared to an increase in temperature.
Similarly, $g_1 g_2$ also exhibits a monotonic increase, with the exception of the warm/wet condition, where the rate of increase is similar among the conditioning states. The monotonic increase implies that an increased creep load also results in an increase in transient creep compliance. The exception in the warm/wet conditioning state needs to be considered separately. During the first test run, loads of $10, 16.6, 23.3$ and 30 MPa were applied, with the 30 MPa load leading to immediate failure. To gather sufficient data points, a second test run was conducted with loads of 5, 10, 15 and 20 MPa, ultimately incorporating the results of 10 and 20 MPa into the final analysis alongside those of 16.6 and 23.3 MPa. As the application of the creep load is performed manually, it cannot be ensured that the initial loading conditions are consistent between the two test runs. This likely led to differing creep strain behaviors. For example, it is evident that the determined Kelvin-Voigt parameters fit better for the load of 16.6 MPa than for the other two cases. This highlights that slight variations in initial conditions during the experiment can lead to significant changes in the temporal behavior, complicating the determination of numerical parameters. Therefore, the non-monotonic behavior of $g_1 g_2$ in the warm/wet climate should be seen less as a peculiarity of the material behavior under these conditions and more as a result of imprecise data collection. Thus, it is critical to note that creep tests are only well-comparable when conducted under identical boundary conditions.
The scaling parameter for time, a_σ, also shows monotonic behavior, decreasing with increasing stress. This can be interpreted as an increase in climatic factors leading to an acceleration of the viscous mechanisms. This aligns with the physical interpretation that an increase in temperature and/or humidity results in greater inter-chain spacing in the polymer, facilitating the sliding of chains over one another.

For the numerical model, functions were fitted to the computed support points of the nonlinear parameters to cover the range between the evaluated creep loads. The symmetric sigmoid function demonstrated sufficient flexibility to encompass the monotonic trends. Based on the fully calibrated model, a final 3D simulation

of the experimentally determined creep tests was conducted using the implemented UMAT. The excellently matching results confirm the applicability of the nonlinear approach according to Schapery with $n = 3$ Kelvin-Voigt elements. However, for the warm/moist conditioning state, the maximum load of $23.3\,\mathrm{MPa}$ shows a deviation of approximately $3\,\%$ in creep strain. Since this deviation is relatively small and the creep behaviors are qualitatively well represented, it can be concluded that the chosen approach and the calculated parameters provide a successful modeling framework capable of representing the nonlinear viscoelastic, climate-dependent material behavior in subsequent simulations.

5 Fiber-matrix interface

5.1 Single fiber pull-out test

As mentioned above in Chapter 2, the single fiber pull-out (SFPO) test is a micro-mechanical experiment to investigate the quasi-static quantities within a fiber-matrix model specimen. The experiment allows for a direct assessment of the interfacial shear strength (IFSS), which is a critical determinant of the load transfer capabilities within a composite material.

For the SFPO test, a lab specimen which contains a single fiber partially embedded in matrix material is used. The fiber is quasi-statically pulled out of the matrix, during which the force and displacement in fiber direction are recorded. The typical result of the SFPO test is schematically drawn in Fig. 5.1. The initial incline of the force signal is still within the elastic region and its slope correlates with the stiffness of the system. As such, it is not to be confused with the stiffness of the interface alone, since the stiffness of the free fiber length, the viscoelastic gripping adhesive and the test rig (even though negligible) contribute to that value. At a certain force value, which in general is the maximum force value $F_{\max}$ measured for one test, the interface fails abruptly which results in a significant drop of the force signal. From that point on the fiber is being pulled out of the matrix with a debonded interface under frictional forces due to residual pressure stresses caused by the difference in thermal expansion coefficients.

The material parameters for describing the fiber-matrix interface include the Interfacial Shear Strength (IFSS) and the energy components of the debonding and frictional segments. The IFSS represents an average strength measure, which

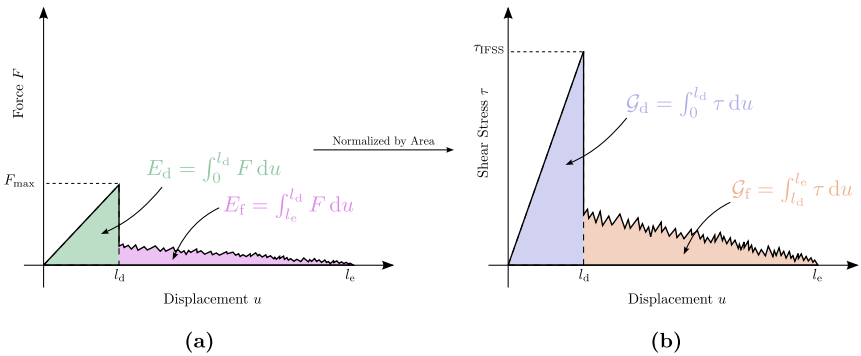

Figure 5.1: Schematic of a typical pull-out curve. (**a**) shows the measured force-displacement plot, while (**b**) shows the embedded area normalized shear stress over displacement. In each diagram, the left (green/blue) area represents the energy (per area) used for breaking the interface, while the right (pink/orange) area represents the energy (per area) due to frictional forces/stresses.

is based on the presumption that the shear stress throughout the experiment is uniformly distributed across the embedded fiber surface and is given with

$$\tau_{\mathrm{IFSS}} = \frac{F_{\max}}{A}, \tag{5.1}$$

where A is the surface area of the embedded fiber length. Based on the equation above, a possible experimental assessment of the IFSS is to perform multiple SFPO tests, record the individual maximum forces and divide those by the hull surface A of the corresponding embedded fiber segment. This will usually produce a high scattering in the data, which motivates to assess statistical moments, such as average/median values and distribution information.

Another assessment method is to treat the IFSS as a constant material parameter, which allows to express the pull-out force $F_{\max}$ as a function of the embedded length. With the assumption of a cylindrical shape of the fiber, the embedded area can be expressed as $A = 2\pi r_{\mathrm{f}} l_{\mathrm{e}}$, so that Eq. 5.1 can be reformulated as

$$\tau_{\mathrm{IFSS}} = \frac{1}{2\pi r_{\mathrm{f}} l_{\mathrm{e}}} F_{\max}. \tag{5.2}$$

Rearranging gives an expression for F_{max} as a function of the embedded length l_{e}

$$F_{\text{max}}(l_{\text{e}}) = \underbrace{2\pi r_{\text{f}} \tau_{\text{IFSS}}}_{=m} l_{\text{e}}, \tag{5.3}$$

which is a linear function passing the origin with slope m. Hence, if all measurements of F_{max} are plotted over the corresponding embedded length l_{e}, the slope of a linear regression is proportional to the IFSS with

$$\tau_{\text{IFSS}} = \frac{m}{2\pi r_{\text{f}}}. \tag{5.4}$$

The fact that according to Eq. 5.3 the linear regression needs to pass the origin is physically meaningful as a vanishing embedded length would imply a vanishing pull-out force F_{max}.

The surface specific debonding energy, or debonding fracture toughness, follows with

$$\mathcal{G}_{\text{d}} = \int_0^{l_{\text{d}}} \tau \, \mathrm{d}u, \tag{5.5}$$

$$\approx \frac{\tau_{\text{IFSS}} \cdot l_{\text{d}}}{2}, \tag{5.6}$$

for which the approximation only applies to a pull-out curve which follows the linear incline as depicted in Fig. 5.1. Since the actual shear stress τ can only be evaluated in an average sense through Eq. 5.1, within this work the evaluation of the surface specific energy follows accordingly as

$$\mathcal{G}_{\text{d}} = \frac{1}{A} \int_0^{l_{\text{d}}} F \, \mathrm{d}u, \tag{5.7}$$

$$= \frac{1}{2\pi r_{\text{f}} l_{\text{e}}} \int_0^{l_{\text{d}}} F \, \mathrm{d}u, \tag{5.8}$$

where it is assumed that the debonding energy is distributed equally along the embedded area of the fiber.

The remaining frictional surface specific energy is given with

$$\mathcal{G}_\mathrm{f} = \int_{l_\mathrm{d}}^{l_\mathrm{e}} \tau \, \mathrm{d}u. \tag{5.9}$$

As mentioned for the IFSS, a linear regression model can be established for the frictional surface specific energy. For this, the frictional energy, i.e.,

$$E_\mathrm{f} = \int_{l_\mathrm{d}}^{l_\mathrm{e}} F \, \mathrm{d}u, \tag{5.10}$$

is assumed to be consumed equally along the area over which the frictional forces are transferred to, so that

$$\mathcal{G}_\mathrm{f} = \frac{E_\mathrm{f}}{2\pi r_\mathrm{f} l_\mathrm{f}}, \tag{5.11}$$

where l_f is the difference between the embedded length l_e and the debond length l_d, i.e., $l_\mathrm{f} = l_\mathrm{e} - l_\mathrm{d}$. Hence, reformulation yields

$$E_\mathrm{f}(l_\mathrm{f}) = \underbrace{2\pi r_\mathrm{f} \mathcal{G}_\mathrm{f}}_{=n} l_\mathrm{f}, \tag{5.12}$$

where n is once more the proportionality factor. E_f needs to vanish for a vanishing l_f, so that the linear regression in Eq. 5.12 needs to pass through the origin. From a least-square fit to experimental data, the frictional surface specific energy can then be assessed through

$$\mathcal{G}_\mathrm{f} = \frac{n}{2\pi r_\mathrm{f}}. \tag{5.13}$$

5.2 Experimental investigation

5.2.1 Micro-mechanical climate chamber

All micro-mechanical tests, which include the micro-mechanical matrix creep test and the single fiber pull-out test are performed using an in-house developed tensile rig for small dimensions. The machine is depicted in Fig. 5.2.

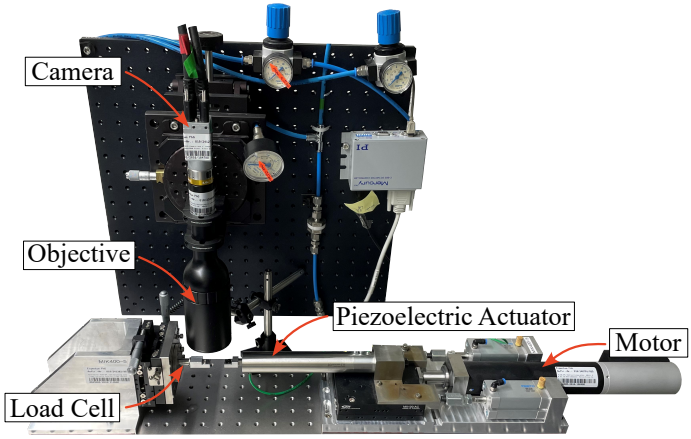

Figure 5.2: Tensile rig for micro-mechanical tests.

To evaluate the effects of climatic boundary conditions on the test results, i.e. creep compliance or IFSS, respectively, the experiments need to be climatized. No commercial climate chamber was found to be small enough to be placed between the test grippers. Moreover, it is not possible to place the whole assembly in a climate chamber, because the used electronic devices are not designed to be used in a hot and wet environment. Consequently, a micro-mechanical climate chamber needs to be developed. To avoid a costly and overly complex development process, the requirements on the climate chamber are stated as:

- simple humidifier mechanism,

- cost efficient,
- easy to reproduce.

The most simple humidifier mechanism would be of passive nature, avoiding any complicated measurement and regulation algorithm based on complex thermodynamic principles. For this, a seemingly suitable approach is found by exploiting the principle of deliquesence, which is explained in detail in Mauer and Taylor [206].

Humidity control through deliquesence

Deliquescence, as elucidated by Zografi [207], is a natural process whereby solutes diminish the equilibrium vapor pressure of water. The magnitude of this reduction in vapor pressure is contingent upon the concentration and nature of the dissolved substance. The saturation limit of a substance represents the point at which the maximum reduction in vapor pressure can be achieved. Consequently, substances that have a high solubility index are often associated with lower deliquescence humidities. It is noteworthy that an escalation in the solubility of a substance due to a rise in temperature inversely affects its deliquescent moisture, resulting in a decrease.

The deliquescence properties of salts can be harnessed to maintain a specific relative humidity within hermetically sealed units, such as desiccators. Given the finite nature of moisture replenishment from the air, a process of self-regulating hysteresis ensues. When the initial air humidity exceeds the deliquescence humidity, the ensuing condensation of moisture on the salt solution induces a reduction in relative air humidity. This continues until equilibrium with the deliquescence humidity is achieved, at which point the air humidity is in equilibrium with the saturated solution [208]. Conversely, when air humidity is lower than the deliquescence humidity, undersaturation occurs above the solution, leading to evaporation of water from the solution and a consequent increase in air humidity. This process persists until equilibrium with the deliquescence humidity is established. This

mechanism, when applied correctly, can be utilized to maintain a stable relative humidity within a container by introducing a saturated salt solution. However, this necessitates the provision of a solution replete with sufficient undissolved sediment. Fig. 5.3 provides a qualitative representation of the deliquescence

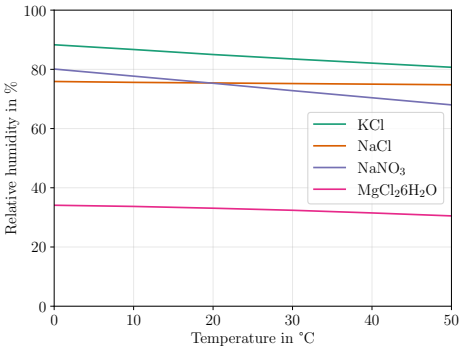

Figure 5.3: Relative humidity due to deliquesence over temperature for different salt solutions based on the data given in [209]. Graphic reused from the author's publication in Christ et al. [210].

humidity for a variety of salt solutions across a spectrum of temperatures. As previously indicated, a surge in temperature corresponds to a minor decrease in relative humidity.

Opting for a passive adjustment of relative humidity through deliquescence, as opposed to an active control system, e.g., proposed by Boulogne [211], eliminates the requirement for a complex control mechanism for air humidification. This not only significantly mitigates the development costs but also fortifies the system's resilience against extrinsic influences.

Temperature control

In contrast to the passive regulation of the humidity within the chamber, the temperature is controlled actively. For this, an Arduino Micro is utilized to regulate

the effective voltage of a 24 V power supply over four power resistors in series based on the difference between a setpoint temperature and the measured temperature, using a Sensirion SHT85 humidity/temperature sensor. The 5 V pulse-width modulation (PWM) signal from the Arduino is first used to control a transistor, which in turn controls a metal-oxide-semiconductor field-effect transistor (MOSFET) using the 24 V power supply, since the Arduino itself cannot provide the appropriate voltage to drive the MOSFET on its own. As a consequence, the control logic is inverted, so that a logic high turns off the MOSFET and vice versa. The circuit diagram is given in Fig. 5.4.

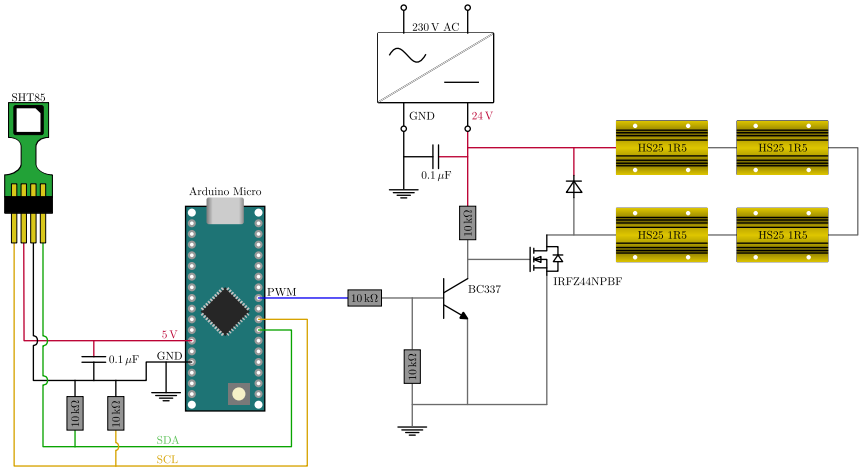

Figure 5.4: Schematic of the circuit used to control the temperature within the climate chamber based around an Arduino Micro and a Sensirion SHT85. The fan control is not included in the diagram.

The readings from the SHT85 humidity/temperature sensor are transferred to the Arduino via I^2C, in which the output PWM signal is calculated based on a proportional-integral-derivative (PID) module and both temperature and humidity values are stored and can be displayed in a live plot during an experiment. The code for the Arduino is given in Appendix F.

5.2.2 Specimens preparation and conditioning

Since the single-fiber pull-out (SFPO) specimens cannot be produced in-house due to a lack of the necessary processing equipment, they are produced at the Faserinstitut Bremen e.V. (FIBRE). To ensure consistent material properties, the same PA6 granulate and carbon fiber strands that are used in the LFT-D process are provided to the FIBRE. For the production of SFPO specimens, the FIBRE utilizes the FIMABOND machine developed by Textechno, which is a subsystem of a more complex system, called FIMATEST, which additionally allows to directly perform the SFPO experiment once the embedding of the fiber in the polymeric resin is complete and the specimen has solidified. A detailed description of the production work flow is given in Stefan et al. [212]. Since the SFPO specimens are supposed to be tested separately in a climatized environment, the experiments are not performed at the FIBRE.

Within the FIMABOND a single PA6 granulate is placed on an aluminum crucible or specimen holder, respectively, and a single carbon fiber is mounted into an air gripper above the crucible (cf. Fig. 5.5a). Following the temperature curve in Fig. 5.6, the system is heated to $80\,°C$ at $100\,K/min$, after which nitrogen gas is flushed into the containing chamber. The purpose of the nitrogen gas is to act as an inert gas which prevents oxidative effects, e.g. the degradation of the polymer surface, and also the build-up of air inclusions during solidification is minimized. Once the chamber is fully flushed with inert gas, the temperature is further increased to $260\,°C$, which is above the crystallization and melting temperature of PA6 at around $180\,°C$ and $215\,°C$, respectively. As a result, the granulate begins to liquify, as can be seen in Fig. 5.5b. The temperature of $260\,°C$ is kept constant for a duration of $5\,min$ to fully liquify the PA6. Due to the surface tension of the liquid PA6, a stable dome shape forms on the top. The carbon fiber is then lowered under eye control until the lower end of the fiber is in contact with the PA6 surface, after which it is further displaced for $100\,µm$ at a displacement rate of $500\,µm/min$. In a preliminary study, the optimal embedded length of $100\,µm$ was determined iteratively through pull-out tests, as a fiber whose embedded length exceeds the critical fiber length would lead to fiber breakage instead of pull-out,

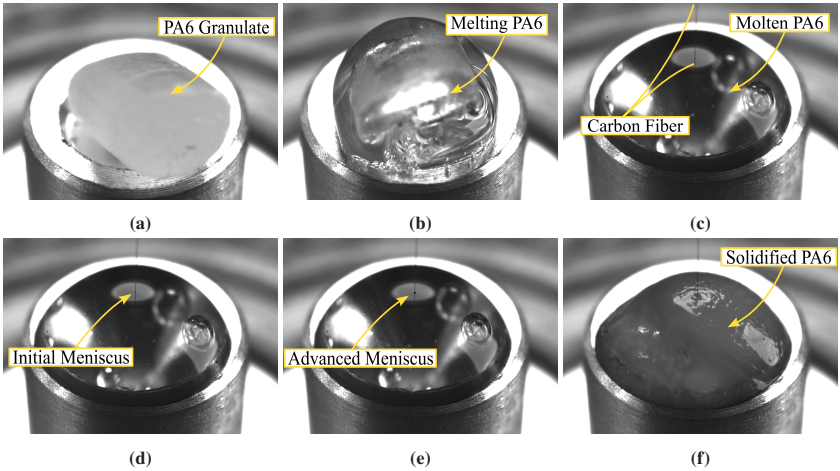

Figure 5.5: Production steps for the pull-out specimens. (**a**) shows the solid PA6 granulate, (**b**) shows the start of the melting of the granulate before inserting the fiber. (**c**) shows the specimen right after inserting the fiber with fully melted PA6, (**d**) shows a later stage with the first formation of a meniscus at the fiber entry point, while (**d**) shows an advanced formation of a meniscus. The fully solidified single fiber pull-out specimen is given in (**f**) with visible deviations of the hemispherical shape due to crystallinity within PA6. The according temperature over time is given in Fig. 5.6. Graphic reused from the author's publication in Christ et al. [210].

while a very short embedded length would lead to fewer data points during the test. With the given embedding length and an average fiber diameter of 7 µm, an average embedded surface area of about 2200 μm^2 is realized. The embedded fiber is depicted in Fig. 5.5c. From 260 °C to 180 °C the specimen is cooled down with a prescribed cooling rate of 10 K/min, at which a clear formation of a meniscus is visible in Fig. 5.5d and Fig. 5.5e. Due to the inherent property of forming crystalline sections within the PA6, the smooth hemispherical surface of the molten state transitions to an irregular, non-convex solidified surface (cf. Fig. 5.5f). As a result, some samples solidify with a pronounced deviating fiber angle to the symmetry axis of the sample holder, as shown in Fig. 5.7.

Once the SFPO specimens were manufactured, they were stored in a sealed container for several weeks to be conditioned in their respective climate. Therefore, the specimens were split into two groups, one for the dry conditioning and one for

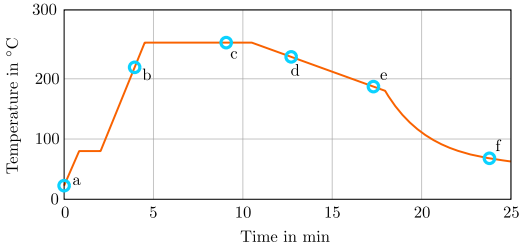

Figure 5.6: Temperature over time during the manufacturing of the pull-out specimens. A representative state of a specimen at the indicated circles is depicted in Fig. 5.5. Graphic reused from the author's publication in Christ et al. [210].

the wet conditioning. The container for the dry conditioning was filled with silica gel, which absorbs the humidity and established a dry climate with a humidity level between $\mathcal{H} = 0\,\%$ and $\mathcal{H} = 10\,\%$. The container for the wet conditioning was filled with a NaCl solution, which has a deliquesence humidity of $\mathcal{H} = 75\,\%$. During the conditioning, the temperature was not controlled.

5.2.3 Test procedure

The test was performed in an in-house developed micro-mechanical tensile machine, which was shown in Fig. 5.2. In the used set-up, the machine is equipped with a XFTC-300-2N load cell from disynet GmbH, Brüggen, Germany, with a load capacity of $\pm 2\,\mathrm{N}$ on the fixed side to the left. A special gripper was designed and is connected to the load cell, which allows for a quick (de)-mounting of the SFPO specimen. It consists of a groove into which the circular base of the aluminum crucible of the SFPO sample can be slid in and out. The movable or displacement-controlled side of the test rig to the right consists of a piezo actuator and an electric stepper motor in series. For the SFPO test, the piezo actuator was kept still, while the displacement rate was prescribed on the electric motor. The set-up allows to adjust the specimen gripper horizontally and vertically, which is necessary to prevent a double off-angled pull-out test. A camera with a magnification lens of x10 is placed above the specimen to check for the alignment of the fiber and to observe the pull-out behavior during the experiment. The specifically

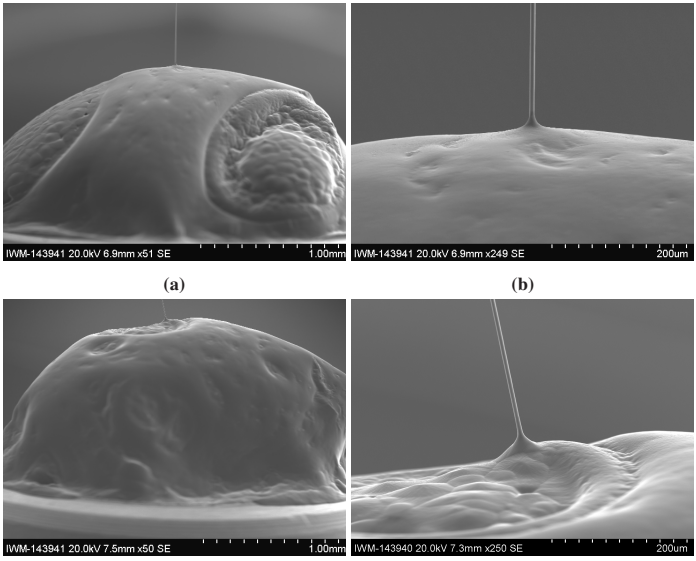

Figure 5.7: SEM image of pull-out specimens with a straight embedded fiber (**a** and **b**) and a deviated embedded fiber due to ireggular crystallization (**c** and **d**). Graphic reused from the author's publication in Christ et al. [210].

designed climate chamber (cf. Section 5.2.1) was placed between the load cell and the piezo actuator with extension rods reaching into the chamber. The setup is given in Fig. 5.8.

Great care had to be taken when handling the SFPO sample to avoid damaging the interface or free fiber end prior to testing. The sample was carefully inserted into the slit of the sample holder with tweezers and slowly lowered to the final position. A flat metal holder attached to the piezo actuator was moved towards the SFPO sample so that there was still a distance of about 1.2 mm between the polymer droplet and the metal holder. The specimen was adjusted vertically, so that the fiber exit point out of the matrix was at the same height as the metal holder on the other side, which could be realized by finding an in-focus plane containing both sides within the shallow depth of field of the camera system. This is equivalent to setting $\beta_{\text{out}} = 0$ in Fig. 5.9. This prevents the fiber from being pulled out up- or

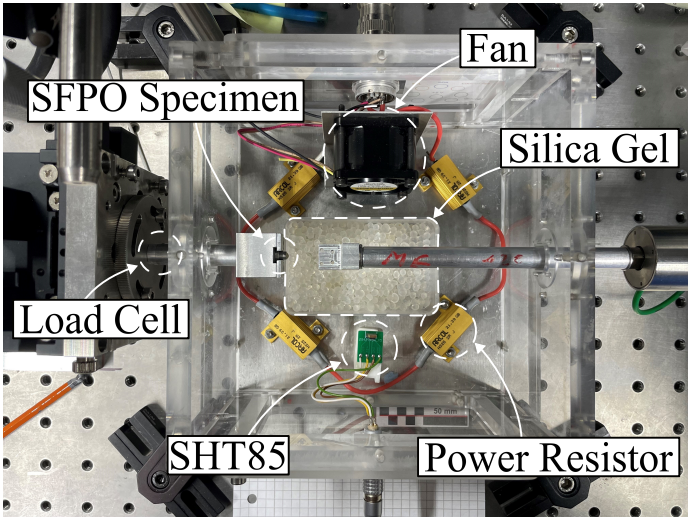

Figure 5.8: Installed microscale climate chamber from above with labeled components. The silica gel was used for the dry testing. For the wet testing, it was replaced with a sodium chloride solution. Graphic reused from the author's publication in Christ et al. [210].

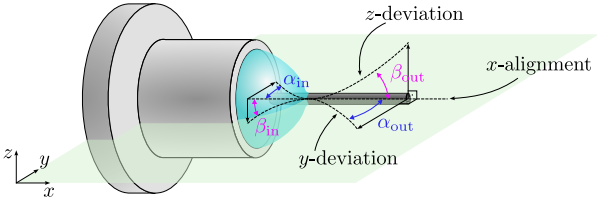

Figure 5.9: Visible is a schematic single fiber pull-out specimen with the fiber being aligned within the x-direction, which would results in a straight pull-out. Possible fiber deviations include non-zero angles of the outer angles α_{out} and β_{out} and the angles inside the embedding α_{in} and β_{in}. The green plane indicates the horizontal pull-out plane.

downwards in relation to the horizontal pull-out plane. However, the embedded section of the fiber might still be angled within the horizontal pull-out plane, i.e., $\alpha_{in} \neq 0$ and/or $\beta_{in} \neq 0$, since this cannot be adjusted once the polymer has completed the crystallization. Additionally, a possible angle within the horizontal plane cannot be ruled out, i.e., $\alpha_{out} \neq 0$, as the crystallization of the PA6 can cause the fiber to deviate from the x-direction (cf. Fig. 5.7).

The fiber is then glued to the metal holder using superglue, which is indicated in Fig. 5.10. After applying the glue, the lid of the climate chamber is closed and the

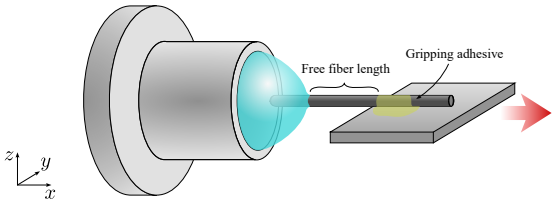

Figure 5.10: Schematic of the gripping mechanism through adhesive glue. The elements shown are not true to scale. Graphic reused from the author's publication in Christ et al. [210].

climate conditions are changed to the desired values. The curing of the superglue is observed through the camera system, which takes up to 20 min depending on the surrounding climate. Due to the deformation of the glue during curing, the fiber can be pulled slightly, so that a manual adjustment of the position of the metal holder might be necessary to keep the measured force value at zero.

Once the glue is cured and the climate is stabilized, the SFPO test is started. A displacement rate of 1 µm/s is applied to the the metal holder to pull out the fiber. During the test, images are taken with a frequency of 1/s.

5.2.4 SEM investigation of the pulled out fiber

To assess the actual embedded fiber length instead of relying on the reported embedded length from the manufacturer, the pulled out fiber was investigated using a S-3400n scanning electron microscope (SEM) from Hitachi Ltd. Corporation, Chiyoda, Japan. This allows to measure the embedded length l_e from the fiber end to the remaining meniscus on the pulled out fiber and the actual fiber radius r_f, as it is indicated in Fig. 5.11. Furthermore, the pulled out fiber is investigated qualitatively to see if the debonding occured along the fiber-matrix interface or within the matrix material itself (based on polymer residues sticking to the fiber surface) and the remaining fiber angle due to crystallization is measured.

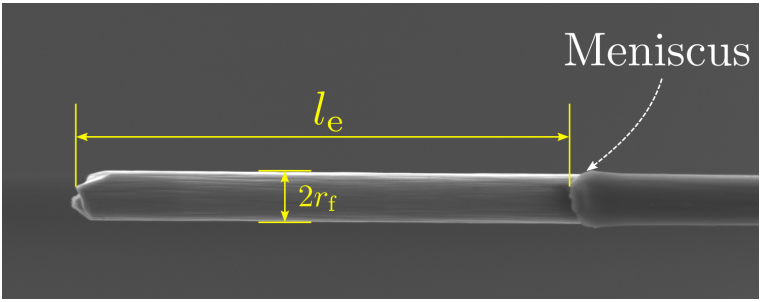

Figure 5.11: Measurement of the embedded fiber length l_e and the fiber radius r_f after pull-out using a SEM. Graphic reused from the author's publication in Christ et al. [210].

For the SEM investigations an acceleration voltage of 10 kV and an emission current of 76000 nA was chosen, while the working distance was kept around 13 mm. When the acceleration voltage was set too high, thermal effects within the adhesive keeping the fiber in place was observed which lead to thermal strains and a consequent movement of the fiber within the SEM. The pulled-out fiber was not sputtered before placing it into the SEM. A SEM image of each specimen was recorded for the full embedded length at a magnification of x1000 and a detailed image was taken of the meniscus of the fiber at a magnification of x2000.

5.2.5 Results

The pull-out curves from the experiments under various conditioning states are presented in Fig. 5.12. Fig. 5.12a illustrates the relationship between force and displacement, while Fig. 5.12b shows the averaged shear stress (force divided by embedded area of the fiber) as a function of displacement. The minor discrepancy in the curves between the conditioning states when using stress values rather than force values signifies the importance of individually measuring the embedded fiber surface area after each test. To process the data without adding substantial smoothing, commonly associated with standard averaging methods, the arc-length based averaging method as described in Hartlen and Cronin [213] was used. This method also offers a confidence envelope for the data. Its key benefit is the

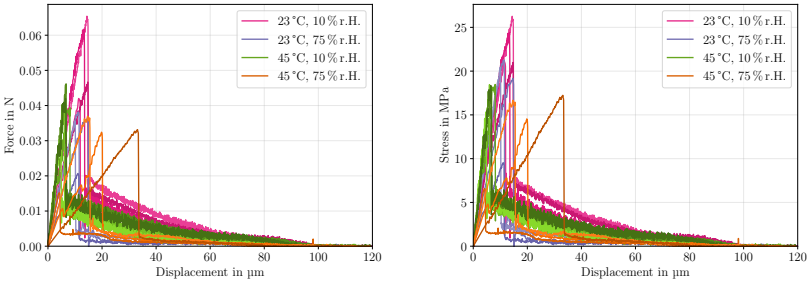

Figure 5.12: Experimental pull-out curves with (**a**) depicting the force displacement curve, while (**b**) shows the stress displacement curve averaging the measured forces with the individual embedded length. Graphics reused from the author's publication in Christ et al. [210].

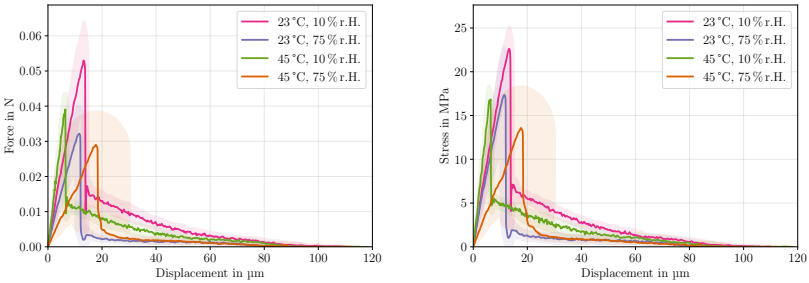

Figure 5.13: Force displacement and stress displacement curve for the pull-out experiment for different conditioning states after filtering the data utilizing the arc-length averaging tool in Hartlen and Cronin [213]. Graphics reused from the author's publication in Christ et al. [210].

preservation of local features, for instance, the abrupt force drop within the averaged curves. The curves derived from this process are depicted in Fig. 5.13.

The pull-out curves noticeably differ across the various conditioning states, which suggests sensitivity to both thermal and hygroscopic effects. The substantial differences observed in the initial gradient of the stress-displacement data between the conditioning states needs to be highlighted. It's important to reiterate that this gradient is intentionally not referred to as stiffness, as drawing inferences about

the fiber-matrix properties can be complex. While the gradients for the two colder conditioning states are almost identical, the warm and dry conditioning exhibits a steeper gradient, and the warm and moist conditioning a significantly less steep one.

The measurements of pull-out force over the embedded length for the different conditioning states and their statistical moments are presented in Fig. 5.14. Gen-

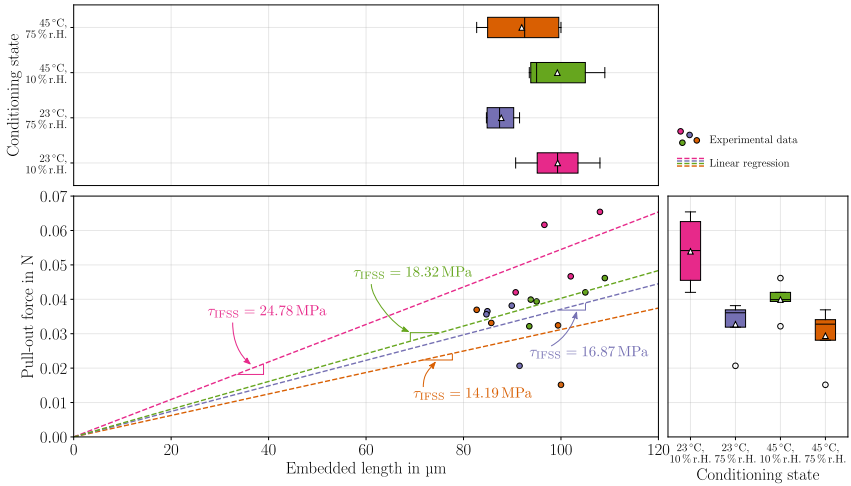

Figure 5.14: Measured pull-out force over embedded length for different conditioning states with linear regression (with forced zero interception) and statistical evaluation of the embedded fiber length (top) and the pull-out force scatter (right). The slope of the regression is proportional to the IFSS. The indication color for each conditioning state can be extracted from the box plots and is in alignment with Fig. 5.13b. Graphic reused from the author's publication in Christ et al. [210].

erally, a subtle differences in the distribution of the embedded fiber length can be observed across the various conditioning states, with lengths primarily within the $80 - 110\,\mu m$ range. The dry and cold conditioning state exhibited the highest mean and median pull-out forces, around $0.054\,N$, as depicted in the right box plot in Fig. 5.14. This is trailed by the dry and warm conditioning state with a mean and median pull-out force of $0.04\,N$, and the cold and wet conditioning with

a mean pull-out force of 0.033 N and median pull-out force of 0.036 N. The warm and wet conditioning state registered the lowest pull-out force, with a mean value of 0.029 N and median value of 0.033 N.

Based on the assumptions established in the methodology, the IFSS for each conditioning state is proportional to the slope of the linear regression in the given figure. Hence, the highest IFSS was computed to be 24.78 MPa for the dry and cold conditioning, succeeded by warm and dry at 18.32 MPa, and cold and wet at 16.87 MPa. The warm and wet conditioning state yielded the lowest IFSS, computed to be 14.19 MPa.

Contrarily, when the IFSS is directly assessed as the average measured pull-out force over the embedded area, rather than being interpreted as the slope of the linear regression, a slightly different perspective emerges. These measurements are presented in Fig. 5.15. The highest average IFSS was recorded for the cold

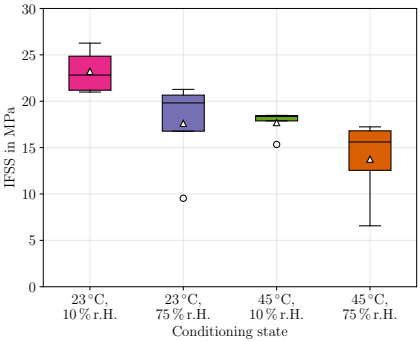

Figure 5.15: Statistical distribution of directly evaluated IFSS for different conditioning states. The indication colors are in alignment with Fig. 5.13b. Graphic reused from the author's publication in Christ et al. [210].

and dry conditioning at approximately 23.2 MPa. This was followed by nearly identical average IFSSs for single elevated environmental factors, i.e., humidity or temperature, which had a mean shear strength of about 17.7 MPa for elevated temperature and 17.6 MPa for elevated humidity. This represents a decrease in IFSS of roughly 24 %. When both climatic conditions are raised concurrently,

a relative drop of 41 % is measured in relation to the IFSS for the dry and cold conditioning, falling just below 13.8 MPa.
Given that the single fiber pull-out test is susceptible to experimental scatter and outliers, which can partially be attributed to angled fibers within the specimen, the median IFSS is a comparatively more reliable measure than the mean IFSS. For the dry and cold conditioning, the median IFSS is 22.8 MPa, which is nearly identical to its mean IFSS, a trend that also holds for the dry and warm conditioning at around 18.4 MPa. The wet conditioning states exhibit a larger discrepancy between the mean and median IFSS. Both cases display a higher median IFSS compared to the mean IFSS, rising to 19.8 MPa and 15.6 MPa for cold and warm temperatures, respectively.

The statistical moments for the debonding length and the debonding energy release rate $\mathcal{G}_\mathrm{d}$ are depicted in Fig. 5.16. Except for the warm and humid conditioning, the

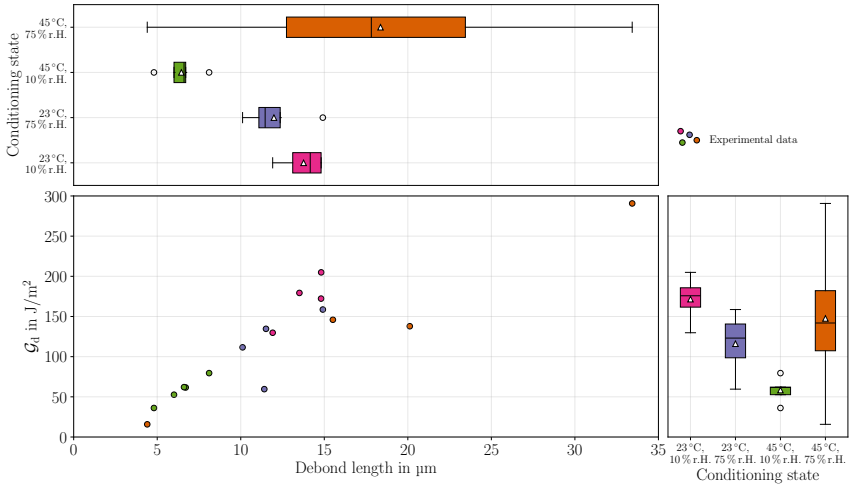

Figure 5.16: Calculated debond energy release rate over debond length for different conditioning states and statistical evaluation of the debond length (top) and the debond energy release rate (right). The indication colors are in alignment with Fig. 5.13b. Graphic reused from the author's publication in Christ et al. [210].

debond length d_debond does not exhibit significant scatter across each conditioning

state. The median debond lengths are roughly $14\,\mu m$ for the dry and cold state, $11.5\,\mu m$ for elevated humidity only, and $6.5\,\mu m$ for elevated temperature only, which are reductions of $18\,\%$ and $54\,\%$, respectively. However, the longest debond length of $18\,\mu m$, with a broad scatter band, was recorded under conditions of simultaneously elevated temperature and humidity, which is an increase of over $28\,\%$ compared to the dry and cold conditioning.
In terms of debond energy release rate $\mathcal{G}_d$, the increase of a single environmental factor results in a decrease from approximately $175.8\,J/m^2$ to $123.1\,J/m^2$ and $61.7\,J/m^2$ for elevated humidity or temperature, respectively, which translates to a reduction of $30\,\%$ and $65\,\%$. Yet, instead of a further decrease, a simultaneous increase in both factors raises the debond energy release rate back to $141.9\,J/m^2$, which represents a reduction to the reference state of merely $20\,\%$.

The influences of humidity and temperature on frictional forces and their energy distributions are depicted in Fig. 5.17, where a direct effect is visible. As a reminder, the frictional length is just the difference between the embedded length and the debond length. Given the large scatter of the debond length for the wet and warm conditioning in Fig. 5.16, the frictional length of this conditioning state shows the greatest scatter, while the other conditioning states have similar values and scatter bands. The energetic portion caused by the frictional stresses show a clear distinction between dry and wet conditioning states, regardless of the ambient temperature. When the humidity is kept low, frictional stresses after debonding are significantly higher compared to a wet environment. The highest median frictional energy was measured for the dry and cold conditioning with about $0.426\,\mu J$, followed by the dry and warm conditioning with $0.313\,\mu J$. Significantly lower are the measured energies for the wet conditionings, with roughly $0.1\,\mu J$ for cold and warm temperatures, respectively. The area specific work of friction again correlates with the slope of the regression. Once more the highest values were measured for the dry conditionings with $223\,J/m^2$ and $157\,J/m^2$ for cold and warm temperatures, respectively. The wet conditionings showed an almost equal specific work of friction with $66\,J/m^2$ and $61\,J/m^2$ for warm and cold temperatures, respectively. The median quantities for the different conditioning states are given in Tab. 5.1.

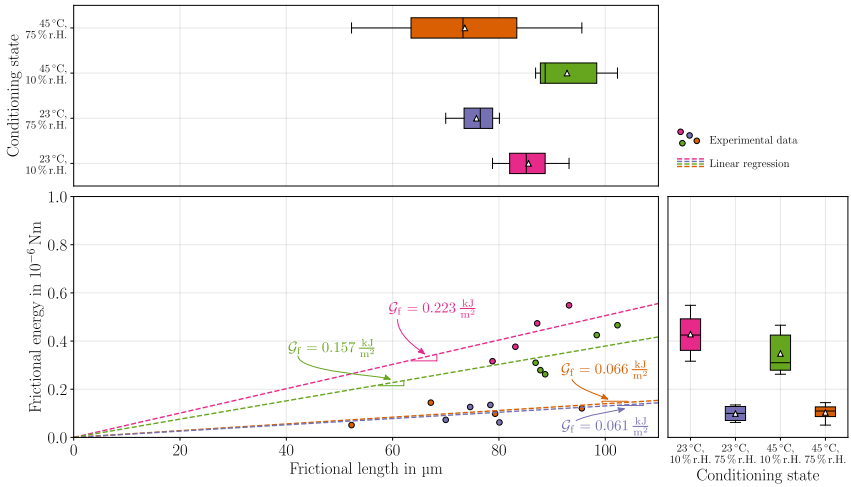

Figure 5.17: Measured frictional energy over frictional length for different conditioning states with linear regression (with forced zero interception) and statistical evaluation of the frictional length (top) and the frictional energy scatter (right). The slope of the regression is proportional to the frictional energy rate. The indication color for each conditioning state can be extracted from the box plots and is in alignment with Fig. 5.13b. Graphic reused from the author's publication in Christ et al. [210].

After successful pull-out each specimen was investigated in the mentioned SEM analysis to measure the embedded length, the fiber radius and qualitatively assess the pulled-out fiber. For each conditioning state a representative fiber is given in Fig. 5.18. It can be seen that for all conditioning states no matrix residue is found on the fiber, i.e., a blank fiber. The embedded lengths can easily be measured by the characteristic formation of a meniscus at the fiber entry point, at which visible matrix fracture occurs after fiber pull out. While the blank fiber surfaces reveal no differences between the conditioning states, a slight deviation in the fracture pattern of the meniscus is visible. For the dried cases, the meniscus seems to fracture more rigidly with a slightly increased fracture surface area, while the wet cases reveal a smoother fracture zone of the meniscus.

Table 5.1: Median interface quantities for different conditioning states.

Label	Conditioning	l_e in µm	l_d in µm	l_f in µm	IFSS in MPa	$\mathcal{G}_\mathrm{d}$ in J/m^2	$\mathcal{G}_\mathrm{f}$ in J/m^2
Cold, dry	23 °C, 10 % r.H.	99.3	14.2	85.1	22.82	175.8	216.6
Cold, wet	23 °C, 75 % r.H.	87.4	11.5	76.5	19.82	123.1	64.3
Warm, dry	45 °C, 10 % r.H.	95.0	6.6	88.7	18.35	61.7	159.1
Warm, wet	45 °C, 75 % r.H.	92.6	17.8	73.2	15.61	141.9	55.0

5.3 Numerical investigation

There is an abundant literature on fitting numerical parameters to experimental results in the case of pull-out tests, e.g., in Tsai et al. [214] and Hoppe [215]. A general question of interest is how different stress components are distributed along the interface. This has been investigated for elastic assumptions in Marotzke [112, 216] and Quek [217]. Andrianov et al. [218] investigated a linear viscoelastic response in the matrix behavior and reveal a negligible time-dependence of the stress distribution along the interface. These investigation are often accompanied with the study of residual thermal stresses, e.g., in Jia et al. [219], because the mismatch of thermal expansion coefficients between fiber and matrix lead to an initial stress field, which may contribute to onset of debonding. A yet unanswered question is to what extend the nonlinearity of the viscoelastic matrix response contributes to the distribution of the stress components along the interface. The literature concerned with this question is sparse, but related research in Holmes et al. [220] showed an increase of the expected critical fiber length through nonlinear effects by $25\,\%$ in contrast to elastic assumptions, while a linear viscoelastic model predicted an increase of only $3.6\,\%$. Similarly drastic was the reduction of the IFSS when a nonlinear viscoelastic response was assumed compared to only linear viscoelasticity.

To address this open question, this section is concerned with investigating the predicted stress field along the fiber-matrix interface during the single-fiber pull out test before failure. Therefore, the above derived and experimentally calibrated

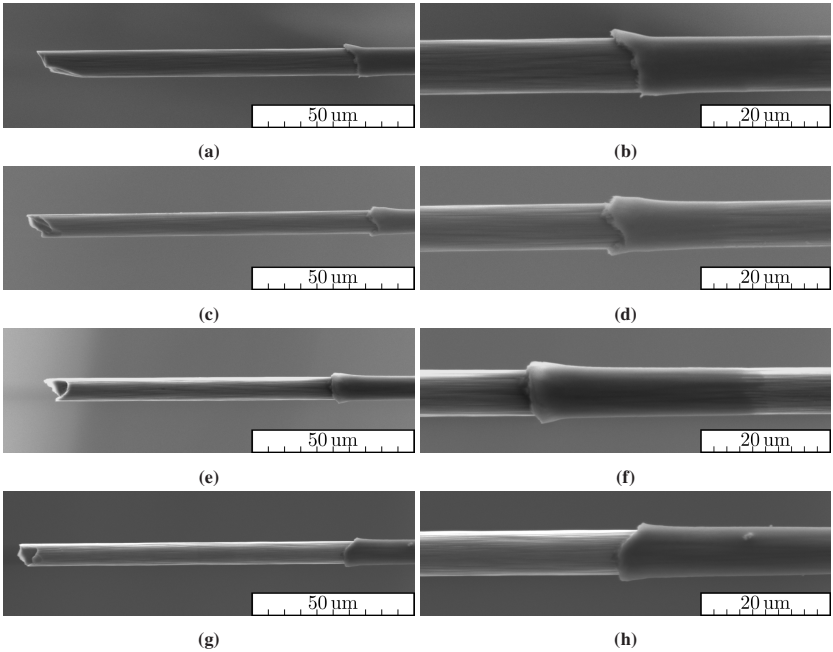

Figure 5.18: SEM image of pulled-out specimens for different conditioning states: dry and cold (**a** and **b**), dry and warm (**c** and **d**), wet and cold (**e** and **f**) and wet and warm (**g** and **h**). All conditionings states were pulled out with a blank fiber with slight differences in the deformation of the meniscus. Graphic reused from the author's publication in Christ et al. [210].

nonlinear viscoelastic model after Schapery is utilized. Thereby, the effects of nonlinear attributes can compared to only linear assumptions and moreover different environmental boundary conditions can be compared.

5.3.1 FEM model

The finite element method (FEM) model utilizes the symmetry around the fiber axis. Hence, all possible angle deviations indicated in Fig. 5.9 are assumed to be zero, so that the fiber is perfectly perpendicular to the embedding matrix. The fiber is modeled with an embedded length of $100\,\mu m$ and a adjustable free fiber length.

The fiber radius is $3.5\,\mu m$. The matrix extends in radial and axial direction to 30 times the fiber radius, i.e., $105\,\mu m$, which exceeds the minimum recommended factor of 20 in reference to Budiman et al. [221]. The mesh consists of 2675 elements with linear shape functions. Towards the material singularities, i.e., the fiber entry point and the fiber end within the matrix, the element size decreases to a minimum element length of $0.5\,\mu m$ to better capture the stress/strain gradients. The model is visualized in Fig. 5.19.

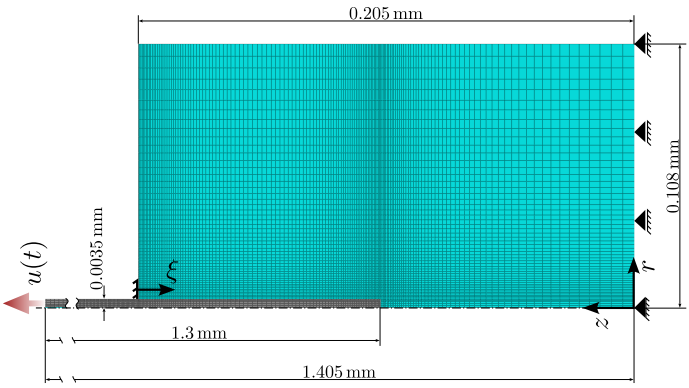

Figure 5.19: Axisymmetric FE-mesh for the single fiber pull-out simulation with dimensions and boundary conditions. The relevant polar coordinates are given with r and z, while the normalized coordinate along the interface is ξ.

There are two FE studies performed for each specimen conditioning form the previous section. The first simulation is concerned with the residual stresses along the interface at different time steps during a hygrothermal history assuming perfect bonding. The second simulation is used to determine the effective interface parameters for the given hygrothermal history in comparison to the experimental results.

For all simulations, an evolving temperature field is prescribed to consider thermal residual stresses in the specimen. The stress free temperature is considered to be the crystallization temperature of $T_c = 180\,°C$. This temperature is homogeneously reduced for fiber and matrix to an ambient temperature of $T = 23\,°C$

over a period of $\Delta t_1 = 10^3$ s, which should resemble the experimental cooling in Fig. 5.6. The residual stresses are caused by a mismatch in the coefficient of thermal/moisture expansion between fiber and matrix. This is a simplified model in which no heat flux/transfer is considered, so that the temperature gradient is zero everywhere. In a second step, the temperature is held constant for $\Delta t_2 = 10^6$ s to allow the pull out specimen to relax, since the real specimens were kept at ambient temperature for a couple of days before testing. In a third step, the temperature is then increased to testing temperature. Since the cold conditioning is tested at $T = 23\,°\text{C}$, this only applies for the warm conditioning states, where the temperature is elevated to $T = 45\,°\text{C}$ over a period of $\Delta t_3 = 1.2 \cdot 10^3$ s.
For the isotropic polymer, the thermal expansion coefficient is assumed to be $8.5 \cdot 10^{-5}$ /°C, based on Raghavalu Thirumalai et al. [222]. The carbon fiber is assumed to have transversely isotropic material symmetry. Since the data sheet for the investigated carbon fiber does not provide all necessary coefficients, literature data is used instead. The closest literature in terms of longitudinal Young's modulus and strength properties in reference to the data sheet is found in Blackketter et al. [223] for a Hercules AS4 PAN-based carbon fiber and in Miyagawa et al. [224] for a Torray T300 PAN-based carbon fiber. Since only the former provides a full set of coefficients, including the transverse thermal expansion coefficient, these coefficients are adapted in the simulation. Therefore, the elastic coefficients are $E_\text{L} = 235\,\text{GPa}$, $E_\text{T} = 14\,\text{GPa}$, $G_\text{LT} = 28\,\text{GPa}$, $G_\text{TT} = 5.5\,\text{GPa}$ and $\nu_\text{LT} = 0.2$. The longitudinal thermal expansion coefficient is given with $-0.36 \cdot 10^{-6}$ /°C, while the transverse thermal expansion coefficient is $18.0 \cdot 10^{-6}$ /°C.
Instead of modeling the expansion caused by the water absorption/desorption directly, the volumetric change is instead considered through a superimposed temperature difference prescribed during the relaxation step after initial cooling. For this, a CME of $3.3 \cdot 10^{-3}$ /m.% is assumed based on Raghavalu Thirumalai et al., who calculated the value based on the experimental data in Monson et al. [225]. The reference humidity at which the humidity induced strains are zero is considered to be at standard climate, i.e., $\mathcal{H} = 50\,\%$. Since the carbon fiber does not inhibit a humidity dependence, only the corresponding temperature of the matrix

material is altered during the relaxation step to account for the swelling/contraction caused by added/removed humidity. To model the humidity strain as thermal strains, their linear expressions with their individual expansion coefficients are set equal

$$\varepsilon_T = \Delta T \cdot \mathrm{CTE} \stackrel{!}{=} \Delta \mathcal{W}_{\mathrm{H_2O}} \cdot \mathrm{CME} = \varepsilon_{\mathcal{H}}, \tag{5.14}$$

with ε_T and $\varepsilon_{\mathcal{H}}$ being thermal and moisture induced strains and CTE and CME are the coefficients of thermal or moisture expansion, respectively. Hence, the necessary temperature change to model moisture induced swelling is

$$\Delta T = \Delta \mathcal{W}_{\mathrm{H_2O}} \frac{\mathrm{CME}}{\mathrm{CTE}}. \tag{5.15}$$

According to the model in Eq. 2.6 for a crystallinity of $X = 0.35$, the change in mass percent between the humid and standard climate is $\Delta \mathcal{W}_{\mathrm{H_2O}} = \mathcal{W}_{\mathrm{H_2O}}(\mathcal{H} = 75\,\%) - \mathcal{W}_{\mathrm{H_2O}}(\mathcal{H} = 50\,\%) = 2.29\,\mathrm{m.\%}$. Hence, the volumetric expansion can be modeled in alignment with Eq. 5.15 with a compensating temperature of $\Delta T = 2.29\,\mathrm{m.\%} \cdot 3.3/8.5 \cdot 10^2\,\mathrm{°C/m.\%} \approx 89\,\mathrm{°C}$. Accordingly, the change in water content for the dry conditioning is $\Delta \mathcal{W}_{\mathrm{H_2O}} = \mathcal{W}_{\mathrm{H_2O}}(\mathcal{H} = 10\,\%) - \mathcal{W}_{\mathrm{H_2O}}(\mathcal{H} = 50\,\%) = -2.17\,\mathrm{m.\%}$, which translates to a compensating temperature difference of $\Delta T = -2.17\,\mathrm{m.\%} \cdot 3.3/8.5 \cdot 10^2\,\mathrm{°C/m.\%} \approx -84\,\mathrm{°C}$. The simulated temperature profiles are illustrated in Fig. 5.20.

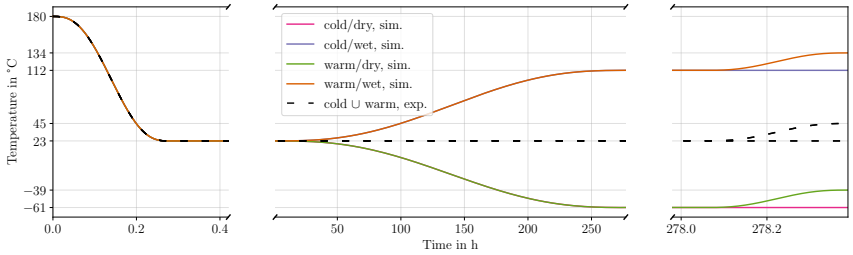

Figure 5.20: Simulated temperature profile to account for humidity induced swelling. The colored profiles apply to the matrix material, while the black and dashed profiles are the true temperatures during the experiment and are applied to the fiber material.

The assumptions made for the simulations are summarized as follows:

- temperature fields are applied homogeneously and thermal conduction is neglected,
- the swelling caused by moisture absorption is modeled through an additional temperature difference,
- the reference humidity, for which $\varepsilon_{\mathcal{H}} = 0$, is considered to be at $\mathcal{H} = 50\,\%$,
- the viscoelastic parameters and nonlinear parameter function coefficients remain constant throughout the simulation for each conditioning case, hence they are assumed to be independent of current temperature or humidity,
- CME and CTE are assumed to not depend on environmental factors and are identical for each conditioning case,
- fiber and matrix are perfectly bonded and no initiation of damage is considered.

To compare the individual results, the radial and shear stresses along the interface are visualized at different points in time. The first one is after the initial cool down at $t_0 = 0.27\,\mathrm{h}$. The second one is after relaxation at $t_1 = 278\,\mathrm{h}$, and the last state is just before pull-out at $t_2 = 278.38\,\mathrm{h}$. All simulations are repeated with the linear viscoelastic model, i.e., $g_0 = g_1 g_2 = a_\sigma = 1$, to evaluate to what extent the nonlinearities contribute to the residual stresses.

In a second simulation, the last assumption is altered to an imperfect interface using cohesive surfaces. The hygrothermal history is repeated, followed by a prescribed displacement rate at the end of the free fiber length of $1\,\mu\mathrm{m/s}$. The cohesive parameters are fitted to the average experimental result of each conditioning state, with the assumption that the interface properties in normal and shear direction are identical. The calibration process is structured as follows: In a first step, the free fiber length is varied iteratively until the initial slope of the force-displacement curves between experiment and simulation match. The damage initiation parameter t_0 is then varied until the damage onset points match.

Since the force signal generally increases linearly until the interface suddenly fails, the debonding fracture toughness $\mathcal{G}_\mathrm{d}$ is simultaneously adjusted to be proportional to the area under the force-displacement curve. A larger value would lead to progressive failure, which has never been observed. Finally, the friction coefficient is manually adjusted to minimize the error between simulation and experiment. Since no measurements of the coefficient of friction were performed for the different conditioning states, it was assumed that the coefficient of friction remains constant for different environmental conditions. Once a set of cohesion parameters and a free fiber length are found, the simulation is repeated with the linear viscoelastic model to evaluate the differences.

5.3.2 Results

The results for the radial and shear residual stresses along the interface are given in Fig. 5.21. The left column shows the radial stresses σ_{rr}, while the right column shows the shear stresses σ_{rz}. The first row is after the initial cooling to room temperature. The second row shows the stress state after relaxation with conditioned humidity level. The last row shows the final stress state, after the final climate is established. The dashed curves are the results of the linear simulations.

Besides the predominantly compressive stress states along the interface after cooling, towards the fiber ends the radial stress is tensile, which is in alignment with FEM results in Marotzke [216] and with the analytical, linear-elastic result in Quek [217]. The stress state is almost symmetric with respect to the center of the embedded length, with a slight shift towards the fiber end. The linear results are cup shaped, for which the stress nearly stays constant over more than half the embedded length along the center. The nonlinear results have a pronounced minimum radial stress around the center of the embedded length, with the exception of the warm/wet conditioning, which is also cup shaped. Around the embedded center, the lowest stress is found for the cold/dry conditioning at $\sigma_{rr} = -19.8\,\mathrm{MPa}$, followed by the warm/dry conditioning with $\sigma_{rr} = -15.0\,\mathrm{MPa}$, the cold/wet conditioning with $\sigma_{rr} = -11.9\,\mathrm{MPa}$ and the highest stress is given for

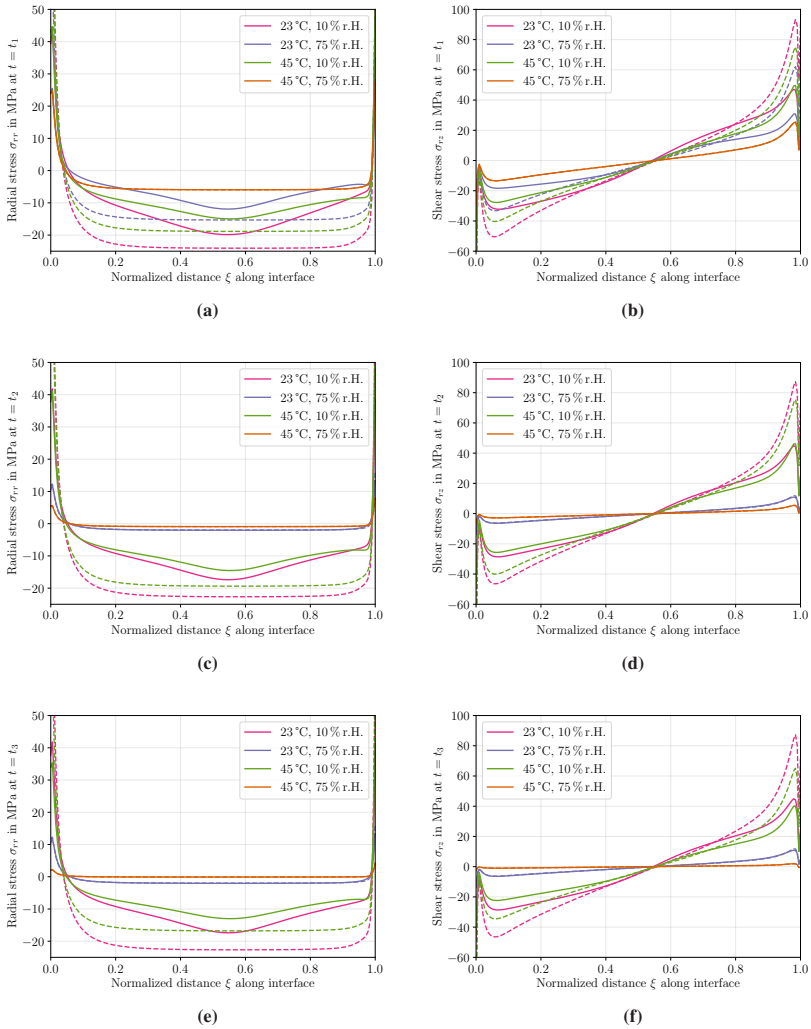

Figure 5.21: Radial (left) and shear (right) stress distribution along interface, where $\xi = 0$ for the fiber entry point into the matrix and $\xi = 1$ at the fiber end for different time points during the hygrothermal history for different conditioning states. The first row is after the initial cooling, the second row after relaxation and the third row after the final climate is established. The solid lines are the results for the nonlinear viscoelastic matrix model, while the dashed lines are the results for disabled nonlinearities, i.e., $g_0 = g_1 g_2 = a_\sigma = 1$.

the warm/wet conditioning with $\sigma_{rr} = -5.9\,\text{MPa}$. In general, a pronounced deviation is visible between the linear and nonlinear viscoelastic results, with the linear results being more extreme. Only the warm/wet conditioning shows identical curves for linear and nonlinear model assumptions. Near the fiber entry point around $\xi \approx 0.005$, the highest tensile stress states are found for all conditioning states. For both wet conditioning states, this stress is $\sigma_{rr} \approx 25\,\text{MPa}$, and for both dry cases it is $\sigma_{rr} \approx 45\,\text{MPa}$. The linear cases exceed these levels (with the exception of the equal warm/wet conditioning), reaching values of $\sigma_{rr} \approx 87\,\text{MPa}$ for the cold/dry conditioning. Slightly lower levels are found at the fiber end around $\xi \approx 1$.

After relaxation, all stress magnitudes have decreased. The nonlinear and linear results for the wet conditioning states are both indistinguishable and close to a stress free state with slight compressive stresses throughout the central part of the interface. Here, the cold conditioning is approximately $-2.0\,\text{MPa}$, while the warm conditioning is just higher than $-1.0\,\text{MPa}$. Before $\xi = 0.06$, the stresses are tensile, with the cold/wet conditioning reaching values short of $12.0\,\text{MPa}$ and the warm/wet conditioning just above $5.0\,\text{MPa}$, which is similar in magnitude at the opposite side. Still a strong deviation between the nonlinear and liner model is visible for the dry conditioning states with generally unaltered curve shapes. The lowest compressive stresses are reduced to $\sigma_{rr} = -17.4\,\text{MPa}$ and $\sigma_{rr} = -14.5\,\text{MPa}$ for the cold/dry and warm/dry conditioning state, respectively. Towards the fiber entry point, both dry states have a tensile state of $\sigma_{rr} \approx 41\,\text{MPa}$, which again is almost mirrored at the other side of the embedded length.

Since the temperature remains unaltered for the cold conditioning states between t_2 and t_3, no variations are evident between the results. For the warm conditioning states, the stresses have relaxed further. Therefore, the compressive stresses for the warm/dry conditioning are reduced to $\sigma_{rr} = -13.0\,\text{MPa}$, while the radial stresses for the warm/wet conditioning along the middle part of the embedded length almost vanish with $\sigma_{rr} = -0.1\,\text{MPa}$. Around the fiber entry point, the warm/dry conditioning has a maximum tensile stress of $\sigma_{rr} \approx 35\,\text{MPa}$, while the tensile stress for the warm/wet conditioning is $\sigma_{rr} \approx 2\,\text{MPa}$.

A different distribution shape arises for the shear stresses σ_{rz} along the interface, visualized in the right column of Fig. 5.21. The general shape of this residual stress is not axis symmetric, but almost point symmetric, with a strong similarity to the analytical model after Nairn (cf. Fig. 2.14). The relationship derived in Quek [217] that the radial stress in the interface is proportional to the derivative of the shear stress along the interface can be confirmed visually. After the initial cooling, visible in Fig. 5.21b, the first half of the embedded length shows a negative shear stress for all conditioning states, which becomes positive around $\xi = 0.55$. For the selected r-φ-z coordinate system, it follows that a negative shear stress corresponds to a stress state that occurs when the fiber is displaced relatively upwards, out of the adjacent matrix. The extreme stress values occur near the material singularities, but fall back to zero at the fiber ends. The shear stress magnitudes just before the embedded fiber end are greater than near the fiber entry point. Around the fiber entry point, the highest stress in magnitude is found for the cold/dry conditioning with $\sigma_{rz} = -32.1\,\text{MPa}$, followed by the warm/dry conditioning with $\sigma_{rz} = -27.7\,\text{MPa}$. Significantly lower in magnitude are the wet cases, with $\sigma_{rz} = -18.3\,\text{MPa}$ and $\sigma_{rz} = -13.4\,\text{MPa}$ for the cold and warm conditionings, respectively. On the other side of the embedded fiber, where $\xi \to 1$, the warm/dry conditioning has slightly higher stresses in magnitude than the cold/dry conditioning with $\sigma_{rz} = 49.7\,\text{MPa}$ and $\sigma_{rz} = 47.2\,\text{MPa}$, respectively. This is followed by the cold/wet conditioning with $\sigma_{rz} = 30.8\,\text{MPa}$ and the warm/wet conditioning with $\sigma_{rz} = 25.4\,\text{MPa}$. In general, the linear results are more extreme than the nonlinear results, in which case the highest shear stress occurs for the cold/dry conditioning with $\sigma_{rz} = 93.3\,\text{MPa}$. Only the warm/wet conditioning, the results for the nonlinear and linear model are indistinguishable. After relaxation and conditioning to humidity levels, visible in Fig. 5.21d, all stresses have reduced in magnitude, which is significantly more pronounced for both wet cases. For these cases, the stresses are bounded between $\sigma_{rz} \in [-7, 12]\,\text{MPa}$, with the cold conditioning being larger in magnitude along the interface. At this state, linear and nonlinear results are equal for the wet conditionings. Both dry conditioning states have relaxed to similar values, with maximum stress values of $\sigma_{rz} \approx -27\,\text{MPa}$ near the fiber entry point and $\sigma_{rz} \approx 45\,\text{MPa}$ towards the embedded end. The differences between linear and nonlinear model

remain pronounced for both dry cases.
As with the previously described results for the radial residual stresses, the shear stresses for warm conditioning reduced once again after reaching the final temperature, as can be seen in Fig. 5.21f, while the cold conditioning states remain unchanged. As a consequence, the shear stress along the interface for the warm/wet conditioning state was reduced to be bound by $\sigma_{rz} \in [-1, 2]$ MPa.

To quantify the deviation between the linear and nonlinear viscoelastic models, the mean relative errors between the linear and nonlinear curves are calculated for the final state of the residual stresses with

$$\langle e \rangle = \frac{\frac{1}{x_2 - x_1} \int_{x_1}^{x_2} |\sigma^{\mathrm{nl}}(\xi) - \sigma^{\mathrm{l}}(\xi)| \, \mathrm{d}\xi}{\frac{1}{x_2 - x_1} \int_{x_1}^{x_2} |\sigma^{\mathrm{l}}(\xi)| \, \mathrm{d}\xi}, \tag{5.16}$$

where σ^{nl} and σ^{l} symbolize the nonlinear and linear results. The reason for not calculating the relative error at each point along the curves is that different curves reach a zero-crossing for different values of ξ, which translates into large relative differences around these points, which otherwise may not be meaningful in an absolute sense. Since the FE results near the singularities at $\xi = 0$ and $\xi = 1$ are not reliable, the interval for the integral is reduced to $x_1 = 0.02$ and $x_2 = 0.98$, i.e., $2\,\%$ of the definition range of the normalized coordinate are not considered at each side. The mean relative errors are listed in Tab. 5.2. A clear pattern arises for

Table 5.2: Mean absolute difference $\langle e \rangle$ between the nonlinear and linear stress distributions along the fiber-matrix interface for the final residual stress state at $t = t_3$.

	$\langle e \rangle$ in %			
Component	cold/dry	cold/wet	warm/dry	warm/wet
σ_{rr}	44.7	3.8	42.0	0.0
σ_{rz}	26.5	3.5	24.4	0.0

the mean relative error $\langle e \rangle$. It is significantly larger for both dry conditioning states compared to the wet conditioning states. The mean relative error is in general

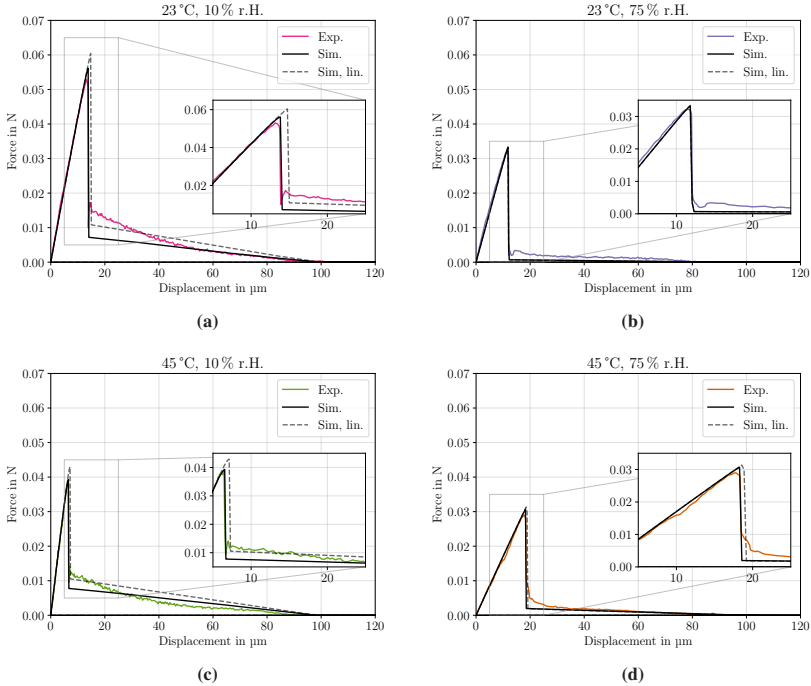

Figure 5.22: Simulated results for the single fiber pull-out experiment with fitted cohesive parameters and free fiber length to the average experimental results from the previous section. The black solid lines are the nonlinear results, while the dashed results are the linear results for the same cohesive parameters.

larger for the radial stresses, compared with the shear stresses. The maximum value is found for the radial stress for the cold/dry conditioning with almost $45\,\%$, indicating the significance of considering nonlinear effects. The error for the wet conditioning states is small and even non-existent for elevated temperatures.

The results for the simulated pull-out experiment are visualized in Fig. 5.22. The final calibrated parameters are listed in Tab. 5.3. It is clearly visible that the simple cohesive zone approach is able to capture the results of the experiments well. The initial incline or slope of the force displacement curve is fitted exactly by adjusting the free fiber length. A longer free fiber length corresponds to a more *compliant*

Table 5.3: Calibrated cohesive parameters and free fiber length for the single fiber pull-out simulation.

Label	Conditioning	l_{free} in mm	t_0 in MPa	$\mathcal{G}_{\mathrm{d}}$ in J/m^2	μ in -
Cold, dry	23 °C, 10 % r.H.	2.01	25.0	110.0	0.38
Cold, wet	23 °C, 75 % r.H.	3.01	15.0	90.0	0.38
Warm, dry	45 °C, 10 % r.H.	1.26	18.5	40.0	0.38
Warm, wet	45 °C, 75 % r.H.	5.02	13.5	110.0	0.38

response, while a shorter free fiber length corresponds to a *stiffer* response of the system. The *stiffness* extremes are given for the warm/dry and warm/wet conditioning, for which the free fiber length was fitted to be $l_{\mathrm{free}} = 1.26$ mm and $l_{\mathrm{free}} = 5.02$ mm, respectively.

The onset of damage and its development, which in the given cases is always catastrophic or sudden, is controlled via the damage initiation parameter t_0 and the debonding fracture toughness $\mathcal{G}_d$. The effect of a sudden force drop is captured well in the numerical model, at the correct force/displacement. When the numerical parameters are compared to the experimental results, i.e., IFSS and $\mathcal{G}_d$ in Tab. 5.1, it is notable that the general magnitude is similar, but the exact values differ. For the cold/dry conditioning, the damage onset parameter is $t_0 = 25.0$ MPa, which is slightly higher than the calculated IFSS of 22.82 MPa. For the cold/wet conditioning, the numerical parameter was fitted to be $t_0 = 15.0$ MPa, whereas the experiment has a larger IFSS of 19.82 MPa. Very similar values are found for the warm/dry conditioning with $t_0 = 18.5$ MPa and an IFSS of 18.35 MPa and a slightly larger deviation is given for the warm/wet conditioning with $t_0 = 13.5$ MPa and a calculated IFSS of 15.61 MPa. The energetic parameters are found to always be lower than the experimentally determined value.

For the frictional behavior, it was assumed that the friction coefficient μ remains constant throughout the different conditioning states. The error between simulations and experiments throughout all conditioning states was minimized with a coefficient of friction of $\mu = 0.38$. For the cold/dry conditioning this leads to an

initial underprediction of the frictional forces, while it approaches a perfect fit in a later stage of the pull-out curve. The friction force for the warm/dry conditioning is generally captured well. For the cold/wet conditioning the friction is constantly underprediction, while it is captured well for the warm/wet conditioning.

When the linear results are compared to the nonlinear results, a clear pattern emerges. The linear results lead to a higher maximum pull-out force and therefore to a delayed onset of damage. Furthermore, higher frictional forces are evident during pull-out for the dry cases. For the wet cases, the frictional forces are much smaller and do not deviate between linear and nonlinear model. Only for the cold/wet conditioning, no deviation is visible in general between the two models.

5.4 Discussion

The preceding results present the experimental pull-out evaluation and the numerical analysis of it under various conditioning states. The experimental findings revealed that the interaction between the fiber and matrix is environment-dependent, as evidenced by the differently calculated interfacial shear strengths (IFSS) and $\mathcal{G}_d$. The reduction of the IFSS through water absorption of $13\,\%$ and $15\,\%$ for the cold or warm temperature, respectively, can be attributed to an increase of the viscoelastic matrix compliance, a reduction in the interfacial properties or a degrading of the chemical/physical interaction between the fiber and the matrix, as stated in Amer et al. [226]. Based on the methodology used, the exact source of the reduction cannot be determined. Further testing on redried specimens would help narrow this down, but based on the calibrated numerical results, a degradation of the interface parameters is likely.

A novel aspect of this work is the development of a testing setup that allows for the examination of the mechanics at the fiber-matrix interface not only for conditioned samples, as previously done in other studies [227, 228, 111], but also to maintain the conditioning state throughout the experiment. This is an extension of the capabilities of the setup in Tanaka et al. [118], which could only control the

surrounding temperature. The principle of deliquescence used here is particularly well-suited for establishing the relevant temperature and humidity range for most polymers within small test volumes. For temperatures significantly above the range studied here, the materials used would need to be adjusted accordingly. Moisture control in very high temperature ranges would likely become obsolete due to the relative humidity in practice approaching zero. In prior studies where samples were conditioned but the tests were conducted at room climate, it cannot be assumed that the samples do not at least partially decondition before the experiment is completed. Given the small dimensions of the specimen and the resulting high surface-to-volume ratio, as well as the short distance from the surface to the center of the sample, it must be assumed that deconditioning occurs faster than the time available for conducting the experiment. Therefore, the methodology presented allows for a cost-effective solution to this issue and is an alternative to, e.g., the approach of Downes and Thomason [109], who conducted humidity controlled micro-bond experiments within a DMA.

The experiments demonstrated that for the given material pairing and undisclosed sizing, damage occurs along the interface without matrix failure. The fact that the fibers were pulled out bare in each case suggests that the interfacial mechanics are mainly dominated by mechanical interlocking and/or physical forces. Signs of a chemical bond, as is usually the case with reacting polymers (thermosets) in the form of an interphase, cannot be interpreted from this. Harris [229, p. 80 ff.] and Kim and Mai [230] describe that for thermoplastic composites, a significant portion of the interfacial shear strength (IFSS) can be explained by the mechanical interlocking of the fiber and matrix, which is based on the eigenstresses along the interface. The eigenstress fields calculated in this study, along with the measured IFSS, which were found to be higher for increased compressive radial stresses at the interface, support this statement. Furthermore, the high environmental sensitivity of the interface properties corresponds well to the findings by Harris et al. [94], who report that a purely mechanical bond is more susceptible for water induced degradation.
The completely exposed, extracted fibers justify the model approach of cohesive formulations, where the local progression of crack growth is predetermined.

The effective behavior of the force-displacement curve during pull-out was well replicated numerically using cohesive surfaces. The analysis of the temporal variation of eigenstresses along the interface showed, on one hand, that significant relaxation processes occur, leading to a reduction in the effective residual stresses. On the other hand, the four different conditioning groups can be classified into two distinct behaviors. While the numerical analysis predicts only low eigenstresses in radial and shear directions for both moist conditioning states, these stresses are significantly elevated for dry conditioning, reaching values in the range of reported IFSS, e.g., in Ahmadvashaghbash et al. [231]. Thus, this preloading due to hygrothermal stress cannot be neglected in the analysis, as was done, e.g., in Marotzke [232].

The experimental results indicated high friction forces for the dry conditioning, while both wet conditioning states exhibited minimal friction forces. A possible hypothesis is a change in the friction coefficient for a Coulomb friction model depending on the hygrothermal state, as reported by Velkavrh et al. [233], who measured an increase in the coefficient of friction for moist PA6. This cannot be ruled out based on the given analysis; however, the resulting residual stresses indicate that this effect can also be explained through the acting radial stresses. The increase in polymer volume due to moisture absorption causes the surrounding matrix to move relatively away from the fiber in the radial direction for the given geometry. The reduced compressive stresses, which could even become tensile for other hygrothermal boundary conditions as indicated by Piggott [234], are significantly lower than for the dry state, where the matrix shrinks onto the fiber. This condition alone can explain the measured difference in friction forces between wet and dry conditioning. This hypothesis is further supported by the numerical results, assuming a constant friction coefficient with the same effect occurring.

Furthermore, during the evaluation of the experimental pull-out results, different slopes for the initial force-displacement behavior were measured. In the subsequent numerical analysis, using the free fiber length as a parameter, it could be shown that this apparent stiffness can be explained as a direct consequence of the free fiber length, rather than being due to increased compliance of the

matrix or the interface. It is possible that, in addition to the free fiber length, an environmental dependency of the adhesive used to fix the fiber contributes to this apparent stiffness, which should be considered in future investigations.

Especially in the field of residual stresses, but also in the simulated pull-out profiles, a significant difference emerged between the linear and the nonlinear viscoelastic material models. In the nonlinear model, the residual stresses are greatly reduced in comparison, due to faster relaxation at higher loads. The stresses that occurred in the numerical study around the interface were large enough to cause a significant difference in the relaxed residual stress field. This demonstrated the importance of considering existing nonlinearities, which are particularly evident in the case of thermoplastics. Although numerous studies have been conducted on the fiber-matrix interface that extend the early elastic assumptions to plastic and linear-viscous models [80, 81, 83, 84], investigations into nonlinear viscoelastic material behavior are scarce. Since the previous investigation already revealed significant differences for a quasi-static pull-out, this also serves to motivate further research into interfacial properties under rapid loading conditions, such as impact loads, where nonlinear properties are likely to play an even greater role and should not be neglected.
A fascinating aspect is that for identical material parameters and cohesive properties, while the linear model predicts significantly higher eigenstresses along the interface, the failure of the interface occurs later in every case compared to the predictions made by the nonlinear model. This initially counterintuitive relationship can be explained by the fact that, although the initial damage due to higher eigenstresses occurs earlier, the higher frictional forces present in the linear model delay catastrophic failure along the entire interface. In the debonded region between the fiber and matrix, the interfacial friction leads to a reduction in stress at the crack tip, resulting in a higher force being required to initiate further crack propagation, as was already stated in Jäger [235]. In general, frictional forces have a benign effect on the quality of the fiber-matrix interface and stabilize the crack propagation, as was already highlighted in other studies [236, 237].

Lastly, the methodology and the assumptions made need to be critically discussed. During the pull-out test, it was not precisely ensured that the free fiber length was

consistent between experiments and, when possible, was minimal. The resulting interpretation range is challenging to close and suggests that future investigations should focus on adjusting the methodology accordingly.
The numerical assumptions are heavily simplified, particularly concerning the neglected heat conduction and the constant material properties along the hygrothermal history. Strictly speaking, the calibrated material models only apply to the respective conditioning state and not during the variation of the climatic conditions, which was nevertheless assumed in the given analysis. Depending on the conditioning state, the hygrothermal history may lead to under- or overshooting the glass transition temperature, followed by a vast variation of material behavior, which was not considered in the above study. Therefore, the calculated residual stresses along the interface should not be regarded as absolute truths. Rather, the results represent a tendency, and the effective pull-out curves derived from them, which align well with the experimental findings, validate their usefulness in relation to each other.

6 Continuous-discontinuous interface

6.1 Climbing drum peel test

6.1.1 Kinematics

In the following the kinematics and measurements of interest of the CDP experiment are discussed in reference to the illustration in Fig. 6.1. The ratio of the displacements of the drum center Δu_d and the upper clamping Δu_0 is given by

$$\frac{\Delta u_\mathrm{d}}{\Delta u_0} = \frac{r_2}{r_2 - r_1}, \tag{6.1}$$

and since $r_2 > r_1$, this ratio is always larger than one making the drum *climb* upwards. The relative crack propagation Δu_c, or newly formed crack length, can be calculated at every point in time with

$$\Delta u_\mathrm{c} = \Delta u_\mathrm{d} - \Delta u_0 = \frac{r_1}{r_2 - r_1}\Delta u_0. \tag{6.2}$$

A schematic force-displacement diagram including the loading and unloading phase of the CDP test is given in Fig. 6.2. The applied work to separate the interface can be calculated from the force-displacement data using

$$W = \oint F \,\mathrm{d}u, \tag{6.3}$$

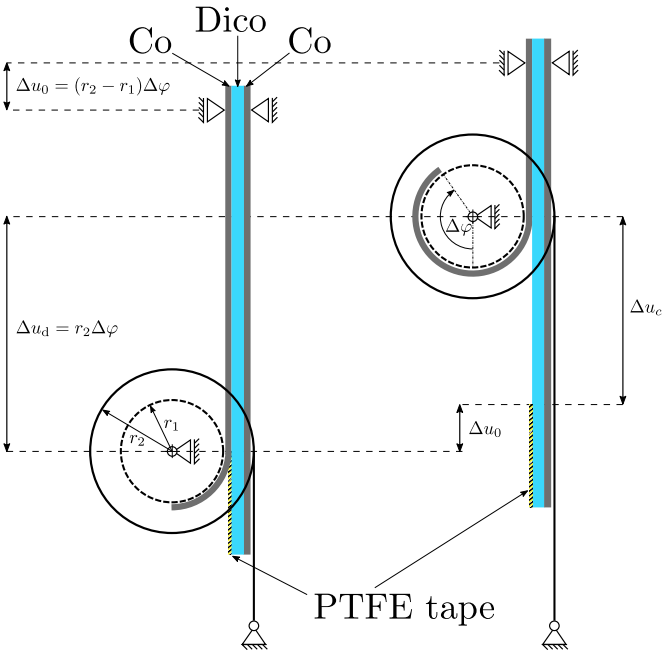

Figure 6.1: Kinematics of the CDP test in reference to Daghia and Cluzel [128]. Δu_0, Δu_d and Δu_c are the increments of the prescribed displacement at the upper clamp, the displacement of the drum with respect to its initial position and the crack length with respect to the structure, respectively. $\Delta\varphi$ is the rotation angle increment of the drum and r_1 and r_2 are the inner and outer radii of the drum, respectively. Graphic reused from the author's publication in Christ et al. [148].

where also the initial effects in the rise of the force signal are considered. To avoid initial and ending effects of the force signal, one can also use an average approach, indicated in Fig. 6.3, and using the following relation

$$W = (F_d - F_w)\Delta u_0, \tag{6.4}$$

where F_d is the average delamination force and F_w is the average winding force, which is caused by the weight of the drum. The measure of interest, i.e., the critical strain energy release rate $\mathcal{G}_c$, can then be calculated by dividing the applied work to separate the interface by the newly created surface area due to

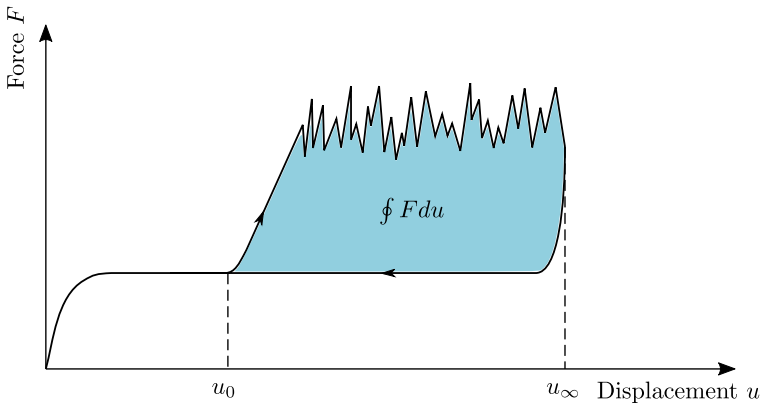

Figure 6.2: Schematic force-displacement diagram of a CDP test for testing the interface of Co-Dico FRPs. Graphic reused from the author's publication in Christ et al. [148].

the crack propagation. For Eq. 6.3, i.e., when the whole separation process is considered, the created surface can either be measured from the separated specimen or calculated by using Δu_c from Eq. 6.2, multiplied by the width of the specimen w. When only a fraction of the created surface is used, as is the case in Eq. 6.4, a measurement is not feasible and the created surface needs to be calculated. The critical energy release rate is then calculated using

$$\mathcal{G}_c = \frac{W}{w\Delta u_c}, \tag{6.5}$$

which is in agreement with [238]. Care has to be taken that Δu_c can either be the full crack length, for when the full work (cf. Eq. 6.3) is used, or it can be a partial crack length.

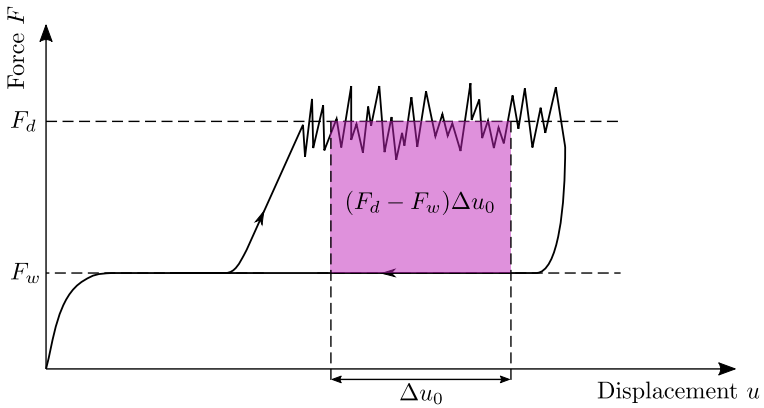

Figure 6.3: Schematic force-displacement diagram of a CDP test for testing the interface of Co-Dico FRPs with an average work approach. Graphic reused from the author's publication in Christ et al. [148].

6.2 Experimental investigation

6.2.1 Co-Dico plates

The Co-Dico specimens are produced in the LFT-D process introduced in Sec. 3.4, which combines the LFT-plastificate with a double UD tape reinforcements on both sides. The manufacturing of this UD plate was described in Sec. 3.3. To initiate a pre-crack between the Dico bulk material and one of the Co plates, a polytetrafluorethylen (PTFE) foil is added to one side of the plate before the following co-molding step, which prevents the consolidation of the covered plate with the LFT plastificate. The pre-heated UD plate with the PTFE foil facing upwards is then placed inside the mold. Time coordinated, LFT plastificates are produced simultaneously in the LFT-D process at a rate of 39 kg/h with a barrel temperature of 280 °C, a screw speed of 59 rpm and a fiber roving count of eleven, which results in a fiber mass (volume) fraction of $w_\mathrm{f} = 34\,\%$ ($v_\mathrm{f} = 26\,\%$). The plastificate is cut to the required length of about 400 mm and is placed on top of the PTFE tape on the same side inside the mold. A second layer of UD reinforcement is placed upon the LFT plastificate without a PTFE tape to

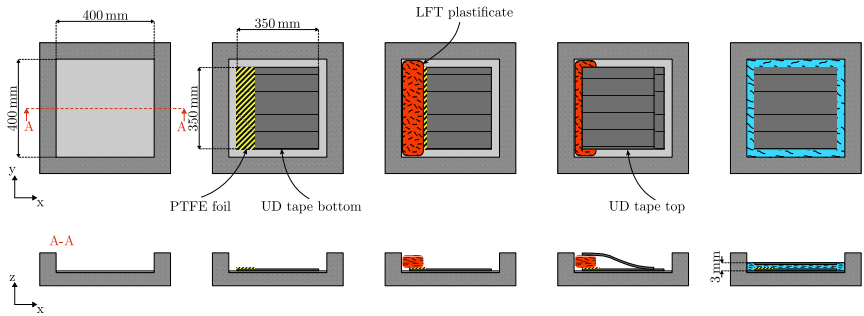

Figure 6.4: Consolidation process of the Co-Dico specimens from left to right: empty press, inlay of lower UD tape with PTFE tape, inlay of LFT plastificate, inlay of upper UD tape, consolidated Co-Dico plate. The upper row represents the top view, while the lower row represents the side view of the process.

allow for full consolidation between the plastificate and the plate above. The reinforcements on both sides share identical fiber orientations in flow direction. The press is closed at a displacement rate of 30 mm/s to minimize the temperature drop of the materials and is later changed to a pressure controlled position at 200 bar for 35 s, which results in a plate thickness of 3 mm. A schematic of the consolidation process is given in Fig. 6.4.

To avoid confusion, it is repeated that the final Co-Dico plate consists of two layers of UD tape per side, which was referred to as a single Co plate before. Hence, the thickness of unidirectionally reinforced material per side is 0.26 mm, so that the final 3 mm thickness of Co-Dico plate consists of 0.52 mm unidirectionally reinforced material, and 2.48 mm discontinuously reinforced material.

6.2.2 Specimen preparation and conditioning

Individual specimens were cut from the produced Co-Dico plates with the predefined pre-crack between one layer of Co and the Dico bulk material (cf. Section 6.2.1). For this, an iCUTwater smart from imes-icore GmbH, Eiterfeld, Germany, was used with a nozzle pressure of 1500 bar, a cutting speed of 200 mm/min and a mass rate of 250 g/min. As cutting sand, Classic Cut 120 garnet from GMA

was used. The side containing the PTFE layer and pre-crack was facing upwards towards the water jet during cutting and the entry point for the water jet was chosen to be on the opposite side of the PTFE tape to avoid early delamination. The finished specimen has the cuboidal dimensions of 272 mm×25 mm×3 mm (length×width×thickness), resulting in an unconsolidated free Co lap of about 72 mm.

Table 6.1: Conditioning procedure of the different conditioning states for the CDP test.

Label	Dried	RC	Moist	Wet
Conditioning	50 °C 0 % r.H. in vacuum	23 °C 45 % r.H.	50 °C 80 % r.H.	50 °C submersed in distilled water
Duration	$\geq$ 240 h	1500 h	240 h	240 h

For the conditioning, the specimens were first dried at 50 °C in a vacuum oven for more than 240 h, while the mass loss due to water evaporation was tracked through gravimetric measurements. When the mass loss converged to zero, the specimens were assumed to be in a dry equilibrium state. A fraction of the dried specimens was stored in an airtight desiccator with silica gel to preserve the humidity free state. To investigate the effects of humidity on the consolidation quality of the Co-Dico material, three different conditioning states were chosen. These include the standard climate at 45 % r.H., an elevated humidity at 80 % r.H. and a fully wet state after full water contact. These conditioning states are referred to as room climate (RC), moist and wet, respectively. For the conditioning of the RC state, the specimens were stored in a climatized lab environment at 23 °C and 45 % r.H., which required a conditioning time of 1500 h for the vapor mass flux to vanish. To accelerate the humidified conditioning process, both the moist and wet conditioning took place in a climate chamber at their respective relative humidity and at an elevated temperature of 50 °C, which shortened the time to reach equilibrium to about 240 h. For the wet conditioning, the material was fully immersed in distilled water within the climate chamber. The data for all

conditioning procedures are also listed in Tab- 6.1. To evaluate the water uptake of each conditioning state, the specimens were weighed once they reached the dry equilibrium and after the respective conditioning.

6.2.3 Test procedure

The testing itself was conducted at room climate, for which the conditioned specimens were moved out of their conditioning climate just before testing, so that a deconditioning is unlikely. The CDP was conducted using a zwickiLine universal testing machine from ZwickRoell AG, located in Ulm, Germany, equipped with a load cell rated for 2.5 kN capacity. For the drum, a hollow aluminum cylinder was utilized, with an outer radius of $r_2 = 62.5$ mm and a inner radius of $r_1 = 50$ mm. To secure the specimen to the drum, a custom drum support was designed to maintain the drum in its initial position. At the outset of the test, a preload of 90 N was applied at a speed of 10 mm/min. Under this preload, the UD layer partially wrapped around the drum without any observable crack growth. Following the application of the preload, the actual test started, with the crosshead moving upward at a speed of 100 mm/min. The test continued for 80 mm of travel before being halted, after which the crosshead was retracted to the starting position at a speed of 50 mm/min, while force measurements continued to be recorded.

6.2.4 Fracture surface analysis

After the test, each specimen was prepared to investigate the fracture surface. For this, the peeled Co material was separated from the rest of the specimen and pictures were taken on both fracture surfaces, i.e., from Co and Dico, with a digital single-lens reflex (DSLR) camera. Selected zones of interest with the dimensions of 20 mm$\times 20$ mm were cut from the Co tape and sputtered with a platinum film of 1 nm thickness on both sides, before placing the rectangle within an Zeiss Supra 40VP SEM. Using an accelerating voltage of 4 kV and a working distance around 15.2 mm, the polymer deformation and interface quality was investigated. The

Dico side was also sputtered and investigated accordingly. Since the individual investigations took place over several days, the brightness and contrast of the SEM image needed to be adjusted manually so that small variations in the image quality was inevitable.

6.2.5 Results

Before conducting the experiments, the specimens were weighed to determine their water uptake in terms of mass percent. The results of this assessment are presented in Tab. 6.2.

Table 6.2: Water uptake for each conditioning state in mass percent.

Label	Dried	RC	Moist	Wet
Conditioning	50 °C 0 % r.H.	23 °C 45 % r.H.	50 °C 80 % r.H.	50 °C submersed
Water uptake	0.00 %	0.99 %	2.00 %	6.35 %

It can be observed that increasing the humidity from room climate (RC) conditioning to moist conditioning resulted in a doubling of the moisture content. Furthermore, immersion in water increased the water content to more than three times that of the moist conditioning.

The experimental force-displacement curves are illustrated in Fig. 6.5a, while the averaged results are depicted in Fig. 6.5b. As in the single fiber pull-out test, the arc-length parametrization introduced in Hartlen and Cronin [213] was employed, which offers the advantage of preserving specific characteristics within the force-displacement signal, such as the magnitude and position of oscillations, and allows for analysis of hysteretic data, as is evident in the loading-unloading experiment.

Based on the kinematic properties of the testing setup, the initial rise in the force signal concludes following a specimen displacement of approximately 2 mm, once

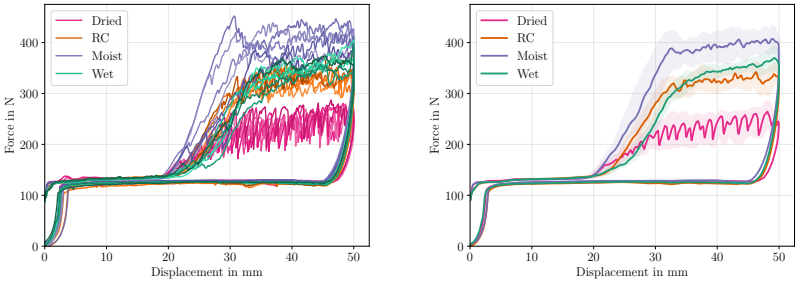

Figure 6.5: Experimental results of CDP test. **a**) shows the individual results, and **b**) is the averaged result for each conditioning class using an arc-length based averaging scheme (cf. Hartlen and Cronin [213]) where the envelopes indicate statistical response corridors. Graphics reused from the author's publication in Christ et al. [148].

the drum is completely elevated, maintaining a constant force of $F_w = 120\,\mathrm{N}$. The force signal remains unchanged until a specimen displacement of about $20\,\mathrm{mm}$. Beyond the PTFE layer, the pre-crack ends, necessitating an increase in the force signal for the crack to propagate. All conditioning states demonstrate an initial slope in which the force does not stabilize. After approximately $32\,\mathrm{mm}$ of displacement, a maximum stable (on average) force level is attained, characterized by periodic oscillations. Notable variations in the force signal are observed across the four conditioning states. Dried specimens show the lowest maximum force, averaging around $220\,\mathrm{N}$, yet they display the most significant oscillations in the force signal, indicating erratic crack propagation, which was also audible during the experiment. As moisture content increases, the maximum force initially ascends, reaching about $320\,\mathrm{N}$ for the RC condition and $400\,\mathrm{N}$ for moist specimens, with the fluctuations diminishing. However, for the specimens submerged in water, the maximum force declines to a level just above the RC value, approximately at $340\,\mathrm{N}$. When the maximum displacement of $50\,\mathrm{mm}$ is achieved, the traverse returns to its original position, slightly reducing the force signal below the initial F_w value. Following the method illustrated in Fig. 6.2, the area enclosed by the force-displacement curve was calculated numerically for all datasets. The newly

generated fracture area was measured, allowing for the computation of the critical energy release rate $\mathcal{G}_c$ using Eq. 6.5. A statistical box plot representing all conditioning states is presented in Fig. 6.6.

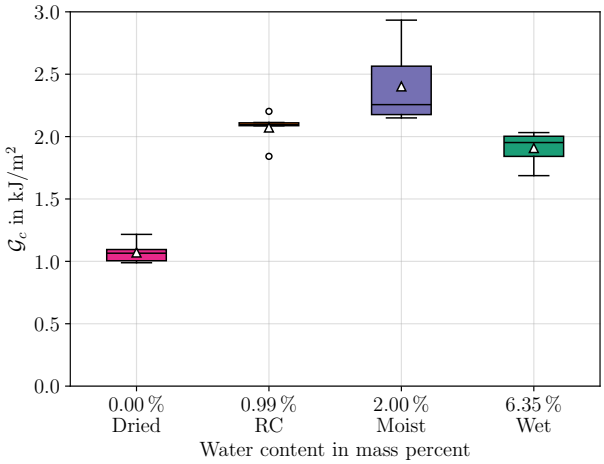

Figure 6.6: Box plot of the critical energy release rate $\mathcal{G}_c$ for all conditioning states. Graphic reused from the author's publication in Christ et al. [148].

It can be seen that the lowest mean $\mathcal{G}_c$ was measured for the dried samples with $\mathcal{G}_c = 1.07\,\mathrm{kJ/m^2}$. The critical energy release rate then rises with $\mathcal{G}_c = 2.07\,\mathrm{kJ/m^2}$ for RC and $\mathcal{G}_c = 2.40\,\mathrm{kJ/m^2}$ for the moist conditioning, indicating a better energy absorption for an increase in moisture. While the variation in experimental results is low for the dried and RC conditioning, an increased variation is observed for the moist conditioning. Contrary to the upward trend in $\mathcal{G}_c$ with increasing moisture content, a further increase of humidity in the case of the immersed samples reduces the critical energy release rate to $\mathcal{G}_c = 1.91\,\mathrm{kJ/m^2}$. Despite the force level reaching higher values in the wet conditioning case, the evaluated critical energy release rate is slightly smaller than for the moist

conditioning. This is caused by the initial incline being more shallow for the wet conditioning.

After testing, the fracture surfaces were investigated, which are shown in Fig. 6.7. A noticeable differentiation among the four conditioning states can be identified

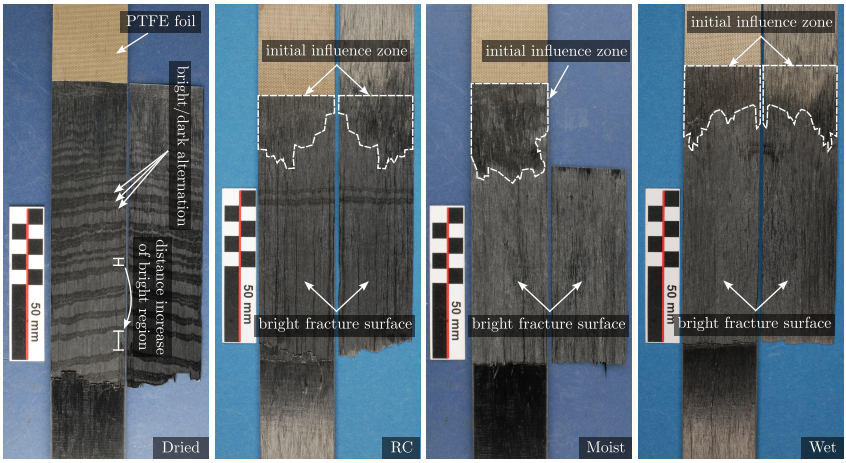

Figure 6.7: Fractography results of CDP test. **a**) shows the fracture surface of the dried specimen with a clear stick-slip (alternating ductile/brittle) fracture pattern (parts of the Co tape were cut away for investigation), **b**) shows the fracture surface of the specimen conditioned at room climate with minor signs of a stick-slip effect. **c**) and **d**) show the fracture surface of the moist and fully immersed specimens, respectively. All specimens show an altered initial zone in the vicinity of the PTFE foil. Graphic reused from the author's publication in Christ et al. [148].

in the fracture surfaces. The fracture surface of the dried specimen (cf. Fig. 6.7a) prominently exhibits an alternating fracture pattern characterized by bright and dark regions, a pattern that is consistently present across all specimens. In this case, the height of the bright regions increases with an increased crack length away from the PTFE foil. The frequency of these oscillations corresponds with the observed force drops on the force-displacement curve for dried specimens. This same pattern is also seen in some fracture surfaces of the conditioned specimens at room temperature, albeit in isolated areas, as illustrated in Fig. 6.7b. In contrast,

at higher humidity levels (see moist and wet specimens), the fracture surface lacks this alternating pattern and instead displays a uniformly bright area. For all conditioning states, the initial few centimeters following the PTFE foil reveal a modified fracture surface with a darker hue, indicating an initial influence zone adjacent to the PTFE foil. The length of this influence zone correlates with the region in the force-displacement diagram prior to reaching a stable force value F_d, where a gradual increase in force was observed (as shown in Fig. 6.5).

A more detailed investigation of the alternating fracture patterns in the SEM reveals that a clear optical distinction between the two zones is also possible, as illustrated in Fig. 6.8. While the left half of the figure exhibits a dull fracture

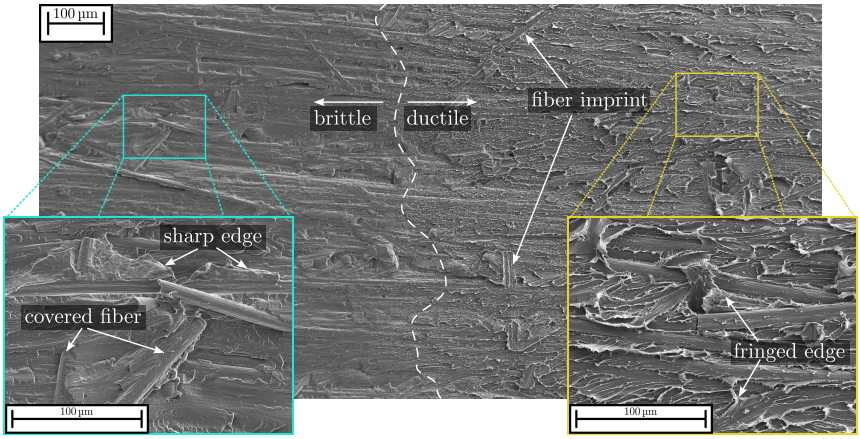

Figure 6.8: SEM images of fracture surface of dried sample with details of brittle and ductile fracture zones on the Co side.

appearance with little variability in the displayed contrast, the right half of the illustrated fracture surface shows a highly contrast-rich fracture surface with a more pronounced three-dimensionality.

In the enlarged images below it is evident that the left fracture surface corresponds to a brittle fracture. The fracture morphology in the polymer-rich regions is characterized by flat, flaky detachment with clearly defined edges. Most of

the fibers running from left to right in the image, which are attributed to the Co reinforcement, remain covered by matrix material. A small number of fibers are partially stripped blank, indicating crack propagation along the fiber-matrix interface. Among these exposed fibers, a significant portion is oriented with an angle to the Co orientation, suggesting that these fibers are the shorter fibers from the Dico side. Therefore, the crack has not merely propagated along the interface between Co and Dico but has also undercut at least some of the superficial Dico fibers.
In contrast, the enlarged images of the right region depict a clear ductile fracture. The thermoplastic exhibits significantly increased plastic deformations that protrude from the fracture plane, terminating in thin, frayed edges. The fraying occasionally tapers to a point, resembling a shark's tooth, and follows horizontal lines along the Co reinforcement or parallel to the crack propagation. Compared to the brittle fracture surface, more imprints of Dico fibers are evident, indicating that the crack has propagated along the fiber-matrix interface, specifically on the side adjacent to the Co material. Consequently, there are hardly any Dico fibers present in the fracture surface on the Co side. The visible fibers are attributed to the reinforcements of the Co material, with more fibers exposed at the fracture surface than is the case on the brittle fracture side. Thus, a preferential progression of the crack is observed along the Co-Dico interface, as well as along the fiber-matrix interface.

The ductile regions within the fracture zone correspond to the brighter sections seen in the images in Fig. 6.7. This brightness can be attributed to a high degree of light scattering caused by the uneven surface created by the polymer fringes, directing more light onto the camera's sensor and resulting in a brighter appearance. Hence, the brighter fracture surfaces observed in the moist and wet specimens must be ductile as well, suggesting that brittle fracture only occurs when moisture is lacking.

A detailed comparison for assessing the morphology of matrix adhesion to fibers within the interface between brittle and ductile regions is illustrated in Fig. 6.9. It is evident that the fibers in the brittle fracture area in Fig. 6.9a are still covered by at least a thin layer of matrix, with the formation of isolated pores being observable.

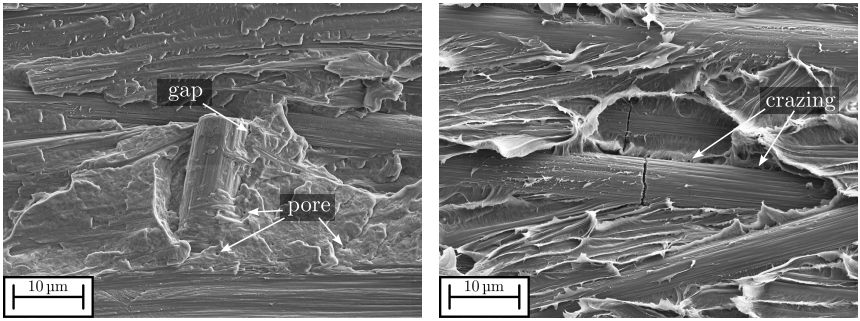

Figure 6.9: Detailed SEM images of matrix residue within brittle (left) and ductile (right) fracture surface for a dried sample on the Co side.

The coverage of the fiber by the polymer is scaly, and small gaps between the matrix and the adjacent fiber are occasionally evident, which may be attributable to the shrinkage of the matrix material due to prior drying.
The matrix remnants in the ductile area in Fig. 6.9b differ significantly from this. The fibers appear to be less covered, allowing the longitudinal grooves of the carbon fibers to be clearly identifiable. Pore formation is less apparent. Conversely, there is evidence of crazing at the transition from exposed to covered fibers. The shark-tooth-like formations extend along the longitudinal grooves of the fiber rather than across them.

The fracture surface on the Co side of the samples conditioned at room climate is shown in Fig. 6.10. Generally, it resembles the ductile fracture morphology observed in the dried samples. Pronounced plastic deformations of the matrix are again evident, exhibiting the previously noted characteristics. Furthermore, within this fracture surface, it can be observed that some fibers from the Dico side were detached during crack propagation and remained on the Co side. Compared to the dried samples, there are fewer empty imprints of Dico fibers; instead, the number of transferred Dico fibers is greater. The side of the interface facing the detector is often only covered by a few remnants of the matrix, with some continuous reinforcement fibers left exposed. Consequently, it is also clear that

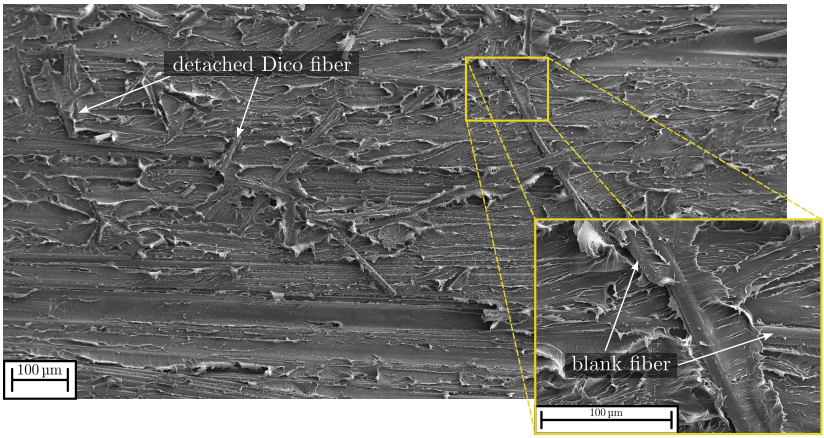

Figure 6.10: SEM images of fracture surface of RC sample on the Co side.

crack propagation partially occurs along the fiber-matrix interface. Macroscopically, the crack propagation is also situated at the interface between Co and Dico materials, with the crack, as mentioned, partially undermining fibers from the Dico side.

The fracture surface for the moist conditioning state is displayed in Fig. 6.11. At first glance, it appears very similar to the ductile areas of the previously discussed conditioning states. Pronounced plastic deformations of the matrix material are again evident, with many empty impressions of Dico fibers that barely adhere to the Co side in the shown section. The extent of matrix deformation seems slightly increased compared to the previous conditioning state. The visible fibers are again partially covered by matrix material and partially exposed, which also applies to the continuous reinforcement fibers.

For the wet conditioning state, where prolonged contact with liquid water occurred, a changed fracture morphology is evident, as shown in Fig. 6.12. Initially, it is apparent that the dominant fracture mode still corresponds to a ductile fracture. However, matrix deformation decreased compared to the two other moistened conditioning states, as indicated by the significantly smaller protruding fringes

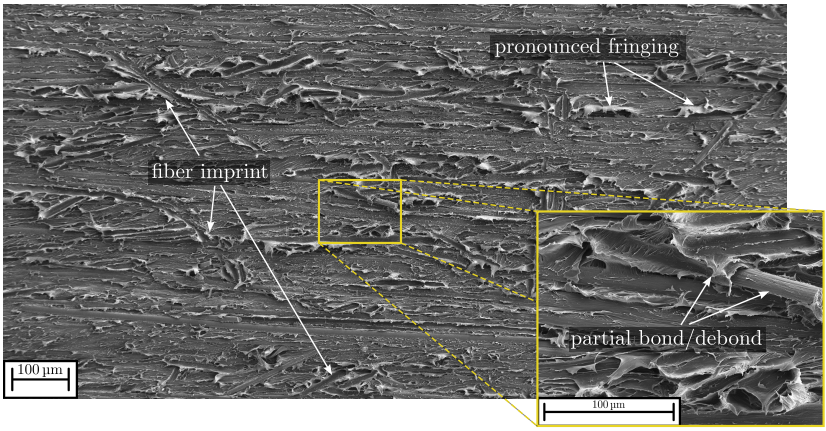

Figure 6.11: SEM images of fracture surface of moist sample on the Co side.

along the fracture surface. Furthermore, there are noticeably more exposed continuous reinforcement fibers of the Co material. It is clear that crack propagation occurred in a deeper layer of the Co material, as supported by the many exposed continuous fibers, some of which even extend visibly beyond the fracture plane. Notably, there are few shorter or transversely oriented fibers from the Dico side included in the fracture surface. In this conditioning state, it is even more evident that little to no matrix remnants adhere to the fibers within the fracture morphology.

The fracture surface counterpart on the Dico side for all conditioning states is shown in Fig. 6.13. In summary, the characteristics previously noted are confirmed here.
For the dry conditioning state in Fig. 6.13a, there is a clear differentiation between brittle and ductile regions, with interface damage for the fiber-matrix bonding being more pronounced in the ductile area. Additionally, there are hardly any imprints or transfers of Co fibers visible in the brittle region.
The two moist states, namely RC and wet in Fig. 6.13b and Fig. 6.13c, consistently

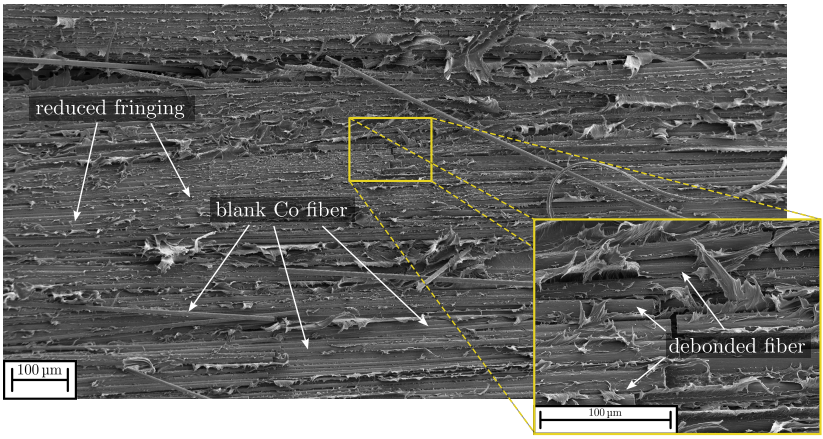

Figure 6.12: SEM images of fracture surface of wet sample on the Co side.

exhibit ductile areas with many exposed Dico fibers. The plastic matrix deformation is notably pronounced. In the wet conditioning state, it is additionally visible that continuous reinforcement fibers are also present in the fracture surface on the Dico side, suggesting partial crack development just below the surface of the Co tape.

The Dico side of the wet conditioned sample in Fig. 6.13d shows a precise counterpart to the fracture surface on the Co side. Countless parallel grooves are evident, in which no fibers remain. These grooves confirm crack development along the fiber-matrix interface of the continuous fibers within the macroscopic interface between Co and Dico. Furthermore, it is also noticeable that the plastic deformation of the matrix material is less pronounced than in the two other moistened conditioning states.

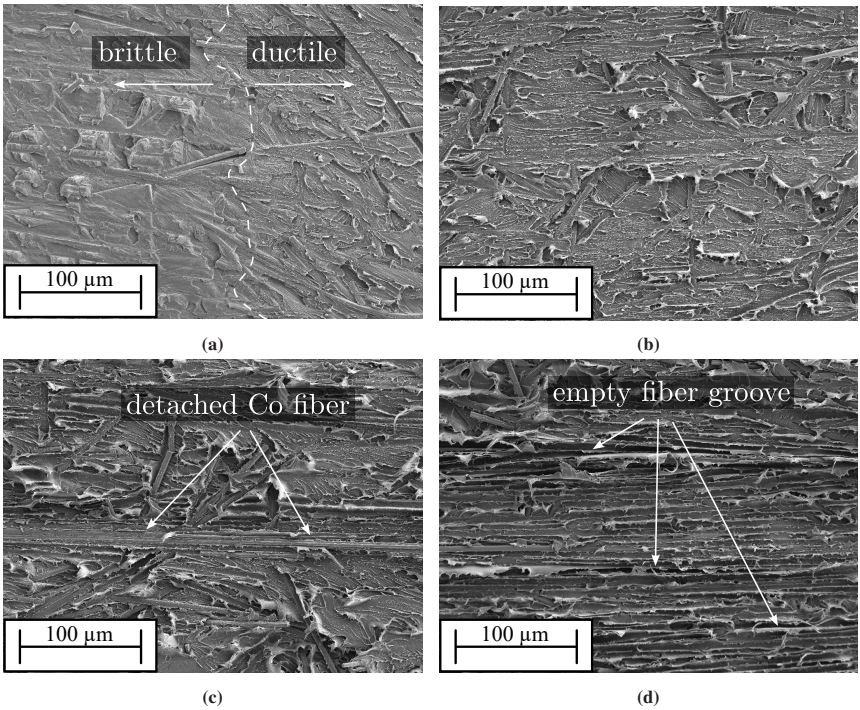

Figure 6.13: SEM images of fracture surface for all conditioning states on the Dico side.

6.3 Numerical investigation

6.3.1 Implementation of homogenization methods

The implementation for the two mentioned homogenization methods, i.e., the Mori-Tanaka and the shear-lag informed Halpin-Tsai method, was realized in the programming language Python as an open source project under the name `HomoPy` and was made available for the scientific community in a Github repository. A schematic of the functionality of `HomoPy` is given in Fig. 6.14.

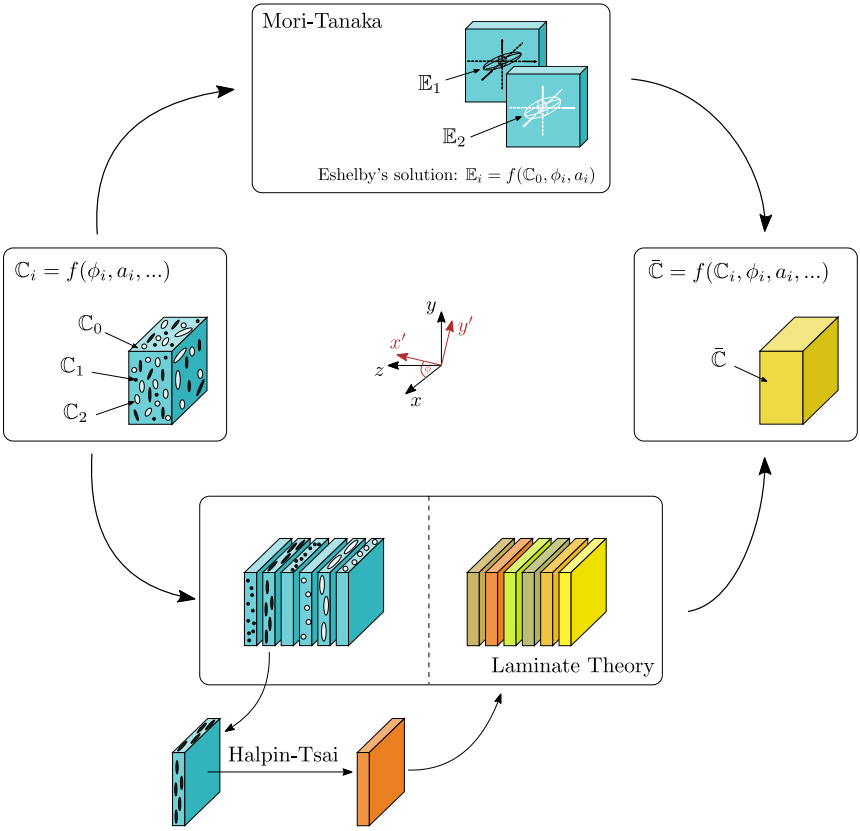

Figure 6.14: Schematic of the functionality of the Python package `HomoPy`. Graphic reused from the author's publication in Christ et al. [239].

The object oriented implementation allows the user to select either the Mori-Tanaka or the shear-lag informed Halpin-Tsai method to calculate the effective stiffness of a fiber reinforced composite. Being a mean-field homogenization method based on tensor algebra, the MT scheme allows the user to select different symmetry classes for the stiffness of the constituents, which include full isotropic and transversely isotropic materials. The inclusion geometry can either be spherical (in the case of round particles), spheroidal (in the case of long fibers) or needle-shaped (in the case of UD reinforcements). Furthermore, it is possible

to homogenize multi-inclusion problems, e.g., carbon and glass fibers reinforcements used together, resorting to an algorithm presented in Jiménez Segura et al. [240], which preserves the necessary symmetry condition of a stiffness tensor. The fiber orientation distribution can be considered using orientation tensors of fourth order, while the length distribution is accounted for by a multi-inclusion approach. The result is a three-dimensional, linear-elastic stiffness tensor, which can be used in subsequent simulations, e.g., in the FE software `Abaqus`.

The shear-lag informed HS scheme is used to model 2D structures. As such, all constituents are treated to be isotropic materials. In contrast to the MT scheme, the HS homogenization method does not directly offer an option to consider orientation and length distributions. Nevertheless, `HomoPy` offers this capability by resorting to the laminate theory, which goes back to the laminate analogy approach (LAA) in Fu et al. [184]. Here, the composite is split into laminas of equal orientation and length. Each lamina is then homogenized treating it as a UD material using the HT scheme and the combination of laminas, i.e. the laminate, is then homogenized using the laminate theory. The result is a two-dimensional, linear-elastic stiffness matrix, which is ideal to be used in shell structures within FE environments.

Lastly, `HomoPy` offers both 2D and 3D visualization tools of the stiffness properties of a given material. This is based on the work in Böhlke and Brüggemann [241] and allows for an easy comparison of the effects of individual attributes within a composite, e.g. aspect ratio or orientation distributions, on the homogenized material. First successful applications of `HomoPy` are found in Schreyer et al. [242] and Scheuring et al. [185].

6.3.2 FEM model

In order to use the qualitative characteristics of the experiments in simulations in which the delamination process must be taken into account, the experiment must be simulated numerically to make statements as to whether this is possible with the model presented below. For the simulation `Abaqus` is used. Since the

experiment is geometric nonlinear with complex contact boundary conditions, an explicit time integration is chosen. The numerical model consists of four parts, all of which make use of the symmetry in the experiment. Therefore, only half of the experiment was simulated. The full assembly and the geometric properties are given in Fig. 6.15.

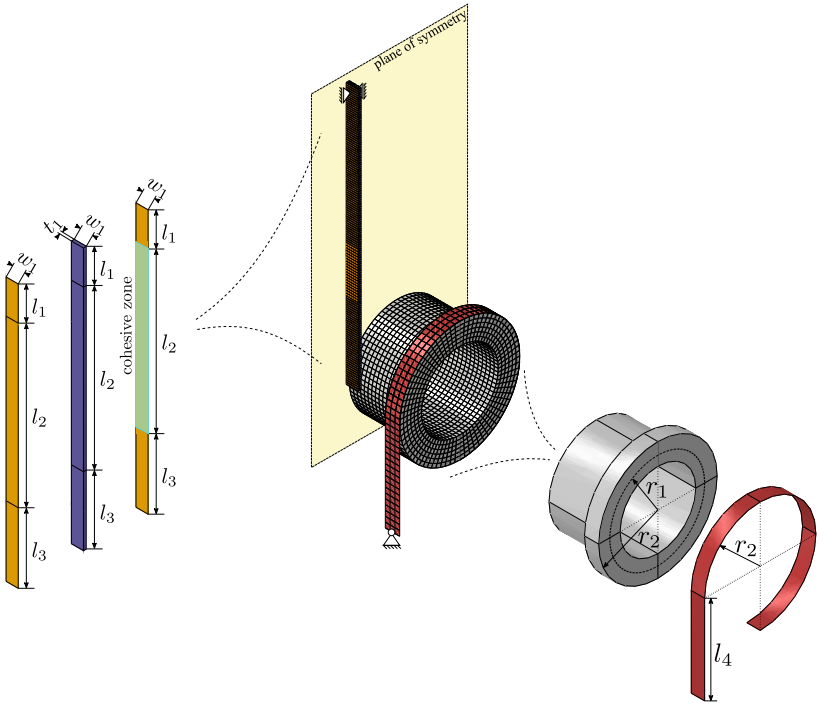

Figure 6.15: Assembly of the numerical model with the mesh structure of the final simulation and corresponding part geometries. The relevant dimensions (and purpose) in the model are $l_1 = 35\,\text{mm}$ (clamping), $l_2 = 165\,\text{mm}$ (cohesive layer), $l_3 = 72\,\text{mm}$ (free end), $w_1 = 12.5\,\text{mm}$ and $t_1 = 3\,\text{mm}$ for the Co-Dico structure, and $r_1 = 50\,\text{mm}$ (peel radius), $r_2 = 62.5\,\text{mm}$ (winding radius) and $l_4 = 100\,\text{mm}$ (free ribbon length) for the test rig dimensions. Graphic reused from the author's publication in Christ et al. [148].

The drum is modeled as a rigid body (R3D4) with a uniformly distributed mass density. Horizontal motion of its center is constrained, allowing only a vertical

displacement. Likewise, all rotational degrees of freedom are constrained, with only the rotation about its central axis left unconstrained. The straps are modeled as an isotropic membrane structure (M3D4R) assuming generic elastic properties of steel. Using membrane elements instead of shell elements has the advantage of avoiding bending moments. The upper part of the band is wrapped contiguously around the drum for $270°$ and the very end is attached to r_2 of the drum. The lower end of the band is fixed. The Dico structure is a 3D deformable model (C3D8R) with an anisotropic material assumption. The Co structure consists of shell elements (S4) with an orthotropic material symmetry. One Co part is attached coherently to the backside of the Dico part without the possibility of separating. The other Co part is attached to the front side of the Dico part using cohesive surfaces, leaving the lower part disconnected where the PTFE foil would be positioned in the experiment. Its lower end is connected to r_1 of the drum. The upper part of the specimen is partitioned and connected coherently to model the clamping of the specimen.
In a previous study [148], the sensitivity of the FEM model with respect to material parameters, mesh density and mass scaling was investigated. This shall not be repeated here. The interested reader is referred to this study.

Simulations were performed with a general contact formulation, with the exception of a cohesive surface definition between the Co, which is to be peeled off, and the Dico structures. Assigning constant cohesive properties along the whole length of the interface would not capture the experimental results well. Instead, this would lead to an imminent jump in the force signal, once the drum position reaches the intact interface. Therefore, the observation of the initial linear increase in force would be ignored. Rather, it is necessary to linearly vary the separation energy over the so called *influence zone*. Therefore, the initial length of 48 mm was partitioned into $n = 20$ segments of equal length, for which the cohesive separation energy was assigned piecewise constant, which is illustrated in Fig. 6.16. From the first segment adjacent to the PTFE foil with a minimal separation energy of close to zero, the separation energy is increased with a constant increment towards the other end of the *influence zone* until the final value of the fracture energy is reached.

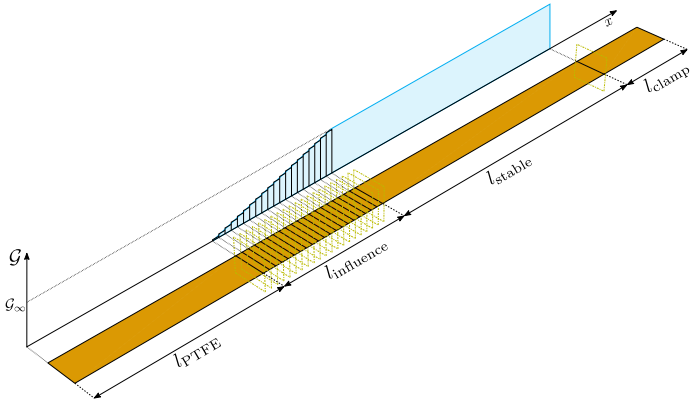

Figure 6.16: Distribution of the separation energy within the cohesive zones for the Co tape. The cohesive length is split into a stable length, where the energy is assumed to be constant, and an influence length, in which the energy increases for each segment by a constant step to approximate the assumption of a linear distribution between the PTFE foil and the stable region. Graphic reused from the author's publication in Christ et al. [148].

The model consists of a single simulation step in which a displacement rate, i.e., a velocity, is prescribed to the upper clamped part of the specimen. Preliminary simulations with the explicit solver revealed excessive vibrations in the model when the displacement rate was assumed to be constant over the whole step. To alleviate this, the displacement rate was applied in the initial phase with a smoothing cosine function. Since gravitational forces also induced significant vibrations in the model, they were removed. Consequently, the average winding force F_w is equal to zero in the simulation, representing an offset or shift to the experimental results. The separation energy in the interface is not affected by this, so that the results can be shifted to the experimental base line.

The linear elastic material parameters for both FRP materials were calculated using a Mori-Tanaka (Dico) and a Halpin-Tsai homogenization procedure in combination with the laminate theory (Co), respectively. The utilized implementation was published in the Python package `HomoPy` [243], which was described above in Sec. 6.3.1. The input parameters for the homogenization methods were taken from a previous study on the same material system [185]. The findings in the mentioned study were that the stiffness properties of carbon long fiber reinforced

PA6 is overestimated when using a Mori-Tanaka homogenization. Reasons for this are that the experimentally determined aspect ratio is not sufficient to describe the complex microstructure including fiber interactions and bundle agglomerations, which were visible in micro-CT scans. As a result, the homogenization methods would overestimate the stiffness properties in the longitudinal direction. To circumvent this, a synthetic aspect ratio in alignment with Suarez et al. [244] was used to fit the longitudinal stiffness properties to the experimental results in Scheuring et al. [185]. Corrected results are compared to experimental findings in Fig. 6.17. All material parameters are listed in Tab. 6.3 and Tab. 6.4. For different conditioning states the material parameters were not changed with respect to humidity effects. Only the parameters within the cohesive surface modeling were fitted to the experiments.

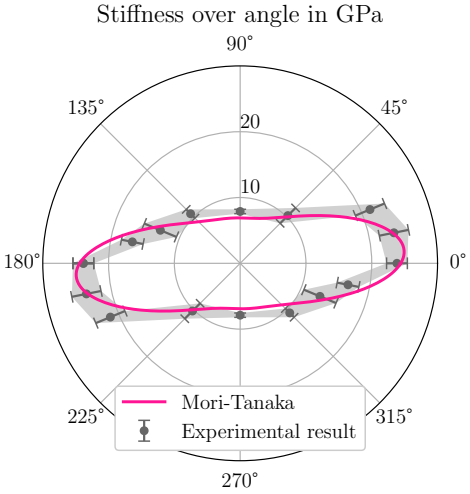

Figure 6.17: Polar plot of the stiffness properties of CF-PA6 (Dico) within the plane parallel to the casting mold: experimental results from Scheuring et al. (2024) and a corrected Mori-Tanaka homogenization using HomoPy (cf. Christ et al. [243]). Graphic reused from the author's publication in Christ et al. [148].

Table 6.3: Material parameters used in the simulation. E_i and G_{ij} are given in MPa and ϱ is given in g/cm^3, respectively.

	E_1	E_2	ν_{12}	G_{12}	G_{13}	G_{23}	ϱ
Drum	-	-	-	-	-	-	2.70
Bands	210000.0	-	0.3	-	-	-	7.85
Co	108700.0	11039.2	0.3	4092.0	4092.0	1118.3	1.48
Dico	see Tab. 6.4						1.27

Table 6.4: Material parameters used for Dico in the simulation in MPa.

D_{1111}	D_{1122}	D_{2222}	D_{1133}	D_{2233}	D_{3333}	D_{1112}
29480.2	6673.9	10412.1	4866.4	4983.5	8362.6	1.2

D_{2212}	D_{3312}	D_{1212}	D_{1113}	D_{2213}	D_{3313}	D_{1213}
51.7	13.9	1736.2	-28.5	-3.0	11.5	8.7

D_{1313}	D_{1123}	D_{2223}	D_{3323}	D_{1223}	D_{1323}	D_{2323}
1840.5	1170.9	142.6	-7.3	-2.7	0.6	3626.0

6.3.3 Results

The final fracture energy for each conditioning scenario was calculated exclusively from the stable region between displacements of 32 mm and 50 mm. This analysis utilized the method illustrated in Fig. 6.3 and is based on Eq. 6.4, with $\Delta u_0 = 18$ mm. The effective fracture energy values $\mathcal{G}_c$ were determined to be $1.0\,\mathrm{kJ/m^2}$ for dried samples, $2.0\,\mathrm{kJ/m^2}$ for those at room environmental conditions, $2.7\,\mathrm{kJ/m^2}$ for moist samples, and $2.07\,\mathrm{kJ/m^2}$ for immersed samples. The damage initiation traction was uniformly established at $t_0 = 1.0$ MPa across all conditions, because higher values lead to pronounced oscillations and lower values lead to early debonding [148]. The numerical results are depicted in Fig. 6.18.

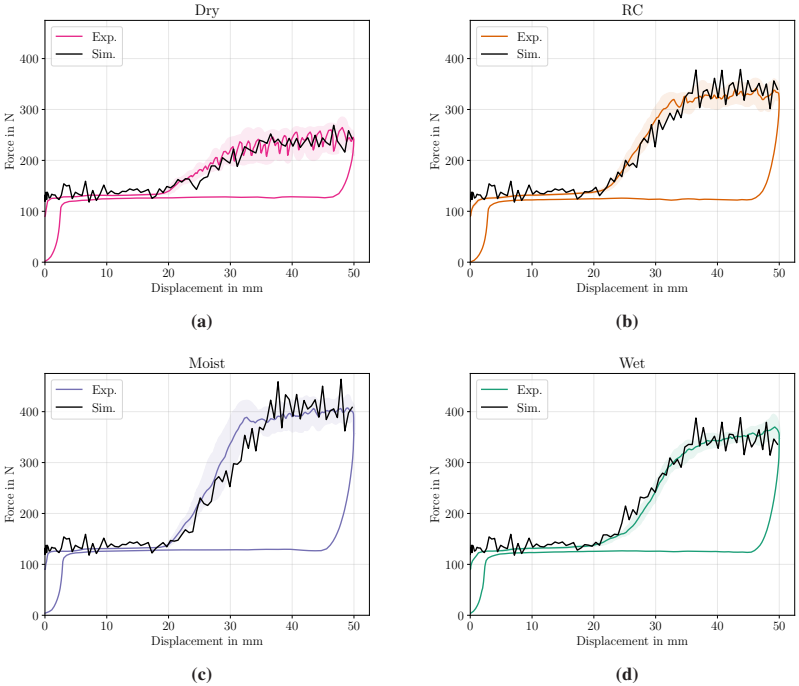

Figure 6.18: Numerical results of CDP test in comparison with the averaged experimental results and calculated response corridors using the arc-length based averaging scheme (cf. [213]). (a) shows the results for dried specimens, (b) for specimens conditioned at room climate, (c) moist specimens and (d) specimens immersed in water. The force signal was multiplied by 2 to account for the symmetric boundary condition and an offset of 129 N was added to account for gravitational forces, which were not considered in the simulation. Graphic reused from the author's publication in Christ et al. [148].

In the initial force signal, increased oscillations are observed that do not appear during the experiments. This phenomenon occurs because, at the beginning of the explicit simulation, oscillations develop that are not dampened due to the absence of viscous properties in the material model. As the crack initiates, these oscillations persist with a slightly higher amplitude. The maximum separation force and energetic characteristics of the experiments are accurately represented across all conditioning states, demonstrating a high sensitivity to the cohesive

parameters, particularly the separation energy. However, the simulation for the moist condition shows a slightly slower rate of increase in the force signal (see Fig. 6.18c), which leads to a delayed average stabilization of the force signal.

A key requirement of the modeling approach used was to divide the influence zone after the PTFE foil into smaller segments with piecewise constant cohesive properties, allowing for a consistent slope of the force signal, similar to what was observed in the experiments. This is an important finding which demonstrates that assuming a constant critical energy release rate across the consolidation zone leads to numerical results which do not align with experimental findings. Once the drum reaches the last segment, the force signal remains relatively constant on average.

It is important to emphasize that the chosen method of utilizing cohesive surfaces, without a model for microstructural processes (such as humidity controlled plasticization), can only capture the general shape of the force-displacement curves. The oscillations present, as seen in Fig. 6.18a, cannot be accounted for by the current model. To improve the modeling capabilities and gain a deeper understanding of the aforementioned microstructural processes, such as the alternating ductile/brittle crack propagation or hydrolytic effects, a more complex material model would need to be developed.

6.4 Discussion

In the previous section, the macroscopic interface between Co and Dico was investigated both experimentally and numerically using the CDP test, considering four different moisture contents. In contrast to investigating the microscopic interface between fiber and matrix, testing was conducted only at room temperature. The recorded change in weight demonstrated that the Co-Dico specimens could absorb over 6 % of their dry mass in water. In contrast, the literature reports that neat PA6 can absorb over 9 % of water in a saturated state [17, p. 340]. Since carbon fibers and the PTFE tape are not hygroscopic structures, water absorption

occurs exclusively in the matrix material, where only the amorphous regions of the semicrystalline polymer contribute to the weight increase. The nominal densities and geometric proportions of Co and Dico, along with their individual weight fractions, yield a total fiber mass and volume fraction of approximately 40 % and 30 %, respectively, according to the relation in Eq. 2.13. If the maximum absorbed amount of water, 6.35 % (by mass), is distributed to the mass fraction of PA6 in the hybrid composite, this corresponds to an uptake of slightly over 10 % compared to its dry weight. Therefore, it can be assumed that the experimental series covers both maximum dry and maximum wet specimens.

There are several commonalities among the conditioning states. In all states, it was observed that the force increase during the initial crack propagation did not occur abruptly but rather increased gradually. This region also exhibited a distinct fracture appearance in the optical images. It can be inferred that the quality of the interface for the investigated specimen geometry is inhomogeneous. During the manufacturing of the specimens, the Dico plastificate was placed above the PTFE tape within the LFT-D process (cf. Fig. 6.4). When the press is closed, the Dico material flows from there to the other side of the mold. The Dico plastificate has a higher core temperature since its surface has already had time to cool after exiting the extruder, as described in Schelleis et al. [191]. Upon closing the press, the cooler Dico plastificate shell is initially consolidated beyond the PTFE tape with the continuous reinforcement tape. As the polymer is compressed further, warmer core material is pushed out of the plastificate and comes into contact with areas of the Co material that are farther from the initial plastificate inlay position, leading to a stronger bond. This temperature gradient of the Dico FRP ultimately leads to an increase in consolidation quality along the flow direction until a stable region is reached. The experimental force-displacement curves suggest this because a sudden jump to the corresponding force level would have been expected if the fracture toughness had been constant along the specimen instead of a gradual increase. The subsequent simulations, in which this region was assigned an increasing rather than constant critical energy release rate that adequately reflected this increase, can corroborate this hypothesis. Contrary, assigning a constant critical energy release rate along the interface in Christ et al.

[148] showed a sudden increase in the force signal. It needs to be highlighted that due to the shell-core effect in the Dico material and the planar fiber orientation of the Co material, fibers do not bridge the interface within the consolidation plane in the Co-Dico hybrid. Rather, it seems fair to assume that a matrix rich region established between Co and Dico during consolidation, as is well known for layered tape reinforcements [245]. This can be followed from the fracture surfaces, e.g., in Fig. 6.13, as no fiber was oriented out of the fracture plane. Therefore, the interface resembles a rather unreinforced section and its quality strongly depends on the consolidation temperature to provide a good polymer bond.

In the force-displacement curves in Fig. 6.5, it was clearly observed that an increase in moisture initially led to an increase in the critical energy release rate. A comparison with the fracture images, both visually and within the SEM, allows for initial conclusions about the underlying mechanisms. In the dry state, a characteristic alternating fracture surface pattern, which switched between ductile and brittle fracture, was observed. This pattern was also occasionally recognizable in the lightly moistened samples (RC). Transferable results have already been reported by Plummer et al. [246]. It was found that reinforced PA6 exhibits moisture and rate-dependent fracture behavior. Higher moisture levels and lower crack propagation rates correlated with ductile fracture patterns, while the absence of moisture or high crack speeds were associated with brittle fractures. The fundamental mechanism reported is the plasticizing effect of water. Applying this to the present results leads to the following interpretation. In the dry state, the chain mobility within PA6 is reduced, which corresponds with a diminished ability for plastic deformation. During the experiment, tensile stresses build up at the crack tip due to the upwards climbing drum. Due to the low deformation potential, the crack tip does not run synchronously with the drum position. Instead, a relative displacement occurs, causing the crack propagation speed to be slower than the advancement of the drum position. This slow speed results in ductile and stable crack growth, when the critical energy release rate is overcome locally. Once the positional difference and the associated stresses reach a critical value, the crack propagates suddenly to relieve the stress at the crack tip. This unstable crack

propagation at high crack tip speeds leads to the observed brittle fracture patterns, since the time increment is too small for the matrix to deform plastically. This sudden crack advancement correlates in the force-displacement diagram with the recurring drops in force, which were only observed in the dry state. Essentially, the observed oscillations for the dry specimens arise from stick-slip behavior during crack propagation, revealing that the crack front does not align with the precise center of the drum at all times. For the other conditioning states, where moisture was present in the specimen, brittle fracture does not occur. Supporting the hypothesis, the increased polymer plasticity allows the crack to propagate along with the drum, giving enough time to deform plastically. Hence, the fracture surface are homogeneous and a stick-slip behavior was not observed.

Particular attention is given to the renewed decrease in the critical energy release rate for the samples that were conditioned in liquid water and, therefore, absorbed the most water. In this case, the optical fracture appearance did not differ from the other two moist conditioning states. However, within the SEM, a changed but still ductile fracture pattern was observed as seen in Fig. 6.12. On one hand, it was noted that crack propagation occurred along the fiber-matrix interface of the continuous reinforcements. On the other hand, it was observed that the deformation of the matrix was reduced compared to the other moist conditioning states. Due to direct contact with water and the high absorption of it, not only plasticizing effects occurred, but much more hydrolytic effects dominated. Hydrolysis effectively shortens the molecular chains and leads to a recrystallization of the polymer, which in turn results in a lower capacity for plastic deformation and, consequently, a reduced fracture surface energy. These mechanisms and their influence on crack propagation under *Mode I* were already addressed by Arhant et al. [53, 54]. Future studies should focus on whether prolonged conditioning would eventually lead to further shortening of the polymer chains due to progressive hydrolysis, followed by a reduction in plastic deformation and eventually brittle fracture patterns.

Furthermore, the trajectory of the crack propagation needs to be addressed. A commonality among all conditioning states is that the crack never significantly breaks out of the imagined interface between Co and Dico, nor does it run exactly

within it. However, differences between the conditioning states are noticeable. For the dry and room-conditioned samples, it is evident that the crack primarily propagates beneath the Dico surface, as indicated by the minimal presence of Co imprints on the Dico side, along with the observation of some Dico fibers in the fracture appearance of the detached Co side. In contrast, for the two more humid conditioning states, distinct Co imprints are visible on the Dico side, and there is even a transfer of Co fibers, indicating partial crack growth beneath the Co surface as well. Particularly prominent are the exposed Co fibers within the fracture surface of the detached Co side for the wet conditioning, suggesting that the crack runs clearly along the fiber-matrix interface of the continuous reinforcing fibers, as was already observed in other studies [247, 248, 249]. It was reported in Gagani et al. [250] that the diffusivity of water in fiber direction is up to 15 times higher than in radial direction, with the interpretation that water diffuses faster along the weak/debonded fiber-matrix interface. With this in mind and the fact that only for the wet conditioning the specimens were fully immersed in water over a longer time period, it seems reasonable to conclude that the diffusion of water into the Co-Dico hybrid is accelerated through the long diffusion paths along the continuous reinforcements. The already mentioned hydrolitic effects, accompanied by increased eigenstresses following moisture induced swelling likely degrades the fiber-matrix interface in this region, paving the way for a pronounced crack propagation along this region of diminished toughness. This correlates well with the observation that the crack propagation occurs predominantly along the continuous interface.

From a linear-elastic fracture mechanics perspective, the observed crack path is consistent with what is expected for a stiff layer bonded to a more compliant substrate. For a bi-material interface, the competition between interfacial crack growth and penetration into one of the adjoining phases is governed by the elastic mismatch and the ratio of fracture toughnesses of the interface and the constituents [251]. It has been shown that, for certain combinations of elastic mismatch and toughness ratios, which includes the case of a relatively tough compliant material bonded to a stiffer phase, a crack tends to deflect into and remain along the interface, particularly when the stiffer material is at least as tough as the interface

[252]. In the present system, the Co is stiffer than the underlying Dico, so the elastic mismatch promotes interfacial cracking as long as the interfacial fracture toughness is lower than that of either phase. The fact that the crack remained confined to the consolidated Co-Dico zone for all conditioning states therefore indicates that, according to these criteria, the interface is the energetically preferred crack path. Deep crack growth into the continuously reinforced phase would require significant fiber breakage. Consequently, the continuous fibers guide the crack along the Co-Dico interface. Although the crack also propagates beneath the Dico surface depending on the conditioning state, a deeper penetration would only prolong the possible crack path. Thus, the crack remains close to the Co-Dico interface due to the tendency to minimize the energy required for crack advance. The occasional transfer of short fibers from the discontinuous layer onto the tape can be interpreted as local crack kinking into the Dico phase followed by fiber pull-out or breakage. This is expected when microstructural heterogeneity and mixed-mode loading locally increase the driving force for cracking in the Dico composite to a level comparable to, or slightly exceeding, that for pure interfacial fracture. Additionally, particularly in the initial crack growth phase, shortly after the PTFE tape, there is poorer consolidation, which facilitates crack propagation along the Co-Dico interface.

7 Discussion

The individual subtopics, including the description of the nonlinear, viscoelastic matrix behavior, the characterization of the fiber-matrix interface, and the characterization of the Co-Dico interface, have been discussed individually in the corresponding chapters (see Chapters 4, 5, and 6). The following will discuss the overarching perspective concerning the initially formulated research questions.

The first question addressed the description of the nonlinear, climate-dependent matrix behavior. The conducted creep experiments clearly demonstrated this nonlinearity. A strong temperature and humidity dependence was observed confirming the findings in the literature [44, 45, 46]. An increase in temperature and/or humidity was consistently associated with increased compliance and accelerated viscous effects. The nonlinearities under loading were particularly amplified by increased humidity. This aligns with the literature regarding the plasticizing effect of water in hygroscopic polyamide 6 [42], wherein the increased chain mobility leads to enhanced sliding of molecular chains for a given load, effectively resulting in a greater tendency for creep.
In selecting the four different climatic conditions, it was taken into account that the glass transition temperature of PA6 is humidity-dependent. Generally, there is no consensus in the literature on an exact value for T_g and its precise functional dependence on humidity. To avoid reliance on external literature data, which can be significantly scattered, values for T_g and crystallinity used here were based on the exact same material examined in related studies [59, 192]. Based on models in the literature, the positions of the various climatic conditions in relation to T_g were determined. The two dry climates lie below T_g, the warm-humid climate is significantly above T_g, and the cold-humid climate is in the transition region. The relative positioning of the climate points with respect to T_g is essential, as the

material behavior varies significantly above and below T_{g}, making both regions technically relevant due to the variability of T_{g}. Thus, T_{g} may be exceeded even at room temperature under increased humidity. Confirmation of this fact can be found in the experimental results, which demonstrate a drastically increased creep tendency for the two humid climates that lie within and above the glass transition. Since these experiments also form the basis for the later interpretation of interfacial mechanisms, a more universal understanding can be established rather than focusing solely on one of the two areas.

For the numerical description, a generalized Kelvin-Voigt material was extended to account for nonlinearities according to Schapery [136, 197, 196, 253]. The numerical results provided an excellent representation of the viscoelastic behavior for the four different climatic conditions. To calibrate the parameters, an algorithm-based error minimization approach was used, thereby avoiding a human-driven and inconsistent calibration process. The resulting parameters fell within a physically meaningful range of values, neither excessively high nor low, allowing for the conclusion that the selected material degrees of freedom are sufficient. Other models in the literature reference similar frameworks with significantly more parameters [254]. While this increases the flexibility of the model, allowing for a near-arbitrary reproduction of experimental results, the uniqueness of the derived parameters is compromised, making physical interpretation considerably more challenging.
Nevertheless, this is not a mechanism-based model. Therefore, the diffusion of water, recrystallization, and hydrolysis effects are only represented indirectly. Other models that explicitly consider these mechanisms could provide additional value by quantifying the contributions of each mechanism to the degrading effects of water and temperature. However, this would significantly increase complexity, further complicating the already ambiguous parameter identification of the chosen material model. A noted disadvantage of the material model used here is that the calibrated parameters are only valid for the selected climate. Thus, interpolation between the studied climates is currently not possible, although theoretically achievable through introduced shift factors in temperature and humidity [255].

The underlying question regarding the climatic influences on interfacial mechanisms and the accompanying literature review uncovered gaps in the conventional experimental methodology, which could be addressed within this study. To the best of the author's knowledge, no literature reports the simultaneous conditioning of micro-samples to characterize the fiber-matrix interface during the course of experimentation. The reasons for this are manifold. On the one hand, conventional conditioning devices are very expensive. On the other hand, the often specialized experimental setups cannot easily accommodate these conventional conditioning devices, which are frequently much larger than the micro-mechanical experimental setup itself. Due to the small sample sizes and the associated rapid deconditioning, a necessity for the further development of conventional methodology was identified.

To close this gap, a cost-effective conditioning system was developed that is capable of quickly maintaining a stable environment within the relevant temperature and humidity ranges. For setting the relative humidity, the process of deliquescence was employed, which has long been known in museum settings for establishing precise humidities to conserve delicate objects [256]. However, this cost-effective methodology has not yet been utilized in experimental mechanics. By choosing an appropriate salt solution, a wide range of desired relative humidities can be set, while the desired temperature can be controlled using a simple PID implementation. The combined principle of active temperature regulation with passive humidity adjustment can, in principle, be applied to a variety of other micromechanical investigations. This would enable the conditioning of other tests, such as the fiber fragmentation test or the microbond test, thereby generating new insights. There are practically no limits to the application scope, so other research areas could also benefit from this methodology, provided there is an interest in conducting continuously climate-controlled experiments at the microscopic scale. It should be noted that it is currently unknown whether this methodology can be transferred to large test volumes. There is a possibility that the extended time required to establish a stable climate could render its use economically unfeasible. The experimental methodology for the macroscopic interface could also be expanded. In this case, a relatively unknown test, the climbing drum peel test, was adapted to gain new insights for atypical test samples, specifically the Co-Dico

specimens. Until now, the macroscopic bonding of fiber reinforced materials has often been studied using the DCB test, which is inadequate due to the inherent asymmetry of the Co-Dico specimens. This work demonstrated that this test is suitable for the qualitative determination of interfacial properties, and that its numerical investigation provides deeper insights. The combined experimental and numerical investigation provided strong evidence that the consolidation quality of unidirectionally reinforced LFT-D is inhomogeneous and depends on the initial position of the Dico plastificate. The temperature gradient between the outside and inside of the plastificate, as noted in another study [191], offers an explanation for why good consolidation only occurs in a later flow region through contact with warmer LFT-D material. In future studies, this could also be systematically investigated using the CDP test, with the temperature gradient being recorded to quantify its influence.

Regarding the interfaces, both at the microscopic and macroscopic scales, it was clearly demonstrated that there is a dependency on the climatic boundary conditions. In the case of the fiber-matrix interface, the measured IFSS continuously decreased with increasing temperature/humidity. The fracture surface energy also decreased, although it increased again in the warm-humid climate. Interestingly, this trend in the applied fracture work is in stark contrast to the results observed for the macroscopic interface. Here, the absorption of water initially led to improved toughness, due to the plasticizing effect of water, which was later reduced again due to hydrolytic effects. This indicates that the influences of moisture on the microscopic and macroscopic interfaces should be evaluated differently. However, there is no contradiction, as the following argument will illustrate. Based on the single fiber pull-out tests, it was shown that the bonding between fiber and matrix is primarily mechanical in nature and that this bond degrades in a humid state. The reasons for this could be found through numerical investigation, particularly in the field of residual stresses. An increased moisture content leads to a volumetric expansion, which causes the matrix material to expand away from the fiber in the single fiber experiment, thereby reducing the radial stresses, which are additionally diminished due to accelerated relaxation processes. Consequently, the mechanical pressure between the matrix and fiber is lower. In the case of

the macroscopic interface, this means that a weaker fiber-matrix bond now represents a lesser constraint on the kinematics of the surrounding matrix material. In other words, a poorer bonding leads to increased freedom of deformation for the surrounding polymer, as described by Horst and Spoormaker [257]. It was reported that a better fiber-matrix bond correlated with lower matrix plasticity. Thus, an overlap of effects occurs. Both a moisture-weakened fiber-matrix interface leads to higher matrix plasticity, and moisture itself, through its plasticizing effect, contributes to greater plasticity. This combination became evident in this investigation, as a moderate increase in moisture led to higher toughness of the Co-Dico interface, which was accompanied by increased damage to the fiber-matrix interface, as evidenced by exposed fibers and fiber imprints. This clearly indicates that the bonding quality of the single fiber does not allow for direct conclusions about the bonding between different types of FRPs. Rather, a poorer fiber-matrix bond can also have positive effects on the macroscopic interface, as demonstrated by the increased toughness.

Nonetheless, it must be emphasized that the single fiber pull-out experiment is a model experiment. The pressures and temperatures present in the actual process cannot be reproduced in this setup. Potential effects on the fiber-matrix interface can only be inferred from the investigations within this work. For instance, it was observed in the macroscopic interface, under real processing conditions, that most fibers retained at least some residue of matrix material. In contrast, all fibers that were pulled out in the pull-out experiment were completely free of matrix material. Therefore, the results are only conditionally transferable from one scale to the next. This fact must be taken into account when performing a scale-crossing interpretation of interfacial properties within fiber composites, as clearly demonstrated by the findings presented here.

8 Summary and outlook

The goal of the present work was to investigate the interfacial mechanics and their mechanisms within carbon fiber reinforced Polyamide 6. The composite under investigation is a hybrid composed of continuous (Co) and discontinuous (Dico) reinforcements, which combines the advantages of local maximum stiffness and strength of Co with the design flexibility of Dico. This results in two interfaces: the microscopic interface between fiber and matrix, and the macroscopic interface between Co and Dico. Polyamide 6, being the matrix material studied, is a semicrystalline thermoplastic. Due to its hygroscopic structure, it tends to absorb water, making it particularly sensitive to climatic boundary conditions in relation to its typical temperature dependence for thermoplastics. Therefore, special attention was paid to the influence of temperature and humidity on the damage mechanisms of the two interfaces.

The first objective of the study was to investigate the viscoelastic behavior of the neat polymer under various environmental influences. Creep tests revealed that the mechanical properties of PA6 are highly dependent on temperature and humidity. An increase in temperature and/or humidity led to increased compliance and a greater tendency for creep, particularly above the glass transition temperature T_g. Additionally, a pronounced nonlinearity in loading was observed. To describe the climate-dependent, nonlinear viscoelastic material behavior, a generalized Kelvin-Voigt model was extended according to Schapery's theory and implemented and validated within a `UMAT` in `Abaqus`. It was demonstrated that the chosen model can excellently reproduce the experimental results.

In the second step, the microscopic interface, specifically the fiber-matrix bond, was characterized. This required an extension of the experimentally established

methodology from the literature, enabling single fiber tests to be conducted under stable climatic conditions. The employed test is the single fiber pull-out test. It was shown that the properties of the fiber-matrix bond are dependent on both temperature and humidity. The numerical investigation, based on the calibrated nonlinear matrix model and cohesive surfaces, was able to replicate the experimental results effectively. In combination with the experimental findings, which resulted in completely bare fibers, a thermo-mechanical study of the residual stress field provided the conclusion that the bonding mechanisms within the investigated CF-PA6 composite are primarily mechanical in nature. The property of PA6 to increase in volume upon water absorption leads to a reduction in the radial stresses between the fiber and matrix. Additionally, the accelerated relaxation processes contribute to further stress reduction at elevated temperatures. Thus, it was demonstrated that the fiber-matrix bond is strongly influenced by the mechanical residual stress field. It was also observed that swelling due to moisture absorption results in a reduction of friction work.

In the final step, the macroscopic interface was examined. To this end, the climbing drum peel test was repurposed, and it was demonstrated that the test is suitable for quantifying the interfacial properties under various moisture contents. It was found that a certain level of moisture increases the fracture toughness of the Co-Dico interface. The cause of this improvement is the plasticizing effect of water in PA6. Humid PA6 exhibits increased plastic deformability compared to dry PA6, resulting in a consistently ductile fracture surface. However, excessive moisture leads to a subsequent decrease in fracture toughness, attributed to the damaging effects of hydrolysis. This results in a renewed reduction in the ductility of the matrix material and an increasing degradation of the fiber-matrix interface, due to the weakening effect of water on the microscopic interface.

In a final discussion, the commonalities of the two interface investigations were brought together. It could be argued that a poor fiber-matrix bond does not necessarily lead to a lower interface quality within the Co-Dico composite. Instead, a relatively weaker fiber-matrix bond can result in increased deformability of the matrix material, which, combined with the additional plasticity gained from water

absorption, even contributes to an increase in the fracture toughness of the hybrid FRP.

Throughout the course of this work, several methodological optimization opportunities arose that should be considered in future studies:

- In the present investigation, simplifying assumptions were made. The numerical models were, in many cases, simplified. It was particularly assumed that material models calibrated under specific environmental conditions could also be applicable throughout a thermal process. This simplification overlooks the fact that significant changes in material behavior occur along the thermal process, which should be better accounted for in future studies.
- During the single fiber pull-out test, no particular attention was paid to keep the free fiber length consistent between each experiment. As a result, the slopes in the force-displacement curves are difficult to compare. In future studies, care should be taken to ensure that the free fiber lengths are comparable and, if possible, kept to a minimum to minimize elastic energy.
- Different conditioning states were considered during the experiments on both scales. However, no comparison was made with reconditioned samples. Only through such a comparison could a statement be made regarding the reversibility of the identified mechanisms.

Furthermore, this work provides a foundation for future studies focusing on the characterization of interfaces within fiber reinforced polymers. On the one hand, it should be noted that previously unconsidered aspects may also contribute to damage, such as aging due to UV radiation. On the other hand, the developed extensions of the experimental methodology can also be applied to other systems that do not necessarily fall within the material class of FRPs.

A Appendix: Shear-lag

Using the shear-lag assumption in Eq. 2.27 and the assumption that the frictional shear stress τ_f acting on the debonded fiber ends is constant, the axial fiber stress is given with

$$\sigma_\mathrm{f} = \begin{cases} 2\tau_\mathrm{f} a(\frac{l_\mathrm{f}}{2}x + 1), & -\frac{l_\mathrm{f}}{2} \leq x \leq \frac{l_\mathrm{f}}{2}(m-1), \\ E_\mathrm{f}\varepsilon_\mathrm{m} + (2\tau_\mathrm{f} - E_\mathrm{f}\varepsilon_\mathrm{m})\frac{\cosh(nx/r_\mathrm{f})}{\cosh(na(m-1))}, & \frac{l_\mathrm{f}}{2}(m-1) \leq x \leq \frac{l_\mathrm{f}}{2}(1-m), \\ 2\tau_\mathrm{f} a(1 - \frac{l_\mathrm{f}}{2}x), & \frac{l_\mathrm{f}}{2}(1-m) \leq x \leq \frac{l_\mathrm{f}}{2}, \end{cases} \tag{A.1}$$

where it was assumed that the shear-lag model after Cox [64] applies for the length in between the debonded ends and that the axial stress is continuous. Accordingly, the shear stress is given with

$$\tau = \begin{cases} -\tau_\mathrm{f}, & -\frac{l_\mathrm{f}}{2} \leq x \leq \frac{l_\mathrm{f}}{2}(m-1), \\ -(2\tau_\mathrm{f} - E_\mathrm{f}\varepsilon_\mathrm{m})\frac{n\sinh(nx/r_\mathrm{f})}{2\cosh(na(m-1))}, & \frac{l_\mathrm{f}}{2}(m-1) \leq x \leq \frac{l_\mathrm{f}}{2}(1-m), \\ \tau_\mathrm{f}, & \frac{l_\mathrm{f}}{2}(1-m) \leq x \leq \frac{l_\mathrm{f}}{2}. \end{cases} \tag{A.2}$$

To calculate the debonding ratio m for given material parameters and a given matrix strain, the following implicit equation needs to be solved

$$m = \frac{E_\mathrm{f}\varepsilon_\mathrm{m} - 2\frac{\tau_{u,\mathrm{f}}}{n}\coth(na(1-m))}{2\tau_\mathrm{f} a}, \tag{A.3}$$

which enforces that the debonding starts at the IFSS.

B Appendix: Fit of the Norton-Bailey model

The fitted Norton-Bailey law for each conditioning state is visualized below in Fig. B.1.

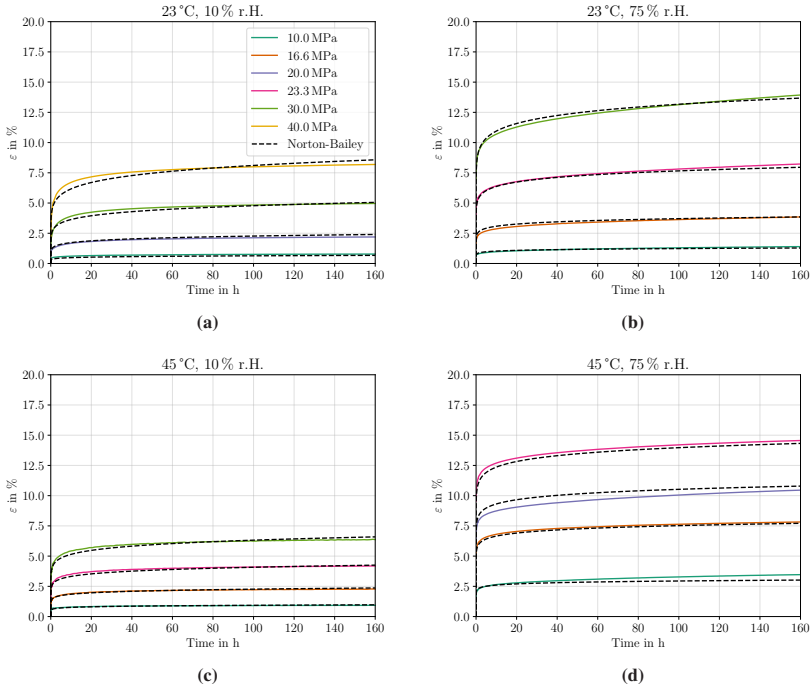

Figure B.1: Fitted Norton-Bailey model for each conditioning state.

C Appendix: Linear viscoelastic model

C.1 1D single element

The Kelvin-Voigt element is a viscoelastic rheological model used for creep modelling consisting of an elastic spring and a viscous dash pot in parallel. It represents a mixture of a linearized elastic solid and a linearly viscous fluid [258, p. 1]. The schematic is shown in Fig. C.1. Keeping in mind that the elastic strain and viscous strain must be identical, the governing equations for the mechanical response for spring and damper are given with

$$\sigma_E(t) = E\varepsilon(t), \tag{C.1a}$$

$$\sigma_\eta(t) = \eta\dot{\varepsilon}(t), \tag{C.1b}$$

respectively. The total stress is given as the sum of elastic and viscous stresses

$$\begin{aligned}\sigma(t) &= \sigma_E(t) + \sigma_\eta(t),\\ &= E\varepsilon(t) + \eta\dot{\varepsilon}(t).\end{aligned} \tag{C.2}$$

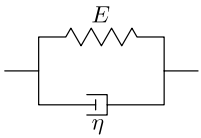

Figure C.1: Schematic of a single Kelvin-Voigt element.

Solution to a stress input

To solve the differential equation in Eq. C.2, it is necessary to first find the homogeneous ε_h solution for

$$\varepsilon_\mathrm{h} + \tau\dot{\varepsilon}_\mathrm{h}(t) = 0, \tag{C.3}$$

where $\tau = \eta/E$. Firstly, the equation is split into two integrals

$$\int \frac{1}{\varepsilon_\mathrm{h}(t)}\,\mathrm{d}\varepsilon_\mathrm{h} = -\int \frac{1}{\tau}\,\mathrm{d}t, \tag{C.4}$$

which gives rise to the following solution

$$\ln \varepsilon_\mathrm{h}(t) = -\frac{t}{\tau} + C. \tag{C.5}$$

Taking the exponent of both sides then gives

$$\varepsilon_\mathrm{h}(t) = C' e^{-\frac{t}{\tau}}, \tag{C.6}$$

where C' is a constant which depends on the initial condition.

To derive the particular solution the constant ansatz of $\varepsilon_\mathrm{p} = C_\mathrm{p}$ is chosen. When plugged into Eq. C.2, this gives

$$C_\mathrm{p} = \frac{\sigma(t)}{E}. \tag{C.7}$$

The combination of homogeneous and particular solution

$$\begin{aligned} \varepsilon(t) &= \varepsilon_\mathrm{h}(t) + \varepsilon_\mathrm{p}(t) \\ &= C' e^{-\frac{t}{\tau}} + \frac{\sigma(t)}{E} \end{aligned} \tag{C.8}$$

can then be solved for the integration constant. Since the dash pot prevents an infinite deformation rate when a load is applied at $t = 0$, the initial condition must be $\varepsilon(t = 0) = 0$, which reveals that $C' = -\sigma_0/E$ and finally gives

$$\varepsilon(t) = \frac{\sigma_0}{E}\left(1 - e^{-\frac{t}{\tau}}\right), \tag{C.9}$$

in the case when a constant stress is applied, $\sigma(t) = \sigma_0$ [204, p. 10].

Laplace transform: Another, arguably more elegant approach to derive a solution for the given rheological model is through the Laplace transform. It can easily be shown that Eq. C.2 transforms to

$$\bar{\varepsilon}(s) = \frac{1}{E + s\eta}\bar{\sigma}(s), \tag{C.10}$$

where $\overline{(\,\cdot\,)}(s) = \mathcal{L}\{\,\cdot\,(t)\}(s)$ indicates the Laplace transform of a function. The application of a sudden load σ_0 at $t = 0$ can mathematically be represented with the Heaviside step function $H(t)$, which has the following properties

$$H(t) = \begin{cases} 1, & \text{if } t > 0, \\ 0, & \text{if } t \leq 0, \end{cases} \tag{C.11a}$$

$$\frac{\mathrm{d}}{\mathrm{d}t}H(t) = \delta(t). \tag{C.11b}$$

Here, $\delta(t)$ is the Dirac Delta function. Together, the stress as a function of time is $\sigma(t) = H(t)\sigma_0$, for which the Laplace transform is given with $\bar{\sigma}(s) = \sigma_0/s$ [204, p. 18]. Inserting the sudden stress load into Eq. C.10 and rearranging gives

$$\bar{\varepsilon}(s) = \frac{1}{s(\frac{1}{\tau} + s)}\frac{\sigma_0}{\eta}. \tag{C.12}$$

Taking the inverse Laplace transform of Eq. C.12 gives the exact same result as in Eq. C.9.

C.2 1D extended Kelvin-Voigt element

Other authors made very comprehensive derivations of the generalized Kelvin-Voigt model, which is out of scope for this publication. The interested reader is revised to Brinson and Brinson [195, p. 173]. The rheological model depicted in Fig. 4.5 is a special case of this generalized Kelvin-Voigt model. It consists of four Kelvin-Voigt elements in which the damping constant of the first element is equal to zero, $\eta_0 = 0$, for which it effectively becomes an elastic spring solely. This leaves an elastic spring in series with three Kelvin-Voigt elements. The governing equations for each element are identical to Eqs. C.1.

Solution to a stress input

It is obvious that the stress for each element is identical and that the total strain is the sum of all individual strains

$$\sigma = \sigma_0 = \sigma_1 = \sigma_2 = \sigma_3, \tag{C.13a}$$

$$\varepsilon = \varepsilon_0 + \varepsilon_1 + \varepsilon_2 + \varepsilon_3. \tag{C.13b}$$

Using the Laplace transform from before, Eq. C.13a and Eq. C.13b can be combined with Eq. C.10 to give the following equality in the Laplace space

$$\bar{\varepsilon}(s) = \left(\frac{1}{E_0} + \sum_{i=1}^{3} \frac{1}{E_i + s\eta_i} \right) \bar{\sigma}(s). \tag{C.14}$$

For now, the stress function is assumed to be of instant type at $t = 0$, $\sigma(t) = H(t)\sigma_0$, which gives

$$\bar{\varepsilon}(s) = \left(\frac{1}{E_0 s} + \sum_{i=1}^{3} \frac{1}{s(\frac{1}{\tau_i} + s)} \frac{1}{\eta_i} \right) \sigma_0. \tag{C.15}$$

Since the Laplace transform is linear, each summand can be transformed back into the real time space individually. The Laplace representation of the addends

in the sum are identical to Eq. C.12, for which the inverse Laplace transform was given in Eq. C.9. Together this gives the following solution for the total strain

$$\varepsilon(t) = \underbrace{\left(\frac{1}{E_0} + \sum_{i=1}^{3} \frac{1}{E_i}\left(1 - e^{-\frac{t}{\tau_i}}\right)\right)}_{=J(t)} \sigma_0, \tag{C.16}$$

where the creep compliance is indicated by $J(t)$. This result is in alignment with Brinson and Brinson [195, p. 174]. The model can then be used to fit the seven material parameters to experimental data. Care must be taken in regards that not all combinations of material parameters are admissible [204, p. 17 ff.].

C.3 Hereditary integral

The preceding section derived the governing equations for the extended Kelvin-Voigt model under a single constant stress jump. In engineering outside of laboratory settings it is common to deal with a complex stress history. The domain of linear viscoelasticity allows for superposition of the strain response as a consequence of n stress jumps at time instances t_i with shifted creep compliances $J(t - t_i)$

$$\varepsilon(t) = \sum_{i=0}^{n} J(t - t_i) H(t - t_i) \Delta\sigma_i. \tag{C.17}$$

In Fig. C.2, this strain response is depicted qualitatively for a single Kelvin-Voigt element for three equal step inputs $\Delta\sigma_i = \Delta\sigma$ at $t_0 = 0\,\mathrm{s}$ and $t_2 = 2t_1$. It is also possible to reverse a stress input at a later time, which is essentially the removing of a load, as it is shown in Fig. C.3, for $\Delta\sigma_0 = \Delta\sigma_2 = -\Delta\sigma_1 = \Delta\sigma$ at $t_0 = 0\,\mathrm{s}$ and $t_2 = 2t_1$. It becomes imminent that any load history can be approximated as the sum of a series of infinitesimal load steps so that Eq. C.17 can be written in an integral expression

$$\varepsilon(t) = \int_{\sigma_0}^{\sigma_\infty} J(t - \tau) H(t - \tau)\, \mathrm{d}\sigma, \tag{C.18}$$

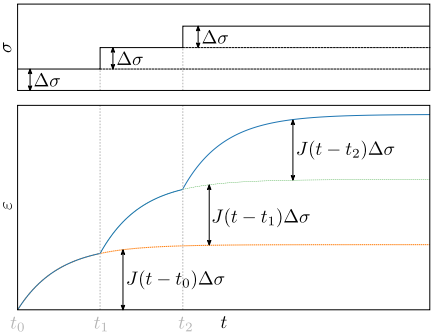

Figure C.2: Strain response of a single Kelvin-Voigt element to subsequent stress inputs.

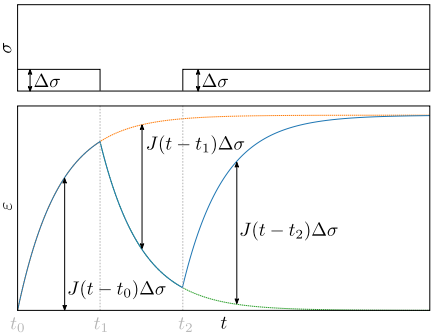

Figure C.3: Strain response of a single Kelvin-Voigt element to subsequent stress inputs when the load input is removed in the interim.

which is called the hereditary integral or memory function, where τ describes the time history variable [199, p. 24]. This again can be written as an integral of time, considering that $\mathrm{d}\sigma(\tau) = \dfrac{\partial\sigma}{\partial\tau}\,\mathrm{d}\tau = \dot{\sigma}\,\mathrm{d}\tau$, which gives

$$\varepsilon(t) = \int_0^t J(t-\tau)H(t-\tau)\dot{\sigma}(\tau)\,\mathrm{d}\tau. \tag{C.19}$$

The Heaviside step function $H(t-\tau)$ is only evaluated in the integral at $t > \tau$, so that $H(t) = 1$. This simplifies Eq. C.19 further to

$$\varepsilon(t) = \int_0^t J(t-\tau)\dot{\sigma}(\tau)\,\mathrm{d}\tau. \tag{C.20}$$

Other, often useful formulation of Eq. C.20, are

$$\varepsilon(t) = \int_0^t \dot{J}(t-\tau)\sigma(\tau)\,\mathrm{d}\tau, \tag{C.21}$$

and

$$\varepsilon(t) = \sigma_0 J(t) + \int_{0^+}^t J(t-\tau)\dot{\sigma}(\tau)\,\mathrm{d}\tau, \tag{C.22}$$

for which the derivations are given in Flügge [204, p. 38].

C.4 Numerical implementation of the extended KV element

Due to computational restrictions it is feasible to transfer the governing equation for the strain response in Eq. C.16 into an incremental form, since this allows for efficient usage of computer memory. The following derivation is done in reference to Woldekidan [199, p. 165 ff.].

Starting with Eq. C.16, the expression can be split into an elastic and a viscoelastic component

$$\begin{aligned}\varepsilon(t) &= \left(\frac{1}{E_0} + \sum_{i=1}^{3}\frac{1}{E_i}\left(1 - e^{-\frac{t}{\tau_i}}\right)\right)\sigma_0 = \left(J_\mathrm{e} + \sum_{i=1}^{3} J_{\mathrm{ve,i}}\right)\sigma_0, \\ &= \varepsilon_\mathrm{e}(t) + \sum_{i=1}^{3}\varepsilon_{\mathrm{ve,i}}(t).\end{aligned} \tag{C.23}$$

Expressing the elastic strain in terms of the Hereditary integral

$$\begin{aligned}\varepsilon_{\mathrm{e}}(t) &= \int_0^t J_{\mathrm{e}}(t-\tau)\dot{\sigma}(\tau)d\tau, \\ &= \frac{1}{E_0}\int_0^t \dot{\sigma}(\tau)d\tau = \frac{\sigma(t)}{E_0},\end{aligned} \tag{C.24}$$

it becomes obvious that the elastic strain increment due to a stress increment must be

$$\Delta\varepsilon_{\mathrm{e}}(t) = \frac{\Delta\sigma(t)}{E_0}. \tag{C.25}$$

Accordingly, the Hereditary integral of the viscoelastic strain reads

$$\varepsilon_{\mathrm{ve}}(t) = \sum_{i=1}^{3}\int_0^t \frac{1}{E_i}\left(1 - e^{-\frac{t-\tau}{\tau_i}}\right)\dot{\sigma}(\tau)\,\mathrm{d}\tau, \tag{C.26}$$

which can further be split into an instantaneous response $\varepsilon^{\mathrm{i}}_{\mathrm{ve}}(t)$, due to the elastic spring solely, and an inherited response $\varepsilon^{\mathrm{inh}}_{\mathrm{ve}}(t)$ to give

$$\varepsilon_{\mathrm{ve}}(t) = \sum_{i=1}^{3}\left(\varepsilon^{\mathrm{i}}_{\mathrm{ve},i}(t) - \varepsilon^{\mathrm{inh}}_{\mathrm{ve},i}(t)\right), \tag{C.27}$$

where

$$\varepsilon^{\mathrm{i}}_{\mathrm{ve},i}(t) = \frac{\sigma(t)}{E_i}, \tag{C.28a}$$

$$\varepsilon^{\mathrm{inh}}_{\mathrm{ve},i}(t) = \int_0^t \frac{1}{E_i}e^{-\frac{t-\tau}{\tau_i}}\dot{\sigma}(\tau)\,\mathrm{d}\tau. \tag{C.28b}$$

According to Eq. C.25, the increment of $\varepsilon^{\mathrm{i}}_{\mathrm{ve},i}(t)$ is

$$\Delta\varepsilon^{\mathrm{i}}_{\mathrm{ve},i}(t) = \frac{\Delta\sigma(t)}{E_i}. \tag{C.29}$$

To derive the increment of the inherited viscoelastic strain $\varepsilon_{\mathrm{ve},i}^{\mathrm{inh}}(t)$, Eq. C.28b is further expanded to

$$\varepsilon_{\mathrm{ve},i}^{\mathrm{inh}}(t) = \underbrace{\int_0^{t-\Delta t} \frac{1}{E_i} e^{-\frac{t-\tau}{\tau_i}} \dot{\sigma}(\tau)\,\mathrm{d}\tau}_{=e^{-\frac{\Delta t}{\tau_i}} \varepsilon_{\mathrm{ve},i}^{\mathrm{inh}}(t-\Delta t)} + \int_{t-\Delta t}^{t} \frac{1}{E_i} e^{-\frac{t-\tau}{\tau_i}} \dot{\sigma}(\tau)\,\mathrm{d}\tau, \tag{C.30}$$

which allows to express the first integral in a recursive manner. Here it becomes clear that each $\varepsilon_{\mathrm{ve},i}^{\mathrm{inh}}$ is a history variable which needs to be tracked for every integration point within the simulation. For the latter integral it is assumed that the stress rate is constant for each time increment $\dot{\sigma}(\tau) = \frac{\Delta\sigma(t)}{\Delta t} = \mathrm{const.}$, so that the integral on the right becomes

$$\begin{aligned} \int_{t-\Delta t}^{t} \frac{1}{E_i} e^{-\frac{t-\tau}{\tau_i}} \dot{\sigma}(\tau)\,\mathrm{d}\tau &= \frac{1}{E_i}\frac{\Delta\sigma}{\Delta t} \int_{t-\Delta t}^{t} e^{-\frac{t-\tau}{\tau_i}}\,\mathrm{d}\tau \\ &= \frac{1}{E_i}\frac{\Delta\sigma}{\Delta t}\tau_i \left(1 - e^{-\frac{\Delta t}{\tau_i}}\right). \end{aligned} \tag{C.31}$$

The assumption of a constant stress rate per time increment is justifiable for the given scope of research, i.e., modeling of the creep behavior, in which the redistribution of stresses within the component takes place rather slowly [1, p. 174]. It must be emphasized that the model loses its validity for rapidly applied or cyclic loadings, e.g. in the case of impact loading. A constant stress rate per time increment also implies that numerical time steps need to be kept rather small to allow for convergence [199, p. 190].

The increment of Eq. C.30 is easily formulated by subtracting $\varepsilon_{\mathrm{ve},i}^{\mathrm{inh}}(t-\Delta t)$, which gives

$$\Delta\varepsilon_{\mathrm{ve},i}^{\mathrm{inh}}(t) = \varepsilon_{\mathrm{ve},i}^{\mathrm{inh}}(t-\Delta t)\left(e^{-\frac{\Delta t}{\tau_i}} - 1\right) + \frac{1}{E_i}\frac{\Delta\sigma(t)}{\Delta t}\tau_i\left(1 - e^{-\frac{\Delta t}{\tau_i}}\right). \tag{C.32}$$

Together, the strain increment is

$$\begin{aligned}\Delta\varepsilon(t) &= \Delta\varepsilon_{\mathrm{e}}(t) + \sum_{i=1}^{3} \Delta\varepsilon_{\mathrm{ve},i}(t), \\ &= \frac{\Delta\sigma(t)}{E_0} + \sum_{i=1}^{3} \left(\frac{\Delta\sigma(t)}{E_i} - \varepsilon_{\mathrm{ve},i}^{\mathrm{inh}}(t-\Delta t) \left(e^{-\frac{\Delta t}{\tau_i}} - 1 \right) \right. \\ &\qquad \left. - \frac{1}{E_i} \frac{\Delta\sigma(t)}{\Delta t} \tau_i \left(1 - e^{-\frac{\Delta t}{\tau_i}} \right) \right).\end{aligned} \tag{C.33}$$

Usually, FE software, such as `Abaqus`, requires a user material subroutine (UMAT) to return the stress increment for each time step instead of the strain increment, which is provided by the software. For this, Eq. C.33 is inverted to result in an expression for the stress increment

$$\Delta\sigma(t) = \tilde{E}(t) \left(\Delta\varepsilon(t) - \sum_{i=1}^{3} \varepsilon_{\mathrm{ve},i}^{\mathrm{inh}}(t-\Delta t) \left(1 - e^{-\frac{\Delta t}{\tau_i}} \right) \right), \tag{C.34}$$

where

$$\tilde{E}(t) = \left(\frac{1}{E_0} + \sum_{i=1}^{3} \frac{1}{E_i} \left(1 - \frac{\tau_i}{\Delta t} \left(1 - e^{-\frac{\Delta t}{\tau_i}} \right) \right) \right)^{-1}. \tag{C.35}$$

3D formulation

To allow for simulations in 3D, it is necessary to extend Eq. C.34 to account for coupling effects in various directions. The derivation is in alignment to [259]. The idea is that Eq. C.34 must reduce to the isotropic Hooke's law when the viscous effects become negligible, which is the case when all $E_i \to \infty$ and/or $\eta_i \to 0$, for $i \geq 1$. This reduction for vanishing viscous effects is therefore also intended for the 3D generalization.

The incremental form of Hooke's law in 3D reads in index notation

$$\Delta\sigma_{ij}(t) = 2G\Delta\varepsilon'_{ij}(t) + 3K\Delta\varepsilon^{\circ}_{ij}(t), \tag{C.36}$$

where G and K are the shear and bulk modulus, respectively, which are material parameters and $\Delta\varepsilon'_{ij}(t)$ and $\Delta\varepsilon^{\circ}_{ij}(t)$ are the deviatoric and volumetric components of the incremental strain tensor, respectively, which are defined as

$$\begin{aligned}\Delta\varepsilon^{\circ}_{ij}(t) &= \frac{\Delta\varepsilon_{kk}(t)}{3}\delta_{ij},\\ \Delta\varepsilon'_{ij}(t) &= \Delta\varepsilon_{ij}(t) - \Delta\varepsilon^{\circ}_{ij}(t),\end{aligned} \tag{C.37}$$

where δ_{ij} is the Kronecker delta

$$\delta_{ij} = \begin{cases} 1, & \text{if } i = j,\\ 0, & \text{if } i \neq j.\end{cases} \tag{C.38}$$

Here, the Einstein summation convention is applied.

Projector formulation: In reference to Itskov [260, p. 134], another form of rewriting Eq. C.36 in the symbolic notation is to use the isotropic projectors

$$\Delta\boldsymbol{\sigma}(t) = (3K\mathbb{P}_1 + 2G\mathbb{P}_2) : \Delta\boldsymbol{\varepsilon}(t), \tag{C.39}$$

which are defined as

$$\mathbb{P}_1 = \frac{1}{3}\boldsymbol{I}\otimes\boldsymbol{I}, \tag{C.40}$$

$$\mathbb{P}_2 = \mathbb{I}^{\mathrm{s}} - \mathbb{P}_1, \tag{C.41}$$

and have the following property

$$\mathbb{P}_i : \mathbb{P}_j = \begin{cases} \mathbb{P}_i, & \text{if } i = j,\\ \mathbb{O}, & \text{if } i \neq j.\end{cases} \tag{C.42}$$

With this property Eq. C.39 can easily be inverted to get

$$\Delta\boldsymbol{\varepsilon}(t) = \left(\frac{1}{3K}\mathbb{P}_1 + \frac{1}{2G}\mathbb{P}_2\right) : \Delta\boldsymbol{\sigma}(t), \tag{C.43}$$

which will become useful later.

It is now assumed that the viscoelastic formulation in Eq. C.34 can be decomposed in the same manner as Hooke's law and that the volumetric and deviatoric parts are likewise separable

$$\begin{aligned}\Delta\sigma_{mn}(t) = 2\tilde{G}(t)\left(\Delta\varepsilon'_{mn}(t) - \sum_{i=1}^{3} {\varepsilon^{\mathrm{inh}}_{\mathrm{ve},i}}'_{mn}(t-\Delta t)\left(1-e^{-\frac{\Delta t}{\tau_i}}\right)\right) \\ + 3\tilde{K}(t)\left(\Delta\varepsilon^{\circ}_{mn}(t) - \sum_{i=1}^{3} {\varepsilon^{\mathrm{inh}}_{\mathrm{ve},i}}^{\circ}_{mn}(t-\Delta t)\left(1-e^{-\frac{\Delta t}{\tau_i}}\right)\right),\end{aligned} \tag{C.44}$$

where the viscoelastic material coefficients are calculated in accordance to Eq. C.35

$$\begin{aligned}\tilde{G}(t) &= \left(\frac{1}{G_0} + \sum_{i=1}^{3}\frac{1}{G_i}\left(1-\frac{\tau_i}{\Delta t}\left(1-e^{-\frac{\Delta t}{\tau_i}}\right)\right)\right)^{-1}, \\ \tilde{K}(t) &= \left(\frac{1}{K_0} + \sum_{i=1}^{3}\frac{1}{K_i}\left(1-\frac{\tau_i}{\Delta t}\left(1-e^{-\frac{\Delta t}{\tau_i}}\right)\right)\right)^{-1},\end{aligned} \tag{C.45}$$

for which identical relaxation times τ_i are assumed, which reduces the amount of independent material parameters. The shear and bulk moduli are calculated in agreement with the theory of isotropic elasticity

$$\begin{aligned}G_i &= \frac{E_i}{2(1+\nu)}, \\ K_i &= \frac{E_i}{3(1-2\nu)},\end{aligned} \tag{C.46}$$

for which the Poisson's ratio ν must be determined experimentally. For semicrystalline thermoplastics it is common practice to assume that the Poisson's ratio is constant and therefore does not change over time [1, p. 44]. This also implies that both the bulk modulus and shear modulus become time dependent. This is

in agreement with Lai and Bakker [261, p. 184] and Fliegener and Hohe [259, p. 4]. The approach of modeling a time dependent Poisson's ratio is discussed in Woldekidan [199, p. 197 ff.]. In this scenario, the bulk modulus is constant in time, with only the shear modulus being a function of time and further being assumed to be incompressible.

In accordance to Eq. C.32, the evolution of the history variables is

$$\begin{aligned}
\Delta\varepsilon^{\mathrm{inh}\,\prime}_{\mathrm{ve},i\,mn}(t) &= \varepsilon^{\mathrm{inh}\,\prime}_{\mathrm{ve},i\,mn}(t-\Delta t)\left(e^{-\frac{\Delta t}{\tau_i}}-1\right)+\frac{1}{2G_i}\frac{\Delta\sigma'_{mn}(t)}{\Delta t}\tau_i\left(1-e^{-\frac{\Delta t}{\tau_i}}\right),\\
\Delta\varepsilon^{\mathrm{inh}\,\circ}_{\mathrm{ve},i\,mn}(t) &= \varepsilon^{\mathrm{inh}\,\circ}_{\mathrm{ve},i\,mn}(t-\Delta t)\left(e^{-\frac{\Delta t}{\tau_i}}-1\right)+\frac{1}{3K_i}\frac{\Delta\sigma^{\circ}_{mn}(t)}{\Delta t}\tau_i\left(1-e^{-\frac{\Delta t}{\tau_i}}\right),
\end{aligned} \tag{C.47}$$

where the factors of $1/(2G_i)$ and $1/(3K_i)$ are added to compensate for the stress-strain relation in Eq. C.39, respectively. To solve the system of equations in the FE software the tangential stiffness $\mathbb{K}(t)$ needs to be calculated, which is

$$\mathbb{K}(t)=\frac{\partial\Delta\boldsymbol{\sigma}(t)}{\partial\Delta\boldsymbol{\varepsilon}(t)}. \tag{C.48}$$

For this, Eq. C.44 is reformulated with the use of the introduced projector formulation

$$\begin{aligned}
\Delta\boldsymbol{\sigma}(t) = &\left(3\tilde{K}(t)\mathbb{P}_1+2\tilde{G}(t)\mathbb{P}_2\right):\Delta\boldsymbol{\varepsilon}(t)\\
&-\left(2\tilde{G}(t)\sum_{i=1}^{3}\boldsymbol{\varepsilon}^{\mathrm{inh}\,\prime}_{\mathrm{ve},i}(t-\Delta t)\left(1-e^{-\frac{\Delta t}{\tau_i}}\right)\right.\\
&\left.+3\tilde{K}(t)\sum_{i=1}^{3}\boldsymbol{\varepsilon}^{\mathrm{inh}\,\circ}_{\mathrm{ve},i}(t-\Delta t)\left(1-e^{-\frac{\Delta t}{\tau_i}}\right)\right),
\end{aligned} \tag{C.49}$$

so that it becomes obvious that the tangential stiffness is

$$\mathbb{K}(t)=3\tilde{K}(t)\mathbb{P}_1+2\tilde{G}(t)\mathbb{P}_2. \tag{C.50}$$

Implementation in `Abaqus`

Since tensor values are stored in the non-normalized Voigt notation in `Abaqus`, the formulations above need to be adjusted to be implemented in a user material (UMAT). `Abaqus/Implicit` uses covariant components (associated with the contravariant basis) for the strain vector, while the stress vector is stored with contravariant components (associated with the covariant basis), i.e., in index notation

$$\sigma^{\alpha} = \begin{pmatrix} \sigma_1 \\ \sigma_2 \\ \sigma_3 \\ \sigma_4 \\ \sigma_5 \\ \sigma_6 \end{pmatrix} = \begin{pmatrix} \sigma_{11} \\ \sigma_{22} \\ \sigma_{33} \\ \sigma_{12} \\ \sigma_{13} \\ \sigma_{23} \end{pmatrix}, \tag{C.51}$$

and

$$\varepsilon_{\beta} = \begin{pmatrix} \varepsilon_1 \\ \varepsilon_2 \\ \varepsilon_3 \\ \varepsilon_4 \\ \varepsilon_5 \\ \varepsilon_6 \end{pmatrix} = \begin{pmatrix} \varepsilon_{11} \\ \varepsilon_{22} \\ \varepsilon_{33} \\ 2\varepsilon_{12} \\ 2\varepsilon_{13} \\ 2\varepsilon_{23} \end{pmatrix}. \tag{C.52}$$

Combining the deviatoric and volumetric parts in Eq. C.47, it follows from comparing coefficients that Eq. C.44 in vector notation in accordance with the `Abaqus` convention gives

$$\underline{\Delta\sigma} = \left(2\tilde{G}(t)\underline{\underline{M}}'_{\varepsilon} + 3\tilde{K}(t)\underline{\underline{M}}^{\circ}\right)\left(\underline{\Delta\varepsilon} - \sum_{i=1}^{3} \boldsymbol{\varepsilon}_{\mathrm{ve},i}^{\mathrm{inh}}(t-\Delta t)\left(1 - e^{-\frac{\Delta t}{\tau_i}}\right)\right), \tag{C.53}$$

where $\underline{\underline{M}}'_{\varepsilon}$ and $\underline{\underline{M}}^{\circ}$ are the deviatoric and volumetric mapping matrices, respectively. They are given with

$$\underline{\underline{M}}'_{\varepsilon} = \frac{1}{6}\begin{pmatrix} 4 & -2 & -2 & 0 & 0 & 0 \\ -2 & 4 & -2 & 0 & 0 & 0 \\ -2 & -2 & 4 & 0 & 0 & 0 \\ 0 & 0 & 0 & 3 & 0 & 0 \\ 0 & 0 & 0 & 0 & 3 & 0 \\ 0 & 0 & 0 & 0 & 0 & 3 \end{pmatrix},$$

$$\underline{\underline{M}}^{\circ} = \frac{1}{3}\begin{pmatrix} 1 & 1 & 1 & 0 & 0 & 0 \\ 1 & 1 & 1 & 0 & 0 & 0 \\ 1 & 1 & 1 & 0 & 0 & 0 \\ 0 & 0 & 0 & 0 & 0 & 0 \\ 0 & 0 & 0 & 0 & 0 & 0 \\ 0 & 0 & 0 & 0 & 0 & 0 \end{pmatrix}. \tag{C.54}$$

Hence, the tangential stiffness is given with

$$\begin{aligned} \underline{\underline{K}}(t) =& \frac{\partial \underline{\Delta\sigma}}{\partial \underline{\Delta\varepsilon}}, \\ =& 2\tilde{G}(t)\underline{\underline{M}}'_{\varepsilon} + 3\tilde{K}(t)\underline{\underline{M}}^{\circ}. \end{aligned} \tag{C.55}$$

To update the history variables, Eqs. C.47 are combined and reformulated to give

$$\begin{aligned} \underline{\Delta\varepsilon}^{\mathrm{inh}}_{\mathrm{ve},i}(t) =& \underline{\varepsilon}^{\mathrm{inh}}_{\mathrm{ve},i}(t-\Delta t)\left(e^{-\frac{\Delta t}{\tau_i}} - 1\right) \\ &+ \frac{\tau_i}{\Delta t}\left(1 - e^{-\frac{\Delta t}{\tau_i}}\right)\left(\frac{1}{2G_i}\underline{\underline{M}}'_{\sigma} + \frac{1}{3K_i}\underline{\underline{M}}^{\circ}\right)\underline{\Delta\sigma}, \end{aligned} \tag{C.56}$$

where $\underline{\underline{M'}}_{\sigma}$ is the deviatoric mapping for stress components, which is given with

$$\underline{\underline{M'}}_{\sigma} = \frac{1}{6}\begin{pmatrix} 4 & -2 & -2 & 0 & 0 & 0 \\ -2 & 4 & -2 & 0 & 0 & 0 \\ -2 & -2 & 4 & 0 & 0 & 0 \\ 0 & 0 & 0 & 12 & 0 & 0 \\ 0 & 0 & 0 & 0 & 12 & 0 \\ 0 & 0 & 0 & 0 & 0 & 12 \end{pmatrix}. \tag{C.57}$$

When a vectorized UMAT (VUMAT) is used for explicit calculations, both the stress and strain components are stored as covariant components, so that

$$\varepsilon^{\beta} = \begin{pmatrix} \varepsilon_1 \\ \varepsilon_2 \\ \varepsilon_3 \\ \varepsilon_4 \\ \varepsilon_5 \\ \varepsilon_6 \end{pmatrix} = \begin{pmatrix} \varepsilon_{11} \\ \varepsilon_{22} \\ \varepsilon_{33} \\ \varepsilon_{12} \\ \varepsilon_{23} \\ \varepsilon_{13} \end{pmatrix}. \tag{C.58}$$

Note that in Eq. C.58 the indices of the last two vector components are swapped compared to Eq. C.52. This is a difference between the notation in `Abaqus/Explicit` and `Abaqus/Implicit`. Due to the different notation conventions, the shear components in the deviatoric mapping matrix need to be scaled by $1/2$, which

requires a third matrix representation of the deviatoric projector preserving the base, resulting in

$$\underline{\underline{M}}' = \frac{1}{6}\begin{pmatrix} 4 & -2 & -2 & 0 & 0 & 0 \\ -2 & 4 & -2 & 0 & 0 & 0 \\ -2 & -2 & 4 & 0 & 0 & 0 \\ 0 & 0 & 0 & 6 & 0 & 0 \\ 0 & 0 & 0 & 0 & 6 & 0 \\ 0 & 0 & 0 & 0 & 0 & 6 \end{pmatrix}, \tag{C.59}$$

omitting the necessity to differentiate between $\underline{\underline{M}}'_{\varepsilon}$ and $\underline{\underline{M}}'_{\sigma}$, which is only valid for the notation in a VUMAT using `Abaqus/Explicit`.

D Appendix: Interconversion between Kelvin-Voigt and Maxwell model parameters

The following equations are extracted from Serra-Aguila et al. [203]. The starting point are the model parameters of the Kelvin-Voigt model of order $n = 2$, which are E_0, E_1, E_2, η_1 and η_2. The parameters are related to the relaxation times τ_1 and τ_2 through

$$\tau_i = \frac{\eta_i}{E_i}. \tag{D.1}$$

To avoid confusion, all parameters within the KV model will use the according superscript, i.e., E_0^{KV}, E_1^{KV}, etc.; the Maxwell (MW) model parameters are indicated with according superscripts, i.e., E_∞^{MW}, E_1^{MW}, etc.

To calculate the MW parameters based on the KV parameters, it is advisable to calculate intermediate parameters first. These are

$$
\begin{aligned}
C_1 &= \frac{E_0^{\mathrm{KV}} E_1^{\mathrm{KV}} E_2^{\mathrm{KV}}}{E_0^{\mathrm{KV}} E_1^{\mathrm{KV}} + E_0^{\mathrm{KV}} E_2^{\mathrm{KV}} + E_1^{\mathrm{KV}} E_2^{\mathrm{KV}}},\\
C_2 &= \frac{{E_0^{\mathrm{KV}}}^2 (E_1^{\mathrm{KV}} + E_2^{\mathrm{KV}})}{E_0^{\mathrm{KV}} E_1^{\mathrm{KV}} + E_0^{\mathrm{KV}} E_2^{\mathrm{KV}} + E_1^{\mathrm{KV}} E_2^{\mathrm{KV}}},\\
C_3 &= \frac{\gamma}{2\eta_1^{\mathrm{KV}} \eta_2^{\mathrm{KV}}},\\
C_4 &= \frac{\sqrt{\gamma^2 - 4\eta_1^{\mathrm{KV}} \eta_2^{\mathrm{KV}} (E_0^{\mathrm{KV}} E_1^{\mathrm{KV}} + E_0^{\mathrm{KV}} E_2^{\mathrm{KV}} + E_1^{\mathrm{KV}} E_2^{\mathrm{KV}})}}{2\eta_1^{\mathrm{KV}} \eta_2^{\mathrm{KV}}},\\
C_5 &= \frac{{E_1^{\mathrm{KV}}}^2 \eta_2^{\mathrm{KV}} + {E_2^{\mathrm{KV}}}^2 \eta_1^{\mathrm{KV}}}{\eta_1^{\mathrm{KV}} \eta_2^{\mathrm{KV}} (E_1^{\mathrm{KV}} + E_2^{\mathrm{KV}})},
\end{aligned}
\tag{D.2}
$$

with

$$
\gamma = E_0^{\mathrm{KV}} (\eta_1^{\mathrm{KV}} + \eta_2^{\mathrm{KV}}) + E_1^{\mathrm{KV}} \eta_2^{\mathrm{KV}} + E_2^{\mathrm{KV}} \eta_1^{\mathrm{KV}}. \tag{D.3}
$$

With these intermediate parameters the relaxation coefficients can be calculated, which are

$$
\begin{aligned}
Y_0 &= C_1 + C_2,\\
p_1 &= \frac{C_2 (C_4 + C_5 - C_3)}{2C_4 (C_1 + C_2)},\\
p_2 &= \frac{C_2 (C_4 - C_5 + C_3)}{2C_4 (C_1 + C_2)},\\
\tau_1^{\mathrm{MW}} &= \frac{1}{C_3 - C_4},\\
\tau_2^{\mathrm{MW}} &= \frac{1}{C_3 + C_4}.
\end{aligned}
\tag{D.4}
$$

The MW parameters are then given with

$$\begin{aligned} E_{\infty}^{\mathrm{MW}} &= Y_0(1-p_1-p_2), \\ E_1^{\mathrm{MW}} &= Y_0 p_1, \\ E_2^{\mathrm{MW}} &= Y_0 p_2, \\ \eta_1^{\mathrm{MW}} &= E_1^{\mathrm{MW}} \tau_1^{\mathrm{MW}}, \\ \eta_2^{\mathrm{MW}} &= E_2^{\mathrm{MW}} \tau_2^{\mathrm{MW}}. \end{aligned} \tag{D.5}$$

E Appendix: UMAT of nonlinear Schapery model

The Fortran code for the implicit UMAT formulation is given below:

```
! ======================================================================
! User Subroutine UMAT for non-linear Schapery model with 3 Kelvin-Voigt elements
! By Nicolas Christ (Karlsruhe Institute of Technology) - May 2024
! ======================================================================
!DEC$ FREEFORM

MODULE FUNCTIONS
CONTAINS

  FUNCTION GET_IND_STRESS(SIGMA) RESULT(IND_STRESS)
    ! Calculate indicator stress IND_STRESS for a given stress state SIGMA
    IMPLICIT NONE
    DOUBLE PRECISION, DIMENSION(6), INTENT(IN) :: SIGMA
    DOUBLE PRECISION :: IND_STRESS

    IND_STRESS = sqrt(SIGMA(1)**2.D0 + SIGMA(2)**2.D0 + SIGMA(3)**2.D0 &
                      - SIGMA(1)*SIGMA(2) - SIGMA(1)*SIGMA(3) &
                      - SIGMA(2)*SIGMA(3) + 3.D0*(SIGMA(4)**2.D0 &
                      + SIGMA(5)**2.D0 + SIGMA(6)**2.D0))

    IF (IND_STRESS .ne. IND_STRESS) THEN
      print *, 'Probably underflow, SIGMA:', SIGMA
      IND_STRESS = 0.D0
    END IF

  END FUNCTION

  FUNCTION GET_G0(IND_STRESS) RESULT(G0)
    ! Calculate G0 for a given indicator stress
    IMPLICIT NONE
    DOUBLE PRECISION, INTENT(IN) :: IND_STRESS
    DOUBLE PRECISION :: G0
    DOUBLE PRECISION :: a, b, c, d

    a = 1.D0
    b = 3.49
    c = 104.23
    d = 19.57
    G0 = d + (a - d)/((1.D0 + (IND_STRESS/c)**b))

  END FUNCTION

  FUNCTION GET_G1G2(IND_STRESS) RESULT(G1G2)
```

```
    ! Calculate G1G2 for a given indicator stress
    IMPLICIT NONE
    DOUBLE PRECISION, INTENT(IN) :: IND_STRESS
    DOUBLE PRECISION :: G1G2
    DOUBLE PRECISION :: a, b, c, d

    a = 0.98
    b = 4.61
    c = 25.19
    d = 3.72
    G1G2 = d + (a - d)/((1.D0 + (IND_STRESS/c)**b))

  END FUNCTION

  FUNCTION GET_A_SIG(IND_STRESS) RESULT(A_SIG)
    ! Calculate A_SIG for a given indicator stress
    IMPLICIT NONE
    DOUBLE PRECISION, INTENT(IN) :: IND_STRESS
    DOUBLE PRECISION :: A_SIG
    DOUBLE PRECISION :: a, b, c, d

    a = 1.01
    b = 4.22
    c = 22.42
    d = 0.26
    A_SIG = d + (a - d)/((1.D0 + (IND_STRESS/c)**b))

  END FUNCTION

  FUNCTION GET_DPSI(dtime, A_SIG) RESULT(DPSI)
    ! Calculate the reduced time increment
    IMPLICIT NONE
    DOUBLE PRECISION, INTENT(IN) :: dtime
    DOUBLE PRECISION :: A_SIG
    DOUBLE PRECISION :: DPSI

    DPSI = dtime/A_SIG

  END FUNCTION

  FUNCTION GET_RES_NORM(DSTRAN_TRIAL, dstran, ntens) RESULT(STRAN_RES)
    ! Calculate the strain residuum norm
    IMPLICIT NONE
    DOUBLE PRECISION, DIMENSION(:), INTENT(IN) :: DSTRAN_TRIAL, dstran
    INTEGER, INTENT(IN) :: ntens
    INTEGER :: I
    DOUBLE PRECISION :: NORM_STRAN, NORM_DIFF
    DOUBLE PRECISION, DIMENSION(ntens) :: STRAN_DIFF
    DOUBLE PRECISION :: STRAN_RES

    STRAN_DIFF = DSTRAN_TRIAL - dstran

    NORM_DIFF = 0.D0
    NORM_STRAN = 0.D0
    DO I = 1, ntens
      NORM_DIFF = NORM_DIFF + STRAN_DIFF(I)**2
      NORM_STRAN = NORM_STRAN + dstran(I)**2
    END DO

    NORM_DIFF = sqrt(NORM_DIFF)
    NORM_STRAN = sqrt(NORM_STRAN)

    STRAN_RES = NORM_DIFF/NORM_STRAN

    IF (STRAN_RES .ne. STRAN_RES) THEN
```

```
    STRAN_RES = 0.D0
  END IF

END FUNCTION

FUNCTION GET_G(G0_NL, G1G2_NL, DPSI, G0, G1, G2, G3, TAU1, TAU2, TAU3) RESULT(G)
  ! Return the effective viscous shear modulus
  IMPLICIT NONE
  DOUBLE PRECISION, INTENT(IN) :: G0_NL, G1G2_NL, DPSI, G0, G1, G2, G3
  DOUBLE PRECISION, INTENT(IN) :: TAU1, TAU2, TAU3
  DOUBLE PRECISION :: G, DECAY1, DECAY2, DECAY3

  DECAY1 = 1.D0 - exp(-DPSI/TAU1)
  DECAY2 = 1.D0 - exp(-DPSI/TAU2)
  DECAY3 = 1.D0 - exp(-DPSI/TAU3)

  G = 1.D0/(G0_NL/G0 + G1G2_NL*(1.D0/G1*(1.D0 - TAU1/DPSI*DECAY1) &
      + 1.D0/G2*(1.D0 - TAU2/DPSI*DECAY2) + 1.D0/G3*(1.D0 - TAU3/DPSI*DECAY3)))

END FUNCTION

FUNCTION GET_K(G0_NL, G1G2_NL, DPSI, K0, K1, K2, K3, TAU1, TAU2, TAU3) RESULT(K)
  ! Return the effective viscous bulk modulus
  IMPLICIT NONE
  DOUBLE PRECISION, INTENT(IN) :: G0_NL, G1G2_NL, DPSI, K0, K1, K2, K3, &
    TAU1, TAU2, TAU3
  DOUBLE PRECISION :: K, DECAY1, DECAY2, DECAY3

  DECAY1 = 1.D0 - exp(-DPSI/TAU1)
  DECAY2 = 1.D0 - exp(-DPSI/TAU2)
  DECAY3 = 1.D0 - exp(-DPSI/TAU3)

  K = 1.D0/(G0_NL/K0 + G1G2_NL*(1.D0/K1*(1.D0 - TAU1/DPSI*DECAY1) &
      + 1.D0/K2*(1.D0 - TAU2/DPSI*DECAY2) + 1.D0/K3*(1.D0 - TAU3/DPSI*DECAY3)))

END FUNCTION

FUNCTION GET_DEPS(SIGMA_NEW, SIGMA_OLD, STRAIN_OLD, STRAN_INH1, STRAN_INH2, &
                  STRAN_INH3, dtime, ntens, G0, G1, G2, G3, K0, K1, K2, K3, &
                  TAU1, TAU2, TAU3,G1G2_NL_OLD, M_PRIME_EPS, M_PRIME_SIG, &
                  M_CIRC) RESULT(DEPS)
  ! Calculate strain increment based on stress increment
  IMPLICIT NONE
  INTEGER, INTENT(IN) :: ntens
  DOUBLE PRECISION, INTENT(IN), DIMENSION(ntens) :: STRAIN_OLD, STRAN_INH1
  DOUBLE PRECISION, INTENT(IN), DIMENSION(ntens) :: STRAN_INH2, STRAN_INH3
  DOUBLE PRECISION, INTENT(IN), DIMENSION(ntens) :: SIGMA_NEW, SIGMA_OLD
  DOUBLE PRECISION, INTENT(IN) :: dtime, G0, G1, G2, G3, K0, K1, K2, K3
  DOUBLE PRECISION, INTENT(IN) :: TAU1, TAU2, TAU3
  DOUBLE PRECISION, INTENT(IN) :: G1G2_NL_OLD
  DOUBLE PRECISION, INTENT(IN), DIMENSION(6, 6) :: M_PRIME_EPS, M_PRIME_SIG
  DOUBLE PRECISION, INTENT(IN), DIMENSION(6, 6) :: M_CIRC
  DOUBLE PRECISION, DIMENSION(ntens) :: DEPS
  DOUBLE PRECISION, DIMENSION(ntens) :: STRESS_NEW, HISTORY_STRAIN
  DOUBLE PRECISION :: IND_STRESS, G0_NL, G1G2_NL, A_SIG_NL, DPSI, DECAY1
  DOUBLE PRECISION :: DECAY2, DECAY3, K, G
  DOUBLE PRECISION :: D_SPHERIC, D_DEVIATORIC

  IND_STRESS = GET_IND_STRESS(SIGMA_NEW)

  G0_NL = GET_G0(IND_STRESS)
  G1G2_NL = GET_G1G2(IND_STRESS)
  A_SIG_NL = GET_A_SIG(IND_STRESS)

  DPSI = GET_DPSI(dtime, A_SIG_NL)
```

```
    DECAY1 = 1.D0 - exp(-DPSI/TAU1)
    DECAY2 = 1.D0 - exp(-DPSI/TAU2)
    DECAY3 = 1.D0 - exp(-DPSI/TAU3)

    D_SPHERIC = G1G2_NL_OLD/DPSI*(TAU1/3.D0/K1*DECAY1 + TAU2/3.D0/K2*DECAY2 &
                                  + TAU3/3.D0/K3*DECAY3)
    D_DEVIATORIC = G1G2_NL_OLD/DPSI*(TAU1/2.D0/G1*DECAY1 + TAU2/2.D0/G2*DECAY2 &
                                     + TAU3/2.D0/G3*DECAY3)

    G = GET_G(G0_NL, G1G2_NL, DPSI, G0, G1, G2, G3, TAU1, TAU2, TAU3)
    K = GET_K(G0_NL, G1G2_NL, DPSI, K0, K1, K2, K3, TAU1, TAU2, TAU3)

    HISTORY_STRAIN = (STRAN_INH1*exp(-DPSI/TAU1) + STRAN_INH2*exp(-DPSI/TAU2) &
                    + STRAN_INH3*exp(-DPSI/TAU3))

    DEPS = matmul((1.D0/(2.D0*G)*M_PRIME_SIG + 1.D0/(3.D0*K)*M_CIRC), SIGMA_NEW) &
         + matmul((D_DEVIATORIC*M_PRIME_SIG + D_SPHERIC*M_CIRC), SIGMA_OLD) &
         - HISTORY_STRAIN - STRAIN_OLD

END FUNCTION

FUNCTION GET_JACOBIAN(SIGMA_NEW, SIGMA_OLD, STRAIN_OLD, STRAN_INH1, &
                      STRAN_INH2, STRAN_INH3, dtime, ntens, G0, G1, G2, G3, &
                      K0, K1, K2, K3, TAU1, TAU2, TAU3, G1G2_NL_OLD, &
                      M_PRIME_EPS, M_PRIME_SIG, M_CIRC, h) RESULT(JACOBIAN)
  ! Calculate Jacobian (numerically)
  IMPLICIT NONE
  INTEGER, INTENT(IN) :: ntens
  DOUBLE PRECISION, INTENT(IN), DIMENSION(ntens) :: STRAIN_OLD, STRAN_INH1
  DOUBLE PRECISION, INTENT(IN), DIMENSION(ntens) :: STRAN_INH2, STRAN_INH3
  DOUBLE PRECISION, INTENT(IN), DIMENSION(ntens) :: SIGMA_NEW, SIGMA_OLD
  DOUBLE PRECISION, INTENT(IN) :: dtime, G0, G1, G2, G3, K0, K1, K2, K3
  DOUBLE PRECISION, INTENT(IN) :: TAU1, TAU2, TAU3
  DOUBLE PRECISION, INTENT(IN) :: G1G2_NL_OLD
  DOUBLE PRECISION, INTENT(IN), DIMENSION(6, 6) :: M_PRIME_EPS, M_PRIME_SIG
  DOUBLE PRECISION, INTENT(IN), DIMENSION(6, 6) :: M_CIRC
  DOUBLE PRECISION, DIMENSION(6, 6) :: JACOBIAN
  DOUBLE PRECISION, DIMENSION(ntens) :: DH
  DOUBLE PRECISION :: h
  INTEGER :: I, J

  DO J = 1, ntens
    DO I = 1, ntens
      IF (I == J) THEN
        DH(I) = h
      ELSE
        DH(I) = 0.D0
      END IF
    END DO
    JACOBIAN(:, J) = 1.D0/(2.D0*h)&
                     *(GET_DEPS(SIGMA_NEW + DH, SIGMA_OLD, &
                                STRAIN_OLD, STRAN_INH1, STRAN_INH2, &
                                STRAN_INH3, dtime, ntens, G0, G1, G2, &
                                G3, K0, K1, K2, K3, TAU1, TAU2, TAU3, &
                                G1G2_NL_OLD, M_PRIME_EPS, M_PRIME_SIG, &
                                M_CIRC) &
                       - GET_DEPS(SIGMA_NEW - DH, SIGMA_OLD, &
                                STRAIN_OLD, STRAN_INH1, STRAN_INH2, &
                                STRAN_INH3, dtime, ntens, G0, G1, G2, &
                                G3, K0, K1, K2, K3, TAU1, TAU2, TAU3, &
                                G1G2_NL_OLD, M_PRIME_EPS, M_PRIME_SIG, &
                                M_CIRC))
  END DO
```

```
  END FUNCTION

END MODULE FUNCTIONS

SUBROUTINE UMAT(stress, statev, ddsdde, sse, spd, scd, rpl, ddsddt, drplde, &
                drpldt, stran, dstran, time, dtime, temp, dtemp, predef, dpred, &
                cmname, ndi, nshr, ntens, nstatv, props, nprops, coords, drot, &
                pnewdt, celent, dfgrd0, dfgrd1, noel, npt, layer, kspt, kstep, &
                kinc)

  USE FUNCTIONS
  IMPLICIT NONE

  integer, intent(in) :: ndi, nshr, ntens, nstatv, nprops, noel, npt, layer
  integer, intent(in) :: kspt, kstep, kinc
  double precision, intent(inout), dimension(ntens) :: stress
  double precision, intent(inout), dimension(nstatv):: statev
  double precision, intent(out), dimension(ntens, ntens):: ddsdde
  double precision, intent(inout) :: sse, spd, scd, pnewdt
  double precision :: rpl, drpldt
  double precision, dimension(ntens) :: ddsddt, drplde
  double precision, intent(in), dimension(ntens) :: stran, dstran
  double precision, intent(in), dimension(2) :: time
  double precision, intent(in), dimension(1) :: predef, dpred
  double precision, intent(in) :: dtime, temp, dtemp, celent
  character(80), intent(in) :: cmname
  double precision, intent(in), dimension(nprops) :: props
  double precision, intent(in), dimension(3) :: coords
  double precision, intent(in), dimension(3, 3) :: drot, dfgrd0, dfgrd1

  integer :: i, j, n, info

  INTEGER :: ITER
  INTEGER, PARAMETER :: ITER_MAX = 50
  DOUBLE PRECISION, PARAMETER :: h = 1E-8
  DOUBLE PRECISION, PARAMETER :: RES_MIN = 1E-6

  DOUBLE PRECISION :: E0, NU, E1, TAU1, E2, TAU2, E3, TAU3, G0, K0, G1, K1
  DOUBLE PRECISION :: G2, K2, G3, K3, G, K
  DOUBLE PRECISION :: DECAY1, DECAY2, DECAY3, DPSI, STRAN_RES
  DOUBLE PRECISION :: G0_NL, G1G2_NL, A_SIG_NL
  DOUBLE PRECISION :: G0_NL_OLD, G1G2_NL_OLD, A_SIG_NL_OLD
  DOUBLE PRECISION :: D_DEVIATORIC, D_SPHERIC
  DOUBLE PRECISION, DIMENSION(6) :: SIGMA_TRIAL, DSIGMA_TRIAL, DSTRAN_TRIAL
  DOUBLE PRECISION, DIMENSION(6) :: DDSTRESS, R, SIGMA_OLD, SIGMA_NEW
  DOUBLE PRECISION, DIMENSION(6) :: STRAN_INH1, STRAN_INH2, STRAN_INH3
  DOUBLE PRECISION, DIMENSION(6) :: HISTORY_STRAIN, STRAIN_DIFF, STRAIN_OLD
  DOUBLE PRECISION, DIMENSION(6) :: STRAIN_NEW
  DOUBLE PRECISION, DIMENSION(6, 6) :: M_PRIME, M_PRIME_EPS, M_PRIME_SIG
  DOUBLE PRECISION, DIMENSION(6, 6) :: M_CIRC, JACOBIAN

  DOUBLE PRECISION, DIMENSION(3, 3) :: A, A_INV
  DOUBLE PRECISION, DIMENSION(3) :: b, x

  DOUBLE PRECISION :: LAMBDA, MU, ind_stress

  M_PRIME_EPS = reshape(1.D0/6.D0*(/4.D0, -2.D0, -2.D0, 0.D0, 0.D0, 0.D0, &
                                   -2.D0, 4.D0, -2.D0, 0.D0, 0.D0, 0.D0, &
                                   -2.D0, -2.D0, 4.D0, 0.D0, 0.D0, 0.D0, &
                                   0.D0, 0.D0, 0.D0, 3.D0, 0.D0, 0.D0, &
                                   0.D0, 0.D0, 0.D0, 0.D0, 3.D0, 0.D0, &
                                   0.D0, 0.D0, 0.D0, 0.D0, 0.D0, 3.D0/), (/6, 6/))

  M_PRIME_SIG = reshape(1.D0/6.D0*(/4.D0, -2.D0, -2.D0, 0.D0, 0.D0, 0.D0, &
                                   -2.D0, 4.D0, -2.D0, 0.D0, 0.D0, 0.D0, &
```

```
                                    -2.D0, -2.D0, 4.D0, 0.D0, 0.D0, 0.D0, &
                                    0.D0, 0.D0, 0.D0, 12.D0, 0.D0, 0.D0, &
                                    0.D0, 0.D0, 0.D0, 0.D0, 12.D0, 0.D0, &
                                    0.D0, 0.D0, 0.D0, 0.D0, 0.D0, 12.D0/), (/6, 6/))

M_PRIME = reshape(1.D0/6.D0*(/4.D0, -2.D0, -2.D0, 0.D0, 0.D0, 0.D0, &
                              -2.D0, 4.D0, -2.D0, 0.D0, 0.D0, 0.D0, &
                              -2.D0, -2.D0, 4.D0, 0.D0, 0.D0, 0.D0, &
                              0.D0, 0.D0, 0.D0, 6.D0, 0.D0, 0.D0, &
                              0.D0, 0.D0, 0.D0, 0.D0, 6.D0, 0.D0, &
                              0.D0, 0.D0, 0.D0, 0.D0, 0.D0, 6.D0/), (/6, 6/))

M_CIRC = reshape(1.D0/3.D0*(/1.D0, 1.D0, 1.D0, 0.D0, 0.D0, 0.D0, &
                             1.D0, 1.D0, 1.D0, 0.D0, 0.D0, 0.D0, &
                             1.D0, 1.D0, 1.D0, 0.D0, 0.D0, 0.D0, &
                             0.D0, 0.D0, 0.D0, 0.D0, 0.D0, 0.D0, &
                             0.D0, 0.D0, 0.D0, 0.D0, 0.D0, 0.D0, &
                             0.D0, 0.D0, 0.D0, 0.D0, 0.D0, 0.D0/), (/6, 6/))

SIGMA_OLD = stress
STRAIN_OLD = stran
STRAIN_NEW = stran + dstran

E0 = PROPS(1)
NU = PROPS(2)
E1 = PROPS(3)
TAU1 = PROPS(4)
E2 = PROPS(5)
TAU2 = PROPS(6)
E3 = PROPS(7)
TAU3 = PROPS(8)

G0 = E0/(2.D0*(1.D0 + NU))
K0 = E0/(3.D0*(1.D0 - 2.D0*NU))
G1 = E1/(2.D0*(1.D0 + NU))
K1 = E1/(3.D0*(1.D0 - 2.D0*NU))
G2 = E2/(2.D0*(1.D0 + NU))
K2 = E2/(3.D0*(1.D0 - 2.D0*NU))
G3 = E3/(2.D0*(1.D0 + NU))
K3 = E3/(3.D0*(1.D0 - 2.D0*NU))

! Build state variables
STRAN_INH1(1) = STATEV(1)
STRAN_INH1(2) = STATEV(2)
STRAN_INH1(3) = STATEV(3)
STRAN_INH1(4) = STATEV(4)
STRAN_INH1(5) = STATEV(5)
STRAN_INH1(6) = STATEV(6)

STRAN_INH2(1) = STATEV(7)
STRAN_INH2(2) = STATEV(8)
STRAN_INH2(3) = STATEV(9)
STRAN_INH2(4) = STATEV(10)
STRAN_INH2(5) = STATEV(11)
STRAN_INH2(6) = STATEV(12)

STRAN_INH3(1) = STATEV(13)
STRAN_INH3(2) = STATEV(14)
STRAN_INH3(3) = STATEV(15)
STRAN_INH3(4) = STATEV(16)
STRAN_INH3(5) = STATEV(17)
STRAN_INH3(6) = STATEV(18)

! Old nonlinear parameters
IF (time(2) == 0.D0) THEN
```

```
    ! Assign non-linear parameters in beginning of simulation
    G0_NL = 1.D0
    G0_NL_OLD = 1.D0
    G1G2_NL = 1.D0
    G1G2_NL_OLD = 1.D0
    A_SIG_NL = 1.D0
    A_SIG_NL_OLD = 1.D0
  ELSE
    G0_NL = STATEV(19)
    G0_NL_OLD = STATEV(19)
    G1G2_NL = STATEV(20)
    G1G2_NL_OLD = STATEV(20)
    A_SIG_NL = STATEV(21)
    A_SIG_NL_OLD = STATEV(21)
  END IF

  ! Get new reduced time increment and time dependent material parameters
  DPSI = GET_DPSI(dtime, A_SIG_NL)

  DECAY1 = 1.D0 - exp(-DPSI/TAU1)
  DECAY2 = 1.D0 - exp(-DPSI/TAU2)
  DECAY3 = 1.D0 - exp(-DPSI/TAU3)

  D_SPHERIC = G1G2_NL_OLD/DPSI*(TAU1/3.D0/K1*DECAY1 + TAU2/3.D0/K2*DECAY2 &
                                + TAU3/3.D0/K3*DECAY3)
  D_DEVIATORIC = G1G2_NL_OLD/DPSI*(TAU1/2.D0/G1*DECAY1 + TAU2/2.D0/G2*DECAY2 &
                                   + TAU3/2.D0/G3*DECAY3)

  G = GET_G(G0_NL, G1G2_NL, DPSI, G0, G1, G2, G3, TAU1, TAU2, TAU3)
  K = GET_K(G0_NL, G1G2_NL, DPSI, K0, K1, K2, K3, TAU1, TAU2, TAU3)

  HISTORY_STRAIN = (STRAN_INH1*exp(-DPSI/TAU1) + STRAN_INH2*exp(-DPSI/TAU2) &
                    + STRAN_INH3*exp(-DPSI/TAU3))
  STRAIN_DIFF = STRAIN_NEW + HISTORY_STRAIN

  SIGMA_TRIAL = matmul((2.D0*G*M_PRIME_EPS + 3.D0*K*M_CIRC), STRAIN_DIFF) &
                - matmul((2.D0*G*D_DEVIATORIC*M_PRIME &
                          + 3.D0*K*D_SPHERIC*M_CIRC), SIGMA_OLD)

  ! Calculate trial strain to check if trial stress is sufficient
  DSTRAN_TRIAL = GET_DEPS(SIGMA_TRIAL, SIGMA_OLD, STRAIN_OLD, STRAN_INH1, &
                          STRAN_INH2, STRAN_INH3, dtime, ntens, G0, G1, G2, &
                          G3, K0, K1, K2, K3, TAU1, TAU2, TAU3, G1G2_NL_OLD, &
                          M_PRIME_EPS, M_PRIME_SIG, M_CIRC)

  ! Calculate residuum
  STRAN_RES = GET_RES_NORM(DSTRAN_TRIAL, dstran, ntens)

  ! ----- Newton-Raphson -----
  ITER = 0
  n = ntens
  DO WHILE (ITER < ITER_MAX .AND. STRAN_RES > RES_MIN)
    ! Calculate Jacobian
    JACOBIAN = GET_JACOBIAN(SIGMA_TRIAL, SIGMA_OLD, STRAIN_OLD, STRAN_INH1, &
                            STRAN_INH2, STRAN_INH3, dtime, ntens, G0, G1, &
                            G2, G3, K0, K1, K2, K3, TAU1, TAU2, TAU3, &
                            G1G2_NL_OLD, M_PRIME_EPS, M_PRIME_SIG, M_CIRC, h)

    ! Solve for DDSTRESS
    R = DSTRAN_TRIAL - dstran
    call linsolv(n, JACOBIAN, -R, DSIGMA_TRIAL, info)

    if (info .ne. 0) then
      print *, 'ITER:', ITER
      print *, 'JACOBIAN:', JACOBIAN
```

```
      CALL XIT()
    end if

    ! Update DSTRESS
    SIGMA_TRIAL = SIGMA_TRIAL + DSIGMA_TRIAL

    ! Update trial strain
    DSTRAN_TRIAL = GET_DEPS(SIGMA_TRIAL, SIGMA_OLD, STRAIN_OLD, STRAN_INH1, &
                            STRAN_INH2, STRAN_INH3, dtime, ntens, G0, G1, &
                            G2, G3, K0, K1, K2, K3, TAU1, TAU2, TAU3, &
                            G1G2_NL_OLD, M_PRIME_EPS, M_PRIME_SIG, M_CIRC)

    STRAN_RES = GET_RES_NORM(DSTRAN_TRIAL, dstran, ntens)

    ITER = ITER + 1
END DO

IF (ITER == ITER_MAX .OR. STRAN_RES > RES_MIN) THEN
    print *, 'Newton-Raphson did not converge (stran_res, time, noel)', &
      STRAN_RES, time, noel

    ! Reduce dtime
    pnewdt = 0.5D0
END IF

SIGMA_NEW = SIGMA_TRIAL

stress = SIGMA_NEW

ind_stress = GET_IND_STRESS(stress)

G0_NL = GET_G0(IND_STRESS)
G1G2_NL = GET_G1G2(IND_STRESS)
A_SIG_NL = GET_A_SIG(IND_STRESS)
DPSI = GET_DPSI(dtime, A_SIG_NL)

DECAY1 = 1.D0 - exp(-DPSI/TAU1)
DECAY2 = 1.D0 - exp(-DPSI/TAU2)
DECAY3 = 1.D0 - exp(-DPSI/TAU3)

! Update state variables
STRAN_INH1 = STRAN_INH1*exp(-DPSI/TAU1) + TAU1/DPSI*DECAY1 &
             *matmul((1.D0/(2.D0*G1)*M_PRIME_SIG + 1.D0/(3.D0*K1)*M_CIRC), &
                     (G1G2_NL*SIGMA_NEW - G1G2_NL_OLD*SIGMA_OLD))
STRAN_INH2 = STRAN_INH2*exp(-DPSI/TAU2) + TAU2/DPSI*DECAY2 &
             *matmul((1.D0/(2.D0*G2)*M_PRIME_SIG + 1.D0/(3.D0*K2)*M_CIRC), &
                     (G1G2_NL*SIGMA_NEW - G1G2_NL_OLD*SIGMA_OLD))
STRAN_INH3 = STRAN_INH3*exp(-DPSI/TAU3) + TAU3/DPSI*DECAY3 &
             *matmul((1.D0/(2.D0*G3)*M_PRIME_SIG + 1.D0/(3.D0*K3)*M_CIRC), &
                     (G1G2_NL*SIGMA_NEW - G1G2_NL_OLD*SIGMA_OLD))

! Write state variables to STATEV
STATEV(1) = STRAN_INH1(1)
STATEV(2) = STRAN_INH1(2)
STATEV(3) = STRAN_INH1(3)
STATEV(4) = STRAN_INH1(4)
STATEV(5) = STRAN_INH1(5)
STATEV(6) = STRAN_INH1(6)

STATEV(7) = STRAN_INH2(1)
STATEV(8) = STRAN_INH2(2)
STATEV(9) = STRAN_INH2(3)
STATEV(10) = STRAN_INH2(4)
STATEV(11) = STRAN_INH2(5)
STATEV(12) = STRAN_INH2(6)
```

```
  STATEV(13) = STRAN_INH3(1)
  STATEV(14) = STRAN_INH3(2)
  STATEV(15) = STRAN_INH3(3)
  STATEV(16) = STRAN_INH3(4)
  STATEV(17) = STRAN_INH3(5)
  STATEV(18) = STRAN_INH3(6)

  STATEV(19) = G0_NL
  STATEV(20) = G1G2_NL
  STATEV(21) = A_SIG_NL

  STATEV(22) = STRAN_RES
  STATEV(23) = ind_stress

  ! Calculate DDSDDE
  DO I = 1, ntens
    DO J = 1, ntens
      DDSDDE(I, J) = 0.D0
    END DO
  END DO

  DDSDDE = 2.D0*G*M_PRIME_EPS + 3.D0*K*M_CIRC

  RETURN
END SUBROUTINE UMAT

SUBROUTINE SDVINI(STATEV, COORDS, NSTATV, NCRDS, NOEL, NPT, &
                  LAYER, KSPT)
! Sets the initial values of the STATEV
  INCLUDE 'ABA_PARAM.INC'
!
  DIMENSION STATEV(NSTATV), COORDS(NCRDS)

  ! Strains of first KV Element
  STATEV(1) = 0.D0
  STATEV(2) = 0.D0
  STATEV(3) = 0.D0
  STATEV(4) = 0.D0
  STATEV(5) = 0.D0
  STATEV(6) = 0.D0

  ! Strains of second KV Element
  STATEV(7) = 0.D0
  STATEV(8) = 0.D0
  STATEV(9) = 0.D0
  STATEV(10) = 0.D0
  STATEV(11) = 0.D0
  STATEV(12) = 0.D0

  ! Strains of third KV Element
  STATEV(13) = 0.D0
  STATEV(14) = 0.D0
  STATEV(15) = 0.D0
  STATEV(16) = 0.D0
  STATEV(17) = 0.D0
  STATEV(18) = 0.D0

  ! Non-linear parameter g0, g1g2, a_sigma
  STATEV(19) = 1.D0
  STATEV(20) = 1.D0
  STATEV(21) = 1.D0

  ! Residuum for Newton iterations
  STATEV(22) = 0.D0
```

```
  ! Indicator stress (should be equal to Abaqus v.Mises)
  STATEV(23) = 0.D0

  RETURN
END

subroutine invert(n, A, Ainv)
  implicit none
  integer n, info
  integer ipiv(n)
  integer nsize
  parameter(nsize=9) ! matrix size
  integer LWORK_MKL
  parameter(LWORK_MKL=64*nsize)
  real*8 WORK_MKL(LWORK_MKL)
  real*8 A(n, n), Ainv(n, n)
  Ainv = A
  ! Intially, Ainv = A.
  ! After linear solve, Ainv = inv(A)
  CALL dgetrf(n, n, Ainv, n, ipiv, info)
  CALL dgetri(n, Ainv, n, ipiv, WORK_MKL, LWORK_MKL, info)
end subroutine invert

subroutine linsolv(n, Ain, b, x, info)
  implicit none
  integer n, info, nrhs
  integer ipiv(n)
  real*8 A(n, n), Ain(n, n), b(n), x(n)
  parameter(nrhs=1)
  A = Ain
  x = b

  ! Initially x = b
  ! After linear solve, x=inv(A)*b
  call dgesv(n, nrhs, A, n, ipiv, x, n, info)

  if (info .ne. 0) then
    write (*, *) '***ERROR INVERTING LOCAL JACOBIAN***', info
  end if
end subroutine linsolv
```

F Appendix: Arduino code

The Arduino code to regulate the voltage of the power resistors and to monitor temperature and relative humidity is given below:

```
#include <Wire.h>
#include "SHTSensor.h"
#include <PID_v1.h>
#define PIN_OUTPUT 5

SHTSensor sht;
int FanPin = 10;
double FanPower = 30;

//Green LED to indicate Arduino is working
int LED_high = 9;
int LED_low = 8;

//Define PID variables
double Setpoint, Input, Output;

//Specify the links and initial tuning parameters
double Kp = 120, Ki = 4, Kd = 0;
PID myPID(&Input, &Output, &Setpoint, Kp, Ki, Kd, DIRECT);

void setup() {

        sht.setAccuracy(SHTSensor::SHT_ACCURACY_LOW);

        pinMode(PIN_OUTPUT, OUTPUT);

        pinMode(LED_high, OUTPUT);
        pinMode(LED_low, OUTPUT);

        digitalWrite(LED_low, LOW);
        digitalWrite(LED_high, HIGH);

        Wire.begin();
        Serial.begin(9600);
        delay(1000);

        if (sht.init()) {
                Serial.print("init(): success\n");
        } else {
                Serial.print("init(): failed\n");
        }
        sht.setAccuracy(SHTSensor::SHT_ACCURACY_MEDIUM); // only supported by SHT3x

        if (sht.readSample()) {
                Input = sht.getTemperature();
```

```
            Setpoint = 30; // desired temperature
        } else{
            Serial.println("Failed to init PID");
        }

        //turn the PID on
        myPID.SetMode(AUTOMATIC);

        pinMode(11, OUTPUT);
}

void loop() {
        analogWrite(FanPin, FanPower); // Fan control: 0 (off) - 255 (max)

        if (sht.readSample()) {
            String temp = String(sht.getTemperature(), 2);
            String hum = String(sht.getHumidity(), 2);
            String per = String(Output, 2); // percentage of max. voltage
            Serial.println(temp + " " + hum + " " + per);

            Input = sht.getTemperature();
            myPID.Compute();
            analogWrite(PIN_OUTPUT, 120);
        } else {
            Serial.print("Error in readSample()\n");
        }

        delay(1000);
}
```

Bibliography

[1] S. Fliegener. *Micromechanical finite element modeling of long fiber reinforced thermoplastics*. PhD thesis, 2015.

[2] M. Schober. *On the Characterization and Modeling of Interfaces in Fiber Reinforced Polymer Structures*. Karlsruher Institut für Technologie (KIT), 2019. doi: 10.5445/IR/1000100455.

[3] B. Rohrmüller. *Characterization and Modeling of Fiber-Matrix Interfaces of a Glass Fiber Reinforced Sheet Molding Compound*. Karlsruher Institut für Technologie (KIT), 2023. doi: 10.5445/IR/1000163632.

[4] EEA greenhouse gases — data viewer | European Environment Agency's home page, 14.08.2025. URL `https://www.eea.europa.eu/en/analysis/maps-and-charts/greenhouse-gases-viewer-data-viewers`.

[5] European Court of Auditors. Special report 01/2024: Reducing carbon dioxide emissions from passenger cars, 14.08.2025. URL `https://www.eca.europa.eu/en/publications?ref=sr-2024-01`.

[6] F. Del Pero, M. Delogu, and M. Pierini. The effect of lightweighting in automotive LCA perspective: Estimation of mass-induced fuel consumption reduction for gasoline turbocharged vehicles. *Journal of Cleaner Production*, 154:566–577, 2017. ISSN 09596526. doi: 10.1016/j.jclepro.2017.04.013.

[7] K. K. Chawla. *Composite Materials*. Springer International Publishing, Cham, 2019. ISBN 978-3-030-28982-9. doi: 10.1007/978-3-030-28983-6.

[8] T. Böhlke, F. Henning, A. Hrymak, L. Kärger, K. Weidenmann, and J. T. Wood, editors. *Continuous–discontinuous fiber-reinforced polymers: An*

integrated engineering approach. Carl Hanser Verlag, Munich, 2019. ISBN 9781569906934. URL https://www.sciencedirect.com/science/book/9781569906927.

[9] Eur-lex - 52020dc0098 - en - eur-lex, 14.08.2025. URL https://eur-lex.europa.eu/legal-content/EN/TXT/?qid=1583933814386&uri=COM:2020:98:FIN.

[10] European Commission. The European Green Deal, 14.08.2025. URL https://commission.europa.eu/strategy-and-policy/priorities-2019-2024/european-green-deal_en.

[11] A. R. Offringa. Thermoplastic composites—rapid processing applications. *Composites Part A: Applied Science and Manufacturing*, 27(4):329–336, 1996. ISSN 1359835X. doi: 10.1016/1359-835X(95)00048-7.

[12] U. N. Gandhi, S. Goris, T. A. Osswald, and Y.-Y. Song. *Discontinuous fiber-reinforced composites: Fundamentals and applications*. Hanser Publishers and Hanser Publications, Munich and Cincinnati, 2020. ISBN 978-1-56990-694-1.

[13] G. W. Ehrenstein. *Polymeric materials: Structure - properties - applications: Zugl.: Karlsruhe, Univ., Habil.-Schr., 1978*. Hanser Gardner and Hanser, Cincinnati and Munich, 2001. ISBN 9781569903100.

[14] K. P. Menard and N. Menard. *Dynamic mechanical analysis*. Taylor and Francis, Boca Raton, 2020. ISBN 9781482255515.

[15] J. D. Ferry. *Viscoelastic properties of polymers*. John Wiley & Sons, New York and Chichester and Brisbane and Toronto and Singapore, third edition edition, 1980. ISBN 0-471-04894-1. URL http://www.loc.gov/catdir/bios/wiley041/79028666.html.

[16] K. Marchildon. Polyamides – still strong after seventy years. *Macromolecular Reaction Engineering*, 5(1):22–54, 2011. ISSN 1862-832X. doi: 10.1002/mren.201000017.

[17] W. Kaiser. *Kunststoffchemie für Ingenieure*. Hanser, München and Wien, 2006. ISBN 3-446-22069-0.

[18] P. Eyerer, editor. *Polymer engineering: Technologien und Praxis ; mit 155 Tabellen*. VDI. Springer, Berlin and Heidelberg, 2008. ISBN 978-3-540-72419-3.

[19] Y. P. Khanna, W. P. Kuhn, and W. J. Sichina. Reliable measurements of the nylon 6 glass transition made possible by the new dynamic DSC. *Macromolecules*, 28(8):2644–2646, 1995. ISSN 0024-9297. doi: 10.1021/ma00112a008.

[20] E. Parodi, L. E. Govaert, and G. Peters. Glass transition temperature versus structure of polyamide 6: A flash-DSC study. *Thermochimica Acta*, 657: 110–122, 2017. ISSN 00406031. doi: 10.1016/j.tca.2017.09.021.

[21] M. C. Righetti, E. Tombari, M. Angiuli, and M. L. Di Lorenzo. Enthalpy-based determination of crystalline, mobile amorphous and rigid amorphous fractions in semicrystalline polymers. *Thermochimica Acta*, 462(1-2):15–24, 2007. ISSN 00406031. doi: 10.1016/j.tca.2007.06.003.

[22] I. Kolesov and R. Androsch. The rigid amorphous fraction of cold-crystallized polyamide 6. *Polymer*, 53(21):4770–4777, 2012. ISSN 00323861. doi: 10.1016/j.polymer.2012.08.017.

[23] J. A. Barnes and G. E. Byerly. The formation of residual stresses in laminated thermoplastic composites. *Composites Science and Technology*, 51(4):479–494, 1994. ISSN 02663538. doi: 10.1016/0266-3538(94)90081-7.

[24] P. P. Parlevliet, H. E. Bersee, and A. Beukers. Residual stresses in thermoplastic composites – a study of the literature – part i: Formation of residual stresses. *Composites Part A: Applied Science and Manufacturing*, 37(11):1847–1857, 2006. ISSN 1359835X. doi: 10.1016/j.compositesa.2005.12.025.

[25] T. J. Chapman, J. W. Gillespie, R. B. Pipes, J.-A. Manson, and J. C. Seferis. Prediction of process-induced residual stresses in thermoplastic composites.

Journal of Composite Materials, 24(6):616–643, 1990. ISSN 0021-9983. doi: 10.1177/002199839002400603.

[26] J. A. Nairn and P. Zoller. Matrix solidification and the resulting residual thermal stresses in composites. *Journal of Materials Science*, 20(1):355–367, 1985. ISSN 0022-2461. doi: 10.1007/BF00555929.

[27] G. Jeronimidis and A. T. Parkyn. Residual stresses in carbon fibre-thermoplastic matrix laminates. *Journal of Composite Materials*, 22(5): 401–415, 1988. ISSN 0021-9983. doi: 10.1177/002199838802200502.

[28] M. Detassis, A. Pegoretti, C. Migliaresi, and H. D. Wagner. Experimental evaluation of residual stresses in single fibre composites by means of the fragmentation test. *Journal of Materials Science*, 31(9):2385–2392, 1996. ISSN 0022-2461. doi: 10.1007/BF01152951.

[29] R. Puffr and J. Šebenda. On the structure and properties of polyamides. xxvii. the mechanism of water sorption in polyamides. *Journal of Polymer Science Part C: Polymer Symposia*, 16(1):79–93, 1967. ISSN 0449-2994. doi: 10.1002/polc.5070160109.

[30] A. K. Sambale, M. Maisl, H.-G. Herrmann, and M. Stommel. Characterisation and modelling of moisture gradients in polyamide 6. *Polymers*, 13(18), 2021. doi: 10.3390/polym13183141.

[31] G. Dlubek, F. Redmann, and R. Krause-Rehberg. Humidity–induced plasticization and antiplasticization of polyamide 6: A positron lifetime study of the local free volume. *Journal of Applied Polymer Science*, 84(2):244–255, 2002. ISSN 0021-8995. doi: 10.1002/app.10319.

[32] V. Venoor, J. H. Park, D. O. Kazmer, and M. J. Sobkowicz. Understanding the effect of water in polyamides: A review. *Polymer Reviews*, 2:1–49, 2020. ISSN 1558-3724. doi: 10.1080/15583724.2020.1855196.

[33] Toray Industries, Inc. Before injection-molding a nylon resin | Amilan™ | Toray Plastics | Toray Industries, Inc., 2024. URL `https://www.plastics.toray/de/technical/amilan/tec_007.html`.

[34] A. Launay, Y. Marco, M. H. Maitournam, and I. Raoult. Modelling the influence of temperature and relative humidity on the time-dependent mechanical behaviour of a short glass fibre reinforced polyamide. *Mechanics of Materials*, 56:1–10, 2013. ISSN 01676636. doi: 10.1016/j.mechmat.2012.08.008.

[35] M. Broudin, V. Le Saux, P. Y. Le Gac, C. Champy, G. Robert, P. Charrier, and Y. Marco. Moisture sorption in polyamide 6.6: Experimental investigation and comparison to four physical-based models. *Polymer Testing*, 43:10–20, 2015. ISSN 01429418. doi: 10.1016/j.polymertesting.2015.02.004.

[36] A. J. Hailwood and S. Horrobin. Absorption of water by polymers: analysis in terms of a simple model. *Trans. Faraday Soc.*, 42(0):B084–B092, 1946. doi: 10.1039/TF946420B084.

[37] Ł. Bratasz, A. Kozłowska, and R. Kozłowski. Analysis of water adsorption by wood using the Guggenheim-Anderson-de Boer equation. *European Journal of Wood and Wood Products*, 70(4):445–451, 2012. ISSN 0018-3768. doi: 10.1007/s00107-011-0571-x.

[38] E. J. Quirijns, A. J. B. van Boxtel, W. K. P. van Loon, and G. van Straten. An improved experimental and regression methodology for sorption isotherms. *Journal of the Science of Food and Agriculture*, 85(2):175–185, 2005. ISSN 0022-5142. doi: 10.1002/jsfa.1773.

[39] S. Suherman, M. Peglow, and E. Tsotsas. Measurement and modelling of sorption equilibrium curve of water on PA6, PP, HDPE and PVC by using Flory-Huggins model. *Reaktor*, 13(2):89, 2012. ISSN 0852-0798. doi: 10.14710/reaktor.13.2.89-94.

[40] M. Sabard, F. Gouanvé, E. Espuche, R. Fulchiron, G. Seytre, L.-A. Fillot, and L. Trouillet-Fonti. Influence of film processing conditions on the morphology of polyamide 6: Consequences on water and ethanol sorption properties. *Journal of Membrane Science*, 415-416:670–680, 2012. ISSN 03767388. doi: 10.1016/j.memsci.2012.05.048.

[41] H. K. Reimschuessel. Relationships on the effect of water on glass transition temperature and Young's modulus of nylon 6. *Journal of Polymer Science: Polymer Chemistry Edition*, 16(6):1229–1236, 1978. ISSN 0360-6376. doi: 10.1002/pol.1978.170160606.

[42] N. S. Murthy. Hydrogen bonding, mobility, and structural transitions in aliphatic polyamides. *Journal of Polymer Science Part B: Polymer Physics*, 44(13):1763–1782, 2006. ISSN 0887-6266. doi: 10.1002/polb.20833.

[43] M. Arhant, P.-Y. Le Gac, M. Le Gall, C. Burtin, C. Briançon, and P. Davies. Modelling the non Fickian water absorption in polyamide 6. *Polymer Degradation and Stability*, 133:404–412, 2016. ISSN 01413910. doi: 10.1016/j.polymdegradstab.2016.09.001.

[44] I. Boukal. Effect of water on the mechanism of deformation of nylon 6. *Journal of Applied Polymer Science*, 11(8):1483–1494, 1967. ISSN 0021-8995. doi: 10.1002/app.1967.070110811.

[45] P.-Y. Le Gac, M. Arhant, M. Le Gall, and P. Davies. Yield stress changes induced by water in polyamide 6: Characterization and modeling. *Polymer Degradation and Stability*, 137:272–280, 2017. ISSN 01413910. doi: 10.1016/j.polymdegradstab.2017.02.003.

[46] H. Piao, Y. Kiryu, L. Chen, S. Yamashita, I. Ohsawa, and J. Takahashi. Influence of water absorption on the mechanical properties of discontinuous carbon fiber reinforced polyamide 6. *Journal of Polymer Research*, 26(3), 2019. ISSN 1022-9760. doi: 10.1007/s10965-019-1695-7.

[47] P. Mohammadkhani, J. Magliaro, F. Rahimidehgolan, T. Khapra, and W. Altenhof. Moisture influence on anisotropic mechanical behavior of direct compounded compression molded PA6/glass LFTs. *Composites Part B: Engineering*, 264:110927, 2023. ISSN 13598368. doi: 10.1016/j.compositesb.2023.110927.

[48] P. Sharma, A. Sambale, M. Stommel, M. Maisl, H.-G. Herrmann, and S. Diebels. Moisture transport in PA6 and its influence on the mechanical

properties. *Continuum Mechanics and Thermodynamics*, 32(2):307–325, 2020. ISSN 0935-1175. doi: 10.1007/s00161-019-00815-w.

[49] H. Shinzawa and J. Mizukado. Water absorption by polyamide (PA) 6 studied with two-trace two-dimensional (2T2D) near-infrared (NIR) correlation spectroscopy. *Journal of Molecular Structure*, 1217:128389, 2020. ISSN 00222860. doi: 10.1016/j.molstruc.2020.128389.

[50] H. Obeid, A. Clément, S. Fréour, F. Jacquemin, and P. Casari. On the identification of the coefficient of moisture expansion of polyamide-6: Accounting differential swelling strains and plasticization. *Mechanics of Materials*, 118: 1–10, 2018. ISSN 01676636. doi: 10.1016/j.mechmat.2017.12.002.

[51] R. Shamey and K. Sinha. A review of degradation of nylon 6.6 as a result of exposure to environmental conditions. *Review of Progress in Coloration and Related Topics*, 33(1):93–107, 2003. ISSN 0557-9325. doi: 10.1111/j.1478-4408.2003.tb00147.x.

[52] M. M. Brette, A. H. Holm, A. D. Drozdov, and J. d. C. Christiansen. Pure hydrolysis of polyamides: A comparative study. *Chemistry*, 6(1):13–50, 2024. doi: 10.3390/chemistry6010002.

[53] M. Arhant, E. Lolive, T. Bonnemains, and P. Davies. A study of pure hydrolysis of carbon fibre reinforced polyamide 6 composites tested under mode i loading. *Composites Part A: Applied Science and Manufacturing*, 152: 106719, 2022. ISSN 1359835X. doi: 10.1016/j.compositesa.2021.106719.

[54] M. Arhant, E. Lolive, T. Bonnemains, and P. Davies. Effect of aging on the fatigue crack growth properties of carbon-polyamide 6 thermoplastic composites using the multi ΔG-control method. *Composites Part A: Applied Science and Manufacturing*, 161:107105, 2022. ISSN 1359835X. doi: 10.1016/j.compositesa.2022.107105.

[55] A. Bergeret, L. Ferry, and P. Ienny. Influence of the fibre/matrix interface on ageing mechanisms of glass fibre reinforced thermoplastic composites (PA-6,6, PET, PBT) in a hygrothermal environment. *Polymer*

Degradation and Stability, 94(9):1315–1324, 2009. ISSN 01413910. doi: 10.1016/j.polymdegradstab.2009.04.009.

[56] Q. Deshoulles, M. Le Gall, C. Dreanno, M. Arhant, G. Stoclet, D. Priour, and P. Y. Le Gac. Origin of embrittlement in polyamide 6 induced by chemical degradations: mechanisms and governing factors. *Polymer Degradation and Stability*, 191:109657, 2021. ISSN 01413910. doi: 10.1016/j.polymdegradstab.2021.109657.

[57] R. F. Gibson. *Principles of composite material mechanics*. Mechanical engineering. CRC Press, an imprint of Taylor and Francis, Boca Raton, FL, fourth edition edition, 2016. ISBN 9780429190582. doi: 10.1201/b19626.

[58] Z. Boming, Y. Zhong, and S. Xinyang. Measurement and analysis of residual stresses in single fiber composite. *Materials & Design*, 31(3):1237–1241, 2010. ISSN 02613069. doi: 10.1016/j.matdes.2009.09.027.

[59] B. M. Scheuring. *Effect of hybridization in CoDico-FRTPs: Orientation-dependent characterization and analytical modeling in various climatic conditions*. Karlsruher Institut für Technologie (KIT), 2024. doi: 10.5445/IR/1000177112.

[60] G. H. Staab. *Laminar composites*. Butterworth-Heinemann an imprint of Elsevier, Amsterdam and Boston, second edition edition, 2015. ISBN 9780128024003.

[61] C. L. Tucker, III. *Fundamentals of fiber orientation: Description, measurement and prediction*. Hanser eLibrary. Carl Hanser Verlag GmbH & Co. KG, München, 2022. ISBN 9781569908761. doi: 10.3139/9781569908761.

[62] J. Bauer. *Fiber Orientation Tensors and Mean Field Homogenization: Application to Sheet Molding Compound*. KIT Scientific Publishing, Karlsruhe, 2023. ISBN 978-3-7315-1262-2. doi: 10.5445/KSP/1000152989.

[63] A. Mehta and M. Schneider. A sequential addition and migration method for generating microstructures of short fibers with prescribed length distribution.

Computational Mechanics, 70(4):829–851, 2022. ISSN 0178-7675. doi: 10.1007/s00466-022-02201-x.

[64] H. L. Cox. The elasticity and strength of paper and other fibrous materials. *British Journal of Applied Physics*, 3(3):72–79, 1952. ISSN 0508-3443. doi: 10.1088/0508-3443/3/3/302.

[65] B. W. Rosen, N. F. Dow, Z. Hashin, General Electric Company, United States. National Aeronautics, and Space Administration. *Mechanical Properties of Fibrous Composites*. NASA contractor report. National Aeronautics and Space Administration, 1964. URL `https://books.google.de/books?id=t63RwOMN9w8C`.

[66] J. Amirbayat and J. Hearle. Properties of unit composites as determined by the properties of the interface. part i: Mechanism of matrix-fibre load transfer. *Fibre Science and Technology*, 2(2):123–141, 1969. ISSN 00150568. doi: 10.1016/0015-0568(69)90004-9.

[67] P. W. Beaumont, C. Soutis, and A. Hodzic, editors. *Structural integrity and durability of advanced composites: Innovative modelling methods and intelligent design*, volume number 57 of *Woodhead Publishing Series in Composites Science and Engineering*. Elsevier/WP Woodhead Publishing, Amsterdam and Boston and Cambridge, 2015. ISBN 0081001371.

[68] S.-Y. Fu and B. Lauke. The elastic modulus of misaligned short-fiber-reinforced polymers. *Composites Science and Technology*, 58(3-4):389–400, 1998. ISSN 02663538. doi: 10.1016/S0266-3538(97)00129-2.

[69] K. L. Goh, R. M. Aspden, and D. Hukins. Shear lag models for stress transfer from an elastic matrix to a fibre in a composite material. *International Journal of Materials and Structural Integrity*, 1(1/2/3):180, 2007. ISSN 1745-0055. doi: 10.1504/IJMSI.2007.013871.

[70] J. A. Nairn. A variational mechanics analysis of the stresses around breaks in embedded fibers. *Mechanics of Materials*, 13(2):131–154, 1992. ISSN 01676636. doi: 10.1016/0167-6636(92)90042-C.

[71] A. Kelly and W. R. Tyson. Tensile properties of fibre-reinforced metals: Copper/tungsten and copper/molybdenum. *Journal of the Mechanics and Physics of Solids*, 13(6):329–350, 1965. ISSN 00225096. doi: 10.1016/0022-5096(65)90035-9.

[72] T. Lacroix, B. Tilmans, R. Keunings, M. Desaeger, and I. Verpoest. Modelling of critical fibre length and interfacial debonding in the fragmentation testing of polymer composites. *Composites Science and Technology*, 43 (4):379–387, 1992. ISSN 02663538. doi: 10.1016/0266-3538(92)90061-7. URL `https://www.sciencedirect.com/science/article/pii/0266353892900617`.

[73] A. Kelly. High strength materials. *Contemporary Physics*, 8(4):313–329, 1967. ISSN 0010-7514. doi: 10.1080/00107516708202157.

[74] M. R. Piggott. *Load-bearing fibre composites*. Pergamon international library of science, technology, engineering, and social studies. Pergamon Press, Oxford and New York, 1st ed. edition, 1980. ISBN 9781483182155. URL `https://www.sciencedirect.com/science/book/9780080242316`.

[75] L. N. McCartney. New theoretical model of stress transfer between fibre and matrix in a uniaxially fibre-reinforced composite. *Proceedings of the Royal Society of London. Series A: Mathematical, Physical and Engineering Sciences*, 425(1868):215–244, 1989. ISSN 1364-5021. doi: 10.1098/rspa.1989.0104.

[76] P. S. Steif. Stiffness reduction due to fiber breakage. *Journal of Composite Materials*, 18(2):153–172, 1984. ISSN 0021-9983. doi: 10.1177/002199838401800205.

[77] W. Wu, M. Desaeger, I. Verpoest, and J. Varna. An improved analysis of the stresses in a single-fibre fragmentation test: I. two-phase model. *Composites Science and Technology*, 57(7):809–819, 1997. ISSN 02663538. doi: 10.1016/S0266-3538(97)00050-X.

[78] J. A. Nairn and Y. C. Liu. Stress transfer into a fragmented, anisotropic fiber through an imperfect interface. *International Journal of Solids and Structures*, 34(10):1255–1281, 1997. ISSN 00207683. doi: 10.1016/S0020-7683(96)00065-0.

[79] W. Wu. Variational approach to the stress-transfer problem through partially debonded interfaces in a three-phase composite. *Composites Science and Technology*, 59(4):519–535, 1999. ISSN 02663538. doi: 10.1016/S0266-3538(98)00097-9.

[80] B. J. Thuruthimattam, A. M. Waas, and A. S. Wineman. Stress transfer modeling in viscoelastic polymer matrix composites. *International Journal of Non-Linear Mechanics*, 36(1):69–87, 2001. ISSN 00207462. doi: 10.1016/S0020-7462(99)00088-8.

[81] S. Da Zhu and B. Q. Gu. Micromechanical analysis of single-fiber pull-out test of fiber-reinforced viscoelastic matrix composites. *Advanced Materials Research*, 399-401:556–560, 2011. doi: 10.4028/www.scientific.net/AMR.399-401.556.

[82] N. Obaid, M. T. Kortschot, and M. Sain. Understanding the stress relaxation behavior of polymers reinforced with short elastic fibers. *Materials (Basel, Switzerland)*, 10(5), 2017. ISSN 1996-1944. doi: 10.3390/ma10050472.

[83] J. Wu, H. Yuan, L. Li, K. Fan, S. Qian, and B. Li. Viscoelastic shear lag model to predict the micromechanical behavior of tendon under dynamic tensile loading. *Journal of theoretical biology*, 437:202–213, 2018. doi: 10.1016/j.jtbi.2017.10.018.

[84] J. Wu, H. Yuan, and L.-y. Li. Effect of viscoelasticity on interfacial stress transfer mechanism in the biocomposites: A theoretical study of viscoelastic shear lag model. *Composites Part B: Engineering*, 164:297–308, 2019. ISSN 13598368. doi: 10.1016/j.compositesb.2018.11.086.

[85] A. S. Carrara and F. J. Mcgarry. Matrix and interface stresses in a discontinuous fiber composite model. *Journal of Composite Materials*, 2(2):222–243, 1968. ISSN 0021-9983. doi: 10.1177/002199836800200208.

[86] M. Topçu, G. S. Madabhushi, and M. Staat. A generalized shear-lag theory for elastic stress transfer between matrix and fibres having a variable radius. *International Journal of Solids and Structures*, 239-240:111464, 2022. ISSN 00207683. doi: 10.1016/j.ijsolstr.2022.111464.

[87] J. A. Nairn. On the use of shear-lag methods for analysis of stress transfer in unidirectional composites. *Mechanics of Materials*, 26(2):63–80, 1997. ISSN 01676636. doi: 10.1016/S0167-6636(97)00023-9.

[88] D. Owen and J. F. Lyness. Investigation of bond failure in fibre-reinforced materials by the finite element method. *Fibre Science and Technology*, 5(2): 129–141, 1972. ISSN 00150568. doi: 10.1016/0015-0568(72)90004-8.

[89] K. L. Goh, R. M. Aspden, and D. Hukins. Review: finite element analysis of stress transfer in short-fibre composite materials. *Composites Science and Technology*, 64(9):1091–1100, 2004. ISSN 02663538. doi: 10.1016/j.compscitech.2003.11.003.

[90] D. Gross and T. Seelig. *Fracture Mechanics*. Springer Berlin Heidelberg, Berlin, Heidelberg, 2011. ISBN 978-3-642-19239-5. doi: 10.1007/978-3-642-19240-1.

[91] R. F. Zollo. Fiber-reinforced concrete: an overview after 30 years of development. *Cement and Concrete Composites*, 19(2):107–122, 1997. ISSN 09589465. doi: 10.1016/S0958-9465(96)00046-7.

[92] L. Sun, Y. Jia, F. Ma, J. Zhao, and C. C. Han. Influence of interfacial properties on crack propagation in fiber–reinforced polymer matrix composites. *Macromolecular Materials and Engineering*, 293(3):194–205, 2008. ISSN 1438-7492. doi: 10.1002/mame.200700337.

[93] S. Huang, Q. Fu, L. Yan, and B. Kasal. Characterization of interfacial properties between fibre and polymer matrix in composite materials – a critical review. *Journal of Materials Research and Technology*, 13:1441–1484, 2021. ISSN 22387854. doi: 10.1016/j.jmrt.2021.05.076.

[94] B. Harris, P. W. R. Beaumont, and E. Moncunill de Ferran. Strength and fracture toughness of carbon fibre polyester composites. *Journal of Materials Science*, 6(3):238–251, 1971. ISSN 0022-2461. doi: 10.1007/BF00550019.

[95] S. Zhandarov and E. Mäder. Peak force as function of the embedded length in pull-out and microbond tests: effect of specimen geometry. *Journal of Adhesion Science and Technology*, 19(10):817–855, 2005. ISSN 0169-4243. doi: 10.1163/1568561054929937.

[96] C. Ageorges, K. Friedrich, T. Schüller, and B. Lauke. Single-fibre Broutman test: fibre–matrix interface transverse debonding. *Composites Part A: Applied Science and Manufacturing*, 30(12):1423–1434, 1999. ISSN 1359835X. doi: 10.1016/S1359-835X(99)00045-7. URL `https://www.sciencedirect.com/science/article/pii/S1359835X99000457`.

[97] A. Hampe and C. Marotzke. Experimental results of a pull-out test performed with single- and multi-fiber samples. *The Journal of Adhesion*, 78(2):167–187, 2002. ISSN 0021-8464. doi: 10.1080/00218460210381.

[98] S.-Y. Fu, C.-Y. Yue, X. Hu, and Y.-W. Mai. Analyses of the micromechanics of stress transfer in single- and multi-fiber pull-out tests. *Composites Science and Technology*, 60(4):569–579, 2000. ISSN 02663538. doi: 10.1016/S0266-3538(99)00157-8.

[99] R. Livingston and B. Koohbor. Characterizing fiber-matrix debond and fiber interaction mechanisms by full-field measurements. *Composites Part C: Open Access*, 7:100229, 2022. ISSN 26666820. doi: 10.1016/j.jcomc.2022.100229.

[100] G. P. Tandon, R. Y. Kim, and V. T. Bechel. Fiber–matrix interfacial failure characterization using a cruciform-shaped specimen. *Journal of Composite Materials*, 36(23):2667–2691, 2002. ISSN 0021-9983. doi: 10.1177/002199802761675575.

[101] P. J. Herrera-Franco and L. T. Drzal. Comparison of methods for the measurement of fibre/matrix adhesion in composites. *Composites*, 23(1): 2–27, 1992. ISSN 00104361. doi: 10.1016/0010-4361(92)90282-Y.

[102] C. L. Schutte, W. McDonough, M. Shioya, M. McAuliffe, and M. Greenwood. The use of a single-fibre fragmentation test to study environmental durability of interfaces/interphases between dgeba/mpda epoxy and glass fibre: the effect of moisture. *Composites*, 25(7):617–624, 1994. ISSN 00104361. doi: 10.1016/0010-4361(94)90193-7.

[103] F. A. Ramirez and L. A. Carlsson. Modified single fiber fragmentation test procedure to study water degradation of the fiber/matrix interface toughness of glass/vinylester. *Journal of Materials Science*, 44(12):3035–3042, 2009. ISSN 0022-2461. doi: 10.1007/s10853-009-3400-4. URL `https://link.springer.com/article/10.1007/s10853-009-3400-4`.

[104] L. T. Drzal and P. J. Herrera-Franco. Measurement methods for fiber-matrix adhesion in composite materials. In *Adhesion Science and Engineering*, volume 16, pages 605–660. Elsevier, 2002. ISBN 9780444511409. doi: 10.1016/B978-0-444-51140-9.50043-3.

[105] M. R. Piggott. Debonding and friction at fibre-polymer interfaces. i: Criteria for failure and sliding. *Composites Science and Technology*, 30(4): 295–306, 1987. ISSN 02663538. doi: 10.1016/0266-3538(87)90017-0.

[106] B. Miller, P. Muri, and L. Rebenfeld. A microbond method for determination of the shear strength of a fiber/resin interface. *Composites Science and Technology*, 28(1):17–32, 1987. ISSN 02663538. doi: 10.1016/0266-3538(87)90059-5.

[107] D. A. Biro, G. Pleizier, and Y. Deslandes. Application of the microbond technique: Effects of hygrothermal exposure on carbon-fiber/epoxy interfaces. *Composites Science and Technology*, 46(3):293–301, 1993. ISSN 02663538. doi: 10.1016/0266-3538(93)90163-b.

[108] A. Straub, M. Slivka, and P. Schwartz. A study of the effects of time and temperature on the fiber/matrix interface strength using the microbond test. *Composites Science and Technology*, 57(8):991–994, 1997. ISSN 02663538. doi: 10.1016/s0266-3538(96)00146-7.

[109] K. A. Downes and J. L. Thomason. A method to measure the influence of humidity and temperature on the interfacial adhesion in polyamide composites. *Composite Interfaces*, 22(8):757–766, 2015. ISSN 0927-6440. doi: 10.1080/09276440.2015.1059114.

[110] H. S. Bedi, B. K. Billing, and P. K. Agnihotri. Interphase engineering in carbon fiber/epoxy composites: Rate sensitivity of interfacial shear strength and interfacial fracture toughness. *Polymer Composites*, 41(7):2803–2815, 2020. ISSN 0272-8397. doi: 10.1002/pc.25577.

[111] S. Bouillaguet, A. Schütt, P. Alander, P. Schwaller, G. Buerki, J. Michler, M. Cattani-Lorente, P. K. Vallittu, and I. Krejci. Hydrothermal and mechanical stresses degrade fiber-matrix interfacial bond strength in dental fiber-reinforced composites. *Journal of biomedical materials research. Part B, Applied biomaterials*, 76(1):98–105, 2006. ISSN 1552-4973. doi: 10.1002/jbm.b.30349.

[112] C. Marotzke. The elastic stress field arising in the single-fiber pull-out test. *Composites Science and Technology*, 50(3):393–405, 1994. ISSN 02663538. doi: 10.1016/0266-3538(94)90027-2.

[113] S. M. Doshi, A. Schneider, J. M. Deitzel, and J. W. Gillespie Jr. Interfacial characterization of S2 glass-epoxy resin using single fiber pullout tests at varying temperature and moisture level. In *American Society for Composites 2023*. Destech Publications, Inc, 9182023. ISBN 9781605956916. doi: 10.12783/asc38/36643.

[114] K. Tanaka, Y. Masabe, and T. Katayama. Evaluation of interfacial properties for carbon fiber/ polyamide model composites by means of single fiber pull-out test. *Journal of the Society of Materials Science, Japan*, 58(7): 635–641, 2009. ISSN 0514-5163. doi: 10.2472/jsms.58.635.

[115] K. Tanaka, S. Mizuno, H. Honda, T. Katayama, and S. Enoki. Effect of water absorption on the mechanical properties of carbon fiber/polyamide composites. *Journal of Solid Mechanics and Materials Engineering*, 7(5): 520–529, 2013. doi: 10.1299/jmmp.7.520.

[116] K. Tanaka, S. Okuda, Y. Hinoue, and T. Katayama. Effects of water absorption on the fiber–matrix interfacial shear strength of carbon nanotube-grafted carbon fiber reinforced polyamide resin. *Journal of Composites Science*, 3 (1):4, 2019. doi: 10.3390/jcs3010004.

[117] P. Chen and M. R. Piggott. Reduction of fiber pull-out stress due to hot water immersion: Carbon/peek. *Journal of Thermoplastic Composite Materials*, 12(1):33–45, 1999. ISSN 0892-7057. doi: 10.1177/089270579901200104.

[118] K. Tanaka, N. Hosoo, T. Katayama, Y. Noguchi, and K. Izui. Effect of temperature on the fiber/matrix interfacial strength of carbon fiber reinforced polyamide model composites. *Mechanical Engineering Journal*, 3(6):16–00158–16–00158, 2016. doi: 10.1299/mej.16-00158.

[119] F. Weidmann, G. Ziegmann, and J. Wieser. A review of mode i dominant interfacial fracture toughness test methods of skin-core bonding for thermoplastic composite sandwich structures. *Journal of Thermoplastic Composite Materials*, page 089270572210834, 2022. ISSN 0892-7057. doi: 10.1177/08927057221083493.

[120] E. S. Greenhalgh, C. Rogers, and P. Robinson. Fractographic observations on delamination growth and the subsequent migration through the laminate. *Composites Science and Technology*, 69(14):2345–2351, 2009. ISSN 02663538. doi: 10.1016/j.compscitech.2009.01.034.

[121] J. M. Hodgkinson. *Mechanical testing of advanced fibre composites*. CRC Press and Cambridge : Woodhead, Boca Raton, FL, 2000. ISBN 1-85573-312-9.

[122] D30 Committee. Test method for mode i interlaminar fracture toughness of unidirectional fiber-reinforced polymer matrix composites.

[123] Y. Uematsu, T. Kitamura, and R. Ohtani. Delamination behavior of a carbon-fiber-reinforced thermoplastic polymer at high temperatures. *Composites Science and Technology*, 53(3):333–341, 1995. ISSN 02663538. doi: 10.1016/0266-3538(95)00005-4.

[124] A. Williams, I. Hamerton, and G. Allegri. Environmental effects of moisture and elevated temperatures on the mode i and mode ii interlaminar fracture toughness of a toughened epoxy carbon fibre reinforced polymer. *Polymers*, 17(11), 2025. doi: 10.3390/polym17111503.

[125] Normenausschuss Luft- und Raumfahrt (NL) im DIN. DIN EN 2243-3:2006-10, Luft- und Raumfahrt – Nichtmetallische Werkstoffe – Strukturelle Klebstoffsysteme – Prüfverfahren – Teil 3: Trommelschälversuch für Wabenkernverbunde; Deutsche und Englische Fassung EN 2243-3:2005, 2006.

[126] D14 Committee. Standard test method for climbing drum peel for adhesives.

[127] S. Michel, F. Hauf, and A. J. Brunner. Evaluation of a climbing drum laminate peel test to determine the interlaminar mode i fracture toughness of thin CFRP laminates—comparison with the standard mode i DCB test and a mandrel laminate peel test proposed by ESIS TC4. *Frontiers in Materials*, 10, 2023. doi: 10.3389/fmats.2023.981647.

[128] F. Daghia and C. Cluzel. The climbing drum peel test: An alternative to the double cantilever beam for the determination of fracture toughness of monolithic laminates. *Composites Part A: Applied Science and Manufacturing*, 78: 70–83, 2015. ISSN 1359835X. doi: 10.1016/j.compositesa.2015.07.010.

[129] S. Joannès, L. Mazé, and A. R. Bunsell. A simple method for modeling the concentration-dependent water sorption in reinforced polymeric materials. *Composites Part B: Engineering*, 57:219–227, 2014. ISSN 13598368. doi: 10.1016/j.compositesb.2013.10.004.

[130] D. Klepach and T. I. Zohdi. Strain assisted diffusion: Modeling and simulation of deformation-dependent diffusion in composite media. *Composites Part B: Engineering*, 56:413–423, 2014. ISSN 13598368. doi: 10.1016/j.compositesb.2013.08.035.

[131] A. K. Sambale, M. Stanko, J. Emde, and M. Stommel. Characterisation and FE modelling of the sorption and swelling behaviour of polyamide 6 in water. *Polymers*, 13(9), 2021. doi: 10.3390/polym13091480.

[132] P. Wetzel, A. K. Sambale, K. Uhlig, M. Stommel, B. Schneider, and J.-M. Kaiser. Hygromechanical behavior of polyamide 6.6: Experiments and modeling. *Polymers*, 15(16), 2023. doi: 10.3390/polym15163387.

[133] P. Sharma and S. Diebels. A mixture theory for the moisture transport in polyamide. *Continuum Mechanics and Thermodynamics*, 33(4):1891–1905, 2021. ISSN 0935-1175. doi: 10.1007/s00161-021-01019-x.

[134] A. Dyck, L. Groß, J. Keursten, L. Kehrer, and T. Böhlke. Modeling and FE simulation of coupled water diffusion and viscoelasticity in relaxation tests of polyamide 6. *Continuum Mechanics and Thermodynamics*, 36(4):935–953, 2024. ISSN 0935-1175. doi: 10.1007/s00161-024-01305-4.

[135] BASF SE. CAMPUSplastics | datasheet Ultramid® B3K, 2024. URL `https://www.campusplastics.com/campus/en/datasheet/Ultramid%C2%AE+B3K/BASF/20/3a22f000`.

[136] R. A. Schapery. A theory of nonlinear thermoviscoelasticity based on irreversible thermodynamics. 1966.

[137] T. Zink, L. Kehrer, V. Hirschberg, M. Wilhelm, and T. Böhlke. Nonlinear schapery viscoelastic material model for thermoplastic polymers. *Journal of Applied Polymer Science*, 139(17):52028, 2022. ISSN 0021-8995. doi: 10.1002/app.52028.

[138] G. T. Camacho and M. Ortiz. Computational modelling of impact damage in brittle materials. *International Journal of Solids and Structures*, 33(20-22): 2899–2938, 1996. ISSN 00207683. doi: 10.1016/0020-7683(95)00255-3.

[139] K. Park and G. H. Paulino. Cohesive zone models: A critical review of traction-separation relationships across fracture surfaces. *Applied Mechanics Reviews*, 64(6), 2011. ISSN 0003-6900. doi: 10.1115/1.4023110.

[140] L. Prandtl. Ein Gedankenmodell für den Zerreißvorgang spröder Körper. *ZAMM - Journal of Applied Mathematics and Mechanics / Zeitschrift für Angewandte Mathematik und Mechanik*, 13(2):129–133, 1933. ISSN 0044-2267. doi: 10.1002/zamm.19330130218.

[141] D. S. Dugdale. Yielding of steel sheets containing slits. *Journal of the Mechanics and Physics of Solids*, 8(2):100–104, 1960. ISSN 00225096. doi: 10.1016/0022-5096(60)90013-2.

[142] G. I. Barenblatt. The mathematical theory of equilibrium cracks in brittle fracture. In H. L. Dryden, H. L. Dryden, and T. von Kármán, editors, *Advances in Applied Mechanics. Volume 7*, volume 7 of *Advances in Applied Mechanics*, pages 55–129. Elsevier, 1962. ISBN 9780120020072. doi: 10.1016/S0065-2156(08)70121-2.

[143] I. Scheider. Numerical simulation of material separation using cohesive zone models. In S. Schmauder, C.-S. Chen, K. K. Chawla, N. Chawla, W. Chen, and Y. Kagawa, editors, *Handbook of Mechanics of Materials*, Springer eBook Collection, pages 1–42. Springer, Singapore, 2019. ISBN 978-981-10-6855-3. doi: 10.1007/978-981-10-6855-3_36-1.

[144] A. Hillerborg, M. Modéer, and P.-E. Petersson. Analysis of crack formation and crack growth in concrete by means of fracture mechanics and finite elements. *Cement and Concrete Research*, 6(6):773–781, 1976. ISSN 00088846. doi: 10.1016/0008-8846(76)90007-7.

[145] E. Martínez Pañeda. Abaqus implementation of cohesive zone models, 2018.

[146] G. H. Paulino and Z. Zhang. Cohesive modeling of propagating cracks in homogeneous and functionally graded composites. In G. Georgios, P. Papanastasiou, and M. Papadrakakis, editors, *Proceedings of GRACM 05*, pages 45–51. Kantzilaris Publications, Nicosia, 2005. ISBN 9963-644-50-3.

[147] A. Salve and S. Jalwadi. Implementation of cohesive zone in ABAQUS to investigate fracture problems. 2015.

[148] N. Christ, B. M. Scheuring, C. Schelleis, W. V. Liebig, J. Montesano, K. A. Weidenmann, and J. Hohe. Characterization and simulation of the interface between a continuous and discontinuous carbon fiber reinforced thermoplastic by using the climbing drum peel test considering humidity. *Polymers*, 16(7), 2024. doi: 10.3390/polym16070976.

[149] P. H. Geubelle and J. S. Baylor. Impact-induced delamination of composites: a 2D simulation. *Composites Part B: Engineering*, 29(5):589–602, 1998. ISSN 13598368. doi: 10.1016/S1359-8368(98)00013-4.

[150] Ingo Scheider. Cohesive model for crack propagation analyses of structures with elastic – plastic material behavior foundations and implementation. 2002.

[151] A. Turon, P. P. Camanho, J. Costa, and J. Renart. Accurate simulation of delamination growth under mixed-mode loading using cohesive elements: Definition of interlaminar strengths and elastic stiffness. *Composite Structures*, 92(8):1857–1864, 2010. ISSN 02638223. doi: 10.1016/j.compstruct.2010.01.012. URL `https://www.sciencedirect.com/science/article/pii/S026382231000022X`.

[152] L. M. Bustamante-Góez, E. Chica-Arrieta, and J. A. Villarraga-Ossa. Assessment of cohesive traction-separation relationship according stiffness variation. *Revista UIS Ingenierías*, 18(2):67–76, 2019. ISSN 16574583. doi: 10.18273/revuin.v18n2-2019006.

[153] A. Cornec, I. Scheider, and K.-H. Schwalbe. On the practical application of the cohesive model. *Engineering Fracture Mechanics*, 70(14):1963–1987, 2003. ISSN 00137944. doi: 10.1016/S0013-7944(03)00134-6.

[154] M. Barral, G. Chatzigeorgiou, F. Meraghni, and R. Léon. Homogenization using modified Mori-Tanaka and TFA framework for elastoplastic-viscoelastic-viscoplastic composites: Theory and numerical validation. *International Journal of Plasticity*, 127:102632, 2020. ISSN 07496419. doi: 10.1016/j.ijplas.2019.11.011.

[155] R. M. Christensen. *Mechanics of Composite Materials*. Dover Civil and Mechanical Engineering. Dover Publications, New York, 2012. ISBN 9780486136660. URL `https://ebookcentral.proquest.com/lib/kxp/detail.action?docID=1894621`.

[156] J. Aboudi, Arnold, Steven, M., and Bednarcyk, Brett, A. *Micromechanics of Composite Materials*. Elsevier, 2013. ISBN 9780123970350. doi: 10.1016/C2011-0-05224-9.

[157] W. Yu. An introduction to micromechanics. *Applied Mechanics and Materials*, 828:3–24, 2016. doi: 10.4028/www.scientific.net/AMM.828.3.

[158] W. Voigt. Ueber die Beziehung zwischen den beiden Elasticitätsconstanten isotroper Körper. *Annalen der Physik*, 274(12):573–587, 1889. ISSN 0003-3804. doi: 10.1002/andp.18892741206.

[159] A. Reuss. Berechnung der Fließgrenze von Mischkristallen auf Grund der Plastizitätsbedingung für Einkristalle. *ZAMM - Journal of Applied Mathematics and Mechanics / Zeitschrift für Angewandte Mathematik und Mechanik*, 9(1):49–58, 1929. ISSN 0044-2267. doi: 10.1002/zamm.19290090104.

[160] W. J. Parnell and C. Calvo-Jurado. On the computation of the Hashin–Shtrikman bounds for transversely isotropic two-phase linear elastic fibre-reinforced composites. *Journal of Engineering Mathematics*, 95(1):295–323, 2015. ISSN 0022-0833. doi: 10.1007/s10665-014-9777-3.

[161] B. Liu, X. Feng, and S.-M. Zhang. The effective Young's modulus of composites beyond the Voigt estimation due to the Poisson effect. *Composites Science and Technology*, 69(13):2198–2204, 2009. ISSN 02663538. doi: 10.1016/j.compscitech.2009.06.004.

[162] Z. Hashin and S. Shtrikman. A variational approach to the theory of the effective magnetic permeability of multiphase materials. *Journal of Applied Physics*, 33(10):3125–3131, 1962. ISSN 0021-8979. doi: 10.1063/1.1728579.

[163] Z. Hashin and S. Shtrikman. A variational approach to the theory of the elastic behaviour of multiphase materials. *Journal of the Mechanics and Physics of Solids*, 11(2):127–140, 1963. ISSN 00225096. doi: 10.1016/0022-5096(63)90060-7.

[164] L. Kehrer, J. T. Wood, and T. Böhlke. Mean-field homogenization of thermoelastic material properties of a long fiber-reinforced thermoset and experimental investigation. *Journal of Composite Materials*, 54(25):3777–3799, 2020. ISSN 0021-9983. doi: 10.1177/0021998320920695.

[165] J. D. Eshelby. The determination of the elastic field of an ellipsoidal inclusion, and related problems. *Proceedings of the Royal Society of London Series A*, 241(1226):376–396, 1957. doi: 10.1098/rspa.1957.0133.

[166] T. Mori and K. Tanaka. Average stress in matrix and average elastic energy of materials with misfitting inclusions. *Acta Metallurgica*, 21(5):571–574, 1973. ISSN 00016160. doi: 10.1016/0001-6160(73)90064-3.

[167] A. V. Hershey. The elasticity of an isotropic aggregate of anisotropic cubic crystals. *Journal of Applied Mechanics*, 21(3):236–240, 1954. ISSN 0021-8936. doi: 10.1115/1.4010899.

[168] E. Kröner. Berechnung der elastischen Konstanten des Vielkristalls aus den Konstanten des Einkristalls. *Zeitschrift fr Physik*, 151(4):504–518, 1958. ISSN 1434-6001. doi: 10.1007/BF01337948.

[169] Z. Hashin. Analysis of composite materials—a survey. *Journal of Applied Mechanics*, 50(3):481–505, 1983. ISSN 0021-8936. doi: 10.1115/1.3167081.

[170] O. Pierard, C. Friebel, and I. Doghri. Mean-field homogenization of multi-phase thermo-elastic composites: a general framework and its validation. *Composites Science and Technology*, 64(10-11):1587–1603, 2004. ISSN 02663538. doi: 10.1016/j.compscitech.2003.11.009.

[171] A. Fritsch, C. Hellmich, and P. Young. Micromechanics-derived scaling relations for poroelasticity and strength of brittle porous polycrystals. *Journal of Applied Mechanics*, 80(2), 2013. ISSN 0021-8936. doi: 10.1115/1.4007922.

[172] C. Morin, V. Vass, and C. Hellmich. Micromechanics of elastoplastic porous polycrystals: Theory, algorithm, and application to osteonal bone. *International Journal of Plasticity*, 91:238–267, 2017. ISSN 07496419. doi: 10.1016/j.ijplas.2017.01.009.

[173] L. J. Walpole. Elastic behavior of composite materials: Theoretical foundations. In *Advances in Applied Mechanics Volume 21*, volume 21 of *Advances*

in Applied Mechanics, pages 169–242. Elsevier, 1981. ISBN 9780120020218. doi: 10.1016/S0065-2156%2808%2970332-6.

[174] Y. P. Qiu and G. J. Weng. On the application of Mori-Tanaka's theory involving transversely isotropic spheroidal inclusions. *International Journal of Engineering Science*, 28(11):1121–1137, 1990. ISSN 00207225. doi: 10.1016/0020-7225(90)90112-V.

[175] G. J. Weng. The theoretical connection between Mori-Tanaka's theory and the Hashin-Shtrikman-Walpole bounds. *International Journal of Engineering Science*, 28(11):1111–1120, 1990. ISSN 00207225. doi: 10.1016/0020-7225(90)90111-U.

[176] D. Lee. Local anisotropy analysis based on the Mori-Tanaka model for multiphase composites with fiber length and orientation distributions. *Composites Part B: Engineering*, 148:227–234, 2018. ISSN 13598368. doi: 10.1016/j.compositesb.2018.04.050.

[177] B. Brylka. *Charakterisierung und Modellierung der Steifigkeit von langfaserverstärktem Polypropylen*. KIT Scientific Publishing, 2017. ISBN 9783731506805. URL `https://directory.doabooks.org/handle/20.500.12854/43020`.

[178] J. K. Bauer and T. Böhlke. On the dependence of orientation averaging mean field homogenization on planar fourth-order fiber orientation tensors. *Mechanics of Materials*, 170:104307, 2022. ISSN 01676636. doi: 10.1016/j.mechmat.2022.104307.

[179] S. G. Advani and C. L. Tucker. The use of tensors to describe and predict fiber orientation in short fiber composites. *Journal of Rheology*, 31(8):751–784, 1987. ISSN 0148-6055. doi: 10.1122/1.549945.

[180] S. W. Tsai, J. C. Halpin, N. J. Pagano, R. T. Schwartz, ONR-ARPA Association of Monsanto, and Washington University. *Composite Materials Workshop*. Technomic Publishing Company, 1968. URL `https://books.google.de/books?id=8blRAAAAMAAJ`.

[181] John C. Halpin. Effects of environmental factors on composite materials. 1969. URL https://api.semanticscholar.org/CorpusID:135872649.

[182] J. C. Halpin and J. L. Kardos. The Halpin–Tsai equations: A review. *Polymer Engineering and Science*, 16(5):344–352, 1976. ISSN 0032-3888. doi: 10.1002/pen.760160512.

[183] S.-Y. Fu, B. Lauke, and Y. W. Mai. *Science and engineering of short fibre-reinforced polymer composites*. Woodhead Publishing Series in Composites Science and Engineering. Woodhead Publishing, Duxford England and Cambridge MA, second edition edition, 2019. ISBN 9780081026236.

[184] S.-Y. Fu, G. Xu, and Y.-W. Mai. On the elastic modulus of hybrid particle/short-fiber/polymer composites. *Composites Part B: Engineering*, 33 (4):291–299, 2002. ISSN 13598368. doi: 10.1016/S1359-8368(02)00013-6.

[185] B. M. Scheuring, N. Christ, J. Blarr, W. V. Liebig, J. Hohe, J. Montesano, and K. A. Weidenmann. Experimental and homogenized orientation-dependent properties of hybrid long fiber-reinforced thermoplastics. *International Journal of Mechanical Sciences*, page 109470, 2024. ISSN 00207403. doi: 10.1016/j.ijmecsci.2024.109470.

[186] T. Böhlke, F. Henning, A. Hrymak, L. Kärger, K. Weidenmann, and J. T. Wood, editors. *Continuous–discontinuous fiber-reinforced polymers: An integrated engineering approach*. Carl Hanser Verlag, Munich, 2019. ISBN 9781569906934. URL https://www.sciencedirect.com/science/book/9781569906927.

[187] DOMO Chemicals GmbH. CAMPUSplastics | datasheet TECHNYL C 216 WT R9010 BL, 2024. URL https://www.campusplastics.com/campus/en/datasheet/TECHNYL+C+216+WT+R9010+BL/DOMO+Chemicals/150/9d752d01/SI?pos=157.

[188] ZOLTEK Corporation. ZOLTEK™ PX35 continuous tow: Technical datasheet, 2025. URL https://zoltek.com/wp-content/uploads/TDS_PX35_Continuious_Tow-1.pdf.

[189] W. Krause, F. Henning, S. Tröster, O. Geiger, and P. Eyerer. LFT-D — a process technology for large scale production of fiber reinforced thermoplastic components. *Journal of Thermoplastic Composite Materials*, 16(4):289–302, 2003. ISSN 0892-7057. doi: 10.1177/0892705703016004001.

[190] C. Schelleis, B. Scheuring, A. Hrymak, and F. Henning. Study on mechanical characteristics of glass fiber-reinforced polycarbonate LFT-D for CoDiCo structures. In *ICCM 2023, 23rd International Conference on Composite Materials. Proceedings*. 2023. doi: 10.24406/H-451656.

[191] C. Schelleis, B. M. Scheuring, L. Schreyer, W. V. Liebig, A. Hrymak, L. Kärger, K. A. Weidenmann, and F. Henning. Process-induced skewness of flow fronts and fiber orientations in LFT-D compression molding considering processing, characterization, and simulation. *Journal of Thermoplastic Composite Materials*, 2025. ISSN 0892-7057. doi: 10.1177/08927057251344252.

[192] N. Afrasiabian, A. Elmoghazy, J. Blarr, B. Scheuring, A. Prahs, D. Schneider, W. V. Liebig, K. A. Weidenmann, C. Denniston, and B. Nestler. Crystallization and crystal morphology of polymers: A multiphase-field study. *Journal of Thermoplastic Composite Materials*, 2024. ISSN 0892-7057. doi: 10.1177/08927057241296472.

[193] F. H. Norton. *Creep of steel at high temperatures*. McGraw-Hill, New York, 1929. ISBN 1172536333.

[194] R. W. Bailey. The utilization of creep test data in engineering design. *Proceedings of the Institution of Mechanical Engineers*, 131(1):131–349, 1935. ISSN 0020-3483. doi: 10.1243/PIME_PROC_1935_131_012_02.

[195] H. F. Brinson and L. C. Brinson. *Polymer engineering science and viscoelasticity: An introduction / Hal F. Brinson, L. Catherine Brinson*. Springer, New York, 2008. ISBN 978-0-387-73860-4.

[196] R. A. Schapery. Further development of a thermodynamic constitutive theory: Stress formulation. 1969.

[197] R. A. Schapery. On the characterization of nonlinear viscoelastic materials. *Polymer Engineering and Science*, 9(4):295–310, 1969. ISSN 0032-3888. doi: 10.1002/pen.760090410.

[198] C. C. Hiel, H. F. Brinson, and A. H. Cardon. The nonlinear viscoelastic response of resin matrix composites. In I. H. Marshall, editor, *Composite Structures 2*, pages 271–281. Springer Netherlands, Dordrecht, 1983. ISBN 978-94-009-6642-0. doi: 10.1007/978-94-009-6640-6_20.

[199] M. F. Woldekidan. *Response Modelling of Bitumen, Bituminous Mastic and Mortar*. Phd thesis, Delft University of Technology, 2011. URL `https://repository.tudelft.nl/islandora/object/uuid:e3f99110-41fe-423d-97e3-eb35ea95b271?collection=research`.

[200] C. P. Buckley and N. G. McCrum. The relation between linear and nonlinear viscoelasticity of polypropylene. *Journal of Materials Science*, 9(12): 2064–2066, 1974. ISSN 0022-2461. doi: 10.1007/BF00540560.

[201] M. Henriksen. Nonlinear viscoelastic stress analysis—a finite element approach. *Computers & Structures*, 18(1):133–139, 1984. ISSN 00457949. doi: 10.1016/0045-7949(84)90088-9.

[202] R. M. Haj-Ali and A. H. Muliana. Numerical finite element formulation of the Schapery non-linear viscoelastic material model. *International Journal for Numerical Methods in Engineering*, 59(1):25–45, 2004. ISSN 0029-5981. doi: 10.1002/nme.861.

[203] A. Serra-Aguila, J. M. Puigoriol-Forcada, G. Reyes, and J. Menacho. Viscoelastic models revisited: characteristics and interconversion formulas for generalized Kelvin–Voigt and Maxwell models. *Acta Mechanica Sinica*, 35 (6):1191–1209, 2019. ISSN 0567-7718. doi: 10.1007/s10409-019-00895-6.

[204] W. Flügge. *Viscoelasticity*. Springer Berlin Heidelberg, Berlin, Heidelberg, second revised edition edition, 1975. ISBN 978-3-662-02278-8. doi: 10.1007/978-3-662-02276-4.

[205] Abaqus. *ABAQUS/Standard User's Manual, Version 6.9*. Dassault Systèmes Simulia Corp, United States, 2009.

[206] L. J. Mauer and L. S. Taylor. Water-solids interactions: deliquescence. *Annual review of food science and technology*, 1:41–63, 2010. ISSN 1941-1413. doi: 10.1146/annurev.food.080708.100915.

[207] G. Zografi. States of water associated with solids. *Drug Development and Industrial Pharmacy*, 14(14):1905–1926, 1988. ISSN 0363-9045. doi: 10.3109/03639048809151997.

[208] S. T. Martin. Phase transitions of aqueous atmospheric particles. *Chemical reviews*, 100(9):3403–3454, 2000. doi: 10.1021/cr990034t.

[209] F. O'Brien. The control of humidity by saturated salt solutions. *Journal of Scientific Instruments*, 25(3):73–76, 1948. ISSN 0950-7671. doi: 10.1088/0950-7671/25/3/305.

[210] N. Christ, P. Gumbsch, and J. Hohe. Single fiber pull-out investigation at different temperature and humidity conditions: Experimental characterization of the fiber-matrix interface in carbon fiber reinforced polyamide 6. *Journal of Thermoplastic Composite Materials*, 2025. ISSN 0892-7057. doi: 10.1177/08927057251314436.

[211] F. Boulogne. Cheap and versatile humidity regulator for environmentally controlled experiments. *The European physical journal. E, Soft matter*, 42 (4):51, 2019. doi: 10.1140/epje/i2019-11813-0.

[212] F. Stefan, M. Edith, M. Andrea, M. Ulrich, P. Claudia, and S. Christina. A new testing system to determine the fiber-matrix adhesion strength by means of pull-out tests. In *SAMPE neXus 2021*. NA SAMPE, 2021. ISBN 978-1-934551-39-4. doi: 10.33599/nasampe/s.21.0608.

[213] D. C. Hartlen and D. S. Cronin. Arc-length re-parametrization and signal registration to determine a characteristic average and statistical response corridors of biomechanical data. *Frontiers in bioengineering and biotechnology*, 10:843148, 2022. ISSN 2296-4185. doi: 10.3389/fbioe.2022.843148.

[214] J. H. Tsai, A. Patra, and R. Wetherhold. Finite element simulation of shaped ductile fiber pullout using a mixed cohesive zone/friction interface model. *Composites Part A: Applied Science and Manufacturing*, 36(6):827–838, 2005. ISSN 1359835X. doi: 10.1016/j.compositesa.2004.10.025.

[215] L. Hoppe. Numerical simulation of fiber-matrix debonding in single fiber pull-out tests. *GAMM Archive for Students*, 2(1):21–35, 2020. doi: 10.14464/gammas.v2i1.437.

[216] C. Marotzke. Determination of the stress field in the single fiber pull-out test with the aid of the finite element method. In *Interfacial Phenomena in Composite Materials '91*, pages 69–72. Elsevier, 1991. ISBN 9780750603560. doi: 10.1016/B978-0-7506-0356-0.50022-8.

[217] M. Y. Quek. Analysis of residual stresses in a single fibre–matrix composite. *International Journal of Adhesion and Adhesives*, 24(5):379–388, 2004. ISSN 01437496. doi: 10.1016/S0143-7496(03)00097-6.

[218] I. V. Andrianov, V. V. Danishevskyy, and H. Topol. Local stress distribution in composites for pulled-out fibers with axially varying bonding. *Acta Mechanica*, 231(5):2065–2083, 2020. ISSN 0001-5970. doi: 10.1007/s00707-020-02634-6.

[219] Y. Jia, W. Yan, and H.-Y. Liu. Numerical study on residual thermal stresses in carbon fibre pullout. volume 3, 2012.

[220] G. A. Holmes, R. C. Peterson, D. L. Hunston, W. G. McDonough, and C. L. Schutte. The effect of nonlinear viscoelasticity on interfacial shear strength measurements. In R. A. Schapery and C. T. Sun, editors, *Time dependent and nonlinear effects in polymers and composites*, ASTM STP 1357, pages 98–117. ASTM International, West Conshohocken, Pa. and W. Conshohocken, Pa., 2000. ISBN 0803126018. doi: 10.1520/stp15831s.

[221] B. A. Budiman, K. Takahashi, K. Inaba, and K. Kishimoto. A new method of evaluating interfacial properties of a fiber/matrix composite. *Journal of Composite Materials*, 49(4):465–475, 2015. ISSN 0021-9983. doi: 10.1177/0021998314521061.

[222] D. P. Raghavalu Thirumalai, T. Løgstrup Andersen, and Aage Lystrup. Influence of moisture absorption on properties of fiber reinforced polyamide 6 composites. In *Proceedings of the 26th Annual Technical Conference of the American Society for Composites 2011 and the 2nd Joint US-Canada Conference on Composites*, volume 1, pages 500–510. Destech Publications, Inc, 2011. ISBN 9781618391964.

[223] D. M. Blackketter, D. Upadhyaya, and T. R. King. Micromechanics prediction of the transverse tensilc strength of carobn fiber/epoxy composites: The influence of the matrix and interface. *Polymer Composites*, 14(5):437–446, 1993. ISSN 0272-8397. doi: 10.1002/pc.750140511.

[224] H. Miyagawa, T. Mase, C. Sato, E. Drown, L. T. Drzal, and K. Ikegami. Comparison of experimental and theoretical transverse elastic modulus of carbon fibers. *Carbon*, 44(10):2002–2008, 2006. ISSN 00086223. doi: 10.1016/j.carbon.2006.01.026.

[225] L. Monson, M. Braunwarth, and C. W. Extrand. Moisture absorption by various polyamides and their associated dimensional changes. *Journal of Applied Polymer Science*, 107(1):355–363, 2008. ISSN 0021-8995. doi: 10.1002/app.27057.

[226] M. S. Amer, M. J. Koczak, and L. S. Schadler. Environmental degradation of the interface in graphite/epoxy single filament composites measured using raman spectroscopy: Effect of hydrothermal and thermal exposure at 100°c. *Composite Interfaces*, 3(1):41–50, 1995. ISSN 0927-6440. doi: 10.1163/156855495X00147.

[227] U. Gaur, C. T. Chou, and B. Miller. Effect of hydrothermal ageing on bond strength. *Composites*, 25(7):609–612, 1994. ISSN 00104361. doi: 10.1016/0010-4361(94)90191-0.

[228] K. Tanaka, K. Minoshima, W. Grela, and K. Komai. Characterization of the aramid/epoxy interfacial properties by means of pull-out test and influence of water absorption. *Composites Science and Technology*, 62(16):2169–2177, 2002. ISSN 02663538. doi: 10.1016/S0266-3538(02)00147-1.

[229] B. Harris. *Engineering composite materials*, volume 673 of *Book / The Institute of Metals, London*. IOM Communications Ltd, London, 2. ed. edition, 1999. ISBN 1861250320.

[230] J.-K. Kim and Y. W. Mai. *Engineered interfaces in fiber reinforced composites*. Elsevier, Amsterdam and Oxford, 1998. ISBN 0-08-042695-6.

[231] S. Ahmadvashaghbash, I. Verpoest, Y. Swolfs, and M. Mehdikhani. Methods and models for fibre–matrix interface characterisation in fibre-reinforced polymers: a review. *International Materials Reviews*, 68(8):1245–1319, 2023. ISSN 0950-6608. doi: 10.1080/09506608.2023.2265701.

[232] C. Marotzke. Influence of the fiber length on the stress transfer from glass and carbon fibers into a thermoplastic matrix in the pull-out test. *Composite Interfaces*, 1(2):153–166, 1993. ISSN 0927-6440. doi: 10.1163/156855493X00040.

[233] I. Velkavrh, S. Klien, J. Voyer, F. Ausserer, and A. Diem. Influence of water absorption on static friction of pure and friction-modified PA6 polymers. *Key Engineering Materials*, 799:59–64, 2019. doi: 10.4028/www.scientific.net/KEM.799.59.

[234] M. R. Piggott. Why interface testing by single-fibre methods can be misleading. *Composites Science and Technology*, 57(8):965–974, 1997. ISSN 02663538. doi: 10.1016/S0266-3538(97)00036-5.

[235] J. Jäger. *Aspekte der Faser-Matrix-Wechselwirkung in carbonfaserverstärkten Polymeren: Zugl.: Augsburg, Univ., Diss., 2014*. Physics. mbv Mensch-und-Buch-Verl., Berlin, 2014. ISBN 9783863875633.

[236] A. S. Nielsen and R. Pyrz. A raman study into the effect of transcrystallisation on thermal stresses in embedded single fibres. *Journal of Materials Science*, 38(3):597–601, 2003. ISSN 0022-2461. doi: 10.1023/A:1021866429394.

[237] F. Teklal, A. Djebbar, S. Allaoui, G. Hivet, Y. Joliff, and B. Kacimi. A review of analytical models to describe pull-out behavior – fiber/matrix

adhesion. *Composite Structures*, 201:791–815, 2018. ISSN 02638223. doi: 10.1016/j.compstruct.2018.06.091.

[238] A. T. Nettles, E. D. Gregory, and J. R. Jackson. Using the climbing drum peel (CDP) test to obtain a G_{IC} value for core/face sheet bonds. *Journal of Composite Materials*, 41(24):2863–2876, 2007. ISSN 0021-9983. doi: 10.1177/0021998307079974.

[239] N. Christ, B. M. Scheuring, J. Montesano, and J. Hohe. A Python package for homogenization procedures in fiber reinforced polymers. *Journal of Open Source Software*, 8(87):5295, 2023. doi: 10.21105/joss.05295.

[240] N. Jiménez Segura, B. L. Pichler, and C. Hellmich. Concentration tensors preserving elastic symmetry of multiphase composites. *Mechanics of Materials*, 178:104555, 2023. ISSN 01676636. doi: 10.1016/j.mechmat.2023.104555.

[241] T. Böhlke and C. Brüggemann. Graphical representation of the generalized Hooke's law. *Technische Mechanik*, 21, 2001.

[242] L. Schreyer, B. M. Scheuring, N. Christ, J. Blarr, C. Krauß, W. V. Liebig, K. A. Weidenmann, T. Böhlke, A. Hrymak, and L. Kärger. Continuous simulation of a continuous-discontinuous fiber reinforced thermoplastic (CoDiCoFRTP) compression molding process. In Queen's University Belfast, University Road, Belfast, Northern Ireland, BT7 1NN, editor, *Proceedings of the 2023 International Conference on Composite Materials*. Queen's University Belfast, 2023. doi: 10.5445/IR/1000163456.

[243] N. Christ, J. Montesano, and J. Hohe. Experimental investigation of carbon long fiber reinforced polyamide 6 exposed to environmental conditions. *PAMM*, 22(1), 2023. ISSN 1617-7061. doi: 10.1002/pamm.202200166.

[244] S. A. Suarez, R. F. Gibson, C. T. Sun, and S. K. Chaturvedi. The influence of fiber length and fiber orientation on damping and stiffness of polymer composite materials. *Experimental Mechanics*, 26(2):175–184, 1986. ISSN 0014-4851. doi: 10.1007/BF02320012.

[245] R. Arquier, I. Iliopoulos, G. Régnier, and G. Miquelard-Garnier. Consolidation of continuous-carbon-fiber-reinforced PAEK composites: a review. *Materials Today Communications*, 32:104036, 2022. ISSN 23524928. doi: 10.1016/j.mtcomm.2022.104036.

[246] C. J. Plummer, M. Mauger, P. Béguelin, G. Orange, and J. Varlet. Fracture resistance of mineral reinforced polyamide 6. *Polymer*, 45(4):1147–1157, 2004. ISSN 00323861. doi: 10.1016/j.polymer.2003.12.022.

[247] S. Alessi, G. Pitarresi, and G. Spadaro. Effect of hydrothermal ageing on the thermal and delamination fracture behaviour of CFRP composites. *Composites Part B: Engineering*, 67:145–153, 2014. ISSN 13598368. doi: 10.1016/j.compositesb.2014.06.006.

[248] Y. Zhao, W. Liu, L. K. Seah, and G. B. Chai. Delamination growth behavior of a woven E-glass/bismaleimide composite in seawater environment. *Composites Part B: Engineering*, 106:332–343, 2016. ISSN 13598368. doi: 10.1016/j.compositesb.2016.09.045.

[249] M. Johar, W. Chong, H. S. Kang, and K. J. Wong. Effects of moisture absorption on the different modes of carbon/epoxy composites delamination. *Polymer Degradation and Stability*, 165:117–125, 2019. ISSN 01413910. doi: 10.1016/j.polymdegradstab.2019.05.007.

[250] A. Gagani, A. Krauklis, and A. T. Echtermeyer. Anisotropic fluid diffusion in carbon fiber reinforced composite rods: Experimental, analytical and numerical study. *Marine Structures*, 59:47–59, 2018. ISSN 09518339. doi: 10.1016/j.marstruc.2018.01.003.

[251] H. Ming-Yuan and J. W. Hutchinson. Crack deflection at an interface between dissimilar elastic materials. *International Journal of Solids and Structures*, 25(9):1053–1067, 1989. ISSN 00207683. doi: 10.1016/0020-7683(89)90021-8.

[252] M.-Y. He and J. W. Hutchinson. Kinking of a crack out of an interface. *Journal of Applied Mechanics*, 56(2):270–278, 1989. ISSN 0021-8936. doi: 10.1115/1.3176078.

[253] R. Schapery. Nonlinear viscoelastic and viscoplastic constitutive equations based on thermodynamics. *Mechanics of Time-Dependent Materials*, 1:209–240, 1997. ISSN 1385-2000. doi: 10.1023/A:1009767812821.

[254] J. Keursten. *Thermoviscoelastic Modeling of Thermoplastic Polymers*. KIT Scientific Publishing, 2025. doi: 10.5445/KSP/1000179538.

[255] M. Jamshidi and M. M. Shokrieh. On the Schapery nonlinear viscoelastic model: A review. *European Journal of Mechanics - A/Solids*, 108:105403, 2024. ISSN 09977538. doi: 10.1016/j.euromechsol.2024.105403.

[256] D. Erhardt and M. Mecklenburg. Relative humidity re-examined. *Studies in Conservation*, 39(sup2):32–38, 1994. ISSN 0039-3630. doi: 10.1179/sic.1994.39.Supplement-2.32.

[257] J. J. Horst and J. L. Spoormaker. Fatigue fracture mechanisms and fractography of short-glassfibre-reinforced polyamide 6. *Journal of Materials Science*, 32(14):3641–3651, 1997. ISSN 0022-2461. doi: 10.1023/A:1018634530869.

[258] M. Bulíček, J. Málek, and K. R. Rajagopal. On Kelvin-Voigt model and its generalizations. *Evolution Equations and Control Theory*, 1(1):17–42, 2012. ISSN 2163-2480. doi: 10.3934/eect.2012.1.17.

[259] S. Fliegener and J. Hohe. An anisotropic creep model for continuously and discontinuously fiber reinforced thermoplastics. *Composites Science and Technology*, 194:108168, 2020. ISSN 02663538. doi: 10.1016/j.compscitech.2020.108168.

[260] M. Itskov. *Tensor algebra and tensor analysis for engineers: With applications to continuum mechanics*. Mathematical engineering. Springer, Cham, fifth edition edition, 2019. ISBN 3319988050. URL `http://www.springer.com/`.

[261] J. Lai and A. Bakker. 3-D Schapery representation for non-linear viscoelasticity and finite element implementation. *Computational Mechanics*, 18(3): 182–191, 1996. ISSN 0178-7675. doi: 10.1007/BF00369936.